Dynamics and mechanics of adherent cells in the context of environmental cues

- Impact of substrate topology, chemical stimuli and Janus nanoparticles on cellular properties -

Dissertation
for the award of the degree
"Doctor rerum naturalium"
of the Georg-August-University Göttingen

within the doctoral program *"Molecular Biology of the Cell"*

of the Georg-August-University School of Science (GAUSS)

submitted by
Jan Henrik Rother

from Birkenfeld (Nahe) / Germany

Göttingen 2014

Thesis Committee

Prof. Dr. Andreas Janshoff
Institute of Physical Chemistry
Georg-August-University Göttingen

Prof. Dr. Mikael Simons
Cellular Neuroscience
Max-Planck-Institute for Experimental Medicine Göttingen

Prof. Dr. Dirk Görlich
Cellular Logistics
Max-Planck-Institute for Biophysical Chemistry Göttingen

Members of the Examination Board
Referee:
Prof. Dr. Andreas Janshoff, Institute of Physical Chemistry, Georg-August-University Göttingen

2nd Referee:
Prof. Dr. Mikael Simons, Cellular Neuroscience, Max-Planck-Institute for Experimental Medicine Göttingen

Further members of the Examination Board
Prof. Dr. Dirk Görlich, Cellular Logistics, Max-Planck-Institute for Biophysical Chemistry Göttingen

Prof. Dr. Jörg Enderlein, III. Institute of Physics, Georg-August-University Göttingen

Prof. Dr. Sarah Köster, Institute for X-Ray Physics, Georg-August-University Göttingen

Prof. Dr. Michael Meinecke, Department. of Biochemistry II, Göttingen University Medical School

Date of oral examination: 11.06.2014

I, Jan Henrik Rother, hereby certify that my doctoral thesis entitled "Dynamics and mechanics of adherent cells in the context of environmental cues - Impact of substrate topology, chemical stimuli and Janus nanoparticles on cellular properties -" has been written independently and with no other sources and aids than quoted.

Jan Henrik Rother
29.04.2014
Göttingen, Germany

to my family

Abstract

Cellular behavior is influenced by many biochemical but also physical factors in the direct cellular environment. Thereby, cells not only react to external cues, the interaction between cells and their environment is also dependent on the properties of the cell itself. The endocytosis of nanoparticles for example depends on the intermolecular forces between plasma membrane and particle as well as on the mechanical properties of the membrane. In the first part of this thesis I focus on the interaction between inorganic Janus nanoparticles, a new type of nanomaterials, which possess amphiphilic properties, and model membranes. In coarse grain simulations it has been demostrated that incubation of membranes with these particles lead either to pore formation in the lipid bilayer or to tubulation and vesiculation by long-range attractive interaction between particles bound to the membrane. Conducting surface plasmon resonance spectroscopy experiments I show that the binding energy of the used inorganic Janus particles to a solid supported monolayer could be sufficient to induce tubulation of tension-free membranes but is to small to provide the energy necessary to form a vesicle. This result is confirmed by fluorescence microscopic examination of giant unilamellar vesicles serving as a model system for the plasmamembrane, which were treated with Janus particles. Vesicles incubated with Janus particles show inwards directed membrane tubes, while incubation of vesicles with isotropic control particles had no effect on the membrane or could be attributed to an osmotic gradient. However, uptake experiments into living cells and cytotoxicity assays show no obvious difference between spherical particles and Janus particles, which hints for a negligible contribution of nanoparticle-induced tubulation or vesiculation to cellular uptake of nanoparticles and cytotoxicity.

On the one hand mechanical properties of the cell influence the interaction between the cell and its environment. On the other hand, mechanical properties of cells change in response to environmental cues. Therefore, in the next part, atomic force microscopy-based microrheology is used to measure frequency-dependent mechanical properties of cells in different conditions. Fixation of cells with different chemical fixatives and transformation of epithelial cells to mesenchymal cells lead to more solid-like mechanical properties, while interaction with the actin cytoskeleton lead to more fluid-like properties. A comparison between malignant cells and non-malignant cells shows that malignant cells are more fluid-like compared to their non-malignant counterparts. Furthermore, the influence of substrate topology on cellular mechanics and cytoskeletal arrangement is examined. Changing physical properties of the

substrate such as stiffness or topography has been shown to affect plenty of cellular processes like migration, proliferation, morphology or differentiation. Here, I investigate the impact of porous substrates on cellular morphology, cytoskeletal organization and elasticity in the context of confluent epithelial monolayers. I found that cells eventually self-organize to match the geometry of the pore pattern and remodel their actin cytoskeleton to reinforce their adhesion zone. Cells fluidize with increasing pore size up to 2 µm but eventually become stiffer if grown on very large pores up to 5 µm.

The adhesion of cells to substrates is further researched by application of metal-induced energy transfer fluorescence lifetime imaging, which is used for the first time for this purpose. The fluorescence lifetime of a fluorophore in proximity to a metal layer is a function of the distance between fluorophore and metal layer. Applying a quantitative model of this interaction facilitates locating the fluorophore with nanometer precision in the axial direction up to 200 nm above the metal layer. By staining of the plasmamembrane I was able to image to basal membrane of three different cell lines and follow spreading of cells with high axial resolution. The introduced method is not restricted to measurement of cell/substrate distance and can be used for applications, which necessitate axial nanometer resolution in a range up to 200 nm.

Table of Content

1. Introduction

During their life cycle, cells are subject to various external cues. In an organism, biochemical signaling via hormones and other messenger molecules is crucial for physiological processes and cell function. An example of a response of cells to a biochemical cue is the epithelial-to-mesenchymal transition (EMT), which plays an important role during in physiological processes like tissue development and wound healing.(Kalluri and Weinberg, 2009) The result of this biochemically triggered event is the transition of cells from an epithelial state into a mesenchymal, more motile phenotype, which encompasses loss of cell-cell contacts as well as cytoskeletal rearrangement. Albeit, EMT can also contribute in a pathophysiological processes like tumor progression. (Thiery, 2002) A key step in the formation of metastasis is the detachment of tumor cells from the primary tumor and invasion into the surrounding tissue, which could be initialized by EMT.(Kumar and Weaver, 2009)

Furthermore, not only soluble molecules or hormones like TGF-β in the cell's environment influence the behavior of a cell, also chemical composition, topography and the rigidity of the underlying substrate are crucial for cellular behavior. In the last decades it has also been demonstrated that rigidity as well as porosity of the substrate influence migration and proliferation of cells and interestingly, is able to direct the fate of stem cell differentiation.(Clark *et al.*, 1991; Engler *et al.*, 2006; Lo *et al.*, 2000; Teo *et al.*, 2013; Wang *et al.*, 2000) Substrate properties are usually sensed via focal adhesions, which facilitate cell adhesion via heterodimeric transmembrane receptors called intergrins. On intracellular side these receptors are associated with a vast variety of proteins including the actin network.(Geiger *et al.*, 2009) Thereby, the tension generated by the actomyosin cytoskeleton has been shown to be crucial for mechanosensing as well as force generation demonstrating a direct link between substrate properties, cellular shape and mechanics.(Janshoff *et al.*, 2010; Tee *et al.*, 2011; Wolfenson *et al.*, 2011)

From a physics point of view an eukaryotic cell consists of a thin, largely inextensible shell made of surfactant molecules, which is filled with an aqueous, colloidal solution of proteins as well as flexible biopolymer networks or gels that are attached to the outer shell via linkers. (Boal, 2012; Zhou *et al.*, 2009) All together contribute to shape and mechanical resistivity of the cell over a wide range of extensional and compressional stresses.

Interaction between an extracellular particle, i.e. a nanoparticle, and a cell is largely governed by membrane mechanics and the strength of the intermolecular forces between membrane and particle as shown in coarse grain simulations.(Yue *et al.*, 2014) Isotropic particles have been demonstrated to be wrapped by the membrane or form inverse micellar structures within the membrane and are usually taken up by the cell via common endocytotic pathways. (Treuel *et al.*, 2013; Yue *et al.*, 2014) However, in recent years a new subset of nanoparticles emerged. Janus particles or grains, named after the two-faced roman god by soft matter physicist Pierre-Gille de Gennes in his nobel lecture, are anisotropic and possess amphiphilic properties.(De Gennes, 1992; Wurm and Kilbinger, 2009) Coarse grain simulations by Reynwar *et al.* and Alexeev *et al.* showed that these particles have effects on the membrane, which differ from the effect of isotropic particles: Janus particles were able to induce large membrane deformations, vesiculation or pore formation. (Alexeev *et al.*, 2008; Reynwar *et al.*, 2007) On the one hand, these mechanisms could be used in medical applications for drug delivery to circumvent the membrane barrier of cells and increase uptake rates substantially. On the other hand, an unintended uptake of nanomaterials by cells could pose threat to human health. Therefore, profound knowledge of the interaction between cells and these new nanoparticles is necessary and experimental evidence for the proposed types of interactions between particles and membrane has to be provided.

The first part of this thesis will focus on the effects of Janus nanoparticles and their isotropic counterparts on artificial membranes and living cells. Giant unilamellar vesicles (GUVs) serve as a model system for the cellular membrane. The influence of Janus particles on the GUVs is followed using confocal laser scanning microscopy. To quantify the interaction between particles and membrane surface plasmon resonance spectroscopy is employed. Furthermore, uptake of the particles is evaluated by fluorescence microscopy. Finally, cytotoxicity of the particles is measured using electric cell-substrate impedance sensing as well as biochemical assays.

As demonstrated in the first part, cellular mechanics play an important role in the interplay between cells and their environment. Therefore, mechanics of cells exposed to different external stimuli will be examined in the next part of this thesis. For this purpose, a technique introduced by Alcaraz *et al.* is introduced in the laboratory enabling the measurement of frequency dependent rheological data using the atomic force microscope.(Alcaraz *et al.*, 2003) This technique is used to measure the influence of different chemical drugs and the aforementioned epithelial-to-mesenchymal transition on cellular mechanics. Furthermore, to compare benign and malign cells according to their mechanical properties, rheological properties of eight different cell

lines with diverging metastatic potential are measured. A difference in the mechanical behavior of malignant and non-malignant cell lines is found. Then, the influence of substrate properties on cellular mechanics and cytoskeletal arrangement is evaluated showing reorganization of the actin cytoskeleton in cells grown on porous substrates, which is accompanied by a softening of cells.

In the final chapter of this thesis, a new technique is presented, which enables measurement of distances between a fluorophore and a metal mirror with nanometer precision by metal-induced energy transfer (MIET) fluorescence lifetime imaging. The method is based on the distance dependent modulation of the fluorescence liftetime of a fluorophore in proximity to a metal a layer up to a fluorophore/metal layer distance of approximately 200 nm. As a first application the distance between the basal membrane of three different cell lines and the substrate is measured. Additionally, the spreading process of cells was followed. However, the method is not restricted to the mapping of the basal membrane of living cells and can be used for applications, which necessitate nanometer resolution in a distance range up to 200 nm.

2. Principles

2.1   Structure of eukaryotic cells and communication with their environment

Life on earth exists for more than three billion years. (Zimmer, 2009) The first living organisms were prokaryotes and, back then as well as today, they hardly consist of more than some water-soluble molecules like RNA and Proteins enveloped by a lipid bilayer. First eukaryotic cells emerged 2 billion years ago. (Zimmer, 2009) In contrast to prokaryotes, these cells carry their genetic information in form of DNA in a separate compartment inside the cell, the nucleus. Furthermore, other important functions are allocated to specialized cellular organelles (see Figure 2.1). Translation of the genetic code into proteins is facilitated by ribosomes, which are located at the rough endoplasmic reticulum.
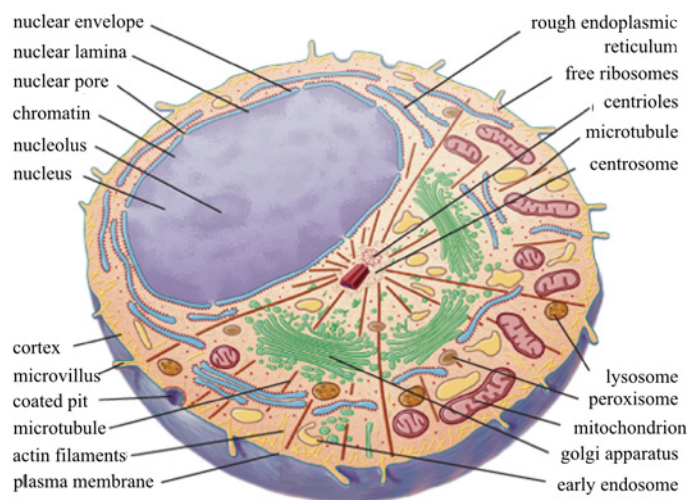
Figure 2.1: Scheme of a eukaryotic cell and its organelles. The cell is enveloped by a plasma membrane, which mainly consists of lipids and embedded or associated proteins. The organelles are located in the aqueous cytosol. The nucleus carries the chromosomes. Ribosomes at the endoplasmic reticulum translate the genetic code into proteins. The Golgi apparatus distributes vesicles and proteins in the cell. Lysosomes are acidic compartments, which are responsible for the digestion. Mitochondria produce the cells energy. The cytoskeletal biopolymers f-actin, the intermediate filaments and the microtubules are involved in cellular transport processes, endocytosis, cell division and migration and are responsible for the cell's structure and morphology. (Pollard *et al.*, 2008)

The Golgi apparatus is responsible for sorting and shipping of vesicles and proteins inside the cell. Other important compartments are the lysosomes, in which nutrients and other molecules are digested. The main task of mitochondria is the production of

the cell's energy in terms of adenosine triphosphate (ATP), but they are also involved in other cellular processes. Mitochondria differ from the before-mentioned organelles. They are surrounded by an additional membrane and possess a short strand of mitochondrial DNA. (Pollard *et al.*, 2008) All cellular organelles "swim" in an aqueous solution called cytosol. They are arranged by cytoskeletal elements, which also define cellular morphology. The cytoskeleton consists of three different filament classes, namely the actin filaments, the intermediate filaments and the microtubules, and is involved in many processes like transport of cargoes, endo- and exocytosis, migration and cell division. A more detailed description of the cytoskeleton and its elements can be found in chapter 2.1.1.

In the following subchapters I will address the cellular structural elements and processes, which are relevant for the understanding and motivation of this work.

2.1.1 Structure, function and mechanical properties of the cytoskeleton

The cytoskeleton consists of three different biopolymers: f-actin, intermediate filaments and microtubules. In general, as structural elements they provide mechanical stability to the cell, but also fulfill many other tasks. For example, during mitosis microtubules first form the spindle apparatus, which separates the sister chromatids from each other. Later, a ring-like structure of actin filaments and myosin II motor proteins facilitates cytokinesis, the cleavage of the mother cell in two daughter cells. As another example, in the respiratory tract, ciliated epithelial cells cover large areas: The cilia are located at the apical side of the cells and are mainly supported by microtubules. Like a broom, the cilia remove pathogens and debris stuck to the mucus from the respiratory tract by active motion produced by motor proteins acting on the microtubule filaments.(Alberts, 2002) In striated muscle cells a regular arrangement of actin filaments and myosin motors together with other actin bundling proteins facilitate a strong, directed contraction of the cell. The present chapter will deal with the structure of the filament types and their arrangement in cells, their tasks as well as their mechanical properties.

2.1.1.1 Microtubules

Microtubules have a tubular structure with an outer diameter of 25 nm and are the thickest of the three biopolymers that compose of the cytoskeleton. The inner diameter comes to 14 nm.(Mofrad and Kamm, 2006) Microtubules consist of α- and β-tubulin monomers, which bind to each other non-covalently and form dimers (see Figure 2.2 A). Each subunit has a molecular mass of approximately 55 kDa and possesses a binding site for guanosin di- or triphosphate (GDP/GTP). Energy from GTP promotes polymerization of microtubules. In the dimer, the GTP binding site of the α-tubulin subunit is nonexchangeable, whereas the GTP at the β-subunit is accessible. If a tubulin dimer binds to an existing microtubule, the contact between the freshly bound α-subunit and the β-subunit at the microtubule accelerates the hydrolysis of GTP at the β-subunit. Thus only the end of microtubules is capped by GTP-bound tubulin dimers, the rest of the microtubule consists of GDP-bound tubulin. If the GTP cap is lost, the microtubules undergo fast depolymerization, a process called catastrophe. By association of GTP-tubulin dimers, the microtubule can grow again. Like actin filaments, microtubules are polarized and possess a plus and a minus end. Association of dimers is faster at the plus end.
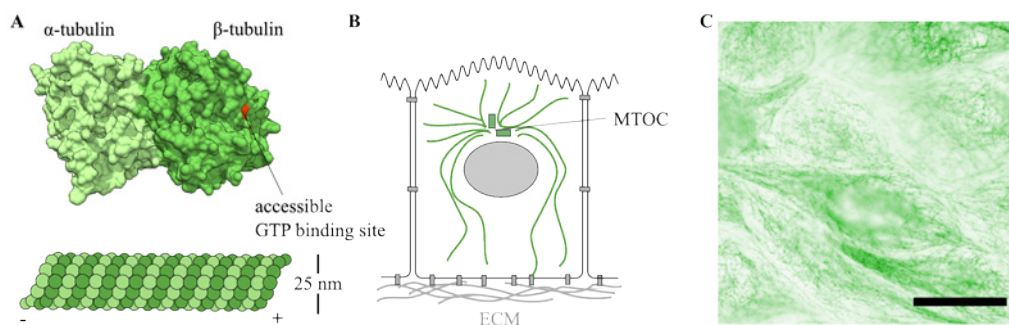
Figure 2.2: Structure of α- and β-tubulin and structure of the microtubules. **A** Structure of a α- and β-tubulin dimer (pdb-file: 1TUB) and structure a single microtubule. Microtubules have cylindrical structure and consist of 11 to 16 protofilaments, which are arranged longitudinally. **B** Schematic drawing of microtubule structure in an epithelial cell. The microtubules spread out from the microtubule-organizing center (MTOC), which is usually located in proximity to the nucleus. **C** Epi-fluorescence image of β-tubulin in MDCK-II cells stained with an Alexa 488-conjugated IgG (pseudocolored). Scale Bar: 20 μm

Growth of microtubules *in vivo* starts in most cases at the microtubule-organizing center, which in most animal cells consists of the centrioles. The centrioles are specialized structures build of two nine microtubule triplets with nearly orthogonal orientation. In the centrioles, the tubulin isoform γ-tubulin serves the nucleation of

tubulin dimers.(Pollard *et al.*, 2008) Due to elongation at the plus end most microtubules in animal cells show orientation from the centrioles (minus end) to the periphery (plus end). Microtubule dynamics are influenced by a large number of microtubule-associated proteins. Microtubules take over important tasks in cells. During mitosis, microtubules form the mitotic spindle, which facilitates the separation of chromatids. In the interphase, microtubules serve as "rails" for motor proteins, which transport cargoes. The two most important motor proteins, that use microtubules as substrate, are kinesin and dynein. Due to the polarity of the microtubules, the proteins show oriented movement, albeit in opposite directions. Dynein transports cargoes from the plus end to the minus end, whereas kinesin moves from minus to plus end. Compared to the other types of cytoskeleton microtubules are rigid rods with a long persistence length L_p in the millimeter regime and a bending rigidity κ_b of 2.6×10^{-23} N/m^2. The elastic modulus is in the range of 1.9 GPa. (Suresh, 2007)

2.1.1.2   Intermediate filaments

Intermediate filaments encompass a group of structural proteins that can be found in eukaryotic cells, which are mainly important for the mechanical stability of the cell. The name "intermediate filaments" results from their thickness of 10 nm, which lies between the diameter of actin filaments and the diameter of microtubules. All intermediate filaments have in common that the monomers consists of head- and tail-domain connected by a rod domain with predominantly α-helical structure. The amino acid sequence varies among the different intermediate filament types. Via non-covalent interactions in the rod-domains, intermediate filaments are able to form dimers, in which the two rod-domains exhibit coiled-coil structure. One organizational level above, two dimers merge to tetramers, where the two dimers align in opposite direction and thus breaking the polarity of the filaments. By further assembly, smooth and flexible intermediate filaments are formed. (Herrmann *et al.*, 2009) The distribution of intermediate filaments is schematically shown in Figure 2.3 B. The type of intermediate filaments expressed by a cell largely depends on the cell type except for lamins, which can be found in the nucleus of most cells. Cells of mesenchymal origin like fibroblasts, for example, express vimentin, whereas epithelial cells express keratins (see Fig. 3 C).
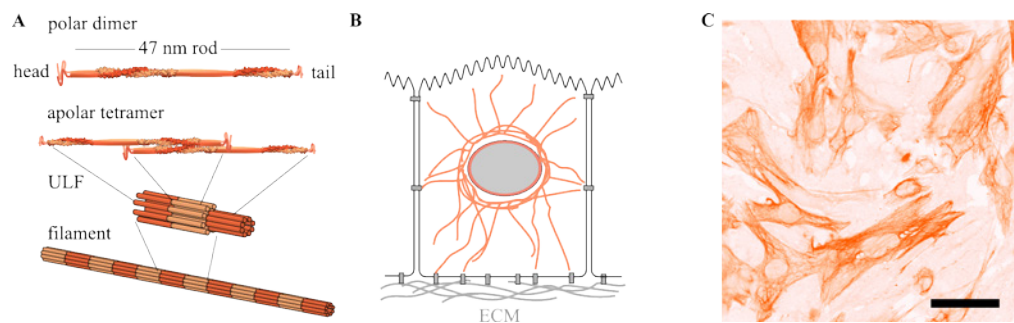
Figure 2.3: Structure of intermediate filaments and arrangement in eukaryotic cells. **A** Organization of (cytosolic) intermediate filaments. Two monomers form a polar dimer, in which the two rod-regions have a coiled-coil structure (here vimentin fragments, pdb-files: 1GK4 and 2HF4). These dimers assemble to tetramers, where the dimers align in opposite direction, thus, breaking the polarity of the filament. Eight tetramers aggregate to a unit-length filament (ULF), which are the building blocks of the intermediate filaments.(Herrmann *et al.*, 2009) **B** Schematic drawing of intermediate filaments in epithelial cell. Epithelial cells express lamin filaments, which decorate the inner membrane of the nuclear envelope, and keratins in the cytosol. Intermediate mediate are also associated to cell-cell and cell-substrate contacts. **C** Epifluorescence micrograph of labeled vimentin in cardiac fibroblasts (Image has been recorded by Jan Rüger, Max-Planck-Institute for Dynamics and Self-Organisation, Göttingen). Scale bar: 30 µm

Proteins associated with intermediate filaments link them to the plasma membrane, e.g. desmoplakin, to the other cytoskeletal elements, e.g. plectin, or in the case of lamins to the inner membrane of the nuclear envelope. Intermediate filaments have a short persistence length of only a few micrometers. Their elastic modulus is in the range from 1 to 5 GPa. The bending modulus κ_b exhibits a value of $(4 - 12) \times 10^{-27}$ N/m^2. (Suresh, 2007)

2.1.1.3   Actin cytoskeleton

Actin filaments are the polymeric form of actin monomers (also globular actin or g-actin). The filaments possess a diameter of 9 nm and are polarized, which facilitates directed motion of motor proteins or directed growth. The structure of the monomers and filamentous actin is depicted in Figure 2.4 A. The monomers have molecular weight of 42 kDa and are able to hydrolyze ATP. Actin polymerization is dependent on the presence of ATP or ADP and divalent cations. Each monomer has one binding site for ATP/ADP. Actin is able to polymerize in both ATP- and ADP-bound state. But the critical concentration of polymerization is lower (0.06 µM) in ATP-bound state compared to the critical concentration in ADP-bound state (0.6 µM).(Le Clainche and Carlier, 2008) This means, that at concentrations above 0.06 µM, ATP-bound actin polymerizes to filaments and hydrolyzes ATP to ADP. If the concentration of ADP-actin is under its critical concentration the filament start to depolymerize at this end. The end

of the filament, at which ATP-actin polymerizes is called barbed end, the other end is called pointed end. In equilibrium state, polymerization at the barbed end and depolymerization at the pointed end exhibit the same rate. Thus, the length of the filament stays constant, but its position relative to a surface changes. Cells like keratinocytes use this process called "treadmilling" for migration. The filaments exert a protrusive force on the membrane and thus push it forwards. The speed of turnover is influenced by a variety of proteins that influence for example the rate of depolymerization (e.g. cofilin) or the rate of ADP exchange in actin monomers (e.g. profilin) thus increasing the concentration of ATP-actin. Other proteins facilitate a branching of the filaments. At focal adhesions (FAs), specialized connection, which facilitate the adhesion of a cell on the underlying substrate, actin filaments form thick bundles, so-called stress fibers. FAs are discussed in more detail in chapter 2.2. Proteins, i.e. α-actinin and filamin, achieve bundling of actin filaments into stress fibers. Pronounced stress fibers can be found in cells, which adhere strongly to their surrounding and show slow migration like fibroblasts or epithelial cells. Additionally, actin filaments form a dense network in the cortex, giving the cell its shape and mechanical stability (see Figure 2.4).
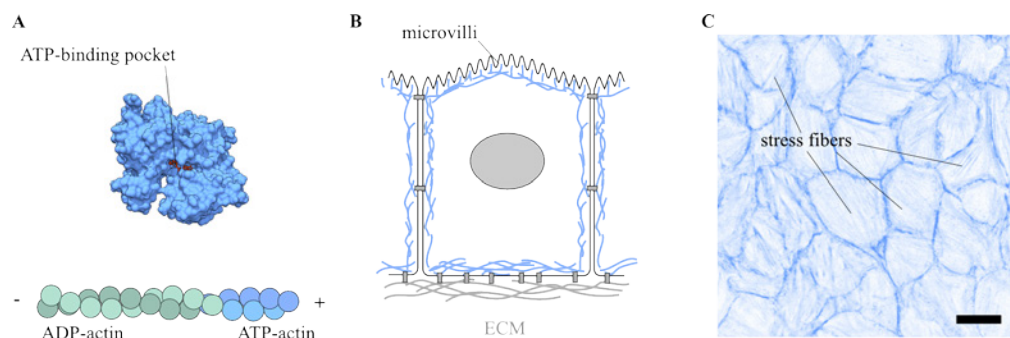

Figure 2.4: Structure of actin monomers and filaments and arrangement of actin cytoskeleton in epithelial cells. **A** Structure of the actin monomer (PDB-file: 2HF4) and schematic drawing of an actin filament. Polymerization of actin takes place ATP-actin at the barbed end (+ end), the filaments depolymersize at the pointed end (- end) **B** Schematic drawing of the actin cytoskeleton structure in epithelial cells. The actin network is strongly connected to the cell-cell and the cell-substrate junctions **C** Confocal image shows the basal actin network of confluent MDCK-II epithelial cells (Alexa546-labeled phalloidin, pseudocolored). Scale Bar: 20 μm

According to electron microscopic images, the cortical actin network shows mesh sizes ranging from 20nm to 250nm and has usually a thickness of 50 nm to 1 μm. (Salbreux *et al.*, 2012). At the apical surface of epithelial cells, the actin cytoskeleton supports the microvilli, finger-like membrane protrusions that increase the surface of cells involved in secretion and absorption. The actin cortex is strongly connected to the plasma membrane via linker proteins for example of the ezrin-radixin-moesin family. (Arpin *et*

al., 2011; Bretscher, 1999) Additionally, adherens junctions as well as tight junctions, which connect one cell to another, are strongly coupled to the cortical actin network (see Figure 4 B and C). Due to the polar structure of single filaments, the actin network is also able to exert contractile forces via motor proteins, i.e. myosin II. In striated muscles like the heart muscle and skeletal muscles periodic arrangement of f-actin and myosin II facilitate the directed contraction of the muscle cells. In epithelial cells, myosin II is responsible for the maintenance of cortical tension and plays an important role during cytokinesis as it facilitates the force generation of the contractile actin ring. With an elastic modulus of 1.3-2.5 GPa, actin filaments exhibit a comparable elasticity to microtubules. (Suresh, 2007) The persistence length L_p of actin filaments is on the order of micrometers and hence three orders of magnitude smaller compared to the persistence length of microtubules (L_p(actin) = 15 µm). This is also reflected in the smaller bending rigidity κ_b of actin (κ_b(actin) $= 7 \times 10^{-26} N/m^2$).(Suresh, 2007)

2.1.1.4   Stress-Strain-Relationship of cytoskeletal biopolymer networks

Experiments by Janmey and coworkers probing the stress-strain relationship of the different cytoskeletal elements in solution by a torsion pendulum revealed that actin shows the highest resistance to external stress among the probed filament types up to a certain critical point, at which the filaments rupture (see Figure 2.5). (Janmey *et al.*, 1991) Microtubules exhibit the lowest resistance to externally applied forces as low stresses already result in strains up to 60%. Both, the actin and the microtubules, show a nearly linear relation between stress and strain, which corresponds to elastic behavior. In contrast, the tested intermediate filament types show strain stiffening, meaning that at larger strains one needs more stress to achieve a certain increase in strain than at lower strains. Note, that the slope of the curves corresponds to the elastic modulus of the respective filament solution.
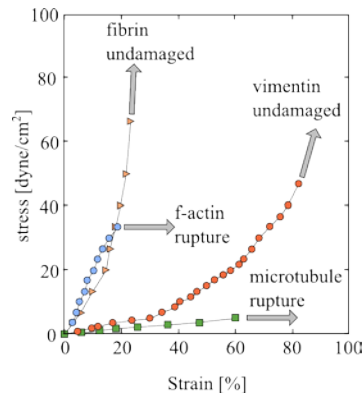
Figure 2.5: Stress-strain relationship of polymer solutions of different cytoskeletal elements measured by a torque pendulum (f-actin, fibrin, vimentin, microtubules). (Reproduced and modified from (Janmey *et al.*, 1991))

These findings, together with the arrangement of actin-filaments in the cortex and its strong connection to the plasma membrane, suggest that the actin cytoskeleton is the most important cytoskeletal structure, when a cell experiences externally applied stress.

2.1.2 Cells exposed to mechanical or topological cues

Cells are able to translate mechanical cues into biochemical or electrical signals, a process called mechanotransduction. Not only sensory cells like the hair cells in the inner ear show this capability, but rather all cell-types. Mechanotansduction is crucial for many cellular functions like migration, proliferation or apoptosis.(Lo *et al.*, 2000; Trichet *et al.*, 2012; Wang *et al.*, 2000) Interestingly, it has also been shown that mechanotransduction can also direct stem cell differentiation. (Engler *et al.*, 2006) However, despite knowledge about multiple effects of mechanical cues on cell behavior, only little is known about the molecular background, by which cells sense the physical properties of their surrounding. Different mediators thought to be involved in mechanotransduction have been reviewed by Donald Ingber.(Ingber, 2006) It is indisputable that stretch-activated ion channels play a role in signal transduction in some cell types like the hair cells in the inner ear. Other mechanical sensors include nuclear structures, cytoskeletal filaments and crosslinkers or cell-cell as well as cell-substrate contacts. To sense changes in substrate rigidity, composition or topography, signaling via integrin-mediated focal adhesion plays a pivotal role.(Geiger *et al.*, 2009)Integrins are transmembrane receptors formed by a α- and a β-integrin subunit. On the extracellular side, the receptors bind to extracellular matrix proteins like fibronectin or collagen. At the intracellular domain, they are associated to the actin

cytoskeleton via adaptor proteins on the one hand, but on the other hand to a huge number of different proteins, e.g. the protein kinase C (PKC), the tyrosin kinase Src or the focal adhesion kinase (FAK), involved in many cellular processes like migration or proliferation (see Figure 2.6). (Geiger *et al.*, 2009) A detailed picture of proteins and cofactors involved in focal adhesion signaling can be found at http://www.adhesome.org (06.01.2014). The maturation of initial focal complexes, which are formed at the cell edges as initial cell substrate contacts, into focal adhesions has been shown to be dependent on tension generated by the actin network in combination with myosin II.(Geiger and Bershadsky, 2002; Wolfenson *et al.*, 2011)
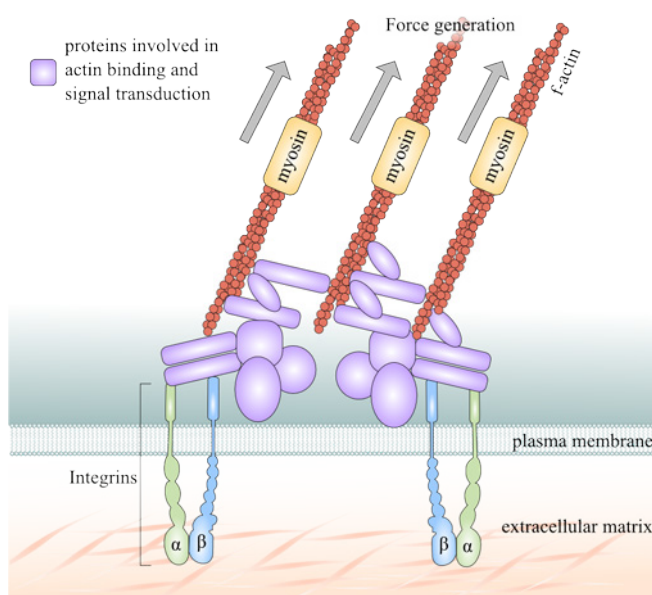

Figure 2.6: Schematic drawing of focal adhesion complex and mechanotransduction. Heterodimeric intergrin receptor binds to specific binding motifs on extracellular matrix proteins. Several proteins involved in actin binding and signaling like talin, vinculin, paxillin, FAK or Src bind to the intracellular domain of the receptor. Some of these associated proteins have already been shown to be force-sensitive enabling them to transduce mechanical signals. Force generation by actin and myosin is a key feature of focal contacts. Inhibition of myosin for example leads to a degeneration of mature focal contacts. (Scheme modified from (Mitra *et al.*, 2005) and (Geiger *et al.*, 2009))

Following this observation, integrin-mediated mechanotransduction may be facilitated by a stretch-mediated exposure of the active or binding site of proteins via stretch-induced conformational changes. An example is the binding of vinculin to talin in nascent focal complexes. As long as no force is applied to talin, some of its vinculin-bindings sites are buried within a five-helix bundle.(Papagrigoriou *et al.*, 2004) Conformational changes, induced by an externally applied force as demonstrated by Sheetz and coworkers, lead to an exposure of additional binding sites and facilitate binding of one or two vinculin molecules, which could lead to force-dependent changes

in signaling. (del Rio *et al.*, 2009) Vinculin, for instance, has been discussed as a mechanosensitive molecule itself, presenting a binding site for MAPK1 (mitogen-activated protein kinase 1) under force-induced conformational changes due to acto-myosin-mediated tensile force.(Holle *et al.*, 2013) MAPK1 plays a role in many cellular processes including proliferation or differentiation. Another player in the mechanotransduction machinery of focal adhesions is the actin-crosslinking protein filamin A. Recently it has been demonstrated, that mechanical load applied to filamin A-crosslinked actin networks reveals a cryptic β-integrin binding site in filamin A. At the same time the filamin A-binding GTPase FilGAP, which influences the activity of the small GTPase Rac, dissociates from filamin A. (Ehrlicher *et al.*, 2011)

Arnold and coworkers found another interesting feature of focal adhesion-based mechanotransduction. (Arnold *et al.*, 2004) In their experiments, they used small gold-nanoparticles coated with Arg-Gly-Asp-peptides (RGD), a well-known ligand of integrins, which is present on the surface of ECM proteins, to vary the spacing between single integrin receptors in cells. Interestingly, mature focal adhesions could only be found in cells seeded on substrates with ligand spacing fewer than 58 nm. Additionally, larger distances between adhesive ligands also resulted in a smaller cell number on the substrate and impaired cell spreading. This behavior has been observed for several cell-types leading to the conclusion that this might be a universal response. This experiment shows that mechanotransduction needs to be amended by a topographic component and, indeed, topographical cues on different dimensions ranging from nm to µm-scale have been found to induce cellular responses as divers as observed for mechanical stimuli. The effects of topographical cues include alignment to topographical features, changes in protein expression and activation and changes in migration. (Curtis and Wilkinson, 1997; Yamamoto *et al.*, 2007) Recently it also been demonstrated that nano-grated polydimethylsiloxane (PDMS) surfaces are able to induce human stem cell differentiation through focal adhesion signaling. (Teo *et al.*, 2013) Further influences of topographical features of the substrate on cell behavior will be discussed in detail in chapter 4.4.

These few examples demonstrate the complexity of integrin-mediated mechanotransduction, which takes place at several levels of focal adhesion organization. Furthermore, mechanotransduction is not an on/off-switch as demonstrated on molecular level by the force-dependent exposure of additional vinculin binding sites on talin rod.(Papagrigoriou *et al.*, 2004) On whole-cell level, the cell reacts to subtle changes in the cell's mechanical and topographical environment by an adapted response, which includes differentiation into one cell-type or another,

durotaxis, a phenomenon, in which cells migrate along stiffness gradients in substrates towards regions with higher stiffness, or also changes in cellular mechanics.(Engler *et al.*, 2006; Janshoff *et al.*, 2010; Lo *et al.*, 2000; Tee *et al.*, 2011; Teo *et al.*, 2013; Trichet *et al.*, 2012)

Regarding the variety of proteins involved in mechanotransduction and the multiple processes that are governed by this process, it is not surprising that multiple diseases are associated to deregulations of the mechanosensing machinery. In their review "Mechanotransduction gone awry", Jaalouk and Lammerding address different diseases, which can, at least partly, be retraced to misregulation or mutations of proteins involved in mechanotransduction. (Jaalouk and Lammerding, 2009) Besides deafness and diseases related to the eye, the authors also discussed the role of mechanical cues in the context of cancer development, which will be subject of the next subchapter.

2.1.2.1   Role of mechanotransduction in cancer

In 2000 Hanahan and Weinberg published their famous review about the "Hallmarks of cancer".(Hanahan and Weinberg, 2000) In their review they state six essential alterations, which go along with malignant cell transformation, which are: self sufficiency of growth signals, insensitivity to anti-growth signals, limitless replication potential, angiogenesis, evading apoptosis as well as invasion and metastasis. In recent years it has become clear, that some of these hallmarks can also be related to a malfunction in mechanotransduction.(Jaalouk and Lammerding, 2009) Tumors are generally stiffer than the surrounding normal tissue and this phenomenon is still used for tumor detection by palpation. Recently, it has been found that stiffening of the tumor is governed by oxidation and crosslinking of the ECM, i.e. collagen.(Leventual *et al.*, 2009) It has been proposed that this stiffening of the ECM is able to promote tumor growth and progression. Paszek *et al.* were able to demonstrate that increased substrate rigidity is able to drive malignant transformation by integrin-mediated mechanotransduction (see Figure 2.7). (Paszek *et al.*, 2005) Non-malignant cells grown on stiff matrices exhibited a disruption of normal cell polarity, delocalization of proteins associated to cell-cell adhesions, increased growth and also showed a higher tension.
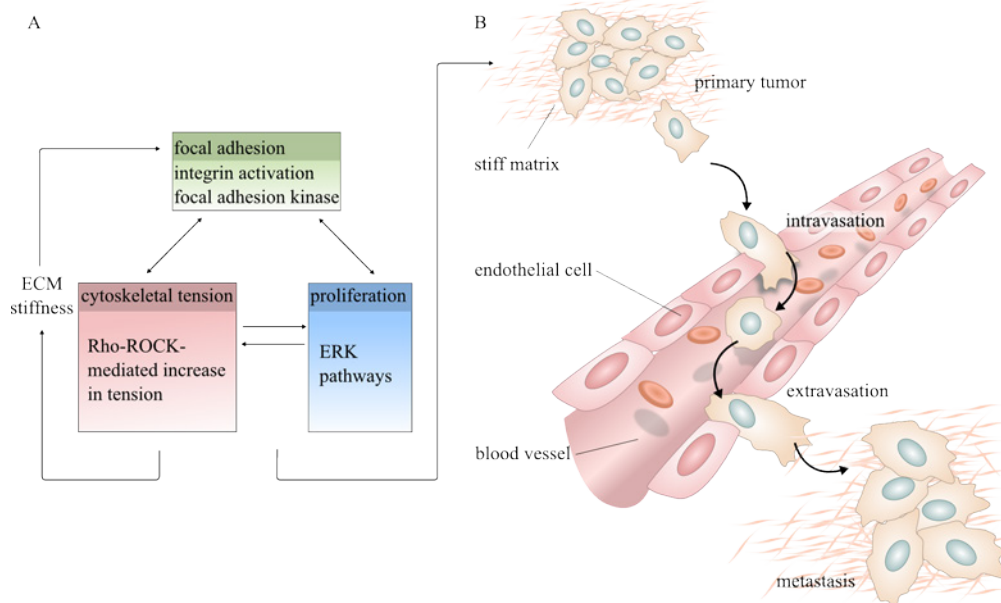
Figure 2.7: Mechanotransduction in tumor cells and formation of metastasis. **A** Mechanotransduction, cytoskeletal arrangement and tension are strongly connected to each other. In cancer cells, a stiffened extracellular matric (ECM) leads to more pronounced focal adhesions and activation of focal adhesion kinase (FAK). Downstream mediators of FAK are among other extracellular signal regulated kinase pathways leading to proliferation and stimulation of Rho-ROCK pathways, increasing the tension of the cytoskeletal network. This increase of tension in turn, enhances the maturation and formation of focal adhesion generating a positive feedback loop. (modified from (Jaalouk and Lammerding, 2009)) **B** In the formation of metastasis, transformed cells that detach from the primary tumor are subject to many mechanical cues and therefore need to adapt to different environmental situations (see also (Kumar and Weaver, 2009)). During intravasation into blood or lymphatic vessels cells need to be very deformable. Via the vascular system cancer cells are able to spread and form metastasis.

The authors found these effects to be dependent on integrin-mediated signaling via a extracellular signal regulated kinases (ERK) and Rho-ROCK-dependent tension generation. However, although whole tumors are usually stiffer than their surrounding and single tumor cells are supposed to be under high tension, a critical step in formation of metastasis is the detachment of single cells from the primary tumor as well as intra- and extravasation, a process demanding high deformability of the cell (see Figure 2.7). Thus, it might not be surprising, that cancer cells have often found to be softer than normal cells of the same tissue.(Agus *et al.*, 2013; Cross *et al.*, 2007; Guck *et al.*, 2005; Xu *et al.*, 2012) This effect is thought to be the result of massive cytoskeletal rearrangements in cancer. (Kumar and Weaver, 2009) Additionally, cancer cells have been shown to lose the requirement to adhere to a substrate and show less sensitivity to substrate rigidity, which possibly facilitates their survival while circulating in the vascular system. (Agus *et al.*, 2013; Wang *et al.*, 2000; Wittelsberger *et al.*, 1981) However, malignant transformation is not entirely dependent on mechanotransduction and it needs mutations, i.e. misregulations, in other proteins, for

example involved in cell cycle or DNA repair, to develop cancer. But, the mentioned examples show, that malignant transformation is at least partially governed by mechanical cues leading also to massive structural and mechanical changes of the cell itself. Therefore, I examine cellular mechanics of cell lines with different metastatic potential in chapter 4.3.

2.1.3 Epithelial-to-mesenchymal transition

Epithelial-to-mesechymal transition (EMT) describes a process, in which epithelial cells dedifferentiate into mesechymal cells. EMT plays an important role in embryonic development and the formation of organs.(Kalluri, 2009) Furthermore, EMT is related to wound healing and fibrosis in the adult organism. But, besides these physiological tasks, this process is also discussed to play a pivotal role in cancerogenesis by transforming tumor cells into motile metastatic phenotypes. The relation between cancer and EMT has been reviewed by Thiery.(Thiery, 2002) In general, EMT is initiated by biochemical stimuli involving different growth factors. One of the most important inducers of EMT is the cytokine transforming growth factor-β (TGF-β1). TGF-β1 binds to transmembrane receptors located in the plasma membrane. The receptor belongs to the receptor tyrosine kinases. Upon binding of the ligand, heterotetramers composed of two TGF-β type-1 and two TGF-β type-2 receptor subunits are formed. On intracellular side, activation of the receptor leads to activation of a variety of downstream signals including SMAD-family proteins (Small Mother Against Decapentaplegic), which can directly act as transcription factors. The effects of EMT on the cell include loss of cell-cell-contacts concomitant with loss of basal/apical-polarization, tremendous cytoskeletal rearrangements, ECM synthesis and increased motility.(Radisky, 2005) The effects of TGF-β1 induced EMT on the mechanical properties of NMuMG cells will be subject of chapter 4.2.

2.1.4 Uptake-mechanisms in eukaryotic cells

The cellular membrane separating the cytosol from the extracellular environment has the function of a highly selective, but active barrier, which is able to transmit mechanical, electrical as well as biochemical cues. (Zellner *et al.*, 2013) The plasma membrane is build by an asymmetric lipid bilayer composed of glycerophospholipids, sphingolipids, cholesterol and embedded or associated proteins, which serve for signal transduction or also as selective gates. For example, some ions are allowed to cross

the membrane via specialized ion channels, which is expressed in the membrane potential of living cells, and small molecules like saccharides are often internalized through mediated transport by transporter proteins. Additionally, steroid hormones, which mainly bind to intracellular receptors, are able to penetrate into the cell due to their hydrophobicity. However, uptake of larger objects like nanoparticles requires specialized routes of entry, which are summarized under the term "endocytosis". Endocytosis encompasses deformation of the membrane and wrapping of the material to be internalized by the membrane. Finally, a vesicle is pinched off from the plasma membrane. Endocytosis also plays an important role in the control of membrane compositions, which has an impact on the long-term sensitivity of a cell to external stimuli as receptors are often removed from the cell surface.(Doherty and McMahon, 2009) Despite many differences, all endocytotic pathways rely on active, energy consuming processes, which for example facilitate fission of the endocytotic vesicle from the plasma membrane or drive the formation of membrane protrusions or membrane ruffles. The main routes of endocytosis are summarized in Figure 2.8 and are discussed briefly in the next subchapters. A detailed description of endocytotic routes can be found in the review by Doherty and McMahon. (Doherty and McMahon, 2009) Furthermore, endocytosis in the context of bio-nano interactions has been summarized by Zellner *et al.*.(Zellner *et al.*, 2013) Endocytosis of Janus nanoparticles will be discussed in chapter 4.1.
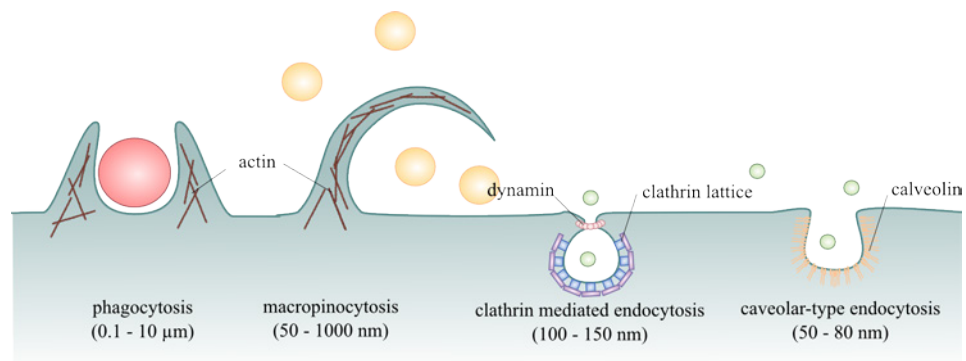
Figure 2.8: Main routes of endocytosis. Phagocytosis is used by cells to engulf large solid objects and relies like macropinocytosis on protrusive forces generated by the actin cytoskeleton. Macropinocytosis enables the cell to take up large volumes of extracellular fluid by the formation of actin-supported membrane ruffles. Small volumes can be taken up by the cell through clathrin-mediated and calveolar-type endocytosis. Dynamin facilitates the fission of the vesicle from the plasma membrane. Size of the vesicles formed by the distinct endocytotic pathways can be found in brackets.(Pollard *et al.*, 2008)(modified from (Conner and Schmid, 2003))

2.1.4.1   Clathrin-mediated endocytosis

Clathrin-mediated endocytosis (CME) is the best understood among the different endocytotic pathways and occurs in nearly all cell types. Many cargoes including nutrients, antigens, growths factors, pathogens and recycling receptors are taken up via this route. It plays also an important role in neurons, where CME is responsible for the regeneration of synaptic vesicles. CME is characterized by the presence of clathrin lattices that coat the membrane invaginations and freshly formed endocytotic vesicles at the cytosolic side. Clathrin itself exhibits the structure of a triskelion and is composed of three heavy chains and three light chains. CME is initiated by the recruitment of adaptor proteins to the membrane, e.g. adaptor protein-2, which serves as a ligand for clathrin. Upon binding, clathrin triskelions form highly organized cages, so called clathrin-coated pits that support the required curved membrane. The formed membrane invaginations are eventually pinched off from the plasma membrane under assistance of the GTPase dynamin. The actin cytoskeleton is responsible for the transport of the vesicle. The clathrin coat is removed from the endocytosed vesicle by the chaperone hsp70 (heat shock protein 70) under ATP-hydrolysis.(Takei and Haucke, 2001)

2.1.4.2   Caveolar-type endocytosis

Caveolae represent another endocytosis route, which facilitates the uptake of rather small cargoes. They have flask-like shape and their assembly relies on the protein caveolin. Hundred to two hundred calveolin molecules can be found per caveola. There are three isoforms of the protein, among whom calveolin1 has been shown to be the only one necessary for the formation of caveolae. It seems to be enriched in membrane domains with high curvature. Caveolin possesses a hairpin structure and binds to the inner leaflet of the plasma membrane, where it serves for the formation of cholesterol-rich microdomains. Depletion of cholesterol has been shown to flatten the caveolae and increase the lateral mobility of caveolin in the membrane. Caveolar-type endocytosis appears to be mainly involved in transcytosis, in which, for example, nutrients are transported from one side of the cell to another.(Doherty and McMahon, 2009)

2.1.4.3   Macropinocytosis

In contrast to the routes of endocytosis discussed previously, macropinocytosis allows the uptake of larger volumes. This pathway has been linked to the presence of membrane ruffles, which are produced by actin-polymerization under the co-assistance of rac1, a small GTPase of the Rho-family. These membrane ruffles engulf extracellular components and form endocytotic vesicles by fusing with themselves. It has been shown, that membrane ruffles are enriched in cholesterol. Cholesterol is important for the recruitment of rac1 to the plasma membrane. Other markers of lipid rafts have also been found in membrane ruffles suggesting a close interplay between inhomogeneity of the membrane and dramatic changes in the intracellular organization at these sides.(Doherty and McMahon, 2009) The uptake of objects by this pathway is rather unspecific but facilitates for example continuous nutrient uptake.(Pollard *et al.*, 2008)

2.1.4.4   Phagocytosis

Like macropinocytosis, phagocytosis relies on protrusive forces acting on the membrane, which are generated by actin polymerization. The actin polymerization at the phagocytic membranes is achieved by recruitment of different regulating proteins to the membrane by the Rho-family protein cdc42. Specialized cells like macrophages, monocytes and neutrophils mainly use phagocytosis to take up pathogens or other opsonized particles.(Doherty and McMahon, 2009)

2.2   **Nanoparticles**

Nanomaterials have a size of 1 to 100 nm and can be composed of organic materials like block copolymers or inorganic materials including metals, metal oxides or semiconductors in many different shapes.(Gupta and Gupta, 2005; Reiss *et al.*, 2009; Robb *et al.*, 2012; Shukoor *et al.*, 2009) On the one hand, nanoparticles offer great opportunities due to their high surface/volume-ratio accompanied by their unique properties, which significantly differ from the properties of the bulk material. The scopes of nanomaterials already include cosmetics, sunscreens, electronics or stain-resistant clothing and in future, nanoparticles will become more and more important for

medicine as imaging agents or for drug delivery.(Nel *et al.*, 2006) On the other hand, as their size is just between single atoms and larger molecules and due to their high reactive surface, they pose a possible threat to human health and to the environment. In the last decade, many researchers have focused on bio-nano interaction addressing questions of opsonization of nanoparticles by proteins, routes of nanoparticle entry into the body and single cells as well as of cytotoxicity of nanomaterials.(Lewinski *et al.*, 2008; Tenzer *et al.*, 2013) It has been shown that many nanomaterials exhibit cytotoxic effects depending on chemical composition, size, shape and surface-functionalization of the nanoparticles.(Lewinski *et al.*, 2008) The influence of chemical composition of nanoparticles becomes obvious when comparing different metal oxide nanoparticles. It could be demonstrated that manganese oxide NPs show a higher cytotoxicity compared to iron oxide nanoparticles due to the production of cytotoxic levels of reactive oxygen species.(Choi *et al.*, 2010; Rother *et al.*, 2013) Moreover, gold nanoparticles (Au-NPs) have been found to show substantial cytotoxicity depending on the surface functionalization and shape as spherical Au-NPs were found to be more toxic than rod-like particles of comparable size. The toxic effect could be correlated with the uptake efficiency of the particles.(Tarantola *et al.*, 2011) Most nanoparticles are taken up by one of the endocytotic pathways described in chapter 2.1.4.(Jiang *et al.*, 2011; Treuel *et al.*, 2013) Recently, another subset of nanoparticles has been demonstrated to potentially undermine the cells own endocytotic pathways. (Alexeev *et al.*, 2008; Reynwar *et al.*, 2007)
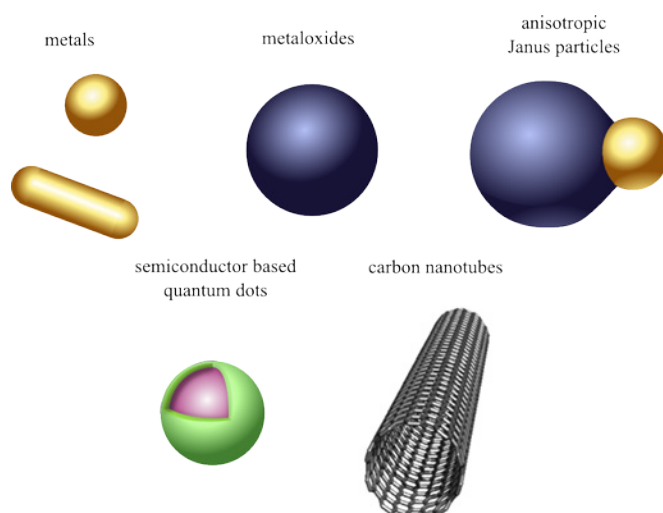
Figure 2.9: Schematic drawing showing different nanoparticle types. (carbon nanotube image from Reilly, "Carbon Nanotubes: Potential Benefits and Risks of Nanotechnology in Nuclear Medicine", J Nucl Med 48, 7, 2007)

In coarse grain simulations, the authors showed that anisotropic nanoparticles composed of a hydrophilic and a hydrophobic part, so-called Janus particles (see

figure 2.9), are able either to deform the membrane and induce tabulation and vesiculation or to insert into the membrane and form pores. On the one hand, this provides the possibility to introduce foreign substances like drugs into cells without assistance by the endocytotic machinery of the cell. On the other hand, the unwanted uptake of nanoparticles also poses threat to human health. Therefore, detailed research of the interactions between Janus-particles and cells is necessary to facilitate a save and controlled application of these promising nanomaterials in medicine or other fields. The interaction of Janus particles with artificial membranes and living cells is subject of chapter 4.1.

3. Methods & Material

3.1 Synthesis of nanoparticles

All nanoparticles were synthesized by the group of Prof. W. Tremel, Johannes-Gutenberg-University, Mainz, Germany. The synthesis of spherical manganese(II)-oxide particles and MnO@Au Janus particles as well as their functionalization has been described in publications by Schladt *et al.* and Schick *et al.* and will be described briefly in next chapters.(Schick *et al.*, 2014; Schladt *et al.*, 2009)

3.1.1 isotropic MnO-particles

For synthesis of isotropic MnO particles, 2 mmol manganese(II)-oleat were dissolved in 10 g of the solvent (octadecene). The mixture was degassed for 2 hours in vacuum. Moisture and oxygen were removed by intermittent addition of argon. Then, the solution was rapidly heated up to a temperatures of 318°C. The mixture was held at reflux for 1 hour. Afterwards, the mixture was cooled down slowly to room temperature, precipitated in acetone and solved in heptane. The produced nanoparticles are soluble in non-polar solvents such as hexane or toluene.

3.1.2 MnO@Au Janus particles

For synthesis of heterodimeric MnO@Au particles, gold-particles serve as a precursor. Monodisperse Au-particles were synthesized by rapid addition of a *tert*-butylamine-borane complex (0.5 mmol) dispersion in 1 ml tetraline and 1 ml oleylamine to 0.3 mmol $HAuCl_4 \cdot (H_2O)_x$, 10 ml oleylamine and 10 ml tetraline.(Peng *et al.*, 2008) Depending on the temperature Au-particles with different radii are formed; lower temperatures (10°C) yield larger particles (8 nm). The solution was stirred for 1 hour until particles were precipitated using methanol. After centrifugation the particles were collected and washed in hexane/ethanol.

The ligand exchange from oleylamine to 1-octadecanethiol (ODT) was achieved by addition of oleylamine-coated particles to 10 ml toluene containing 3 mmol ODT under argon atmosphere. After stirring the solution at room temperature overnight, the

particles were precipitated, centrifuged and washed with hexane/ethanol. These particles were now used as precursors in the synthesis of MnO@Au particles.

Asymmetric growth of MnO on the gold particles was achieved by addition of 10 mg ODT-functionalized Au-particles to a solution of 0.4 mmol manganese(II)-oleate in 20 ml 1-octadecene in presence of 6 mmol oleic acid and 6 mmol oleylamine at 80°C under argon atmosphere. The mixture was slowly heated up to 318°C and held at reflux for 90 minutes. Afterwards, the solution was cooled down to room temperature. The produced particles were washed by precipitation in acetone, centrifugation and dissolution in hexane.

3.1.3 Surface modification of the MnO-particles or -domains

Hydrophilization of MnO-domains of Au@MnO Janus particles and isotropic MnO-particles was either achieved by encapsulation with SiO_2 using reverse microemulsion technique or by using polyethylene glycol carrying dopamine as an anchor group (DOPA-PEG-OMe and DOPA-PEG-NH₂). A detailed description of the silica encapsulation can be found in the publication of Schladt *et al.*.(Schladt *et al.*, 2009) Briefly, 10 mg of Au@MnO were dissolved in 1 ml cyclohexane and added to a solution of Igepal CO-520 (2.0 g) in 35 ml cyclohexane.
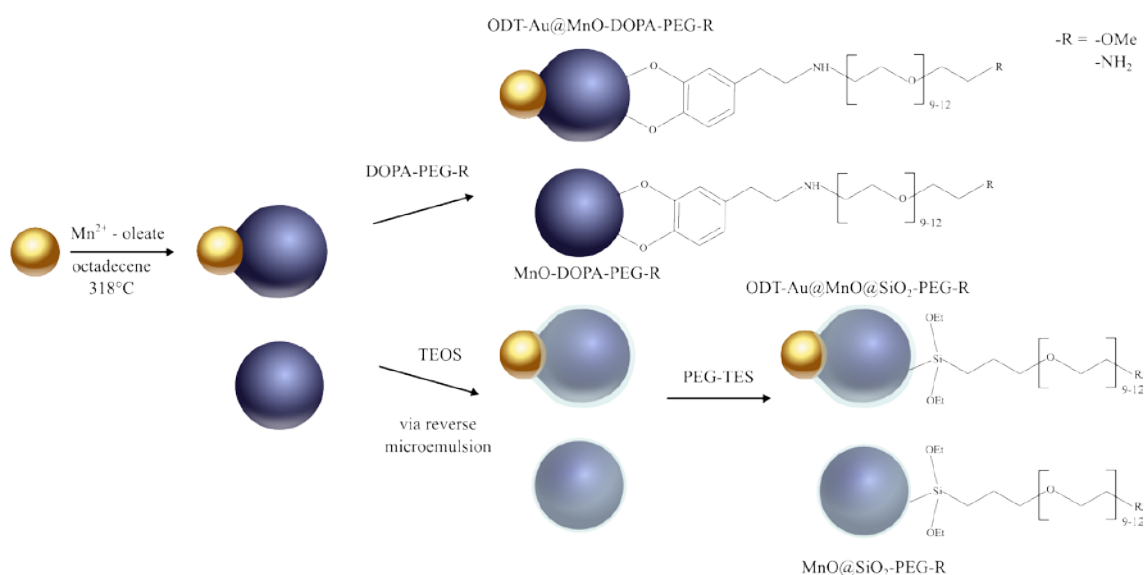
Figure 3.1: Scheme of seed mediated Janus particle synthesis and further functionalization of particles.

The solution was degassed using a gentle stream of argon. Now, 200 µl aqueous NH₄OH were added dropwise, which lead to the formation of micelles. After 5 minutes

112 µl tetraethoxysilane (TEOS) were added and the mixture was stirred under argon atmosphere overnight. The silica shell was further functionalized using 2-methoxy-(polyethyleneoxy)-propyltrimethoxysilane (-PEG-OMe) or 2-amino-(polyethyleneoxy)-propyltrimethoxysilane (-PEG-NH$_2$).(Schick *et al.*, 2014) Figure 3.1 shows a scheme of nanoparticle synthesis and further modification of the nanoparticles used in this study. Functionalized particles were solved in deionized water. Mn^{2+}-concentrations of the solutions were obtained from atomic absorption spectroscopy (AAS, Perkin-Elmer 5100 ZL) as described in Schick *et al.*.(Schick *et al.*, 2014) The AAS experiments were conducted by Isabel Schick (Johannes-Gutenberg-University, Mainz, Germany). Table 3.1 shows an overview of the particles and their stock solution concentrations used in this study.

Table 3.1: Radii obtained from TEM images and concentrations of stock solution of all nanoparticles used throughout this study. Concentrations were obtained from AAS measurement of nanoparticle solution previously dissolved in conc. HNO$_3$.

	$R \pm$ STD/ nm	c(Mn^{2+}) / µg/ml
ODT-Au@MnO-DOPA-PEG-OMe	7.5 ± 0.6 (MnO) 3.5 ± 0.2 (Au)	336
MnO-DOPA-PEG-OMe	5 ± 0.4	72
ODT-Au@MnO-DOPA-PEG-OMe	10 (MnO) 2 (Au)	123
MnO-DOPA-PEG-OMe	10	238
ODT-Au@MnO-DOPA-PEG- NH$_2$	10 (MnO) 2 (Au)	108
MnO-DOPA-PEG- NH$_2$	10	297
ODT-Au@MnO@SiO$_2$-PEG-OMe	10 ± 1.0 (MnO) 5 ± 0.2 (Au)	1742
MnO@SiO$_2$-PEG-OMe	10± 1.4	583
ODT-Au@MnO@SiO$_2$-PEG-NH$_2$	10 ± 1.0 (MnO) 5 ± 0.2 (Au)	1247
MnO@SiO$_2$-PEG-NH$_2$	10 ± 1.4	127

3.2   Dynamic light scattering of nanoparticle solutions

Dynamic light scattering (DLS) allows calculation of the hydrodynamic radii R_h of particles in solution. In DLS, time traces of the light scattered by a particle solution are recorded.(Winter and Noll, 1998) Depending on the particle size, the time traces are more correlated (larger particles) or a less correlated (smaller particles).

DLS experiments were performed by Isabel Schick (Johannes-Gutenberg-University, Mainz, Germany). For this purpose, nanoparticles were diluted in 5 mM NaBr solutions (dilution: 1/8) and were filtered into dust-free cylindrical scattering cells (Hellma, Suprasil, 2 cm diameter) using syringe filters (PALL GHP 450 nm). The measurements were performed using a Uniphase He/Ne laser (λ=632.8 nm, 22 mW), a ALV-SP125 Goniometer, a ALV/High QE avalanche photodiode with fiber optical detection, a ALV 5000/E/PCi-correlator and a Lauda RC-6 thermostat unit. All samples were measured at an scattering angle of 90° 3 times for 45 seconds. The first order correlation function $g_1(q, t)$ is obtained from the scatter data using the Siegert relation. The wave vector q is dependent on refractive index of the sample, the wavelength of light and the scattering angle. The correlation functions were fitted using a biexponential function, which allowed calculation of the apparent diffusion coefficient D_{app}. Using the Stokes-Einstein-equation the hydrodynamic radius R_h can be obtained.

3.3   Surface plasmon resonance spectroscopy

To evaluate the interaction between nanoparticles and lipid bilayers surface plasmon resonance spectroscopy (SPR) was used. SPR has widely been used to measure binding kinetics.(Homola *et al.*, 1999) The technique bases on excitation of surface plasmons in a thin Au-layer, which is achieved by coupling light into a prism with high refractive index (see Figure 3.2). At the prism/buffer interface the laser beam is totally reflected at an angle larger than the critical angle. If an Au-layer is placed in proximity to this interface, the evanescent field is able to excite surface plasmons in the gold layer. Excitation of surface plasmons leads to a decrease in intensity of the reflected light, which is detected by a photodiode. Thus, the reflected light shows a minimum intensity at a certain angle, which is dependent on the refractive index of the environment close to the gold surface.
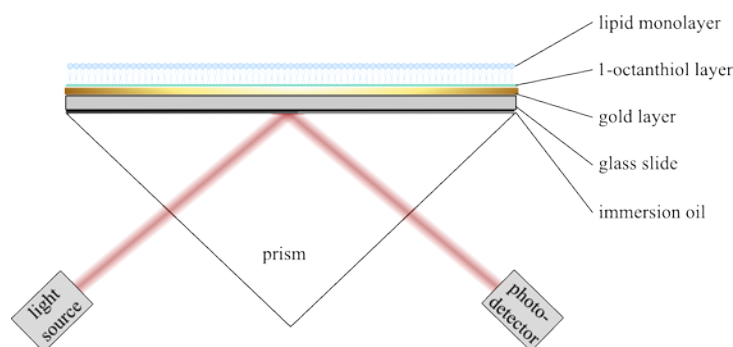
Figure 3.2: Schematic drawing of the setup used in surface plasmon resonance (SPR) spectroscopy experiments

Upon binding of an analyte to the surface the angle of incident, at which the minimum intensity is detected, changes, which can be used to measure association and dissociation of an analyte.

3.3.1 Experimental procedure and data analysis

For experiments all used buffers were filtered through a 0.2 μm porous membrane (Minisart, Satorius, Göttingen, Germany) and degassed by a vacuum.

Experiments were carried out using a Reichelt SR7000DC-SPR setup (Reichelt Life Sciences, Seefeld, Germany). Immediately before experiments, a glass slide coated with a 50 nm thick gold layer, which has been incubated in a 1.6 mM 1-octanthiol solution at 4°C overnight, was rinsed using ethanol p.a. and dried using a gentle nitrogen stream.

After mounting, the system was rinsed using 2 mM TrisHCl buffer with pH 7 and equilibrated at a flow rate of 10 μl/min for 10 minutes. Then, a solution of 1,2-dioleoyl-s,n-glycerol-3-phosphatidylcholine- (DOPC-, Avanti Polar Lipids, AL, Alabaster, USA) small unilamellar vesicles (SUVs) in 2 mM TrisHCl buffer (0.25 mg / 700 μl) was injected. Details about production of SUVs can be found in chapter 3.4. After 1 hour the system was rinsed with 2 mM TrisHCl buffer. After equilibrium was reached, nanoparticle solutions in 2 mM TrisHCl with increasing concentrations were injected at a flow rate of 20 μl/min. Association of nanoparticles to the lipid monolayer was monitored for 15 minutes. Afterwards the system was rinsed with 2 mM TrisHCl for 10 minutes, which allowed following dissociation of particles from the lipid layer.

For data analysis the recorded signals were averaged. The changes in reflectivity units $μRfU$ as a function of the nanoparticle concentration were fitted assuming Langmuir adsorption kinetics:

$$\mu RfU = \frac{\mu RfU_{\max} \cdot K_D^{-1} \cdot c}{1 + K_D^{-1} \cdot c}, \qquad\qquad (3.1)$$

with the maximal change in reflectivity units μRfU_{max} and the dissociation constant K_D. Data were fitted using a weighted fit by IGOR Pro (WaveMetrics, Lake Oswego, OR, USA).

3.4   Production of unilamellar vesicles

3.4.1   Production of small unilamellar vesicles

For the production of small unilamellar vesicles lipid films are required. These are produced by adding 0.25 mg of lipids (DOPC) solved in chloroform into a previously cleaned test tube. To remove the chloroform the test tube was put into a water bath with a temperature of 30°C and a gentle nitrogen stream was applied. Afterwards, test tubes were put into the vacuum oven at 40°C for at least 3 hours. The formed lipid films were stored at 7°C.

To form SUVs the lipid films were first dissolved in 2 mM TrisHCl buffer, which was previously filtered through a porous filter (0.2 µm, Minisart, Satorius, Göttingen, Germany). Then, the solution was sonicated for 30 minutes (Bandelin sonoplus with UW2070, Bandelin electronics, Berlin, Germany), which leads to the formation of SUVs.

3.4.2   Production of giant unilamellar vesicles

Giant unilamellar vesicles were produced by electroformation. This method, developed by Angelova and Dimitrov, is based on hydration of dried lipid films on the surface of indium tin oxide (ITO) electrodes, while an alternating electric field is applied. (Angelova and Dimitrov, 1986; Walde *et al.*, 2010) Amplitude and frequency of the electric field are dependent on the ionic strength of the buffer, which is used in the experiment.

For electroformation of vesicles, 20 µl of a 1 mg/ml DOPC/ TexasRed® 1,2-dihexadecanoyl-sn-glycero-3-phosphoethanolamine (TR-DHPE, Life Technologies, Carlsbad, CA, USA) (99.5/0.5) solution in chloroform were applied to the surface of two ITO covered glass slides (Präzisions Glas & Optik, Iserlohn, Germany). A schematic

drawing of the electroformation chamber can be seen in Figure 3.3. After evaporation of the chloroform, the lipid flims were dried in a vacuum oven at 40 °C for at least 3 hours. After complete removal of the solvent, the electroformation chamber was assembled as follows: First, a conductive copper tape was glued to the ITO electrodes on both slides. Then, the ITO covered glass slides with the lipid films were placed on each other after a margin made of silicon was put onto the ITO slides to form the reaction chamber. The reaction chamber was then filled with either a solution of 100 mM sucrose in deionized water (experiments with –DOPA-PEG-R functionalized nanoparticles) or a solution of 100 mM sucrose in 2mM TrisHCl buffer with pH 7 (experiments with SiO_2-PEG-R functionalized particles). All solutions were filtered through porous filter (0.2 µm, Minisart, Satorius, Göttingen, Germany). After assembly, the electroformation chamber was connected with a frequency generator (Agilent 33220A, Santa Clara, USA) via the copper tape. For electroformation of giant unilamellar vesicles a peak-to-peak voltage of 1.6 V and 12 Hz (100 mM sucrose in deionized water) or 2.3 V and a frequency of 70 Hz (100 mM sucrose in 2 mM TrisHCl pH7) was applied for at least 2 hours at room temperature. The formed GUV solutions were transferred into a 1.5 ml vial and stored at 4°C.
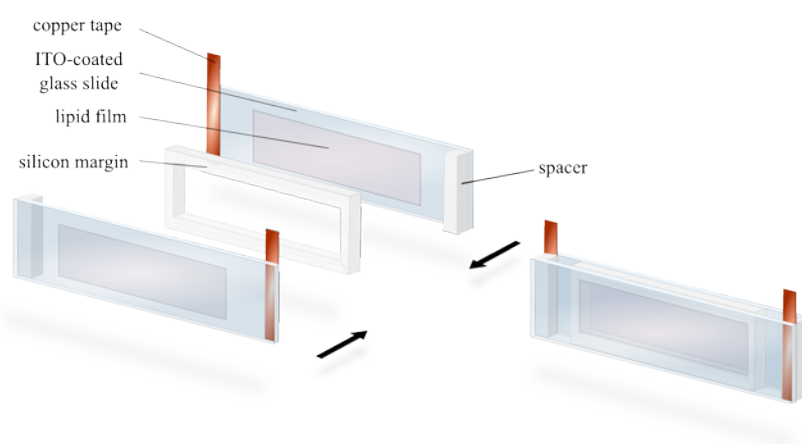
Figure 3.3: Schematic drawing of a electroformation chamber.

Used ITO-covered glass slides and silicon margins were rinsed using ethanol p.a. and water and then cleaned in 2% Hellmanex-II-solution in an ultrasonic bath for 15 minutes followed by 2 times rinsing in deionized water in the ultrasonic bath for 15 minutes. Finally, the parts were rinsed with ethanol *p.a.* and dried using a nitrogen stream.

3.5 Porous cell culture substrates

Porous cell culture substrates were used to examine their effect on cellular morphology, cytoskeletal arrangement and cell mechanics (see chapter 4.4.1). Substrates with a pore diameter of 0.45 µm, 0.8 µm and 1.2 µm were purchased from fluXXion B.V. (Eindhoven, Netherlands). The porous membrane of these substrates consists of siliconnitride and displays a regular hexagonal pore pattern. The porosity varies between 20 and 30 %.

Porous substrates with larger diameters were produced by Dr. Siegfried Steltenkamp (CAESAR Institute, Bonn, Germany). Briefly, (1-0-0) oriented SOI wafers with a device layer thickness of 8 µm and a handle layer thickness of 525 µm were used. First, a SiO_2 layer with a thickness 0.5 µm was formed by wet thermal oxidation. Pores with diameters ranging from 3.5 µm to 5.5 µm were imprinted by means of UV lithography (AZ1518, MicroChemicals GmbH, Ulm, Germany). Then, the pores were etched into the wafer using wet-etching (buffered HF, room temperature) and deep reactive ion etching (STS MACS Multiplex ICP, UK).(Laerme et al., 1999) The SiO_2 layer between the handle and device layer was used as an etch-stop for this process and a well-defined pore depth of 8.5 µm. Details of the process can be found in a recent publication by Frese et al..(Frese et al., 2013) To achieve a hydrophilic surface, the pores were covered with a SiO_2 layer of 500 nm thickness by means of wet-thermal oxidation. After cleaning the substrates in argon plasma, all substrates were coated with a 30 – 35 nm thick gold layer by thermal evaporation (Balzers, BAE 250 coating system) or first sputtered with a thin titanium layer (Cressington 108auto Sputter coater, Watford, UK) and gold-coated afterwards (BAL-TEC MED 020 Coating System). Before use, the substrates were sterilized in pure ethanol and incubated in cell culture medium before inoculation of the cells.

3.6 <u>Cell culture and sample preparation</u>

3.6.1 Cell culture conditions

Cells were cultured by Anja Herdlischke and Angela Rübeling (Institute of Organic and Biomolecular chemistry, Georg-August-University, Göttingen, Germany) All cell lines were cultured in cell culture flasks (TPP, Switzerland) in a humidified incubator at a temperature of 37°C and at 7.5% CO_2. For cell passage, cells were released using trypsin/EDTA (0.5%/0.2%, Biochrom, Berlin, Germany), added to stop solution containing full medium and fetal calf serum, centrifuged and resuspended in cell culture medium. All cell lines were subcultured weekly. The compositions of the cell culture media are summarized in Table 3.2.

Table 3.2: Composition of cell culture media of the cell lines used in this study.

Cell line	Composition of cell culture medium
MDCK-II	MEM with Earle's salts (Biochrom) 2.2 g/L $NaHCO_3$ 10% FCS (PAA) 4mM L-glutamine (Biochrom)
A549	DMEM (Lonza) 10% FCS (PAA) 4 mM L-glutamine (Biochrom)
NIH 3T3	see A549 cells
NMuMG	DMEM (Lonza) 10% FCS (PAA) 4 mM L-glutamine 200 mM (Biochrom) 0.1 mg/L Insulin (Biochrom)

Table 3.2: Composition of cell culture media of the cell lines used in this study. (Continued)

Cell line	Composition of culture medium
SW-13	see A549 cells
MCF-7	DMEM-F12 (Lonza) 1.2 g/L NaHCO$_3$ 3.6 g/L HEPES 10% FCS (PAA) 4 mM L-glutamine 200 mM (Biochrom)
MDA-MB-231	see A549 cells
CaKi-1	DMEM (Lonza) 10% FCS (PAA) 4 mM L-glutamine 200 mM (Biochrom) 1 ml / 100 ml NEAA 100× (PAA)

MEM (Minimum essential medium, Biochrom, Berlin, Germany), FCS (fetal calf serum, PAA, Pasching, Austria), DMEM (Dulbecco's modified eagle medium, Lonza, Basel, Switzerland), DMEM-F12 (Lonza, Basel, Switzerland) NEAA (non-essential amino acids, PAA, Pasching, Austria)

For experiments penicillin (0.2 mg/ml, PAA, Pasching, Austria), streptomycin (0.2 mg/ml, PAA, Pasching, Austria) and amphotericin B (5 µg/ml, PAA, Pasching, Austria) as well as HEPES (15 µM, PAA, Pasching, Austria) were added to the cell culture media.

3.6.2   Sample preparation

3.6.2.1   Cell fixation or treatment with different drugs for AFM-experiments

For experiments described in chapter 4.2, cells were seeded onto glass slides or gold-covered porous substrates (Fluxxion, Eindhoven, Netherlands) (see also chapter 3.5), which were placed into a petri dish (2.5 cm, TPP, Switzerland) in a density of 500,000 cells and incubated at 37°C and 5% CO$_2$. After 2 days, cells either were fixated using a

4% paraformaldehyde (PFA, FLUKA, Switzerland) solution in phosphate buffered saline (PBS, Biochrom, Berlin, Germany) or a 2.5% glutardialdehyde (GDA, Acros Organics, Geel, Belgium) solution in PBS for 20 minutes at room temperature or treated with a 2 μM Cytochalasin D (CytD, Life technologies, Carlsbad, CA, USA) or 50 μM Blebbistatin (Bleb, Sigma-Aldrich, St. Louis, MO, USA) solution in cell culture medium at 37°C. In the latter case, AFM- experiments were started 15 minutes after addition of the drug. Experiments with fixed cells were performed in PBS at room temperature.

Epithelial-to-mesenchymal transition was induced by treating NMuMG cells 24 hours after seeding with 10 ng/ml TGF-β1 (Invitrogen, Karlsruhe, Germany) for 48 hours.

3.6.2.2   Microrheological characterization of cell lines

For AFM-experiments described in chapter 4.3, all cell lines were cultured on glass slides (3.5 cm, Asylum Research, Santa Barbara, CA, USA), which were placed into a petri dish (diameter, TPP, Switzerland) with a density of 50,000-750,000 cell/slide at 37°C and 5% CO_2 and were measured one to four days after seeding. For measurements, the glass slides were mounted into the BioHeater™ sample stage (ASYLUM RESEARCH, Santa Barbara, CA, USA) and covered with the appropriate HEPES-buffered medium.

3.6.2.3   Cell culture on porous substrates

Details about the preparation of porous substrates can be found in chapter 3.5. For experiments, substrates were placed into a petri dish (2.5 cm, TPP, Switzerland). Cells were seeded in a density of 500,000 cells per petri dish and incubated for 2 days at 37°C in a 5% CO_2 - humidified incubator.

3.7   Electric cell-substrate impedance sensing

3.7.1   Setup

Electric cell-substrate impedance sensing (ECIS) is a non-invasive biosensor, which facilitates monitoring morphological changes of living cells in real time. (Giaever and Keese, 1984, 1993)
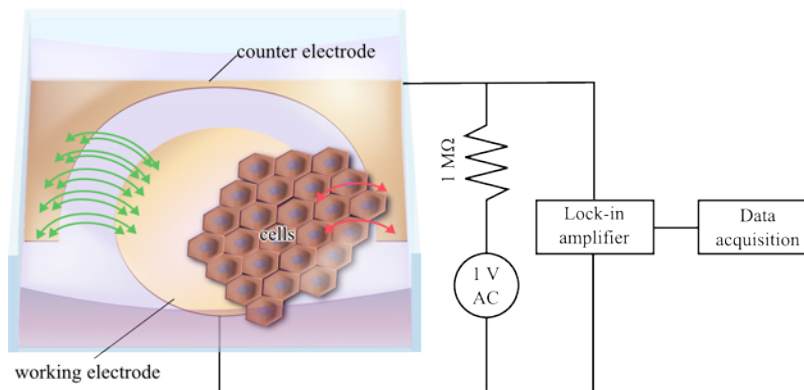
Figure 3.4: Scheme of an ECIS-setup. The working electrode and the counter electrode are immersed in cell culture medium. An applied alternating current (AC, green arrows) can flow unhindered between both electrodes as long as the electrodes are uncovered. When cells adhering to the electrode form a monolayer, current flow is reduced and the impedance increases (red arrows). A lock-in amplifier measures amplitude and phase of the voltage.

The method measures the complex impedance Z of an alternating current (AC), which is applied between a small working electrode and a larger counter electrode (see Figure 3.4). Impedance spectra of uncovered ECIS electrodes can be modeled by an Ohmic resistor R_{bulk} in series with a constant phase element (CPE) accounting for the capacitive properties of the electrodes (see Figure 3.5). Adhesion and spreading of cells on the electrodes and formation of a monolayer influence the current flow due to insulating properties of cells and thus, lead to a characteristic increase of Z depending on the AC-frequency. The high-frequency regime ($\omega > 10$ kHz) of the complex impedance is dominated by the capacitance of the cell membrane C_m, which scales with $1/C_m$.(Lo *et al.*, 1998) At lower frequencies the impedance is characterized by current flow through intercellular gaps, which can be modeled by an Ohmic resistance R_b and is a measure for the density of cell-cell contacts, i.e. tight junctions. Another contributions comes from current flow through the cleft between cell and substrate, which can be modeled by a parameter α_{ECIS}. α_{ECIS} is inversely proportional to the

square root of the cell-substrate distance. Measurement of Z at a frequency at which the impedance is largely influenced by the parameter α_{ECIS} allows to monitor the so-called micromotion, collective changes of the cell-substrate distance on the order of nanometers.(Giaever and Keese, 1991)
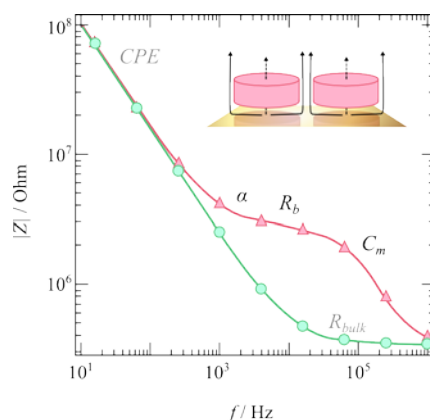
Figure 3.5: Impedance spectrum of a cell-free (green) and a cell-covered (red) ECIS electrode. Inlet: Schematic drawing of the current flow (black arrows) on a cell-covered electrode. Cells are symbolized by red discs. (Diagram modified from (Schneider *et al.*, 2011))

3.7.2   Experimental procedure

ECIS was used to examine the cytotoxicity of nanoparticles. All measurements were carried out using a ZΘ setup from Applied Biophysics (Troy, NY, USA). During measurement the cells were incubated at 37°C and 5% CO_2. To examine the cytotoxicity of nanoparticles, either 8-well chambers (8W1E, Applied Biophysics, Troy, NY, USA) or 96-well chambers (96W1E, Applied Biophysics, Troy, NY, USA) were used. 200,000 cells (8 well chamber) or 20,000 cells (96 well chamber) were seeded into each well. Impedance was measured at a constant AC-frequency of 4 kHz for MDCK-II cells or 8 kHz for A549 cells. When a constant signal of Z was reached (24 to 50 hours after seeding of cells), nanoparticles solutions were added into the wells.

The measured data were analyzed using a self-written MATLAB-program (ECIS96.m, Mathworks, Natick, MA, USA). To calculate the normalized, absolute impedance $|Z|_{norm}$, $|Z|$ of the cell free electrode is subtracted from the measured data. These corrected data were then divided by the impedance at the time of nanoparticle addition yielding $|Z|_{norm}$.

For variance analysis the time traces of $|Z|$ were first detrended using a moving average algorithm. In the case of data acquired using an 8-well chamber a window size of 36 data points was chosen. Data from the 96-well chambers were detrended using a window size of 3 points. After the trend was removed the variance of the signal was

obtained by calculating the variance in a moving window. The variance of each window was assigned to the time point of the first data point in the window. For the data measured using an 8-well chamber, the variance was calculated over 1200 points, for data measured with 96-well chambers a window of 100 points was used.

3.8   <u>MTS-Assay</u>

The MTS-assay is used to evaluate the cytotoxicity of different nanomaterials (see chapter 4.1). In MTS-assay, a tetrazolium salt is reduced by the cells reduction equivalents $NADH|H^+$ and $NADPH|H^+$ to a colored, water-soluble formazan product. The amount of the formazan product is photometrically detected at a wavelength of 490 nm. As the reduction equivalents are only produced in living cells, the MTS-assay can be used to determine the relative amount of living cells in a sample compared to a reference sample with untreated, living cells.

3.8.1   Experimental procedure

MTS reagent was purchased from Promega (CellTiter 96® AQueous One Solution Cell Proliferation Assay, Madison, WI, USA) and used according to the manufacturers instructions. Briefly, cells (MDCK-II or A549 cells) were cultured in 96 well plates (TPP, Trasadingen, Switzerland). Both cell lines were seeded in a density of 20.000 cells per well and cultured for 24 h (MDCK-II cells) or 48 h (A549 cells) in an humidified incubator at 37°C and 5% CO_2. Afterwards, cells were treated with nanoparticles in different concentrations. After 24 h cells were the nanoparticle solutions were removed and cells were rinsed once with culture medium. Then, 100 µL cell culture medium and 20 µL of the MTS reagent were added into each well. After 15 minutes to 60 minutes, the absorbance A of the samples was measured at a wavelength of 490 nm using a 96-well plate reader (Thermomax, Molecular Devices, Sunnyvale, CA, USA). Additionally, to avoid artifacts from scattering of the sample, the absorbance at a wavelength of 650 nm was measured. MTS-assays with DOPA-PEG-functionalized particles were conducted by Sebastian Heise in his bachelor thesis.

Relative cell viability was obtained by first subtracting A_{650nm} and from A_{450nm}. Then, samples of the same category were averaged and divided by the average absorbance of the untreated control after subtraction of the average absorbance of cell-free samples.

3.9   Atomic Force Microscopy

3.9.1   Setup

The atomic force microscope (AFM) was developed in 1986 by Binning, Quate and Gerber as an advancement of the scanning tunneling microscope (STM), which was restricted to samples with a conductive surface and operation in dry conditions.(Binnig *et al.*, 1986) The new technique opened the field of scanning probe techniques (SPMs) to biological samples, which now could be researched under physiological conditions. The AFM uses a tip with a size of a few nanometers attached to a flexible cantilever to scan the topography of a sample. The deflection of the cantilever is often measured by an infrared laser, which is reflected at the surface of the cantilever and guided to a four-quadrant photodiode. The lateral and the axial deflections of the cantilever are calculated by the photocurrents of the single quadrants according to eq. 3.2 and 3.3:

$$I_x = \frac{(I_2 + I_4) - (I_1 + I_3)}{I_{sum}} \qquad\qquad (3.2)$$

and

$$I_y = \frac{(I_1 + I_2) - (I_3 + I_4)}{I_{sum}}, \qquad\qquad (3.3)$$

where I_x and I_y are the output currents of the signals in x or y direction, I_1 to I_4 are the photocurrents of the single quadrants (top left: (1), top right (2), bottom left (3) and bottom right (4)) and I_{sum} is the total photocurrent of all quadrants. The axial position of the cantilever is controlled by a piezoelectric element, which transfers an applied voltage to an expansion of the piezoelectric element according to the inverse piezoelectric effect. This enables positioning of the cantilever with a precision of a few nanometers. Further piezoelectric elements in the sample stage facilitate scanning of the sample in x- and y-direction. Cantilevers can be produced by a variety of materials and with spring constants ranging from approximately 1 to 500 pN/nm. A schematic drawing of a typical AFM-setup is shown in Figure 3.6.
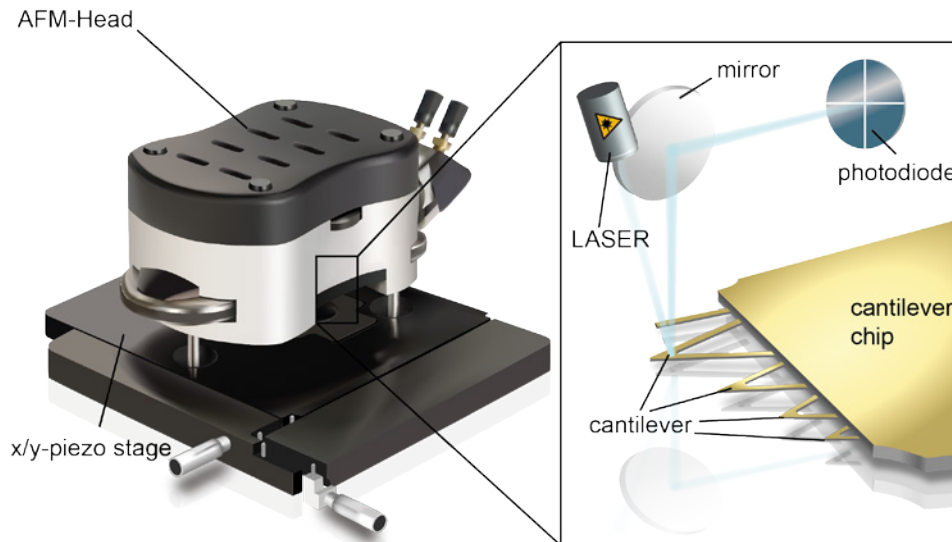
Figure 3.6: Schematic drawing of an atomic force microscope

There are different possibilities to image the topography of a surface using the AFM. The simplest is the contact mode. In contact mode, the tip is constantly in contact to the surface. The sample is scanned either using a constant expansion of the piezoelectric element (constant height) or using a constant force by controlling the deflection of the cantilever (constant force). In the latter case, feedback control is achieved via a proportional-integral controller. The force applied to the sample is proportional to the deflection of the cantilever according to Hook's law:

$$F = k_c \cdot x \qquad\qquad (3.4)$$

with the Force *F*, the deflection *x* of the cantilever and the spring constant k_c of the cantilever, which is a function of the material the cantilever is made of and of the length, width and thickness of the cantilever itself. The spring constant of the cantilever k_c can be calculated by different methods. The most common one is the calibration by thermal noise method, which is described here briefly.(Butt *et al.*, 2005) First, the change in voltage of the photodiode per nanometer deflection is determined by deflecting the cantilever on an incompressible surface. In the next step, the spring constant is calculated from the thermal noise spectra of the cantilever deflection by integration of the first resonance peak. Based on equipartition of energy the spring constant of a cantilever assumed as a harmonic oscillator is given by

$$k_c = \beta \frac{k_B T}{\langle x^2 \rangle}$$

(3.5)

With mean squared displacement of the cantilever tip $\langle x^2 \rangle$, the thermal energy $k_B T$ and the correction factor β (= 0.971 for the first vibration mode of a rectangular cantilever) correcting for the multiple vibration modes of a non-ideal oscillator.(Butt *et al.*, 2005)

3.9.2 Force spectroscopy using the AFM

Knowledge of the applied force facilitates application of the AFM in force spectroscopy. By subtraction of the z-piezo extension from the cantilever deflection one can calculate the depth, which the cantilever tip penetrates into the sample, the so-called indentation depth δ. A typical force-indentation-cycle measured on a cell is shown in Figure 3.7.
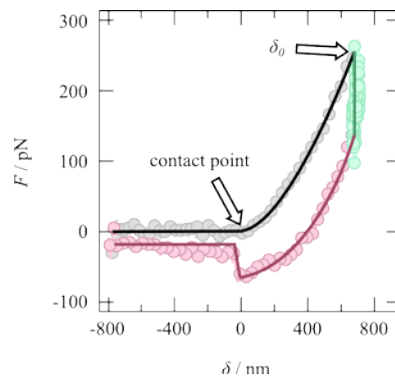
Figure 3.7: typical force-indentation cycle taken on living cells. Extension of the z-piezo is shown in black, a dwell of 1.5 s is shown in green and the retraction of the z-piezo in red. Circles show data measured on MCF-7 cells.

Upon contact between cantilever tip and sample the force acting on the cantilever starts to increase. The z-piezo extends until the pre-set force-setpoint (at δ_0) is reached. This force-indentation curve can be described by Hertzian or related contact mechanical models yielding the cell's elastic modulus E according to

$$F = g \frac{E}{(1 - \upsilon^2)} \delta^n \ ,$$

$(1 < n < 2)$

(3.6)

with coefficients g and n accounting for the indenter geometry and the Poisson ratio υ. (Briscoe *et al.*, 1994) These models have been frequently used to quantify cellular

mechanics. (Kuznetsova *et al.*, 2007; Radmacher, 1997) However, in many cases, simple contact mechanical models only describe force-indentation curves at low indentation depth and elastic moduli measured on the same cell using two different indenter geometries differ up to two orders of magnitude. (Carl and Schillers, 2008; Pietuch *et al.*, 2013) Pietuch and coworkers demonstrated that the liquid droplet is less dependent on the indenter geometry and force curves were well described even at high indentation depth.

3.9.3   Liquid droplet model

A detailed description of the liquid droplet model can be found in publications by Sen *et al.*, Schneider *et al.* and Pietuch *et al.*. (Pietuch *et al.*, 2013; Schneider *et al.*, 2013; Sen *et al.*, 2005) Briefly, the liquid droplet model assumes adhering cells as an isotropic shell. Thus, the pressure difference P across the membrane is given by the Young-Laplace equation for a thin membrane separating two volumes (eq. 3.7):

$$P = 2TH \tag{3.7}$$

with the isotropic tension T of the membrane and the mean curvature H. The isotropic tension consists of two contributions: one coming from the pre-tension of the cortex T_0, the other from area dilation of the membrane due to stretching. Thus the tension T is given by

$$T = T_0 + \tilde{K}_A \frac{\Delta A}{A_0}, \tag{3.8}$$

where

$$\tilde{K}_A = K_A \frac{A_0}{A_0 + A_{ex}}. \tag{3.9}$$

$\tilde{K}_A$ denotes the apparent area compressibility modulus, which accounts for excess membrane A_{ex} stored by the cell in membrane reservoirs like microvilli or calveolae. A_0 is the apparent membrane area before indentation and ΔA is the change in membrane area due to stretching.(Pietuch *et al.*, 2013)

Knowing the initial shape of the apical cap before indentation facilitates calculation of the force response acting on the cantilever under assumption of constant volume and curvature of the cap. The apical cap of the cell can be described by two parameters: the contact angle φ and the cap radius R_1 (see Figure 3.8).(Sen *et al.*, 2005)
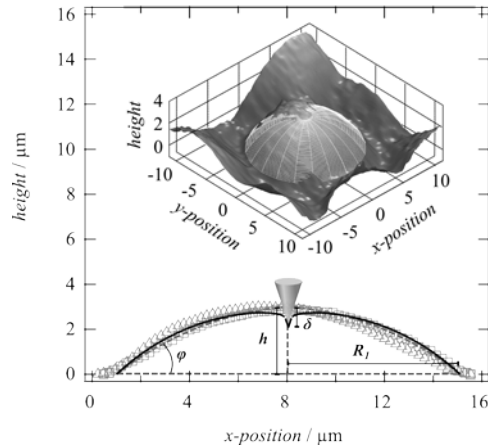
Figure 3.8: Parameterization of the apical cap of cells. The diagram shows height profiles (hollow symbols) of a MDCK-II cell imaged with AFM in contact mode and the parameters (the contact angle φ and the radius at the base R_1) used to describe the shape of the apical cap of cells. Dashed line shows the shape of the cell before indentation, the solid black line after indentation. Inlet: AFM height image overlaid with the calculated apical cap after indentation (white lines).

Non-linear fitting of the calculated force response to force-indentation curves finally permits the determination of the pre-tension T_0 and the apparent area compressibility modulus $\tilde{K}_A$. Thereby, the pre-tension dominates the force response at low indentation depth, while $\tilde{K}_A$ dominates the force response at larger strains.

In this work, the liquid droplet model was used to describe averaged force-indentation curves of MDCK-II cells grown on substrates with different pore sizes.
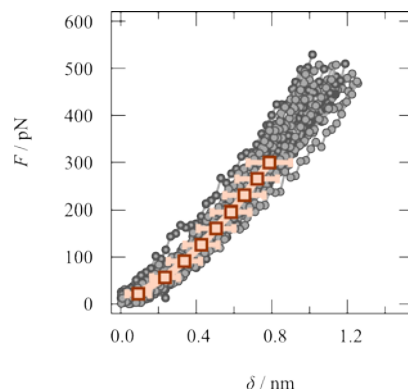
Figure 3.9: Averaging of force-indentation curves by interpolation of indentation depth at given force values. 20 exemplary force-indentation curves are shown in grey, averaged curve is shown in red.

Averaging of force-indentation curves of one force map was performed by interpolating the indentation depth values of each preselected force-distance curve in the contact region by searching for the nearest indentation depth value at a given force (for pre-selection criteria see chapter 3.9.6). An example of an averaged force-indentation curve is shown in Figure 3.9. The resulting curves were subject to fitting with the parameters of the liquid droplet model as detailed previously. Experimental details can be found in chapter 3.9.5 and 3.9.6.

3.9.4   AFM-based microrheology

Although force-indentation curves can be well described by the liquid droplet model, a hysteresis between indentation of the cantilever tip into a cell and its retraction indicates, that cells cannot be regarded as purely elastic solids or shells as energy is dissipated during indentation. Instead, cells are viscoelastic bodies, which exhibit fascinating rheological features. A possibility to capture cellular rheology using the AFM has been developed by Shroff *et al.* and was refined by Alcaraz and coworkers. (Alcaraz *et al.*, 2003; Shroff *et al.*, 1995) A detailed description of the method can be found in the publication of Alcaraz *et al.*. Briefly, upon indentation of the cantilever tip into the sample, it is excited to oscillate with small amplitudes and the force response is measured (see Figure 3.10).
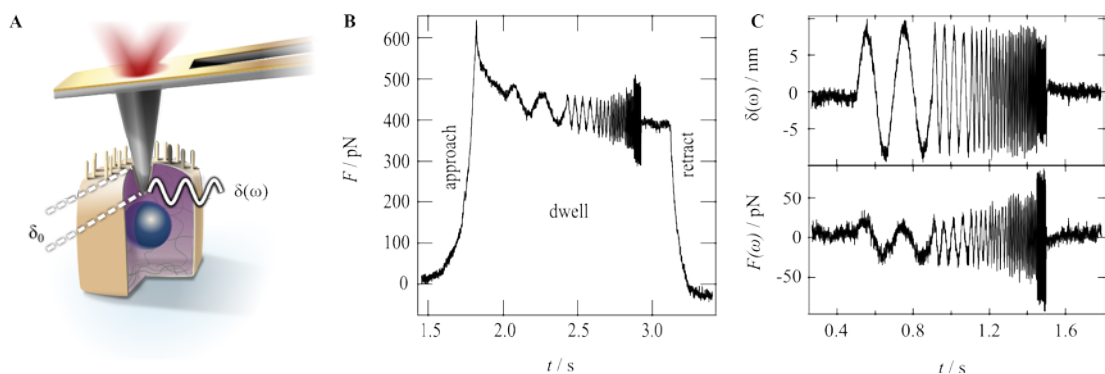
Figure 3.10: A Schematic drawing of the experiment: The cantilever oscillates around the indentation depth δ_0 with an amplitude δ at the frequency ω. **B** Time course of force during the measurement of a force-distance curve. When the cantilever gets into contact with the sample, the force increases rapidly until the present trigger point is reached. During dwell, the cantilever is excited to sinusoidal oscillations. Afterwards, the cantilever is retracted and the procedure repeated at a different position. **C** Indentation oscillation $\delta(\omega)$ with frequencies from 5 to 200 Hz around the indentation depth δ_0 and corresponding force signal $F(\omega)$ after detrending.

A quantitative description can be achieved employing contact mechanics. Starting with Hertzian contact mechanical model for a four-sided pyramidal indenter (Bilodeau, 1992)

$$F = \frac{3E \tan(\alpha)}{4(1 - \upsilon^2)} \delta^2 \,,$$
(3.10)

where E is the elastic modulus, α is the half opening angle and ν is the Poisson ratio, one obtains, after linearization and by use of the relation $G=2E/(1+\nu)$, the frequency-dependent complex shear modulus G^*:(Alcaraz et al., 2003)

$$G^* = G' + iG'' = \frac{(1 - \upsilon)}{3 \tan(\alpha) \delta_0} \cdot \frac{F(\omega)}{\delta(\omega)} = \frac{(1 - \upsilon)}{3 \tan(\alpha) \delta_0} \frac{A_F}{A_\delta} \exp(i(\varphi_F - \varphi_\delta))$$
(3.11)

with oscillations of the force F and indentation depth δ with the frequency ω and the indentation depth of the cantilever tip δ_0 (see also Figure 3.7). The ratio $F(\omega)/\delta(\omega)$ can be described by the ratio of the amplitudes of the force oscillation (A_F) and indentation depth (A_δ) and the difference of phases (φ_F-φ_δ). The complex shear modulus consists of a real part G' called storage modulus, which accounts for the energy stored in the system and an imaginary part G'' called loss modulus, which accounts for energy dissipated in the sample. The ratio between loss modulus and storage modulus is called loss tangent η and is given by the tangent of the phase shift (φ_F-φ_δ) between the two sinusoidal signals of $F(\omega)$ and $\delta(\omega)$:

$$\eta = G'' / G' = \tan(\varphi_F - \varphi_\delta) \,.$$
(3.12)

The loss tangent is a model-independent parameter, which does not rely on geometrical factors. For an elastic solid η is zero, while it approaches infinity for a viscous fluid.

Furthermore, the force response of the cantilever during oscillation in an aqueous medium is influenced by hydrodynamics. To correct for these influences, a method introduced by Alcaraz et al. was used.(Alcaraz et al., 2002) Thereby, the force response of the cantilever at different frequencies and distances from a glass cover slide is measured (Figure 3.11 A and B).
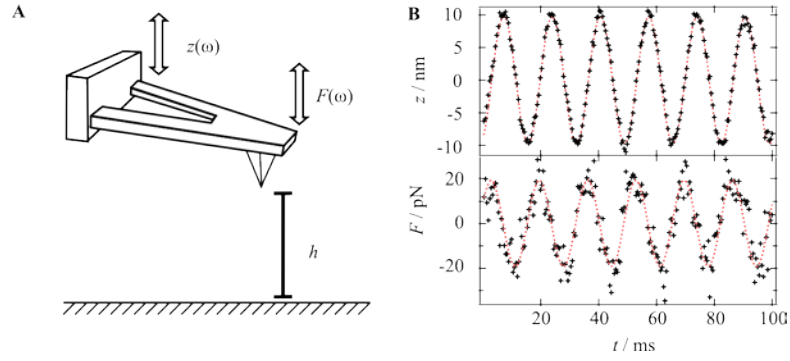
Figure. 3.11: A Scheme of the correction of force data for hydrodynamic drag. The triangular cantilever is kept at a height h above the surface and oscillates with a z-displacement of $z(\omega)$ at its basis. The force response $F(\omega)$ is determined over the deflection of the cantilever and its spring constant. **B** Piezo movement $z(\omega)$ and the measured force signal $F(\omega)$ as a function of time. Dots represent the measured data; the dashed line shows the fit of both signals using the sum of a sine and a cosine function with a pre-set frequency.

Before calculation of the drag coefficient, the phase shift between excitation and force response was set to 90°, as the experimentally obtained phase shifts differed from the theoretical 90° in a Newtonian viscous fluid. This was achieved by fitting the experimental mean deviation φ_{lag} from 90° using a linear fit (see Figure 3.12).
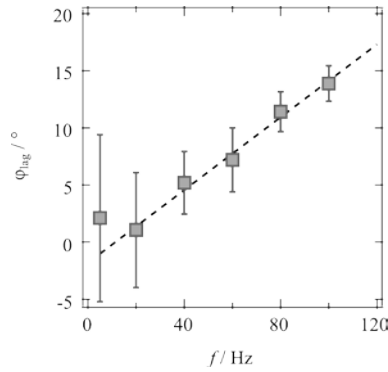
Figure 3.12: Example of deviation from 90° phase shift between $z(\omega)$ and $F(\omega)$ (squares) as a function of the oscillation frequency measured in viscous medium. Data were fitted using a linear fit applied to all data above an oscillation frequency of 10 Hz.

The results of the fit were then subtracted from the phase shift between excitation and force response (φ_F-φ_z) for hydrodynamic correction as well as from (φ_F-φ_δ) for calculation of $G^*(\omega)$.

After correction of the phase shift, the complex transfer function

$$H_d* = \frac{F_d(\omega)}{z(\omega) - x(\omega)}$$ (3.13)

is determined, where $z(\omega)$ denotes the oscillation of the piezo, $F_d(\omega)$ is the drag force and $x(\omega)$ is the cantilever deflection, as a function of the frequency at a distinct distance h from the glass cover slide. A linear increase of the imaginary part of the transfer function H_d'' is obtained, while the real part shows a constant value around 0 mN/m (see Figure 3.13 A). Thereby, the slope is dependent on the drag coefficient $b(h)$. Linear fitting of H_d'' provides the drag coefficient $b(h)$ as the slope m of the fit is given by $m=2\pi b(h)$.(Alcaraz *et al.*, 2002)
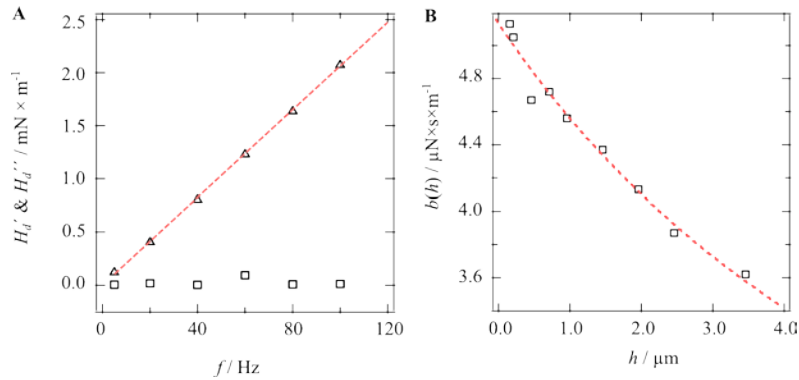
Figure 3.13: A Real part of the transfer function H_D' (squares) and imaginary part H_D'' (triangles) as a function of the oscillation frequency f at a fixed tip surface distance h. The dashed line shows linear fit of H_D'' with the slope $2\pi b(h)$. **B** Drag coefficient $b(h)$ (squares) as a function of the tip-sample separation h. The data were fitted using a scaled spherical model described by Alcaraz and coworkers (eq. 3.14, dashed line). Extrapolation of the fit to $h = 0$ nm delivers the drag coefficient $b(h_0)$ used for the hydrodynamic drag correction.

The drag coefficient is determined at tip-sample separations ranging from 200 nm to 3500 nm. The dependency of the drag coefficient $b(h)$ from the tip-sample separation is shown in Figure 3.13 B. At low tip-substrate distances, a higher drag coefficient is observed. The drag coefficient as a function of the tip-sample separation is fitted with the scaled spherical model of the cantilever to obtain the drag coefficient at an extrapolated tip-sample separation of 0 nm ($b(h_0)$):(Alcaraz *et al.*, 2002)

$$b(h) = \frac{6\pi\eta a_{eff}^2}{h + h_{eff}} \quad , \tag{3.14}$$

where η denotes the viscosity of the medium and a_{eff} and h_{eff} are fitting parameters describing the cantilever geometry. Finally, $b(h_0)$ is subtracted from the imaginary part of $F(\omega)/\delta(\omega)$ leading to the following expression for the complex shear modulus:

$$G* = G' + iG'' = \frac{(1-\upsilon)}{3\tan(\alpha)\delta_0}\left[\frac{F(\omega)}{\delta(\omega)} - i\omega b(h_0)\right], \qquad (3.15)$$

where

$$\frac{F(\omega)}{\delta(\omega)} = \frac{A_F(\omega)}{A_\delta(\omega)}\exp\left\{i((\varphi_F(\omega) - \varphi_\delta(\omega)) - \varphi_{lag}(\omega))\right\}. \qquad (3.16)$$

3.9.5 Experimental procedure

AFM-experiments were carried out using a MFP-3D™ (Asylum Research, Santa Barbara, CA, USA) setup equipped with a BioHeater™ mounted on an inverted Olympus IX 51 microscope (Olympus, Tokio, Japan). MLCT cantilevers (C-lever, nominal spring constant 10 pN/nm, length 200 μm, tip height 8 μm, Bruker, Camarillo, CA, USA) with a pyramidal tip were used for imaging and force spectroscopic experiments. Prior to each experiment, the spring constant of the cantilever and the hydrodynamic drag force acting on the cantilever were determined on a flat glass slide. After calibration of the spring constant and hydrodynamic drag coefficient, the glass slide was replaced by the substrates used for cell culturing. A homemade holder of spring steel fixed the substrates during the measurement inside the BioHeater™. The temperature was set to 37°C throughout the measurement. Before each force spectroscopic measurement, the area of interest was imaged in contact mode.

Force spectroscopy and frequency dependent rheological data were acquired by approaching the cantilever towards the surface with a velocity of 3 μm/s. When the pre-set trigger point was reached, the cantilever movement was stopped for 0.5 s before it was excited to oscillate with frequencies between 5 Hz and 100 Hz (5 Hz to 150 Hz (A549 cells)) at small oscillation amplitudes (A_δ = 20 - 50 nm, peak to peak). After an additional quiescent period of 0.5 sec it was retracted from the surface. Per area of interest, usually 1024 of these force-distance curves where recorded in a 32 point × 32 point grid (force map). Per force map 2 to 15 cells were probed.

3.9.6 Data processing

The measured data were analysed using a self-written MATLAB-program $\mathrm{ShearFM.m}$ (Mathworks, Natick, MA, USA), which allowed hydrodynamic drag correction and selection and spatial analysis of force-indentation curves.

A selection of force-indentation curves, obtained from the center of the cell, was chosen from the overall 1024 force-distance curves per force map. The selection avoids artifacts from the underlying substrate. Additionally, force-distance curves, which did not increase monotonically with the indentation depth, were also excluded from analysis. The contact point was set manually. Drifts in force-distance curves were subtracted by fitting a line to the approach curve.

In contrast, for analysis of different cell lines (chapter 4.3) force-indentation curves were selected according to their indentation depth δ_0 between 300 and 800 nm.

The obtained frequency-dependent data of the complex shear modulus $G*$ were fitted by the power-law structural damping (PLSD) model as used by Alcaraz and coworkers using a non-linear least squares fitting routine (MATLAB, Mathworks, MA, USA).(Alcaraz *et al.*, 2003) In the PLSD model the storage modulus G' of a sample to the loss modulus G'' via the power law coefficient according to

$$G* = G_0(1+i\tan(\frac{\alpha_{PLSD}\pi}{2}))\left(\frac{\omega}{\omega_0}\right)^{\alpha_{PLSD}} + i\omega\mu, \qquad (3.17)$$

with the scaling factor G_0 describing the stiffness of the sample, the power law coefficient α_{PLSD}, the angular frequency ω, the scaling factor of the frequency ω_0 and the Newtonian viscosity μ.

3.10 Scanning ion conductance microscopy

3.10.1 Setup

To measure contact free, non-invasive images of the cell surface scanning ion conductance microcopy (SICM) experiments (ICnano-S, ionscope, Melbourn, UK) were performed. SICM was first used to image the apical membrane of living cells by Korchev and coworkers.(Korchev *et al.*, 2000) The technique uses an electrode in a micropipette, which is filled with an electrolyte solution, as a probe (see Figure 3.14). The counterelectrode is immersed in the same solution.
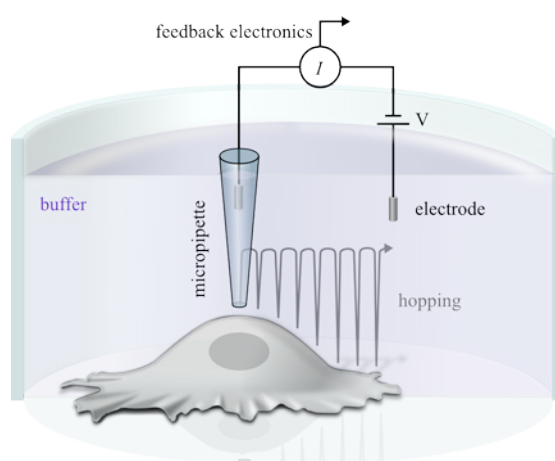
Figure 3.14: Scheme of the experimental setup of a scanning ion conductance microscope. As the current flow between the electrode in the micropipette and the counterelectrodes is a function of the pipette-sample separation, the distance between pipette and sample can be controlled by a feedback loop. In hopping mode, the pipette is moved towards the sample as long as the current between both electrodes is higher than the setpoint. When the setpoint is reached the pipette is retracted and moved to the next position where the procedure is repeated.

When a voltage is applied between both electrodes the current flow is a function of the ionic strength of the electrolyte solution, of the inner radius of pipette and also of the pipette-sample distance. This effect can be used to acquire images of a surface non-invasively by using the current flow as a feedback signal. In hopping mode, the pipette is moved towards the surface. As the pipette approaches the surface the resistance increases and the current I decreases. When the current falls below the setpoint the pipette is retracted and moved to the next position.

3.10.2 Experimental procedure

Before measurement, MDCK-II cells were fixed for 10 minutes in a 4% paraformaldehyde solution. After fixation cells were immersed in PBS-buffer. The pipettes used in SICM experiments were produced from glass capillaries (GB 100F-8P, Science Products, 0.58 mm × 1.00 mm × 80 mm) using a P-1000 micropipette horizontal puller (Flaming/Brown, Sutter Instrument, Novato, USA).

Images of the cell surface of MDCK-II cells with a size 20 × 20 µm^2 and 128 px × 128 px were acquired using hopping mode. Images have been acquired by Helen Nöding (Georg-August-University, Göttingen, Germany) during her master thesis.

To visualize the fine structure of the cell surface the main curvature of the cell's apical membrane was removed using a self-written 2D moving average algorithm (PlotTool.m, MATLAB, Mathworks, Natick, MA, USA) was used. The 2D-moving average determines the mean value of an 11 × 11 pixel window and assigns it to the center pixel of the window. The window is moved over the whole height image pixel by pixel. To maintain the original size of the image mirror padding was used for the edge regions. One should note that the 2D-moving average produces a convolution of the surface, which is dependent on the shape and the size of the window used for average calculation. The resulting mean height image is then subtracted from the original height image yielding the curvature corrected surface structure

3.11 Fluorescence microscopic methods and fluorescence staining

3.11.1 Epi-fluorescence microscopy and confocal laser scanning microscopy

3.11.1.1 Staining of the actin cytoskeleton

Fluorescence microscopy was used to examine the actin-cytoskeleton arrangement in MCDK-II cells, which were treated with drugs interfering with the actomyosin network or were cultured on porous substrates, and NMuMG cells before and after epithelial-to-mesenchymal transition. Staining of MDCK-II samples grown on porous substrates was performed by Helen Nöding in her master thesis. NMuMG cells were stained by David Schneider (Georg-August-University, Göttingen, Germany) To stain the actin cytoskeleton, cells were first rinsed 2 times using PBS and fixed using 4% PFA (FLUKA, Switzerland) for 15 minutes at room temperature. Afterwards, samples were rinsed 2 times with PBS and incubated for 45 minutes with blocking buffer (5% bovine serum albumin (BSA) and 0.3% Triton-X-100 in PBS) at room temperature. After removal of the blocking buffer, a 165 nM Alexa Fluor® 546 Phalloidin (Life Technologies, Carlsbad, CA, USA) in dilution buffer (1% BSA and 0.3% Triton-X-100 in PBS) was applied and samples were incubated for 1 hour. In a next step, samples were washed 2 times for 5 minutes using washing buffer (0.1% BSA in PBS). Finally, DNA was stained using a 500 ng/ml solution 4,6-diamidin-2-phenylindol (DAPI). After 10 minutes incubation, samples were again washed 2 times for 5 minutes using PBS.

The samples were examined using either an Olympus BX51 epi-fluorescence setup (Olympus, Tokyo, Japan) or a confocal laser scanning microscope (LSM 710, Zeiss, Göttingen, Germany) equipped with an Argon-laser (LASOS Lasertechnik, Jena, Germany).

3.11.1.2 Sample preparation for fluorescence microscopic examination of GUVs exposed to nanoparticles

To examine the effect of nanoparticles on artificial lipid bilayers, GUVs prepared by electroformation (see chapter 3.4) were added into a solution of nanoparticles in buffer prepared either in ibidi µslide 8 well (ibidi, Martinsried, Germany) and 96-well plates for

examination using epi-fluorescence (IX81, Olympus, Tokyo, Japan) or in glass bottom petri dishes (MatTek, Ashland, MA, USA) for studies using confocal laser scanning microscopy (LSM 710, Zeiss, Göttingen, Germany). Prior to experiments, glass bottom petri dishes were treated with a 0.1% BSA solution in deionized water for 1.5 hours to passivate hydrophilic glass surface and prevent GUVs from spreading.

3.11.1.3   Uptake of pyranine-stained nanoparticles solutions into A549 cells

To examine the uptake of nanoparticles, which are not fluorescently labeled themselves the plasma membrane of A549 cells was first stained using a 5 µg/ml Cell Mask™ Deep Red Plasma Membrane Stain (Life Technologies, Carlsbad, CA, USA) solution in cell culture medium at 37°C. After 5 minutes the staining solution was replaced by cell culture medium and incubated at 37°C and 5% CO2 for 15 minutes. Then, the normal cell culture medium was replaced by 5 µg/ml nanoparticle solution in cell culture medium, which additionally contained 2 mM pyranine. The cells were incubated for 30 minutes at 37°C and 5% CO_2. Afterwards, cells were rinsed using PBS and fixed using a 4% PFA solution in PBS. The samples were imaged using a confocal laser scanning microscope (LSM 710, Zeiss, Göttingen, Germany) equipped with an Argon-laser (LASOS Lasertechnik, Jena, Germany).

For data analysis, maximum intensity projections of the pyranine channel of z-stack images were subject to grain analysis using the open source software Gwyddion (http://gwyddion.net). The following parameters were used for grain detection: height = 20%, slope = 12% and curvature = 100%. Histograms of the equivalent radii of the found grains were created using IGOR Pro (WaveMetrics, Lake Oswego, OR, USA).

3.11.2 Fluorescence near metal surfaces

3.11.2.1   Experimental setup and data evaluation

A description of the experimental setup and data evaluation can be found in the publication of Chizhik, Rother *et al.*. (Chizhik *et al.*, 2014a) In brief, a conventional home build confocal laser scanning microscopy setup, which is able to perform fluorescence lifetime measurements (see also chapter 4.4.2), was used with one modification: the cover slide was coated with a 20 nm gold layer. The acquired data were analyzed by Dr. Alexey Chizhik (III. Physical Institute, Georg-August-University,

Göttingen, Germany) according to the model of Chance, Prock and Salbey, which correlates the fluorescence lifetime of a fluorophore to its distance from a metal layer.(Chance *et al.*, 1978) Due to energy transfer from the excited state of the fluorophore to the metal layer the fluorescence is quenched in a distance dependent manner. In general, the model requires the following input parameters: 1) the quantum yield of the fluorophore in free solution, 2) the emission spectrum of the fluorophore and 3) the dielectric function of the metal layer at the used wavelengths.

3.11.2.2   Sample preparation for metal-induced energy transfer fluorescence lifetime imaging and staining of the plasma membrane

For metal induced energy transfer- (MIET-) fluorescence lifetime imaging (FLIM) experiments, approximately 20,000 MDA-MB-231 cells were seeded into a small reservoir with a diameter of 1 cm, which was melted on top of the cover slide. Cell-substrate distance was monitored with MIET FLIM within two days after seeding. A549 cells and MDCKII were seeded in the same density on gold-coated glass bottom petri dishes (MatTek, Ashland, MA, USA).

Prior to the measurement, the plasma membrane of cells was stained by incubating living cells with HEPES-buffered cell culture medium containing 5 µg/ml Cell Mask™ Deep Red Plasma Membrane Stain (Life Technologies, Carlsbad, CA, USA) for 5 minutes at 37°C. For the actual measurement, the staining medium was replaced by HEPES- buffered cell medium, which allowed the investigation of living cells up to one hour after staining at 37°C.   To examine the spreading of MDCK-II cells, the cells were released from the culture flask by trypsinization for 5 minutes (trypsin/EDTA 0.5%/0.2%, Biochrome, Berlin, Germany) and kept in suspension in a density of $1×10^6$ cells/ml. The cells were used for up to 1 hour. For the adhesion experiments the gold-coated glass bottom petri dishes were incubated for 30 minutes with HEPES buffered cell medium. The cell medium was replaced by 400 µL of the staining solution (cell culture medium containing 5 µg/ml Cell Mask™ Deep Red Plasma Membrane Stain) and 50,000 cells were added. After 5 minutes at 37°C the staining solution was carefully replaced by HEPES-buffered cell culture medium and the measurement was started.

3.12 <u>Scanning electron microscopy (SEM)</u>

Scanning electron microscopy was used to examine the cytoskeletal arrangement of MDCK-II cells cultured on porous substrates. For culture conditions see chapter 3.6. MDCK-II cells grown on different substrates were washed in PBS before they were treated for 2 minutes with a 4% Triton-X-100 solution in PBS. After rinsing the samples in PBS the cells were fixed using a 2.5 % glutardialdehyde solution (Acros Organics, Belgium) in PBS. The samples were incubated for 1 hour at room temperature. Then, cells were again washed in PBS and dehydrated using an ethanol series with increasing ethanol proportion (50%, 70%, 80%, 90%). The samples were incubated in each ethanol solution for 1 hour at room temperature and stored overnight in ethanol p.a. at 4°C. Finally, the samples were dried using a gently nitrogen stream and subsequently coated with a 5 nm gold layer by thermal evaporation (Balzers, BAE 250 coating system).

Images were acquired using a Zeiss Leo Supra 35-setup (Zeiss, Oberkochen, Germany) and an accelerating voltages of 2.0 kV. Gold-coating of samples, image acquisition and analysis of line densities have been carried out by Matthias Büchsenschütz-Göbeler (I. Institute of Physics, Georg-August-University, Göttingen, Germany).

Line densities of filaments were determined by analysing SEM images of the same category with a magnification of 50k. For each pore size a spatially linear sequence of at least 20 images was recorded. Furthermore, lines with an average length of 2 µm and random orientation were drawn into each image. Finally, the number of single filaments crossing an individual line was counted yielding the line densities in 1/nm. This was repeated for at least 100 lines resulting in line density distributions for the different pore sizes (see chapter 4.4.1).

3.13 <u>Finite element simulations</u>

COMSOL multiphysics (version 4.3, Göttingen, Germany) was used for finite element simulation of stress distribution in a thin elastic sheet simulating the basal actin network of MDCK-II cells grown on a porous substrate (chapter 4.4.1). A long, 200 nm thin sheet crossed by two orthogonal sheets simulated the actin cytoskeleton. The sheet's elastic modulus was set to 1 MPa and the Poisson ratio to 0.49. To account for the pores, circular holes were drawn at the two crossing points of the three sheets. An isotropic inwards-directed pressure of 5 Pa was applied to the boundaries of the pores.

3.14 <u>Measurement of osmolalities</u>

Osmolalities of nanoparticle solution and buffers used in chapter 4.1 were measured using a OSMOMAT 3000 freezing point osmometer (Gonotec, Berlin, Germany). 50 µl of the solutions were added into a 250 µl vial, which was put onto the sensor. After each measurement the probe was cleaned using a dust-free wipe and deionized water.

4. Results and Discussion

4.1 Inorganic Janus Particles: Menace or Opportunity?

4.1.1 Introduction

Janus particles, named after the two-faced roman god, provide multiple surface platforms that facilitate site-specific anchoring of biomolecules, electrical connections and chemically directed assembly of colloidal nanostructures.(Chen *et al.*, 2011; Nie *et al.*, 2007) Various synthetic approaches have been used to produce binary as well as ternary heterostructures.(Gu *et al.*, 2005; Kwon and Shim, 2005; Pellegrino *et al.*, 2006; Shi *et al.*, 2006) Metal-semiconductor hybrid nanocrystals including CdS-, CdSe- and CdTe-based heterostructures offer potential opportunities for solar energy conversion and photocatylsis due to their nanoscopic dimensions and accompanied quantum confinement effect in the semiconducting part.(Costi *et al.*, 2008; Milliron *et al.*, 2004; Subramanian *et al.*, 2004) Furthermore, Janus particles with two domains carrying opposite charges can be aligned in an electric field, which for example is applicable in e-paper displays.(Dendukuri and Doyle, 2009) Janus particles of amphiphilic nature also offer great opportunities in emulsification, as the surface area stabilized by one particle is much larger than the particle's cross-section.(Wurm and Kilbinger, 2009) In summary, nanoscopic heterostructures are the next generation of nanoparticles with obvious opportunities and advantages, and it is expected that Janus particles will enter industry and consumer products in near future.

Therefore, a profound understanding of the interaction between Janus particles and cells is important for a safe use of these nanoparticles. Especially, uptake of nanomaterials by cells plays an important role in the further processing. It has been shown, that most isotropic nanoparticles are taken up into the cell via conventional endocytotic mechanisms like receptor-mediated endocytosis, pinocytosis or phagocytosis.(Jiang *et al.*, 2011; Treuel *et al.*, 2013; Zhang *et al.*, 2002b) However, uptake of particles into cells appears to be dependent on particle shape, size and surface functionalization and on the cell type.(Sohaebuddin *et al.*, 2010; Tarantola *et al.*, 2011) When nanoparticles come into contact with cells, they are also able to directly interact with the plasma membrane. Possible interactions of isotropic nanoparticles and lipid bilayers have been simulated by Yue and coworkers and include wrapping of particles as well as formation of inverse micellar structures around single particles inside the lipid bilayer.(Yue *et al.*, 2014; Yue *et al.*, 2013) Ding *et al.*

could also demonstrate wrapping of Janus particles in simulations.(Ding and Ma, 2012) In contrast, simulations by Reynwar and coworkers simulating the interaction of amphiphilic heterostructures with lipid bilayers showed that these materials are able to induce tubulation and eventually vesiculation.(Reynwar *et al.*, 2007) Upon binding of amphiphilic particles local bending of the membrane produces long-range attractive forces between single particles, leading eventually to aggregation of several particles and thus, to the formation of membrane tubes. This mechanism of tube formation is similar to effects observed for the B-subunit of Shiga toxin in cells and artificial membrane systems.(Romer *et al.*, 2007) Alexeev *et al.* proposed another type of interactions of amphiphilic Janus particles with lipid bilayers.(Alexeev *et al.*, 2008) In their simulations, the authors demonstrated that Janus particles could also incorporate into the lipid bilayer and induce formation of pores, in which the Janus particles align along the pore rim.
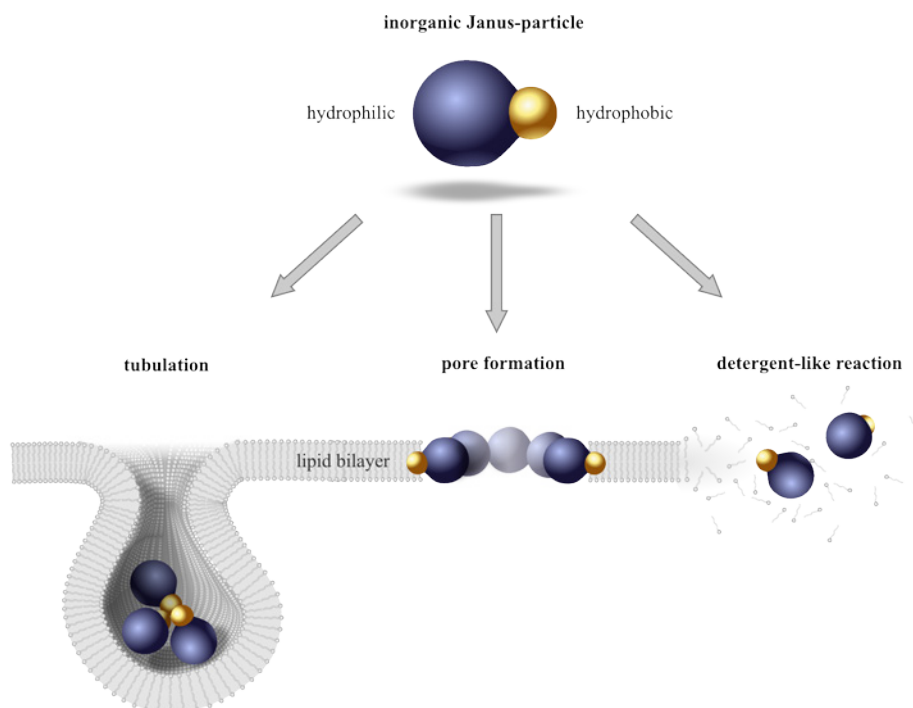
Figure 4.1.1: Scheme of possible Janus particle-membrane interactions. Simulations either predict the formation of membrane tubes or pores by amphiphilic Janus particles, but the particles could also lead to detergent-like reactions dissolving the membrane.

These types of interaction as well as the possibility of site specific surface modifications make Janus particles a promising tool for drug delivery, as these particles are able to overcome the natural barrier of cells without "hitchhiking" an endocytotic pathway. On the other side, unintended uptake of Janus particles into cells or pore formation leading to destruction of the bilayer integrity could also have a severe

impact on cell viability. A scheme of the possible Janus particle/membrane interactions is shown in Figure 4.1.1. However, so far no experimental evidence has been provided for one or the other of the proposed Janus-particle/membrane interaction and little is known about the cytotoxicity of Janus particles.

Here, I focus on the interaction of inorganic MnO@Au-based Janus nanoparticles with artificial lipid bilayers. In my experiments, the MnO domain with a size between 15 and 20 nm is covered with hydrophilic silica and/or polymer-coatings, while the Au domain, which has a diameter between 4 and 10 nm, is hydrophobic carrying a self-assembled monolayer of an alkanethiol. Using "tension-free" giant unilamellar vesicles (GUVs) as artificial membrane system I found evidence for the mechanism of tube formation proposed by Reynwar *et al.*. On the other hand, Janus particles failed to induce tubulation in GUVs with elevated membrane tensions. Additionally, uptake experiments into living cells showed no difference to the untreated sample or to samples treated with isotropic MnO-particles suggesting that particle-induced endocytosis might play a minor role in living cells.

4.1.2   Results & Discussion

4.1.2.1   Interaction of methoxy-functionalized manganese(II)-oxide Janus particles with giant unilamellar vesicles

The interaction with the cellular membrane is a crucial step in the further processing of nanomaterials by cells.(Vasir and Labhasetwar, 2008) Especially Janus particles, which represent anisotropic particles with at least two chemically or physically different domains, are supposed to show substantial membrane activity due to their amphiphilic nature. In first experiments, I use anisotropic Janus particles, which consist of a manganese(II)-oxide part with a size of 14.9 ± 1.1 nm and a gold part with a diameter of 6.7 ± 0.4 nm, to research the interaction of Janus particles with artificial membranes. To verify successful synthesis of Janus type particles transmission electron microscopy experiments are conducted (TEM, experiments performed by Isabel Schick, Institute of Inorganic and Analytical Chemistry, Johannes-Gutenberg university, Mainz, Germany). Representative TEM images can be found in Figure 4.1.2 A and B. The Au-domains of the Janus particles appear dark in TEM images due to their high electron density (see Figure 4.1.2 B). The MnO domain is brighter. Figure 4.1.2 B shows heterodimeric composites of MnO and Au in which both parts are exposed to the media implying that real anisotropic Janus particles are formed during synthesis. Further details about

synthesis of Janus particles can be found in chapter 3.1 or in the publication by Schick *et al.*.(Schick *et al.*, 2014) Schick and coworkers as well as Schladt and coworkers also demonstrated that the choice of the surfactant stabilizing the gold precursor particles during synthesis is crucial for the asymmetric growth of the metal oxide on the gold lattice.(Schladt *et al.*, 2010) Using oleic acid and oleylamine as surfactants lead to epitaxial growth of MnO domains on the gold surface producing nanocomposites with a flowerlike structure. Here, 1-octadecanethiol was used to stabilize the Au-seed particles during the thermal decomposition of manganese(II)-oleat leading to anisotropic growth of a MnO-domain on the gold particle.
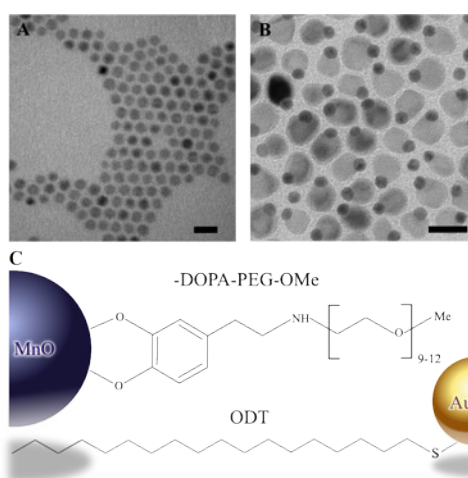
Figure 4.1.2: Representative TEM images of **A** spherical MnO-particles and **B** Au@MnO-Janus particles (Images have been measured by Isabel Schick, Institute of Inorganic and Analytical Chemistry, Johannes-Gutenberg University, Mainz, Germany). Scale bars: 20 nm **C** Scheme of functionalization of the different domains. The metal oxide domain was functionalized with polyethylene glycol (PEG), which is attached to the nanoparticle surface via a dopamine anchor. The other end of the PEG carried a methoxy-group. The gold part is functionalized with 1-octadecanethiol (ODT).

In the present study, the MnO-domain of the Janus particles is functionalized with polyethylene glycol with an average molecular weight of 600 g/mol (PEG$_{600}$), which binds to the metal oxide via an attached dopamine anchor (DOPA) in a nearly covalent manner.(Xu *et al.*, 2004) The other end of the PEG carries a methoxy-group. This functionalization renders the MnO-domain hydrophilic, whereas the gold-domain is hydrophobic due to functionalization with 1-octadecanethiol (ODT). A scheme of the surface functionalization can be found in Figure 4.1.2 C. For comparison, I use spherical MnO-particles with a diameter of 10.1 ± 0.7 nm. Again, the surface of the metal oxide is functionalized with DOPA-PEG-OMe.

To examine the interaction of amphiphilic Janus particles with artificial lipid bilayers I use giant unilamellar vesicles (GUVs) produced by electroformation. GUVs were

produced from 99.5 mol% 1,2-dioleoyl-s,n-glycerol-3-phosphatidylcholine (DOPC) and 0.5 mol% of TexasRed® 1,2-dihexadecanoyl-sn-glycero-3-phosphoethanolamine (TR-DHPE) to allow for fluorescence microscopic exploration of the membrane. DOPC is a natural lipid and its main phase transition temperature lies at -17°C (http://avantilipids.com, 14.03.2014). Thus, at room temperature it is in the liquid-crystalline (L_α-)phase.
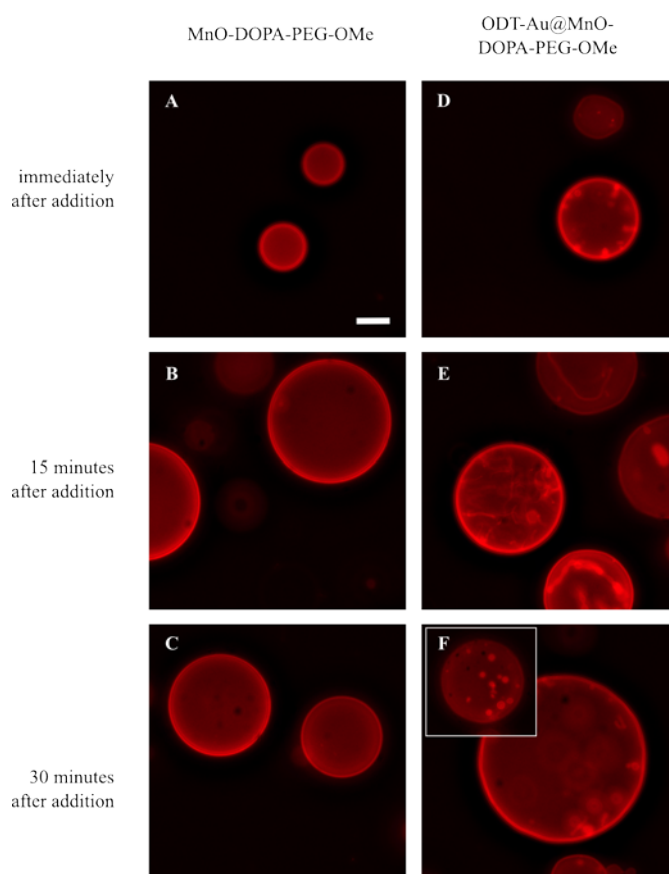
Figure 4.1.3: Interaction of Janus particles with GUVs **A, B, C** epifluorescence images of DOPC/TR-DHPE GUVs treated with 1 µg/ml spherical MnO-DOPA-PEG-OMe nanoparticles in the equatorial focal plane. **D, E, F** epifluorescence images of DOPC/TR-DHPE GUVs treated with 1 µg/ml ODT-Au@MnO-DOPA-PEG-OMe Janus-nanoparticles in the equatorial focal plane. Scale bar: 20 µm **Inlet in F**: upper half of the GUV shown in F treated with ODT-Au@MnO-DOPA-PEG-OMe Janus-nanoparticles.

DOPC/TR-DHPE-GUVs filled with a 100 mM sucrose solution were added to a 90 mM solution of glucose, which allowed the particles to sediment and produced an osmotic gradient across the membrane, which prevented unintended deflation of vesicles. 1 µg/ml nanoparticles were added to the GUV solution. The effects of Janus particle administration to DOPC-GUVs were followed for 30 minutes using epi-flourescence microscopy (see Figure 4.1.3). Figure 4.1.3 A, B and C show GUVs, which are exposed to spherical isotropic MnO particles. The GUVs do not show any irregularities

in shape or in the membrane over the whole time. In contrast, immediately after addition of ODT-Au@MnO-DOPA-PEG-OMe Janus particles, the membrane of the GUVs starts to form membrane tubes to the inside of the GUVs. These membrane tubes become even more pronounced after 15 minutes incubation and eventually lead to the formation of small vesicles inside the GUVs (see Figure 4.1.3). Notably, the smaller vesicles inside the GUVs can be exclusively found in the top half of the GUV indicating that they are taken up by the GUV and contain media with lower density (90 mM glucose) compared to media filling the GUV (100 mM sucrose). To ensure, that the observed effect does not result from a change in the osmotic gradient, I controlled the osmolalities of the used solutions. The observed osmolalities of the used solutions can be found in table 4.1.1.

Table 4.1.1: Osmolality of solutions used in GUV experiments.

	osmolality / **mosmol/kg**
100 mM sucrose	119
1 µg/ml ODT-Au@MnO-DOPA-PEG-OMe + 90 mM glucose	96
1 µg/ml MnO-DOPA-PEG-OMe + 90 mM glucose	96

The measured osmolalities indicate that both glucose-nanoparticle solutions were hypoosmolar compared to the sucrose solution inside GUVs. Thus, the membrane of vesicles is set under tension, which also prevents thermal membrane undulations that are observed for tension-free membranes.(Boal, 2012) Apparently, attractive forces between Janus particles and DOPC/TR-DHPE GUVs are sufficient to induce membrane deformations, but are not high enough to promote complete membrane wrapping of single particles as demonstrated in simulations by Ding *et al.* for Janus particles or by Yue *et al.* for spherical particles.(Ding and Ma, 2012; Yue *et al.*, 2013) This is conceivable since the hydrophobic Au-domain experiences repulsive forces from the polar head groups of the membrane lipids. However, as depicted in Figure 4.1.1 Janus particles could also insert into the lipid bilayer and form pores as proposed by Alexeev and coworkers.(Alexeev *et al.*, 2008) Using coarse grain simulations, the authors could demonstrate that small Janus particles are able to produce pores in lipid bilayers in which the Janus particles line the pore rim. Thereby, the hydrophobic part of

the particles interacts with the hydrophobic chains of the lipids. Although I cannot completely rule out this way of interaction between the Janus particles and the lipid bilayer at this point, it appears to be very unlikely because pores in the membrane would presumably allow molecules, e.g. the sucrose to diffuse into the vesicles, and thus, to eliminate the osmotic gradient. Without the osmotic gradient one would observe membrane undulations, which did not appear in my measurements as the contour of the GUVs remains completely circular (Figure 4.1.3). Additionally, the Janus particles used in the simulations were small having a size comparable to the lipid bilayer thickness. Particles used in this study are larger with a diameter of the gold part of 6.7 nm and insertion into the lipid bilayer appears therefore less likely. Anyhow, vesicles treated with Janus particles exhibit massive membrane deformations and eventually vesicles form from tubulations. Energetically, deformation of a lipid bilayer can be described by the local bending energy per unit area, which amounts to $2\kappa_B/R^2$, where κ_B denotes the bending modulus and R is the radius of curvature.(Boal, 2012) For lipid bilayers κ_B has a value of $10-20 \ k_BT$. Thus, formation of a spherical vesicle with a surface of $4\pi R^2$ from a planar lipid bilayer costs approximately $500 \ k_BT$ of energy and is independent of vesicle radius.(Reynwar et al., 2007) Zimmerberg and coworkers calculated that the interaction between a single curvature-inducing protein, e.g. BAR-domain protein, and the lipid bilayer is on the order of $10 \ k_BT$, which is one order of magnitude lower than the energy needed to form a vesicle.(Zimmerberg and McLaughlin, 2004) However, Reynwar et al. proposed a mechanism for cooperative membrane bending by proteins or Janus particles. (Reynwar et al., 2007) In coarse grain simulations, the authors showed that Janus particles placed on a lipid bilayer interact with each other via long-range interactions. A single particle on a lipid bilayer produces a local curvature in the membrane. When the local curvatures induced by two particles overlap, the particles experience a long-range attractive force due to energy minimization of the elastic energy stored in the membrane due to the induced local curvature. Thus, particle pairs form and produce a larger membrane tubule, which attracts more particles. Eventually, a particle filled vesicle pinches off, demonstrating a passive (not actively driven by the cell) way of endocytosis in this artificial lipid bilayer system. As I observe similar steps of membrane perturbation in my experiments, it is likely that the examined Janus particles follow the route described by Reynwar and coworkers. Nevertheless, the modes of interaction between particles and membrane remain unclear, as the particles are invisible in my experiments. I also performed experiments, in which the methoxy group was replaced by a fluorescein isothiocyanate (FITC), but vesicles treated with these particles did not show any tubulation (data not shown) suggesting a change in the interaction between membrane and particle. To

increase the biocompatibility of our MnO-based nanoparticles, the MnO-domain was coated with a thin silica layer, which is supposed to preserve leakage of Mn^{2+}-ions. The effect of this functionalization on the nanoparticle-membrane interaction will be examined in the next chapter.

4.1.2.2 Interaction between silica-coated manganese(II)-oxide Janus particles and giant unilamellar vesicles

In the last chapter, I examined the effect of methoxy-functionalized MnO-based inorganic Janus particles on artificial membranes. Artificial membranes, i.e. GUVs, exhibited strong tubulation and vesiculation after treatment with Janus particles, which might demonstrate a possible entry route into living cells without involvement of active endocytotic mechanisms. On the one hand, this effect could be used for effective delivery of drugs into cells. On the other hand, an uncontrolled uptake of particles could promote cytotoxicity of such nanomaterials and would not occur in a cell-specific manner. With the final goal to minimize cytotoxic effects of the nanoparticles, while their amphiphilic properties are preserved, I here use silica-coated MnO-based Janus particles to explore their activity on artificial membranes.
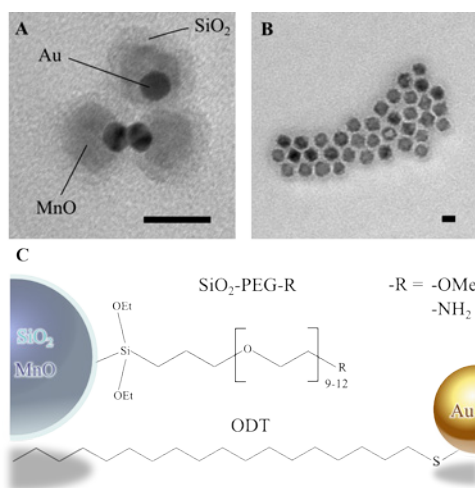
Figure 4.1.4: Representative TEM images of **A** Au@MnO@SiO$_2$-particles and **B** spherical MnO@SiO$_2$-Janus particles (Images have been taken by Isabel Schick, Institute of Inorganic and Analytical Chemistry, Johannes-Gutenberg University, Mainz, Germany). Scale bars: 20 nm **C** Scheme of functionalization of the different domains. The metal oxide part was coated with a thin SiO$_2$-layer. Using PEG-silanes the silica coating was functionalized. The PEG either carried an amino-group or a methoxy-group at the end. The gold part is functionalized with octadecanethiol (ODT).

The silica coating prevents leakage of ions from the metal oxide core and demonstrates a less reactive interface compared to manganese oxide. (Peng *et al.*, 2011; Schladt *et al.*, 2012) All nanoparticles were synthesized by Isabel Schick (AK Tremel, Institute of Inorganic and Analytical Chemistry, Johannes-Gutenberg University, Mainz, Germany). Representative TEM-images of the Janus particles and spherical control particles can be found in Figure 4.1.4 A and B. Figure 4.1.4 A shows three Au@MnO@SiO$_2$ Janus particles. Like in Figure 4.1.2 the Au domains appear dark in the TEM image. The MnO domain is brighter and the SiO$_2$ coating on the MnO domain almost shows the same contrast as the background. In average the MnO-domain has a diameter of 20 nm, while the Au-domain is smaller with a diameter of 10 nm. Spherical MnO nanoparticles have also a diameter of 20 nm (Figure 4.1.4 B). The silica coating of nanoparticles iss functionalized with PEG carrying either an amino-group or a methoxy-group at the end.

Methoxy-functionalized Au@MnO@SiO$_2$ Janus particles

Prior to experiments with GUVs, the functionalized particles were characterized according to their hydrodynamic radius R_h and dissociation constant K_D between particles and lipids, which allows to estimate if the particles could have an effect on the membrane of GUVs.

The hydrodynamic radius R_h of PEG-OMe functionalized particles was examined by dynamic light scattering (DLS, experiments were performed by Isabel Schick, AK Tremel, Institute of Inorganic and Analytical Chemistry, Johannes-Gutenberg University, Mainz, Germany). Figure 4.1.5 shows the correlation function as a function of the lag time τ.
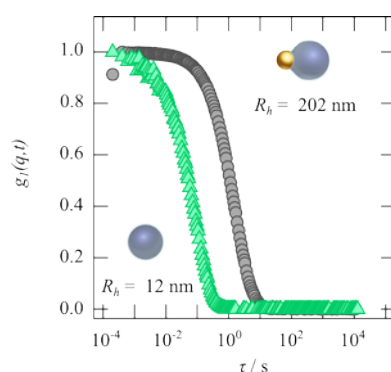
Figure 4.1.5: Correlation function $g_1(q,t)$ of spherical MnO@SiO2-PEG-OMe (▲) and ODT-Au@MnO@SiO2-PEG-OMe Janus particles (●) in 5 mM NaBr solution at a scattering angle of 90°.

For small particles the intensity signal of the scattered light is less correlated in time leading to a decrease of the correlation function g_l at smaller lag times τ. The correlation function g_l of the intensity signal of scattered light of solutions containing larger particles becomes uncorrelated at larger τ. Fitting of $g_l(q,t)$ with a biexponential function allows determination of the hydrodynamic radius R_h. Spherical MnO@SiO$_2$-PEG-OMe particles possess a hydrodynamic radius of 12 nm, which is in good agreement with the radius derived from TEM images. However, Janus particles exhibit a large hydrodynamic radius of 202 nm in aqueous solution. Presumably, the Janus particle form aggregates or micellar structures due to their hydrophobic Au-domain. Also two of the three particles in the TEM image (see Figure 4.1.4 A) are in contact with each other over the Au-domains. As the TEM samples are prepared by drying of an aqueous particle solution on a TEM grid, this might also be a hint for the formation of micellar structures in aqueous solution.

To evaluate the interaction between Janus particles and DOPC lipids I used surface plasmon resonance (SPR) spectroscopy. For this purpose, the gold film of the SPR sensor was functionalized with 1-octanethiol (OT), which forms a self-assembled monolayer (SAM) on the gold surface. Rinsing the OT-functionalized sensor with an aqueous solution of small unilamellar DOPC vesicles resulted in the formation of a DOPC monolayer on top the SAM. Details of the preparation can be found in chapter 3.3. I then added nanoparticle solutions with increasing concentrations in 2 mM TrisHCl buffer under constant flow conditions. Figure 4.1.6 shows the results of the SPR measurement for spherical and Janus particles carrying the PEG-OMe functionalization.
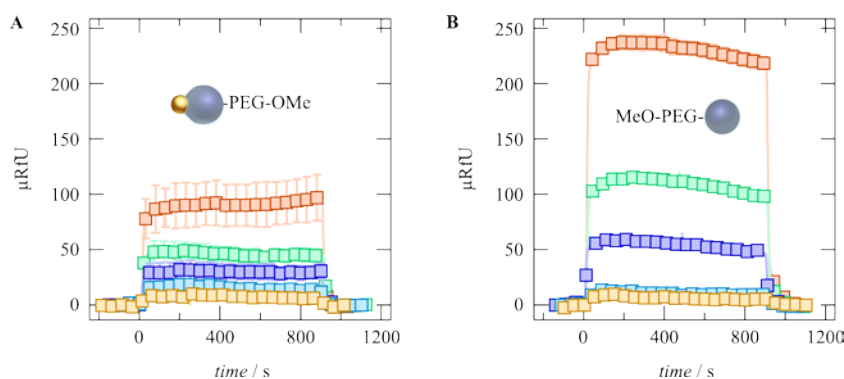
Figure 4.1.6: Surface plasmon resonance spectroscopy of methoxy-PEG functionalized Au@MnO@SiO2 Janus (**A**) and spherical MnO@SiO2 particles (**B**) on DOPC monolayer. (■ 25 µg/ml, ■ 10 µg/ml, ■ 5 µg/ml, ■ 1 µg/ml, ■ 0.5 µg/ml) Markers show every 50th point.

At $t = 0$ s the particle solutions are added. A change in reflectivity units μRfU indicates alterations in the dielectric properties in proximity to the sensor surface. Addition of ODT-Au@MnO@SiO$_2$-PEG-OMe Janus particles as well as spherical MnO@SiO$_2$ particles lead to a concentration dependent increase in μRfU. All samples reach a dynamic equilibrium after no more than 100 s. When switched to nanoparticle free buffer the signal drops to its initial value within 100 s indicating a completely reversible binding of nanoparticles to DOPC lipids. In general, spherical particles induce a higher signal compared to the Janus particles. The dissociation constant K_d of both particle types is determined by fitting the average dynamic equilibrium value using Langmuir adsorption kinetics (see chapter 3.3). Figure 4.1.7 shows the isotherms fitted to the data measured by SPR.
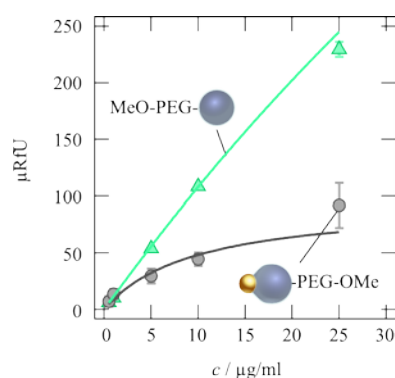
Figure 4.1.7: μRfU as a function of concentration (MnO@SiO2-PEG-OMe (▲ ± STD) and ODT-Au@MnO@SiO$_2$-PEG-OMe Janus particles (● ± STD)). Measured SPR-spectroscopy data obtained from addition of Janus particles to a lipid monolayer prepared on the SPR chip were fitted by a Langmuir adsorption isotherm (solid lines).

As both particles do not reach saturation in the examined concentration range, the K_d values obtained by the Langmuir fit are quite error-prone but allow a rough estimation of the interaction strength between particles and membrane. For ODT-Au@MnO@SiO$_2$-PEG-OMe we found a K_D-value of 10 ± 7 µg/ml. As the concentration is determined by AAS and given in mass Mn^{2+}-ions per volume (see chapter 3.1) one needs to calculate the molar concentration of particles in solution. To obtain a molar concentration, the particles are assumed to consist of an ideal MnO sphere (also for the MnO domain of the Janus particles) with a radius of 10 nm. With the density of MnO of 5.45 g/cm^3 (GESTIS Stoffdatenbank, 13.02.2014) I obtain a mass of a single MnO sphere of 2.3×10^{-17} g. 77% of this weight come from manganese. Knowing the number Mn^{2+}-ions per particle one is now able to calculate a molar concentration of particles. For the Janus particles one finally ends up with a K_D value of 0.9 ± 0.7 nM, which is around 10,000 times weaker than the biotin/streptavidin interaction.[Holmberg, Electrophoresis, 2005] With a K_D of 138 ± 34 µg/ml (or 13.1 ± 3.1 nM) spherical

particles show a weaker binding to the DOPC lipids. Using the relationship between dissociation constant K_D and Gibbs free energy

$$\Delta G^\circ = RT \ln(K_D \cdot c_0^{-1}), \tag{4.1}$$

where R denotes the gas constant, T is the absolute temperature and the standard concentration c_0 = 1 mol/l, one can calculate the energy that is released upon binding of the particles to the lipid monolayer. Thus, for binding of the used nanoparticles to a lipid monolayer values of ΔG° on the order of 45 - 50 kJ/mol are obtained. Calculation of the binding energy per particle at 25°C yields a energy of roughly 20 $k_B T$, which is one order of magnitude lower than the bending energy of 500 $k_B T$ required to form a spherical vesicle from a flat lipid bilayer.(Reynwar *et al.*, 2007) Thus, single particles won't induce vesiculation of the lipid bilayer.

On the other hand, this is in the range of protein membrane interactions and the simulations by Reynwar and coworkers showed that cooperative effects could lead to tubulation and vesiculation despite weak interaction of single particles with the membrane. Table 4.1.2 summarizes the physical properties of methoxy-functionalized Au@MnO@SiO$_2$ Janus particles and spherical MnO@SiO$_2$ nanoparticles.

Table 4.1.2: Characterization of methoxy-functionalized Au@MnO@SiO$_2$ Janus particles and spherical MnO@SiO$_2$ nanoparticles. R denotes the radius of domains measured from TEM images, R_h is the hydrodynamic radius obtained from DLS measurements, K_d is the dissociation constant between DOPC and particles obtained from SPR measurements fitting the measured data with a Langmuir adsorption isotherm. ΔG was calculated from K_D values using equation 4.1.

	R / nm	R_h / nm	$K_D \pm STD$ / nM	ΔG° / kJ/mol
ODT-Au@MnO@SiO$_2$-PEG-OMe	10 (MnO) 5 (Au)	202	0.9 ± 0.7	-50
MnO@SiO$_2$-PEG-OMe	10	12	13.1 ± 3.1	-45

As Janus particles are supposed to exhibit substantial membrane activity the effect of the methoxy-functionalized particles on DOPC/TR(99.5/0.5 mol%)-GUVs was examined. In contrast to previous experiments, GUVs were prepared in 100 mM sucrose solution in 2 mM TrisHCl with pH 7. The experiments were carried out in 95 mM glucose solution containing additionally 2mM of the fluorescent dye pyranine in

the same buffer. 5 µg/ml of the particles were added to the GUV solutions. The osmolalities of the media are shown in Table 4.1.3.

Table 4.1.3: Osmolality of solutions used in GUV experiments. Nanoparticles were solved in 95 mM glucose solution.

	osmolality / **mosmol/kg**
100 mM sucrose in 2mM TrisHCl (1)	111
95 mM glucose, 2mM pyranine in 2mM TrisHCl (2)	112
5 µg/ml ODT-Au@MnO@SiO$_2$-PEG-OMe in (2)	112
5 µg/ml MnO@SiO$_2$-PEG-OMe in (2)	115

As expected from previous calculations of the particle number per milliliter, addition of particles in a concentration of 5 µg/ml does not have strong effects on the osmolalities of the solutions. All solutions exhibit a similar osmolality minimizing the osmotic pressure across the GUV membrane.

The interaction between DOPC/TR-GUVs and ODT-Au@MnO@SiO$_2$-PEG-OMe Janus particles as well as MnO@SiO$_2$-PEG-OMe nanoparticles was examined using confocal laser scanning microscopy. Thereby, staining of the outer medium with pyranine facilitated to follow formation of pores in the membrane or uptake of the surrounding medium into the GUVs as the particles were not fluorescent themselves. The results are shown in Figure 4.1.8.
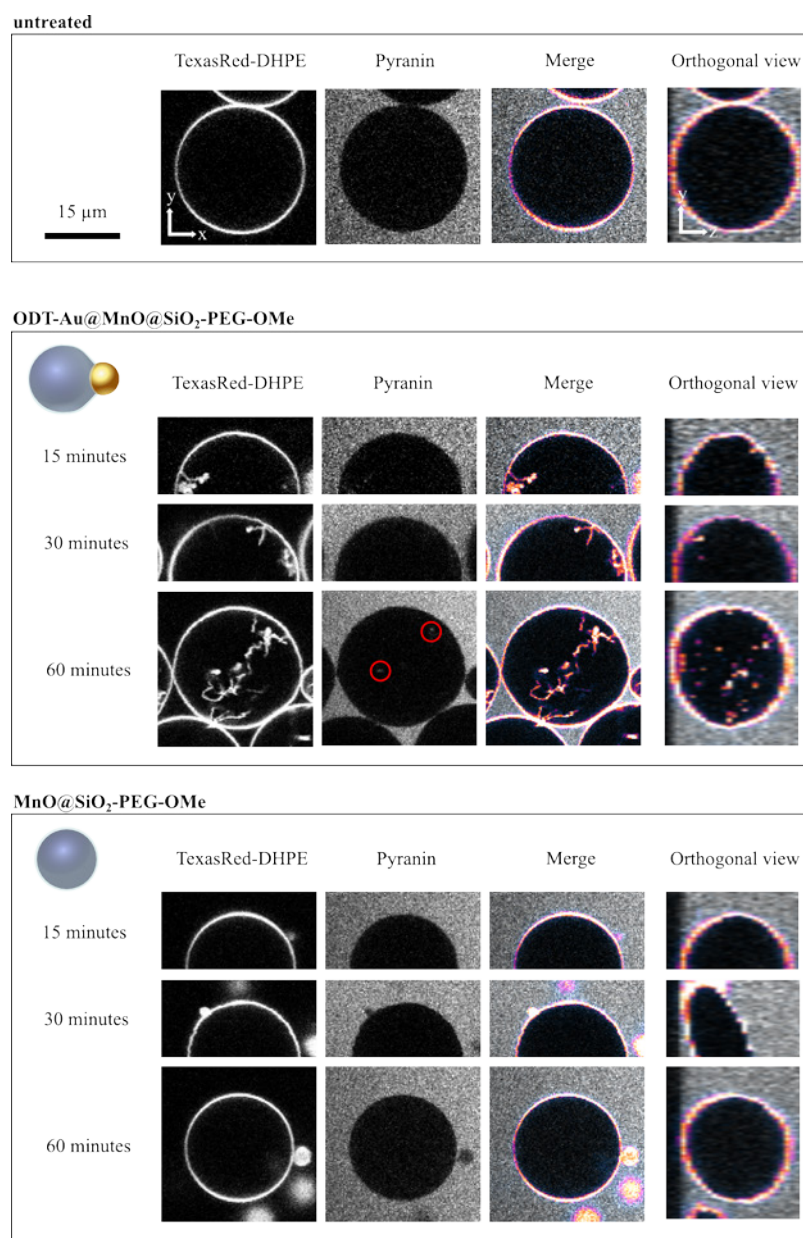
Figure 4.1.8: DOPC/TR-giant unilamellar vesicles treated with 5 µg/ml solutions of methoxy-functionalized Au@MnO@SiO$_2$ Janus particles and spherical MnO@SiO$_2$ nanoparticles imaged using confocal laser scanning microscopy. The nanoparticle solution additionally contained 2mM pyranine. GUVs are shown in the equatorial and meridian plane (orthogonal view). Images of single channels are shown in grey scale. In merged images TR-DHPE channel is shown in pseudocolors (ImageJ, Look up table: gem)

When the GUVs were treated with ODT-Au@MnO@SiO$_2$-PEG-OMe Janus particles, after 15 minutes incubation small membrane tubes start to form, which become larger in time. After 60 minutes, large tubulations are visible in the whole vesicle. The orthogonal view confirms that tubulations are present within the whole vesicle. The pyranine channel also shows that a small amount of the outer medium can be found inside the tubular structures (red circles in Figure 4.1.8). In contrast, GUVs treated with spherical particles do not show any effect. Note that the vesicle shown after 30 minutes

of incubation was moving, which leads to a orthogonal view in which the vesicles appears oblate. As all vesicles in Figure 4.1.8 show nearly spherical shape after 60 minutes of incubation one can assume that osmotic shrinking of the vesicles cannot be responsible for the observed effects. Notably, in contrast to our previous results no vesicles are found, which are pinched off from the membrane tubes. Presumably the interaction between membrane and particles is weaker for the ODT-Au@MnO@SiO$_2$-PEG-OMe Janus particles compared to ODT-Au@MnO-DOPA-PEG-OMe particles. The energy needed to form a membrane tube from a plane membrane sheet is one order of magnitude lower than the force needed to form a vesicle.(Zimmerberg and McLaughlin, 2004) To quantify tubulation, I counted the number of vesicles, which show tubulation related to the total number of examined vesicles.
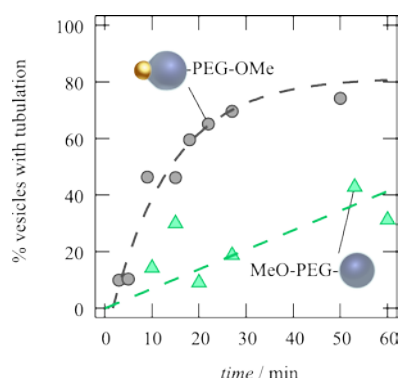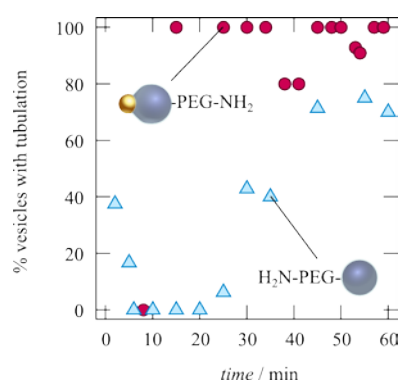

Figure 4.1.9: Quantification of tubulation in DOPC/TR-GUVs induced by methoxy-functionalized Au@MnO@SiO$_2$ Janus particles (●) and spherical MnO@SiO$_2$ nanoparticles (▲). A minimum number of 7 vesicles was examined. Dashed lines are merely guide to the eye (exponential increase of the relative number of vesicles, which show tabulation, in case of incubation with Janus particles and a linear increase in the case of incubation of GUVs treated with spherical particles)

Figure 4.1.9 shows that incubation of GUVs with methoxy-functionalized Janus particles generally leads to a higher relative number of vesicles showing tubulations compared to vesicles incubated with spherical particles carrying the same functionalization. After 5 minutes of incubation in only 10% of the vesicles treated with ODT-Au@MnO@SiO$_2$-PEG-OMe Janus particles exhibited membrane tubes. The relative number of vesicles with tubulations then increased exponentially to a value of 74% after 50 minutes incubation. In the case of spherical MnO@SiO$_2$-PEG-OMe the relative number of vesicles showing tubulation varies between 9 and 43% for the complete duration of the experiment.

Furthermore, no tubulation is observed, when the osmotic pressure in the GUVs is increased by 10 mosmol/kg using a hypoosmotic solution of 90 mM glucose in 2 mM TrisHCl with an osmolality of 100 mosmol/kg (see Figure 4.1.13), which leads to a

proportional increase in membrane tension according to Young-Laplace-equation (eq. 4.2):

$$\Delta P = T \left(\frac{1}{R_1} + \frac{1}{R_2} \right),$$ (4.2)

where ΔP denotes the pressure difference across the membrane, T is the tension produced by the pressure difference and R_1 and R_2 are the radii of curvature. The lack of tubulations in tensed vesicles indicates that binding of Janus particles to the membrane on the one hand is sufficient to deform membranes with low tension but on the other hand is too small to induce bending of membranes at an elevated tension (see Figure 4.1.10).
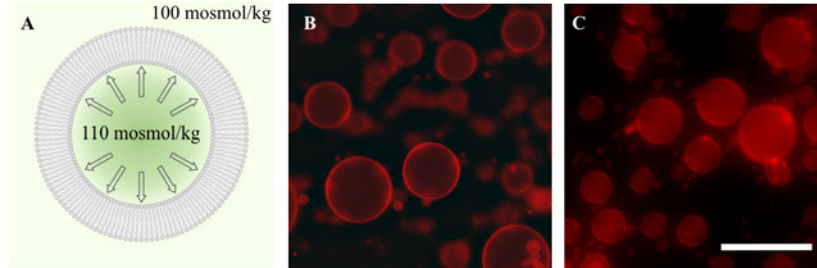
Figure 4.1.10: A Schematic drawing of an osmotically stressed GUV. **B** and **C** Epi-fluorescence images of osmotically stressed DOPC/TR-DHPE-GUVs treated with 5 µg/ml solutions of methoxy-functionalized Au@MnO@SiO$_2$ Janus particles (B) and spherical MnO@SiO$_2$ nanoparticles (C) after 60 minutes incubation. Scale bar: 50 µm

The Gibbs free energy of nanoparticle binding to DOPC lipids was calculated to be on the order of -45 – -50 kJ/mol (*vide supra*) or roughly 20 k_BT per particle, which is not sufficient to induce membrane vesiculation (500 k_BT, *vide supra*) or wrapping of single particles. However, cooperative effects induced by long-range interactions between Janus particles, which occur due to minimization of bending energy in the membrane, could induce tubulation and vesiculation.(Reynwar and Deserno, 2011) A possible reason, why I do not observe tubulation in tensed vesicles is that the adhesion between particles and membrane is not high enough to induce this initial bending of the membrane. Additionally, I only observe tubulation of the lipid bilayer but no vesiculation like before for the ODT-Au@MnO-DOPA-PEG-OMe Janus particles. A possible reason is that tube formation from a plane membrane sheet costs nearly one order of magnitude less energy than formation of a vesicle. The bending energy E_b needed to for a tube with the length L and the radius r can be calculated by $E_b = \pi \kappa_B L / r$, with the bending modulus κ_B (10 – 20 k_bT for membranes).(Zimmerberg and McLaughlin, 2004)

Results and Discussion

With length L and radius r of a membrane tube on the scale of a single particle ($r = 10$ nm, $L = 15$ nm), one obtains bending energies on the order of $50 - 100$ k_bT for the formation of a membrane tube from a flat sheet. This admittedly simple calculation demonstrates that tubulation will more likely occur than vesiculation of the membrane.

Amino-functionalized Au@MnO@SiO$_2$ Janus particles

To examine the impact of different head-groups of the PEG-functionalization, I use amino-functionalized silica-coated particles. Like for the methoxy-functionalized particles these particles are first characterized according to their physical properties.

First, DLS measurements are conducted to determine the hydrodynamic radius of Au@MnO@SiO$_2$ Janus particles and MnO@SiO$_2$ nanoparticles. Experiments were performed by Isabel Schick (AK Tremel, Institute of Inorganic and Analytical Chemistry, Johannes-Gutenberg University, Mainz, Germany). Figure 4.1.11 shows the correlation functions of the scattered light signal from both particles types measured in 5 mM NaBr solution.
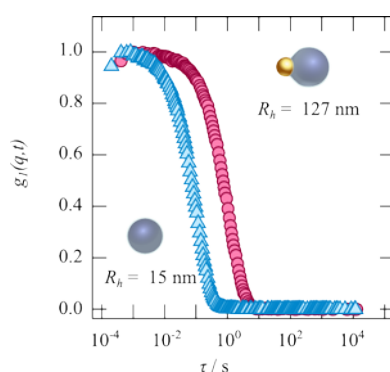
Figure 4.1.11: Correlation function $g_1(q,t)$ of spherical MnO@SiO$_2$-PEG-NH$_2$ (▲) and ODT-Au@MnO@SiO$_2$-PEG-NH$_2$ Janus particles (●) in 5 mM NaBr solution at a scattering angle of 90°.

Again we find a less correlated signal for spherical particles compared to the Janus particles, which is also reflected in the hydrodynamic radius R_h of 15 nm vs 127 nm for the latter. ODT-Au@MnO@SiO$_2$-PEG-NH$_2$ Janus particles exhibit a hydrodynamic radius of 127 nm, which lies far above the value that is expected for a single particle with a MnO domain with 10 nm in radius and a Au-domain with 5 nm in radius. Thus, the formation of aggregates or micellar structures in aqueous solutions is likely due to the amphiphilic nature of the particles. Compared to their methoxy-functionalized counterparts (R_h = 202 nm), amino-functionalized Janus particles seem to form smaller aggregates.

By measuring the adsorption of amino-functionalized nanoparticles on a solid supported DOPC-monolayer using surface plasmon resonance (SPR) spectroscopy, one is able to quantify the membrane-nanoparticle interaction. As described for the methoxy-functionalized particles, I again added different concentrations of nanoparticles under constant flow conditions and waited for establishment of a dynamic equilibrium. Figure 4.1.12 shows that the change in reflectivity units μRfU observed upon binding of amino functionalized Janus particles lies in the same regime as previously observed for both methoxy functionalized particles.
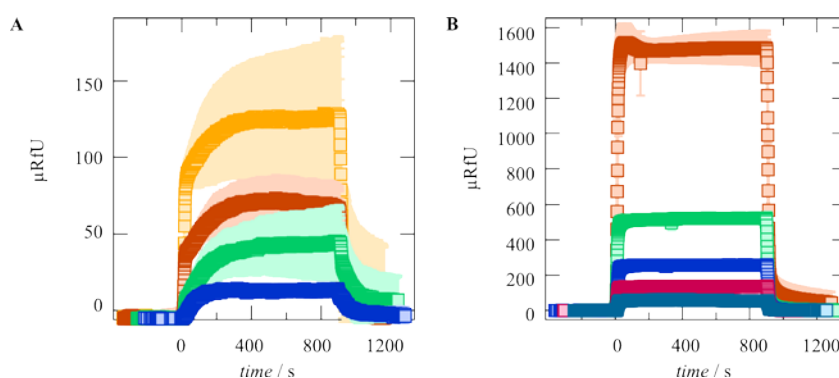
Figure 4.1.12: Surface plasmon resonance spectroscopy of amino-PEG-functionalized Au@MnO@SiO2 Janus (**A**, ■ 5 µg/ml, ■ 10 µg/ml, ■ 25 µg/ml, ■ 50 µg/ml) and spherical MnO@SiO2 particles (**B**, ■ 1 µg/ml, ■ 2.5 µg/ml, ■ 5 µg/ml, ■ 10 µg/ml, ■ 25 µg/ml) on DOPC monolayer.

The association phase of particles shows two different regimes: a first phase showing a fast increase of the signal within a few seconds and the second regime in which the signal slowly increases until it reaches a dynamic equilibrium value. The origin of the occurrence of these two regimes remains unclear. A control measurement using solvent of the nanoparticles (deionized water) does not show any effect on the signal. Nevertheless, upon changing from nanoparticle solutions to buffer conditions results in a complete recovery of the signal to its initial value indicating reversible binding.

Binding of spherical MnO@SiO$_2$-PEG-NH$_2$ particles is also reversible. Albeit, addition of 25 µg/ml of the spherical particles leads to an increase in μRfU of nearly 1500, which exceeds the signal produced by binding of all other particles at the same concentration by at least one order of magnitude and is also a higher signal as observed for the establishment of a DOPC monolayer on the 1-octanethiol monolayer (see also chapter 3.3). Supposedly, this effect of binding of particles to lipids is superimposed by a buffer effect. Another hint is the fast change to the equilibrium conditions as well as the nearly linear increase of the equilibrium value with the concentration (see also Figure 4.1.13).

For the amino-functionalized Janus particles, one can estimate the dissociation constant by fitting the equilibrium values of the SPR experiment as a function of particle concentration using Langmuir adsorption model (see also chapter 3.3). Like for the methoxy-functionalized particles saturation is not reached in the examined concentration range. Figure 4.1.13 shows the equilibrium values plotted against the concentration.
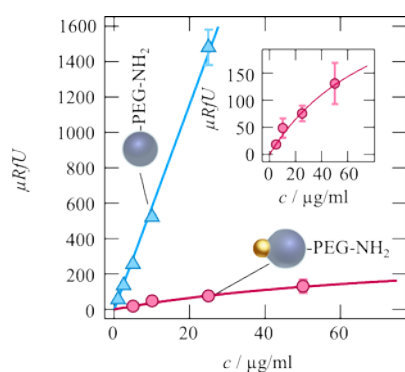
Figure 4.1.13: μRfU as a function of concentration (MnO@SiO2-PEG-NH$_2$ ($\triangle \pm$ STD) and ODT-Au@MnO@SiO$_2$-PEG-NH$_2$ Janus particles ($\bullet \pm$ STD)). The measured SPR-spectroscopy data obtained from addition of Janus particles to a lipid monolayer were fitted by a Langmuir isotherm (red line). Blue line represents a linear fit of the data obtained from addition of spherical particles to a lipid monolayer. Inlet shows a magnification of measured SPR-spectroscopy data obtained from addition of Janus particles to a lipid monolayer prepared on the SPR chip and the corresponding Langmuir isotherm fit.

As spherical particles showed a linear increase of the equilibrium value of μRfU with the concentration, fitting the measured changes in μRfU using the Langmuir adsorption model was not possible.

For the Janus particles, one obtains a dissociation constant of 90 ± 86 µg/ml (or 8.5 ± 8.1 nM), which lies between binding constants of methoxy-functionalized Janus particles (10 ± 7 µg/ml) and methoxy-functionalized spherical particles (138 ± 34 µg/ml).

Using equation 4.1 a value of -46 kJ/mol is measured for binding of Janus particles onto the DOPC lipids. Physical properties of amino-functionalized Au@MnO@SiO$_2$ Janus particles and spherical MnO@SiO$_2$ particles are summarized in Table 4.1.4.

Table 4.1.4: Characterization of amino-functionalized Au@MnO@SiO$_2$ Janus particles and spherical MnO@SiO$_2$ nanoparticles. *R* denotes the radius of domains obtained from TEM images, R_h is the hydrodynamic radius obtained from DLS measurements, K_d is the dissociation constant between DOPC and particles obtained from SPR measurements fitting the measured data with a Langmuir adsorption isotherm. ΔG was calculated from K_d values using equation 4.1. K_d and ΔG could not be determined for spherical particles (see text).

	R / nm	R_h / nm	$K_D \pm STD$ / nM	ΔG / kJ/mol
ODT-Au@MnO@SiO$_2$-PEG-OMe	10 (MnO) 5 (Au)	127	8.5 ± 8.1	-46
MnO@SiO$_2$-PEG-OMe	10	15	–	–

After characterization particles were used in GUV experiments to examine their effects on lipid membranes. Like before, GUVs were filled with 100 mM sucrose solution in 2mM TrisHCl with a pH-value of 7 (see Table 4.1.3). Nanoparticle stock solutions were diluted to a final concentration of 5 µg/ml in a 95 mM glucose solution containing also 2mM TrisHCl and 2 mM pyranine. The measured osmolalities of the solutions can be found in Table 4.1.5.

Table 4.1.5: Osmolality of solutions used in GUV experiments. Nanoparticles were solved in 90 mM glucose solution. Osmolality of the 100 mM sucrose solutions in TrisHCl (1) and 95 mM glucose solution in TrisHCl buffer (2) can be found in Table 4.1.3

	osmolality / mosmol/kg
5 µg/ml ODT-Au@MnO@SiO$_2$-PEG-NH$_2$ in (2)	113
5 µg/ml MnO@SiO$_2$-PEG-NH$_2$ in (2)	146

For amino-functionalized Janus-particles we find nearly isoosmolar conditions between nanoparticle solution and the solution inside the vesicles. In contrast, the osmolality of the 5 µg/ml solution of amino-functionalized exceeds the osmolality of the sucrose solution in the vesicles by 30 mosmol/kg. Addition of 5 µg/ml nanoparticles to the buffer should not have a large influence on its osmolality. Supposedly, the solution of spherical amino-functionalized particles contains low molecular weight impurities as we find a reasonable hydrodynamic radius of 15 nm for spherical particles with a radius of 10 nm obtained from TEM images. Larger impurities would lead to artifacts in DLS measurements represented by larger hydrodynamic radii, while low molecular weight impurities would have no or only little effect on the measurement. These low molecular

impurities could also change the dielectric properties of the buffer, which might explain the effects of MnO@SiO$_2$-PEG-NH$_2$ particles observed in SPR experiments.

To examine the effects of amino-functionalized Au@MnO@SiO$_2$ Janus particles and their spherical counterparts on lipid membranes, fluorescently labeled GUVs were incubated with 5 µg/ml solutions of both nanoparticle-types (see Figure 4.1.14).
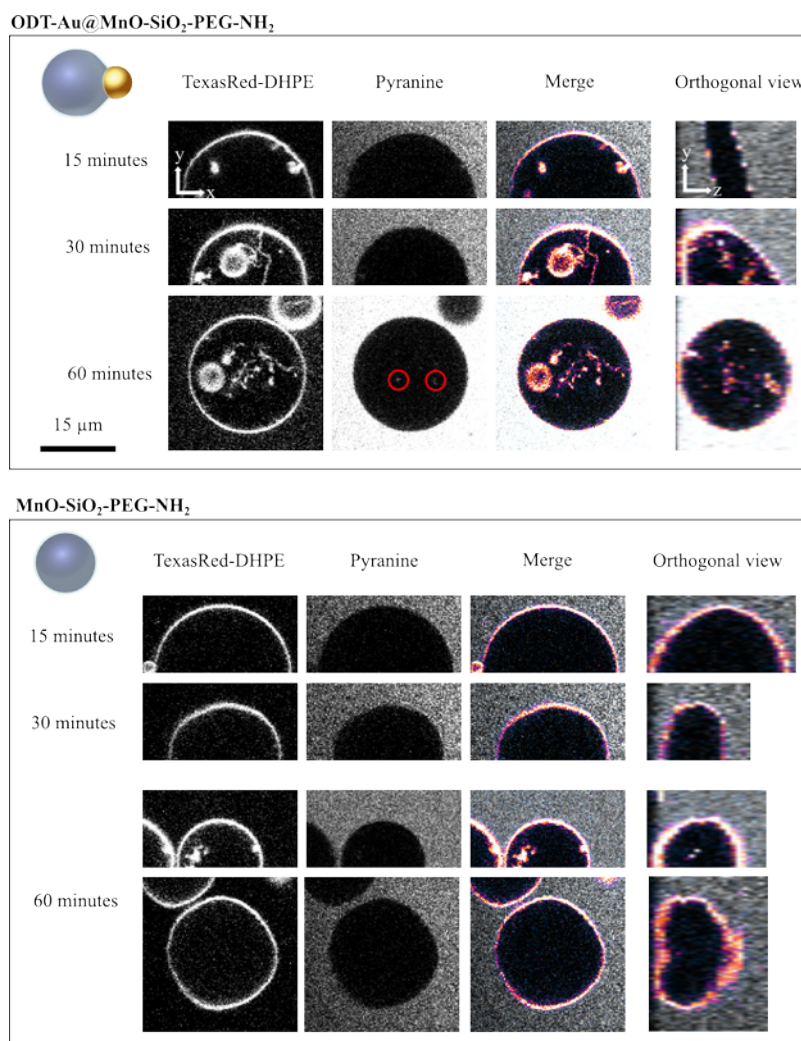
Figure: 4.1.14: Exemplary DOPC/TR-giant unilamellar vesicles treated with 5 µg/ml solutions of amino-functionalized Au@MnO@SiO$_2$ Janus particles and spherical MnO@SiO$_2$ nanoparticles imaged using confocal laser scanning microscopy. The nanoparticle solution additionally contained 2mM pyranine. GUVs are shown in the equatorial plane and meridian plane (orthogonal view). Images of single channels are shown in grey scale. In merged images TR-DHPE channel is shown in pseudocolors (ImageJ, Look up table: gem)

15 minutes after addition of amino-functionalized Janus particles formation of small membrane invaginations can be observed. The membrane tubes grow with time. After 60 minutes, the tubulations fill the complete volume of the vesicle as previously observed for methoxy-functionlized Au@MnO@SiO$_2$ Janus particles (see orthogonal view). It should be noted that the smaller vesicle inside the GUV was there before

incubation with particles. Otherwise, it would be filled with the nanoparticle solution containing pyranine. However, some of the membrane tubes contain small amounts of the surrounding media as they show weak intensities in the pyranine channel (red circles). Notably, the vesicles incubated with the Janus particles keep their spherical shape over the whole duration of the experiment as can be seen in the orthogonal view after 60 minutes. When GUVs were treated with spherical particles at first no tubulation of the membrane is observed. But after 60 minutes the vesicles show an irregular shape in their equatorial plane and the upper one of the two depicted vesicles shows also some membrane tubes. Looking at the meridian cross-section reveals that the vesicle in the lower panel has lost much of its volume after 60 minutes. This effect is presumably driven by the osmotic gradient across the membrane of the GUV (see Table 4.1.5) leading to a leakage of water from the GUV.

In a next step, I quantified the tubulation occurring in GUVs by counting the number of vesicles showing tubulations. The result is shown in Figure 4.1.15.

Figure 4.1.15: Quantification of tubulation in DOPC/TR-GUVs induced by methoxy-functionalized Au@MnO@SiO$_2$ Janus particles (●) and spherical MnO@SiO$_2$ nanoparticles (▲). 4 - 21 vesicles were examined per time point.

Nearly all vesicles treated with amino-functionalized Janus particles show tubulation after 10 minutes of incubation. The relative number of vesicles with membrane invaginations does not fall below 80%. As amino-functionalized Janus particles exhibit a similar change in Gibbs free energy compared to methoxy-functionlized particles it is not surprising that both particles lead to similar effects, i.e. tubulations. In contrast, a tri-phasic behavior is found for vesicles treated with spherical particles. Shortly after addition of particles approximately 40% of the GUVs show tubulations. Within 5 minutes the number drops to 0. During next 15 minutes no vesicles with tubulations were observed. In the remaining 40 minutes the value increases to nearly 80%, which might be an effect of the osmotic deflation of the vesicles. Lipowsky was able to demonstrate that osmotic pressure difference across the membrane of giant

unilamellar vesicles is sufficient to produce membrane tubes by spontaneous curvature of the membrane.(Lipowsky, 2013) In principle, one can find in-tubes, penetrating into the vesicle volume from the outside and exchange media with the surrounding medium, or out-tubes protruding the membrane from the vesicle volume to the outside, thus filled with the medium enclosed in vesicles. However, out-tubes are found to be unstable, while in-tubes are stable, which can explain the increasing number of vesicles showing inwards directed tubulation.

Mild increase of the osmotic pressure acting on the membrane from the inside of the vesicle by incubation of DOPC/TR-DHPE GUVs in 5 µg/ml nanoparticles solution in 90 mM glucose in 2mM TrisHCl buffer with an osmolality of 100 mosmol/kg leads to a disappearance of the tubulation for both, amino-functionalized Janus particles as well as spherical particles as visible in Figure 4.1.16 (see scheme in Figure 4.1.10). Like for the methoxy-functionalized particles, the binding energy of the particles to the membrane might not be sufficient to produce bending or, at later stages, tubulation in tensed membranes. However, the plasma membrane of living cells exhibits a tension of roughly 10^{-4} N/m showing that in living cells membrane tension might play a large role in passive particle uptake. (see also chapter 4.4.1).(Pietuch *et al.*, 2013; Schafer *et al.*, 2013)
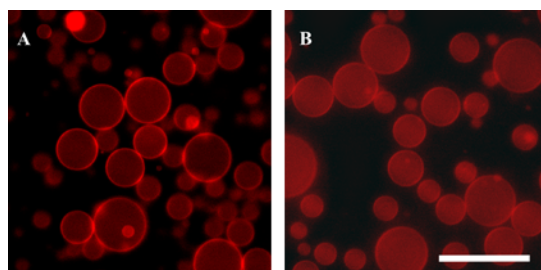
Figure 4.1.16: Epi-fluorescence image of DOPC/TR-DHPE-GUVs treated with 5 µg/ml solutions of amino-functionalized Au@MnO@SiO$_2$ Janus particles (**A**) and spherical MnO@SiO$_2$ nanoparticles (**B**) after 60 minutes incubation. Scale bar: 50 µm

Thus, it remains an open question if tubulation (and vesiculation) induced by the used Janus particles in GUVs might also play a role in particle uptake and processing in living cells. The increased uptake via particle induced tabulation and vesiculation could potentially increase their cytotoxicity. Therefore, I conducted cytotoxicity of DOPA-PEG functionalized and silica-coated particles. Additionally, uptake of ODT-Au@MnO@SiO$_2$-PEG-OMe particles into A549 cells was examined.

4.1.2.3 Cytotoxicitic of manganese(II)-oxide Janus particles added to MDCK-II cells

To examine the cytotoxicity of DOPA-PEG-R (R= OMe or NH_2) functionalized Janus particles, MDCK-II epithelial cells were used. MDCK-II cells form confluent epithelia with pronounced cell-cell-contacts and have been used in previous nanotoxicity studies.(Tarantola *et al.*, 2011; Tarantola *et al.*, 2009) The cells were treated with ODT-Au@MnO-DOPA-PEG-OMe Janus particles and their spherical, isotropic counterparts made of MnO only. The MnO domain of the particles has a diameter of 20 nm in diameter and a smaller Au domain with a diameter of only 4 nm. Additionally, I used particles functionalized with an amino group at the end of the PEG instead of the methoxy-group to examine the influence of the polymer end-groups on cytotoxicity. Cytotoxicity of nanoparticles on confluent cell monolayers was measured using two independent methods: 1. A photometric viability assay based on the reduction of a chromophore by natural reduction equivalents NADH|H^+ and NADPH|H^+ (MTS-Assay). 2. Electric cell substrate impedance sensing (ECIS), a biophysical viability assay, which uses an alternating current with voltage amplitudes of a few millivolts to measure morphological changes of cells. Nanometer sized motions in the basal membrane of living cells induce changes in the complex valued impedance Z of the applied current recorded at an AC frequency of 4 kHz. Thus, it allows real-time measurements of active motions of cells. Experiments were carried out by Sebastian Heise in his bachelor thesis. For further information see also chapter 3.7. Figures 4.1.17 A and C show the impact of different concentrations of ODT-Au@MnO-DOPA-PEG-OMe and MnO-DOPA-PEG-OMe nanoparticles on the absolute value of the impedance $|Z|_{norm@4kHz}$ normalized to the impedance level before particle addition ($|Z|_{norm@4kHz}$ = 1) and to that of the bare electrode immersed in culture medium (($|Z|_{norm@4kHz}$ = 0). Figures 4.1.17 B and D show the variance of the raw absolute value of the impedance $|Z|_{@4kHz}$ for the same treatments.
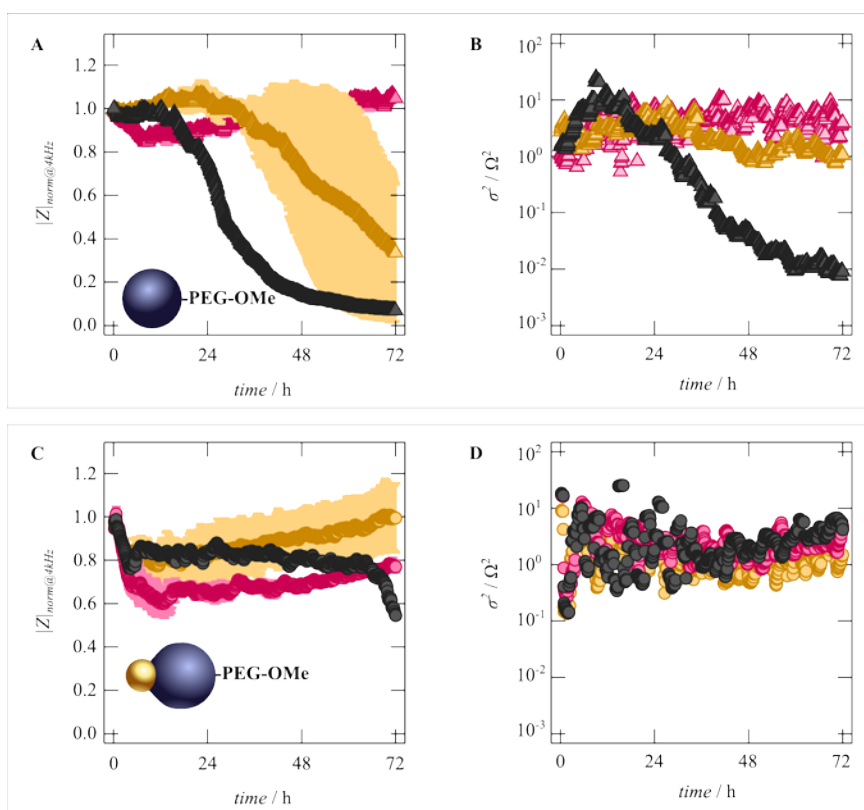
Figure 4.1.17: ECIS measurement of MDCK-II cells treated with DOPA-PEG-OMe functionalized Au@MnO Janus particles (circles) and spherical MnO nanoparticles (triangles). (1 µg/ml (n=2), 10 µg/ml (n=2), 20 µg/ml (n=1)) **A** Time course of $|Z|_{norm@4kHz}$ (± STD) after treatment of cells with spherical MnO-DOPA-PEG-OMe particles. **B** Variance of raw $|Z|$@4kHz time courses after treatment with MnO-DOPA-PEG-OMe particles. **C** Time course of $|Z|_{norm@4kHz}$ (± STD) after treatment of cells with ODT-Au@MnO-DOPA-PEG-OMe Janus particles. **D** Variance of raw $|Z|$@4kHz time courses after treatment with ODT-Au@MnO-DOPA-PEG-OMe Janus particles. The diagrams show every hundredth point of the time courses for better visibility.

The absolute impedance $|Z|_{norm@4kHz}$ is normalized to the moment of addition of particles at t = 0. Figure 4.1.17 shows $|Z|_{norm@4kHz}$ for MDCK-II cells treated with spherical particles. When treated with 1 µg/ml nanoparticle solution the impedance remains at around 1.0 after a short initial decrease, which indicates an intact cell monolayer over the whole experiment. In contrast, cells incubated with 10 µg/ml MnO-DOPA-PEG-OMe particles show a decrease of the impedance signal starting approximately 24 h after addition of nanoparticles. At the end of the experiment, $|Z|_{norm@4kHz}$ has dropped to 35% of its initial value. Increasing the concentration to 20 µg/ml leads to an earlier decrease of the impedance signal, which falls bellow 50% of its initial value approximately after 24 hours. Using ECIS, the time course of the absolute value of impedance is only one parameter accessible to evaluate toxicity. I also calculated the variance σ^2 of the raw impedance signal $|Z|_{@4kHz}$ as a measure for the cell-induced fluctuations of $|Z|_{@4kHz}$, induced by collective nanometer motions in the basal membrane of cells (so-called micromotion). The impedance signal of an electrode covered with

living cells exhibits a variance between 1 $\Omega^{\square}$ and 10 $\Omega^{\square}$ (for the conditions chosen for calculation of σ^2: moving average window of 36 point, variance calculation over 1200 points). The variance σ^2 of MDCK-II cells treated with the highest concentration of MnO-DOPA-PEG-OMe particles of 20 µg/ml shows an increase directly after addition of particles to values above 10 Ω^2 before it starts to decrease. After 48 hours σ^2 exhibits only values between 0.01 and 0.1 indicative for cell death as it approaches the variance of an uncovered electrode. Lower concentrations lead not to a significant decrease of the variance.

In contrast to spherical particles, Janus particles show a smaller impact on the impedance $|Z|_{norm@4kHz}$ as well as the variance. For all concentrations, addition of Janus particles to a confluent MDCK-II monolayer induces an initial drop of $|Z|_{norm@4kHz}$. The lowest concentration shows the largest effect. After this initial phase the impedance of samples treated with the two lower concentrations (1 µg/ml and 10 µg/ml) slowly increases with time. $|Z|_{norm@4kHz}$ of the sample incubated with 20 µg/ml Janus particles remains nearly unchanged until it starts to decrease 65 hours after addition of the nanoparticles. At the end of the experiment the sample exhibits approximately 55% of its initial impedance value. The variance of the Janus particle treated samples shows values ranging between 0.1 Ω^2 and 10 Ω^2 over the complete duration of the experiment. In the first 30 hours after addition, one can observe a large distribution of values for the variance, which then becomes smaller. In the end, σ^2 of all samples is between 1 Ω^2 and 10 Ω^2 indicating living cells.

To examine the influence of surface functionalization on the cytotoxicity of Janus particles on MDCK-II cells we compared the previous results obtained for DOPA-PEG-OMe coated particles with particles, in which an amino group replaced the methoxy-group at the end of the PEG, which might influence the interaction between particle and cell membrane. The results of the ECIS measurement can be found in Figure 4.1.18.
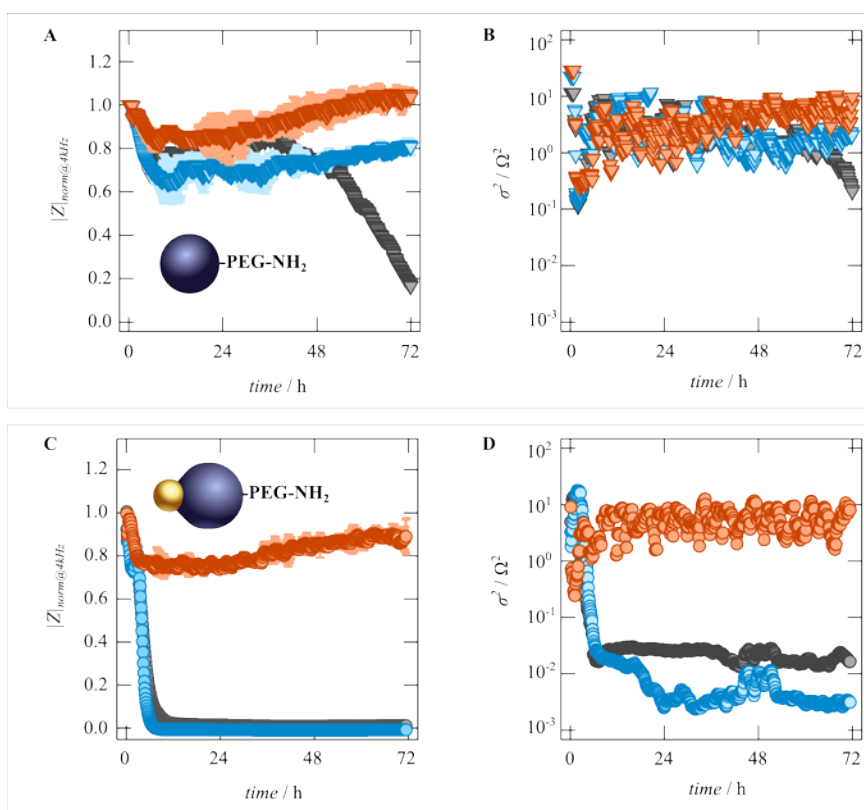
Figure 4.1.18: ECIS measurement of MDCK-II cells treated with DOPA-PEG-NH$_2$ functionalized Au@MnO Janus particles (circles) and spherical MnO nanoparticles (triangles) on MDCK-II cells measured by ECIS. (1 µg/ml (*n*=2), 10 µg/ml (*n*=2), 20 µg/ml (*n*=1)) **A** Time course of $|Z|_{norm@4kHz}$ (± STD) after treatment of cells with spherical MnO-DOPA-PEG-OMe particles. **B** Variance of raw |Z|@4kHz time courses after treatment with MnO-DOPA-PEG-OMe particles. **C** Time course of $|Z|_{norm@4kHz}$ (± STD) after treatment of cells with ODT-Au@MnO-DOPA-PEG- NH$_2$ Janus particles. **D** Variance of raw |Z|@4kHz time courses after treatment with ODT-Au@MnO-DOPA-PEG- NH$_2$ Janus particles. The diagrams show every hundredth point of the time courses.

In contrast to the methoxy-functionalized particles, spherical MnO-DOPA-PEG-NH$_2$ particles are largely non-toxic in the examined concentration range. Solely the highest concentration shows a cytotoxic effect as the impedance $|Z|_{norm@4kHz}$ starts to decrease 48 hours after addition of the particles and reaches 20% of its initial value after 72 hours. The variance σ^2 of the signal follows after approximately 65 hours but does not fall below 0.1 $\Omega^\square$ after 72 hours. The other samples show (like the sample treated with ODT-Au@MnO-DOPA-PEG-OMe Janus particles before) an initial decrease of the impedance, which then increases slowly. The variance mostly exhibits values between 1 Ω^2 and 10 Ω^2, indicating that the used concentrations are essentially non-toxic. In contrast, Janus particles carrying the same functionalization show substantial cytotoxic effects when added in concentrations above 1 µg/ml. The normalized impedance $|Z|_{norm@4kHz}$ of both samples drops to a value of the cell free electrode within 8 –10 hours

after addition of nanoarticles. Accordingly, the variance of both samples decreases. A concentration of 1 µg/ml did not result in any cytotoxic effects.

To confirm the results of the ECIS-based cytotoxicity analysis, I conducted a standard cell viability assay based on reduction of a tetrazolium salt to a formazan product (see also chapter 3.8). The result after 24 hours of incubation with methoxy- and amino-functionalized Janus particles as well as their isotropic counterparts can be found in Figure 4.1.19.
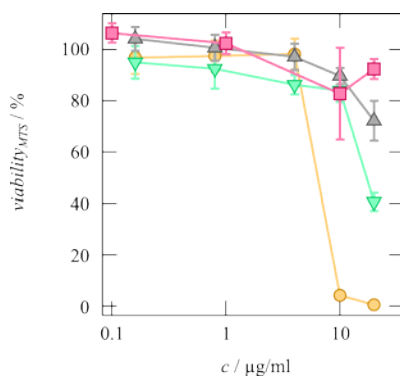
Figure 4.1.19: Viability (± STD) of MDCK-II cells as a function of particle concentration after 24 hours incubation with methoxy and amino functionalized Janus particles and spherical control particles carrying the same functionalizations measured by MTS-Assay. (n=6) ● ODT-Au@MnO-DOPA-PEG-NH2, ■ ODT-Au@MnO-DOPA-PEG-OMe, ▲ MnO-DOPA-PEG-OMe, ▼ MnO-DOPA-PEG-NH$_2$.

In the MTS-Assay, concentrations of all particles up to 4 µg/ml appear to be non-toxic after 24 hours of incubation. At 10 µg/ml only ODT-Au@MnO-DOPA-PEG-NH$_2$ Janus particles become toxic showing a drop in viability to nearly 0%. The other samples show a viability of at least 80 %. Incubation of MDCK-II cells with 20 µg/ml of the spherical amino-functionalized MnO-particles results in a viability of 40 % after 24 hours. Both methoxy-functionalized samples are less toxic, whereas spherical particles lead to a larger decrease in viability to approximately 70% at 20 µg/ml compared to 90% viability of the cells treated with the Janus particles.

In general, the results show that MnO based nanoparticles are toxic after 24 hours starting at a concentration of 10 µg/ml. Cytotoxicity of MnO-based nanoparticles has been reported previously. (Choi *et al.*, 2010; Rother *et al.*, 2013) In a previous study, I also found a comparable cytotoxicity of PEGylated MnO-based nanoparticles administered to A549 lung cancer cells.(Rother *et al.*, 2013) Presumably the toxicity of MnO-based particles arises from the production of reactive oxygen species (ROS) on the surface of nanoparticles.(Choi *et al.,* 2010) ROS are produced by the cell in physiological conditions in low amounts and are easily neutralized by anti-oxidative mechanisms.(Nel *et al.,* 2006) However, imbalance of the oxidative stress in cells can

lead to cell damage. Furthermore, my experiments demonstrate the importance of surface functionalization for cellular uptake and nanotoxicity. I found that Janus particles coated with DOPA-PEG-NH$_2$ are more toxic than the methoxy-functionalized particles in the MTS-assay. In contrast, spherical particles appeared to be more toxic in ECIS-experiments, when functionalized with DOPA-PEG-OMe. Influences of surface modifications on nanotoxicity have also been demonstrated in other studies. Tarantola and coworkers could, for example, show that gold nanoparticles coated with cetyl triamethylammonium bromide (CTAB) exhibit a dramatically higher cytotoxicity as PEG-coated particles.(Tarantola *et al.*, 2009) Additionally, rod-shaped Au-particles coated with an amino-functionalized PEG were found to be non-toxic, whereas particles, which carried carboxy-functionalized PEG, showed weak cytotoxic effects. The high toxicity of CTAB coated particles was attributed to enhanced uptake of these particles compared to the PEGylated particles. Zhang and coworkers, however, reported about an increased uptake of PEGylated magnetite nanoparticles into cancer cells but a repression of uptake into macrophages.(Zhang *et al.*, 2002b) Comparing the cytotoxicity of Janus particles with the cytotoxicity of spherical particles with the same functionalization one has to distinguish according to the surface functionalization. Whereas DOPA-PEG-NH$_2$-functionalized Janus particles are more toxic than the spherical particles, one finds the opposite trend in the methoxy-functionalized particles. According to the dramatic effects observed for methoxy-functionalized particles on GUVs (see chapter 4.1.2.1), we expected a general increase in uptake and cytotoxicity of Janus particles compared to spherical particles as the particles are able to enter cells easily circumventing conventional endocytotic routes (see also chapter 2.1.4). Due to a reduced ratio between the sizes of the Au-domain and the MnO-domain (~1/5) compared to the Janus particles used in the GUV experiments (~1/2) the effect on the cell membrane might be smaller for the particles used in the cytotoxic assays. Additionally, opsonization of the nanoparticle surface might change the properties of particles and shielding their amphiphilic properties.(Tenzer *et al.*, 2013) In studies by Tenzer *et al.* this so-called protein corona was formed within 30 s in human plasma on the surface of silica and polystyrene nanopartciles and evolved over time. The authors were able to demonstrate that the protein corona also effects uptake and cytotoxicity of the nanoparticles. Furthermore, nanomaterials are taken up by cells via active endocytotic mechanisms, which might exceed the portion of Janus particles entering the cells via induced tabulation and vesiculation (see also chapter 2.1.4).(Treuel *et al.*, 2013) On the other hand, the amino-functionalized nanoparticles exhibit the strongest cytotoxic effect, which might hint to an increased uptake of this particle-type. How the Janus particles specifically interact with cells remains unclear so far, as the particles

are not visible in our experiments. Experiments of Schick *et al.* demonstrated that Janus particles, which were - apart from a silica coating on the MnO domain - comparable to the particles used here, are taken up into cervical and renal cancer cells easily.(Schick *et al.*, 2014) Therefore, cytotoxicity of silica-coated MnO-based Janus particles and their uptake into cells will be examined in next chapters.

4.1.2.4 Cytotoxicity of silica-coated Janus particles and uptake into living cells

As Janus particles were shown to elicit strong membrane tubulation in GUVs (see previous chapters), this mechanism could also play a role in the uptake of these particles into living cells. This way of passively induced endocytosis on the one hand might be used for drug delivery purposes. On the other hand, unintended uptake of particles into cells increases the risk of cytotoxic effects. Therefore, I conducted, like for nanoparticles without silica coating, biochemical MTS- as well as ECIS-assays to examine the cytotoxicity of the particles used in chapter 4.1.2.2. For experiments, we used A549 lung cancer cells, which have been used in previous nanotoxicity studies of spherical MnO particles.(Rother *et al.*, 2013)

4.1.2.4.1 Cytotoxicity of methoxy-functionalized, silica-coated nanoparticles

First, I examined the cytotoxicity of ODT-Au@MnO@SiO$_2$-PEG-OMe Janus particles in comparison to their spherical counterparts MnO@SiO$_2$-PEG-OMe. The result of ECIS-assay is shown in Figure 4.1.20. When confluence of the cell layer was reached, A549 cells were treated with different concentrations of both nanoparticle types ranging from 10 to 100 µg/ml for three days. For A549 cells, the impedance Z was measured at an AC frequency of 8 kHz (see chapter 3.7).
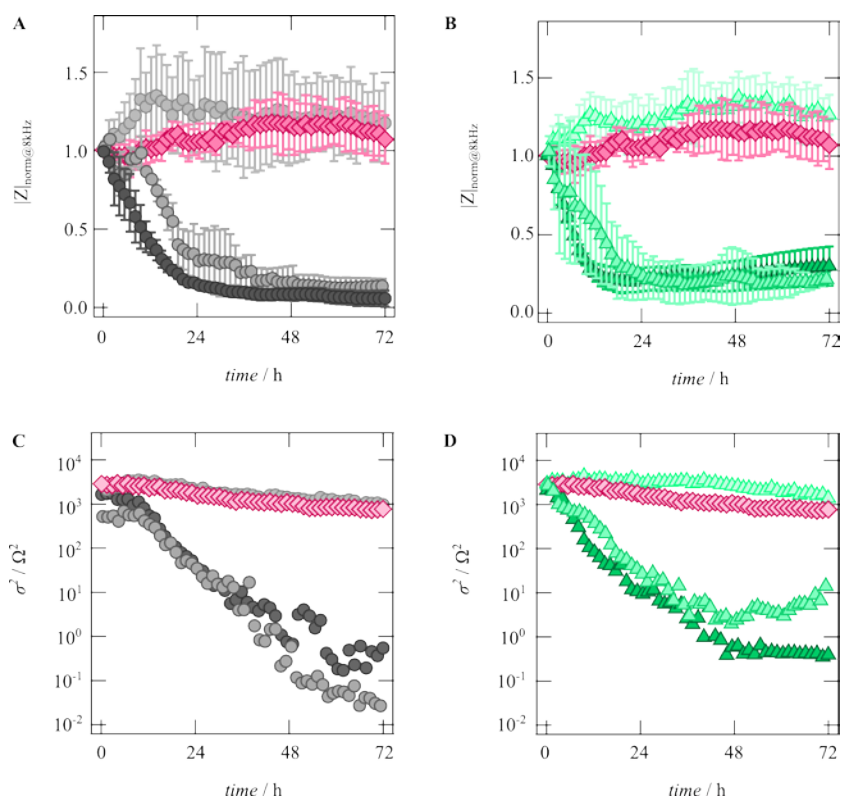
Figure 4.1.20: Cytotoxicity of -PEG-OMe functionalized Au@MnO@SiO₂ Janus particles ((● 10 µg/ml (*n*=6), ● 50 µg/ml (*n*=2), ● 100 µg/ml (*n*=6))) and spherical MnO@SiO₂ nanoparticles (triangles) on A549 cells measured by ECIS. (▲ 10 µg/ml (*n*=6), ▲ 50 µg/ml (*n*=2), ▲ 100 µg/ml (*n*=6)). The untreated sample is shown as ◆ **A** and **B** Time course of the average normalized impedance $|Z|_{norm@8kHz}$ (± STD) **C** and **D** Time course of the average variance of raw |Z|@8kHz (for calculation of the variance see chapter 3.7). The diagrams show every 100th point of the time courses.

The normalized impedance $|Z|_{norm@8kHz}$ of the untreated sample as well as samples treated with 10 µg/ml of Janus and spherical particles is close to one for the whole duration of the experiment. Higher concentrations lead to a decrease of $|Z|_{norm@8kHz}$ to values close to the impedance of the uncovered electrode indicating cytotoxic effects of the particles. Thereby, samples incubated with intermediate concentrations shows a retarded decrease compared to higher concentrations. No significant difference is observed when comparing Janus particles and spherical particles. The variance σ^2 of $|Z|_{@8kHz}$ being a measure for motion of cells confirms that nanoparticle concentration lower than 50 µg/ml are essentially non-toxic. Variances of samples incubated with concentrations of 50 µg/ml or more exhibit a decrease within the first 48 hours to values on the order of 1 Ω^2 indicating cell death. Solely, the sample treated with 50 µg/ml of spherical methoxy-functionalized particles shows a very slow recovery of the variance starting 48 hours after addition of the particles indicating that some cells survived. Thus, according to the ECIS-measurement, both particle types exhibit a similar toxicity.

To confirm this finding with an independent method, I also performed an MTS-assay (see chapter 3.8). Figure 4.1.21 shows the calculated viabilities of A549 cells incubated for 24 hours with nanoparticle concentrations between 1 µg/ml and 100 µg/ml. Lower concentrations did not affect cell viability.
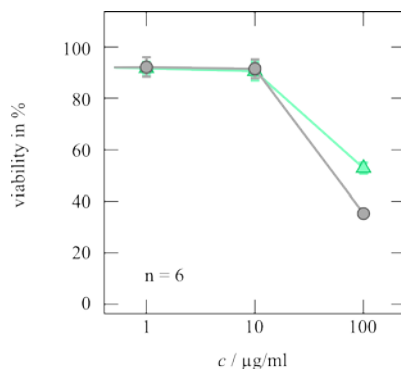
Figure 4.1.21: Viability of A549 cells incubated with methoxy-functionalized Au@MnO@SiO2 Janus particles ($\bullet$ ± STD) and spherical MnO@SiO$_2$ particles ($\blacktriangle$ ± STD).

Like the ECIS-assay, the MTS-assay shows that up to a concentration of 10 µg/ml both particle types are essentially non-toxic. At 100 µg/ml Janus particles are more toxic showing a viability of less than 40%, whereas A549 cells treated with spherical particles exhibit a viability of more than 50%.

In summary, both methods showed that methoxy-functionalized, silica-coated particles are non-toxic in concentrations up to 10 µg/ml. At higher concentrations Janus particles exhibit a slightly higher toxicity compared to spherical particles, which might be an effect of increased uptake of Janus particles due to induction of tubulation (and vesiculation) of the plasma membrane of living cells. In my studies, I observe a higher cytotoxicity in comparison to studies by Schick *et al.*, who found no toxic effect for similar Janus particles in concentrations up to 100 µg/ml in CaKi-1 cells.(Schick *et al.*, 2014) However, cytotoxicity is also a function of the cell type.(Sohaebuddin *et al.*, 2010) Thus, comparison between both studies is difficult. Cytotoxicity of silica-coated particles and those coated with DOPA-PEG is also comparable. In previous studies, we used MnO nanoparticles as a carrier system for immunostimulating DNA-sequences. Treatment of A549 cells with 25 µg/ml of these particles resulted in a viability of approximately 70% after 24 hours.(Rother *et al.*, 2013)

To research if uptake of Janus particles is preferred in comparison to spherical particles, I incubated A549 cells in cell culture medium containing additionally 2 mM pyranine and 5 µg/ml of methoxy-functionalized Janus particles or spherical particles for 30 minutes. Staining of the solution using pyranine was necessary, as the particles were not fluorescently labeled. To identify cell borders, I additionally stained the

membrane using CellMask DeepRed plasma membrane stain (Invitrogen, Germany). After incubation cells were fixed and imaged using a confocal laser scanning microscope. Maximum intensity projections of exemplary confocal images along the z-axis can be found in Figure 4.1.22. In a next step, I performed a grain analysis using Gwyddion (Gwyddion.net). For further information see chapter 3.11.1.3.
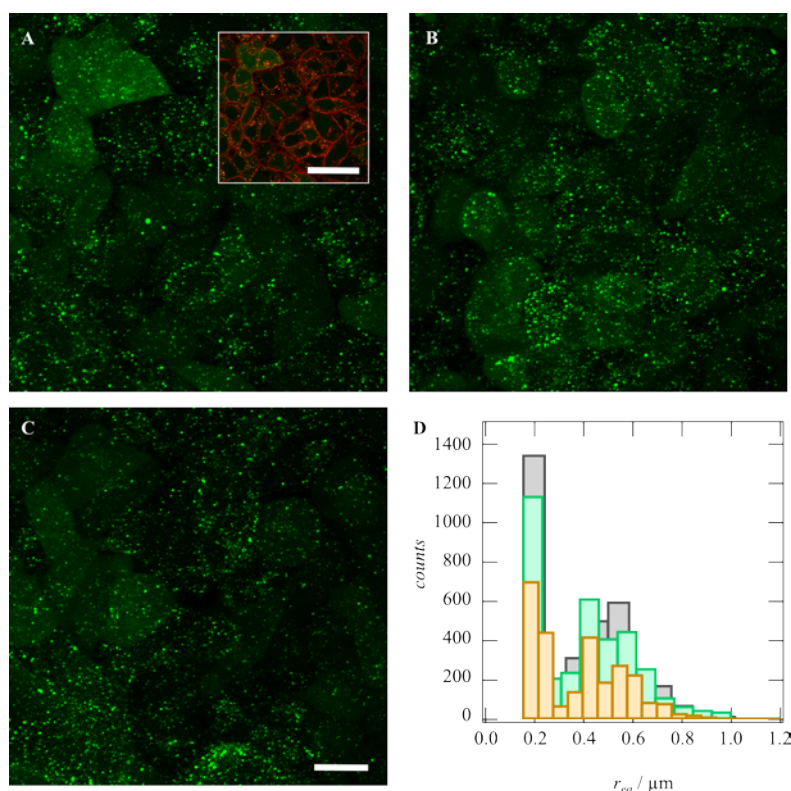
Figure 4.1.22: Quantification of endocytosis by A549 treated with 5 µg/ml methoxy-functionalized Janus and spherical particles. Images A – C show maximum intensity projections of the pyranine channel of z-stacks measured by confocal LASER scanning microscopy. Contrast was enhanced for image representation. **A** Untreated cells. Inlet: confocal image of the area shown in A showing the plasma membrane of cells (CellMask DeepRed plasma membrane stain, Invitrogen) Scale bar (inlet): 50 µm **B** Cells treated with spherical particles **C** cells treated with Janus particles. Scale bar: 20 µm **D** Histograms of the equivalent vesicle radius found by grain analysis of maximum intensity projections (■ Au@MnO@SiO$_2$ Janus particles, ■ spherical MnO@SiO$_2$ particles and ■ untreated control).

Figure 4.1.22 shows the distribution of vesicle radii in A549 cells treated with ODT-Au@MnO@SiO$_2$-PEG-OMe Janus particles and spherical MnO@SiO$_2$ particles. Maximum intensity projections of all examined samples show small vesicles filled with the medium containing pyranine. Some of the cells show also elevated fluorescence intensity in the cytoplasm. However according to the images, a difference in endocytosis cannot be found. Also quantification of the endocytosed vesicles does not show large differences in cells treated with nanoparticles. Vesicles of all samples exhibit a radius of around 0.45 µm. The peak at smaller vesicle radii can be explained

by noise detected by the grain analysis. The total amount of endocytosed vesicles seems to be reduced in untreated cells. However, counting all vesicles with radii larger than 0.3 µm shows no significant difference between untreated cells (779 ± 473 (n=2)) and A549 cells treated with nanoparticles (ODT-Au@MnO@SiO$_2$-PEG-OMe: 999 ± 36 (n=2), MnO@SiO$_2$-PEG-OMe: 1152 ± 16 (n=2)). Apparently, tubulation and vesiculation induced by methoxy-functionalized Janus particles as found for artificial membranes plays a minor role in the uptake of particles in living cells. This could have different reasons: 1) the cellular membrane is a complex composite of lipids, proteins and carbohydrates, which form the so-called glycocalyx on extracellular side. Thus, the interaction between particles and plasma membrane will drastically change in comparison to simple, artificial DOPC-lipid bilayers. 2) The membrane tension of living cells is on the order of 10^{-4} N/m (see also chapter 4.4.1.2).(Pietuch *et al.*, 2013; Schneider *et al.*, 2013) As the particles did not show any effect on osmotically stressed GUVs (see Figure 4.1.19), it is not likely, that Janus particles are able to produce membrane tubulations in living cells. 3) Cells possess active pathways of endocytosis (see chapter 2.1.4), which might play a larger role in the uptake of nanoparticles compared to "passive" endocytosis induced by Janus particles. However, we observed a small difference in the cytotoxicity of Janus particles and spherical particles. Possibly, passive entry of Janus particles into the cell and further processing is responsible for this small increase in cytotoxicity of the Janus particles.

4.1.2.4.2   Cytotoxicity of amino-functionalized, silica-coated nanoparticles

Like for methoxy-functionalized Janus Particles, I also examined the cytotoxic potential of amino-functionalized Janus particles in comparison to the spherical particles with the same functionalization. Amino-functionalized Janus particles were used in concentrations between 10 to 100 µg/ml. In contrast, spherical particles were used in concentrations up to 50 µg/ml as the stock solution of these nanoparticles exhibited a low concentration of 127 µg/ml. Figure 4.1.23 A shows the time course of the normalized impedance $|Z|_{norm@8kHz}$. It can be seen that $|Z|_{norm@8kHz}$ of samples treated with 10 µg/ml and 50 µg/ml of the spherical nanoparticles decreases within the first 20 hours after addition of particles to constant values of approximately 30 to 60% of the initial signal. Janus particles produce the same effect but at higher concentrations of 50 µg/ml and 100 µg/ml. Samples treated with 10 µg/ml Janus particles show no decrease in $|Z|_{norm@8kHz}$.
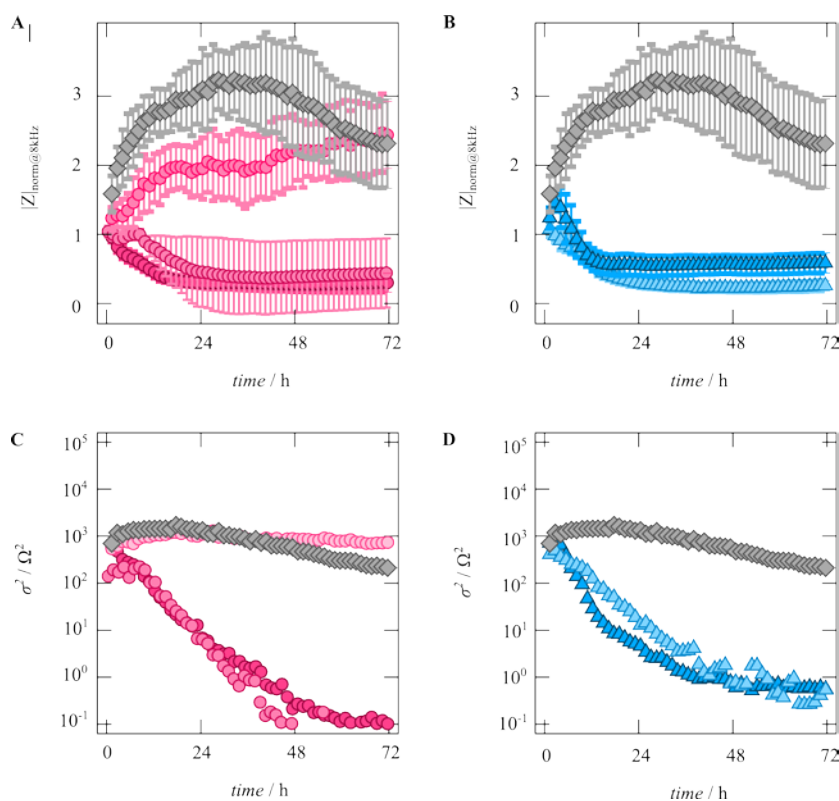
Figure 4.1.23: Cytotoxicity of -PEG-NH$_2$ functionalized Au@MnO@SiO$_2$ Janus particles (● 10 µg/ml (n=6), ● 50 µg/ml (n=2), ● 100 µg/ml (n=6)) and spherical MnO@SiO$_2$ nanoparticles (triangles) on A549 cells measured by ECIS. (▲ 10 µg/ml (n=6), ▲ 50 µg/ml (n=6)). The untreated sample is shown as ◆ **A** and **B** Time course of the average normalized impedance $|Z|_{norm@8kHz}$ (± STD) **C** and **D** Time course of the average variance of raw $|Z|@8kHz$ (for calculation of the variance see chapter 3.7). The diagrams show every 100th point of the time courses.

A similar trend is observed in the variance σ^2 of the impedance signal. Concentrations of 10 and 50 µg/ml lead to a decrease of σ^2 to values below 10 Ω^2 with 24 hours indicating a reduction of the fluctuation in the impedance signal produced by active motion of cells. The same is observed for samples treated with Janus particles solutions with concentrations of 50 µg/ml and 100 µg/ml. The variance of the 10 µg/ml samples remained at its initial value at t = 0. In summary, the ECIS assay shows that amino-functionalized spherical particles exhibit a higher toxicity than Janus particles. However, cytotoxicity of spherical particles might also be an effect of the high ratio between nanoparticle stock solution and cell medium due to the low particle concentration in stock solution. A 10 µg/ml solution of spherical MnO@SiO$_2$-PEG-NH$_2$ nanoparticles already contains nearly 8% of the particle stock solution, which could for example lead to changes in the osmolality of the cell culture medium, which affect cellular behavior.

The MTS-Assay shows comparable results for amino-functionalized particles (see Figure 4.1.24). After 24 hours, cells treated with spherical particles in concentrations

above 1 μg/ml exhibit a lower viability than A549 cells treated with Au@MnO@SiO$_2$ Janus particles. But, the differences between both particle types is not as pronounced as in ECIS experiments. Additionally, one finds comparable cytotoxicities for amino-functionalized particles and methoxy-functionalized particles. Only spherical amino-functionalized particles exhibit a higher toxicity, which might be induced by the low nanoparticle concentration in stock solution.
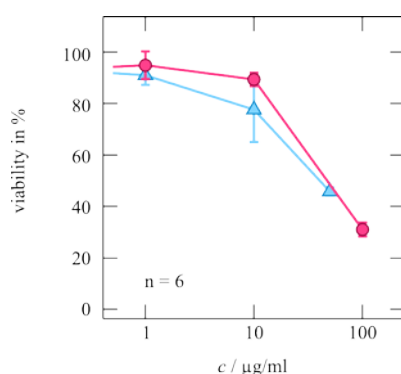
Figure 4.1.24: Viability of A549 cells incubated with amino-functionalized Au@MnO@SiO2 Janus particles (● ± STD) and spherical MnO@SiO$_2$ particles (▲ ± STD).

Comparison of the cytotoxicity of amino-functionalized silica-coated Janus particles with the cytotoxic effects observed for ODT-Au@MnO-DOPA-PEG-NH2 particles (see chapter 4.1.2.2) reveals a reduced cytotoxicity in particles with silica coating. The silica coating might prevent the leakage of Mn^{2+}-ions from the particle core, which could lead to toxic effects. Additionally, the reactive MnO surface is not exposed to the cell culture medium preventing ROS production observed in experiments by Choi *et al.*.(Choi *et al.*, 2010)

4.1.3 Conclusion

During the last decades, much effort has been put into understanding the interaction of isotropic nanomaterials with cells. Thereby, many studies reported on uptake of nanoparticles by cells via conventional endocytotic pathways.(Jiang *et al.*, 2011; Treuel *et al.*, 2013) However, in recent years, chemists succeeded in producing amphiphilic Janus particles opening new fields of application like emulsions or technical products like e-paper displays, but also their use in medicine is conceivable. Therefore, profound knowledge about the bio-nano-interaction is inevitable for a save use of these particles. Coarse grain simulations demonstrated that amphiphilic particles are able to induce the formation of membrane tubes and vesicles or could induce the formation pores in lipid

bilayers showing that nanoparticles are also able to enter cells via unconventional ways.(Alexeev *et al.*, 2008; Reynwar *et al.*, 2007)

Here, I examined the interaction between MnO@Au-based Janus particles with artificial lipid bilayers and cells experimentally. In SPR-experiments using Janus particles with a hydrophilic, silica-coated metal oxide domain and a hydrophobic gold-domain I found that the binding energy of the particles to DOPC lipids should be sufficient to induce membrane bending and tubulation but not vesiculation in tension-free membranes. Experiments using DOPC-giant unilamellar vesicles as artificial membranes showed that Janus particles were able to induce membrane tubulation under isosmotic conditions. No differences were observed for silica coated particles carrying amino-functionalized or methoxy-functionalized PEG. An increase of the membrane tension, which accounts for an elavated membrane tension observed in living cells, by an osmotic gradient lead to a disappearance of the tubulations. Thus, an entry of the Janus particles used here into living cells via self-induced tubulation of the plasma membrane and subsequent vesiculation is not expected.
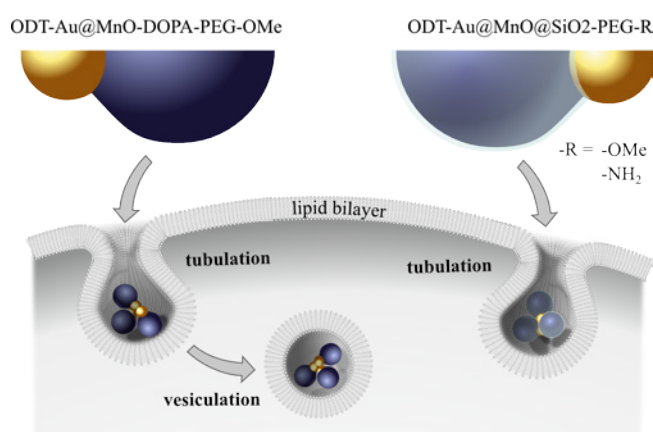
Figure 4.1.25: Scheme of the effects induced by Janus particles in lipid bilayers.

This assumption was confirmed by cytotoxicity studies and uptake experiments, in which Janus particles did not show large differences in comparison to spherical MnO-particles carrying the same functionalization. Furthermore, Janus particles, in which the MnO-domain was functionalized with dopamine-coupled PEG, showed stronger effects on DOPC-GUVs. After 30 minutes of incubation smaller vesicles were formed hinting for a stronger interaction of these particles with the lipid bilayer in comparison to silica-coated particles. The main effects on lipid membranes are also summarized in Figure 4.1.25. Taken together, this work provides experimental evidence for the effects of amphiphilic Janus particles on lipid bilayers predicted by simulations of Reynwar *et al.*.(Reynwar *et al.*, 2007)

4.2   <u>Alteration of cellular mechanics by chemical stimuli</u>

4.2.1 Introduction

Cellular mechanics are important for many biological processes like migration, cell division and mechanotransduction (see chapter 2.1.2) but also for the interaction between nanoparticles and cells as demonstrated in the last chapter. To assess mechanical properties of cells, various methods have been employed over the last decades including atomic force microscopy (AFM), optical tweezers, microplate rheometers or micropipette aspiration technique.(Pullarkat *et al.*, 2007) Among these methods, AFM is the technique with the highest lateral resolution. In recent years, most studies using the AFM to measure mechanical properties of cells recorded force-indentation curves and calculated elastic moduli from these curves by application of an area contact model.(Kuznetsova *et al.*, 2007; Radmacher, 1997) By assessment of the elastic modulus the viscous properties of the cells are neglected, which appear in force indentation experiments in form of a hysteresis between indentation curve and retraction curve. Shroff and coworkers developed an experimental procedure, which allowed the measurement of viscoelastic behavior using the AFM, thus, giving a more precise description of the natural situation.(Shroff *et al.*, 1995) Small amplitude oscillations of a cantilever, which is in contact with the sample, are used to measure a complex valued dynamic modulus. Through application of contact mechanical concepts, it is possible to calculate the complex shear modulus as an intrinsic material property.(Alcaraz *et al.*, 2003; Mahaffy *et al.*, 2000)

Here, I use AFM-based microrheology to examine the influence of drugs with known effects (on mechanics) of MDCK-II cells. Cellular microrheology of cells is determined at frequencies from 5 Hz to 100 Hz. As chemical agents I either use fixating chemicals (paraformaldehyde (PFA) and glutardialdehyde (GDA)) to examine how stabilization affects frequency-dependent cellular mechanics or agents interfering with the actomyosin network (Cytochalasin D (CytD) or Blebbistatin (Bleb)) to observe the effect of cytoskeletal destabilization on the microrheology of cells. Furthermore, I research the influence of administration of TGF-β1 on the mechanics of normal murine

mammary gland cells (NMuMG cells). TGF-β1 is known to induce dedifferentiation of NMuMGs from epithelial cells to mesenchymal cells (see chapter 2.1.4). Epithelial-to-mesenchymal transition (EMT) plays an important role in physiological processes like embryogenesis or wound healing. However, it has also been shown that EMT can be linked to malignant transformation of tumor cells.(Thiery, 2002) The transformation from an epithelial phenotype to a mesenchymal, fibroblast like morphology goes along with massive cytoskeletal rearrangement such as stress fiber formation or loss of cell-cell contacts accompanied by changes in cellular mechanics.

4.2.2   Results and Discussion

4.2.2.1   Mechanical stabilization and destabilization of canine kidney epithelial cells

Prior to the microrheological characterization, cells were imaged by AFM using contact mode imaging. Figure 4.2.1 shows deflection images of untreated MDCK-II cells as well as MDCK-II cells treated with stabilizing and destabilizing agents. Untreated MDCK-II cells show typical epithelial structure with pronounced cell-cell-contacts, which can be seen in the image as a bulge between adjacent cells. The bulge is the result of the relative compliance of untreated MDCK-II cells. AFM imaging in contact mode is an invasive method and during imaging the apical membrane is deformed. While the apical membrane can be easily deformed the lateral actin cortex of cells appears stiffer resulting in a bulge between cells with strong intercellular connections in AFM contact mode images. This deformability of the membrane is also the reason, why the network structure of the cytoskeleton can be observed in AFM contact mode images. Henderson et al. and Rotsch et al. were able to co-localize the network structure observed in contact mode images with the fluorescent-labeled actin cytoskeleton.(Henderson *et al.*, 1992; Rotsch and Radmacher, 2000) Structures formed by microtubules could not be found in AFM images suggesting that the main response as a response to indentation results from the mechanical properties of the membrane and the underlying actin cortex. Upon fixation of MCKD-II cells using a 4% PFA solution, which reacts with free amino- and other nucleophile groups under formation of covalent bonds, the network structure on the surface becomes less pronounced in the AFM image and also the bulge at the cell-cell-interface is less visible. Fixation with GDA leads to a complete disappearance of the network structure and the bulge. However, new structures appear on the surface. The dot-like structures

on the AFM-image can be attributed to microvilli, actin-based finger-like structures on the cell surface (see also chapter 2.1.1.3).
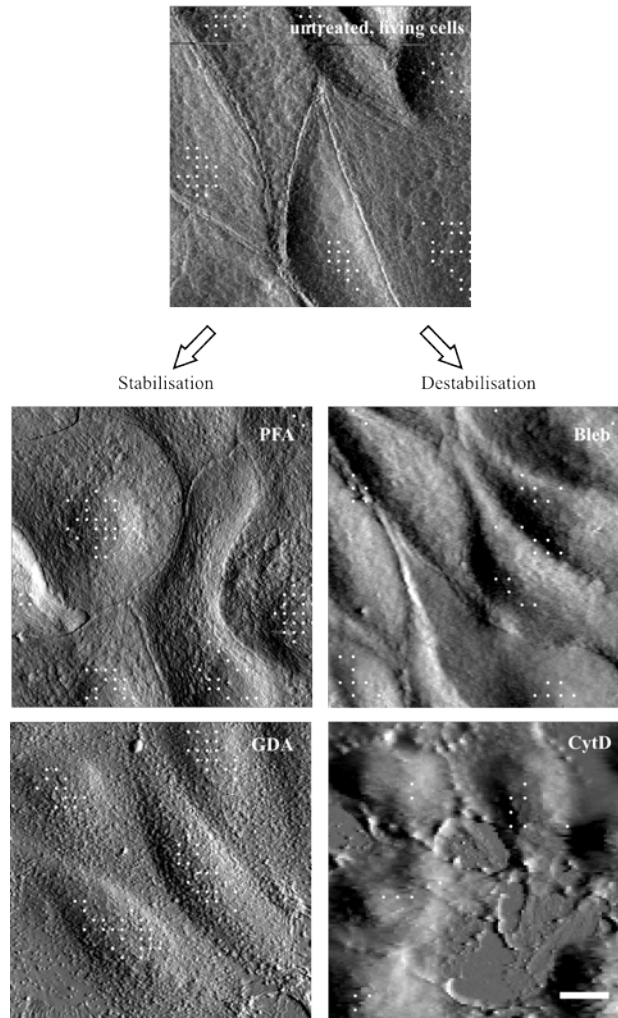
Figure 4.2.1: Exemplary AFM deflection images of MDCK-II cells treated with different drugs, which either stabilize or destabilize to the cell. White dots mark the positions of the microrheological measurements. Samples treated with stabilizing drugs and the control sample were cultured on glass substrates. Scale bar: 10 µm.

GDA has in contrast to formaldehyde two aldehyde residues allowing for crosslinking between proteins, which further stiffens the cell. In contrast, when treated with Blebbistatin, the surface of MDCK-II cells becomes blurry in AFM deflection images indicative of a softening of the structures, while their overall morphology is less affected. Blebbistatin is a potent myosin II inhibitor. It interferes with the myosin-ADP-Pi complex in an actin-detached state, thus, preventing rigid actomyosin crosslinking.(Kovacs *et al.*, 2004) Thus, the tension of the actin network decreases making it more difficult to image the cell surface with the AFM. MDCK-II cells treated with CytD exhibit an even more perturbed structure. Moreover, the CytD treated cells

seem to loose their cell-cell contacts as the substrate becomes visible in the image and detach from the substrate. CytD is a fungal toxin, which inhibits actin filament growth and induces actin-filament depolymerization by binding to the barbed end of the filaments.(Cooper, 1987)

To observe the effects on the actomyosin network f-actin was stained in cells after adminitartion of Blebbistatin and CytD. (see Figure 4.2.2). While untreated cells show many stress fibers spanning through the cell from one end to the other, MDCK-II cells treated with Blebbistatin show only few, short stress fibers. Moreover, the interface between single cells becomes irregular at the basal side, which might be induced by the degradation of mature focal ahesions. Myosin II is crucial for tension generation in epithelial cells and thus, for formation and maintenance of mature focal adhesions, which are tightly linked to stress fibers (see also chapter 2.1.2). Release of the tension leads to the degeneration of mature focal adhesions in favor of focal complexes, which are not dependent on tension generated by the cytoskeleton.(Geiger *et al.*, 2009; Wolfenson *et al.*, 2011)
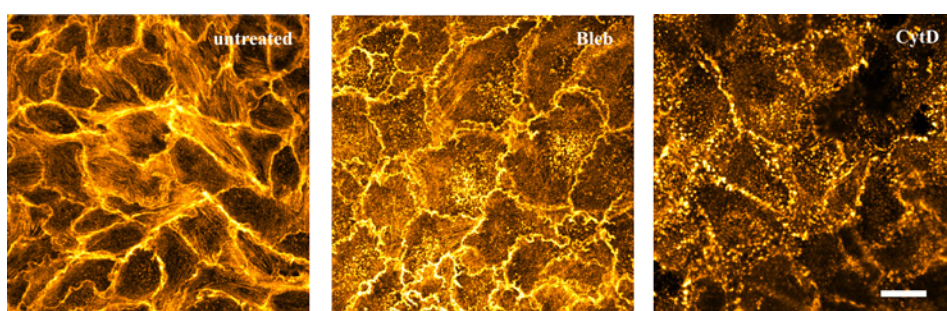
Figure 4.2.2: Confocal fluorescence images showing the arrangement of actin-cytoskeleton in the basal plane of MDCK-II cells, which have been treated with drugs interfering with the actomyosin network. (AlexaFluor546-labelled phalloidin, pseudocolored) Images have been recorded by Helen Nöding (Institute of Physical Chemistry, Georg-August-University, Göttingen, Germany). Scale Bar: 20 µm

The actin cytoskeleton of MDCK-II cells, which have been incubated with 2 µM CytD, appears to be completely disrupted. Only small actin foci are found.

As observed in AFM images, CytD treated cells are not able to maintain their epithelial structure. These tremendous effects on cellular morphology induced by Blebbistatin and CytD are also reflected in changes in cellular mechanics. Figure 4.2.3 shows the effect of cell treatment with stabilizing and destabilizing drugs. The averaged force-indentation curves qualitatively describe the force response to indentation of the different samples. MDCK-II cells treated with fixating agents exhibit a steeper increase in force with increasing indentation of the cantilever compared to the other samples indicating stiffer properties and a higher elastic modulus due to crosslinking of proteins

by imine bonds.(Lulevich *et al.*, 2006) Moreover, GDA treated samples are even stiffer than PFA treated samples. In contrast, interfering with the actomyosin network by administration of Blebbistatin or CytD leads to a softening of the cell, which is indicated by a shallower increase of force in indentation experiments and a lower elastic modulus E. The values of the elastic moduli E calculated from the averaged curves can be found in Table 4.2.1. Figures 4.2.3 B and C show the influence of fixation and Blebbistatin and CytD treatment on the real part G' and the imaginary part G'' of the complex shear modulus measured by AFM-based microrheology. G' is a measure for the energy that is elastically stored in the system upon oscillatory indentation (see also chapter 3.9), G'' is a measure for the amount the energy that is dissipated in the system. Untreated MDCK-II cells exhibit a value of 679 Pa for G' at an oscillation frequency of 5 Hz. Furthermore, G' increases with increasing frequency according to a weak power-law with an exponent α of 0.23 (see also Table 4.2.1). G'' of untreated cells, on the other side, shows lower values compared to G′ at low frequencies, but as it shows a steeper increase with frequency it eventually exceeds G' at high frequencies. This is also reflected in the loss tangent η, which is the ratio between G'' and G'. At low frequencies, η is smaller than 1 indicative for a more solid-like behavior. With increasing frequency, η becomes larger until it reaches values larger than 1. Here, more energy is dissipated than stored. The cells behave more fluid-like. When the cells are fixed using PFA, G' shifts to higher values at all frequencies, whereas lower frequencies are more affected. This is reflected in a smaller power law coefficient α of 0.02. Moreover, G'' shifts to higher values, but is not as much affected as G'. Thus, G'' does not exceed G' in the observed frequency range and the loss tangent η remains smaller than 1 over the whole frequency range. Cells treated with GDA appear even stiffer and show almost a constant value in G' over all frequencies indicating a nearly elastic, solid-like behavior, which is also reflected in the loss tangent.
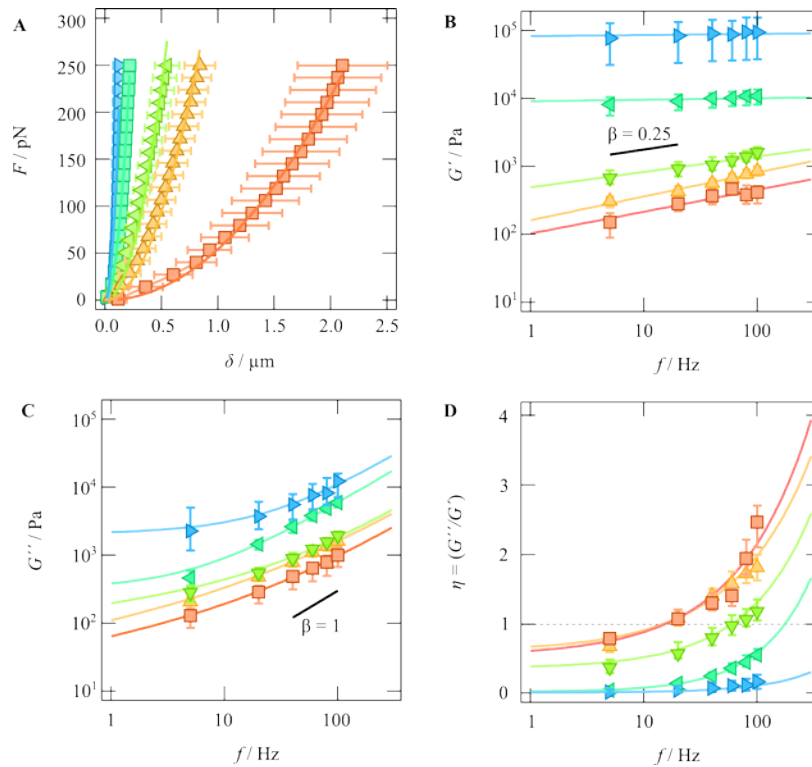
Figure 4.2.3: Cellular mechanics of MDCK-II cells treated with stabilizing and destabilizing drugs. (▼ untreated cells, ▲ blebbistatin, ■ Cytochalasin D, ◄ PFA, ► GDA) **A** Averaged force-indentation curves for the different treatments (number of averaged curves: untreated cells (*n*=78), blebbistatin (*n*=38), Cytochalasin D (*n*=34), PFA (*n*=79), GDA (*n*=72)) and Hertz-Model fit of the data (solid lines). **B,C and D** microrheological data of chemically treated cells (number of samples: untreated cells (*n*=141), blebbistatin (*n*=83), Cytochalasin D (*n*=39), PFA (*n*=79), GDA (*n*=72)). Real part of complex shear modulus G' as a function of the oscillation frequency. Black line indicates a power-law exponent of 0.25 **C** Imaginary part of the complex shear modulus G'' as a function of the oscillation frequency. Black line indicates a power-law exponent of 1 **D** Loss tangent η as a function of the oscillation frequency. Solid lines: power-law structural damping model fit. (see chapter 3.9) Untreated sample has been measured by Helen Nöding(Institute of Physical Chemistry, Georg-August-University, Göttingen, Germany).

Ablation of the actin cytoskeleton by CytD treatment or release of cytoskeletal tension by administration of Blebbistatin induces an opposite effect. G' as well as G'' exhibit lower values compared to the untreated control. Again, lower frequencies are impacted more leading this time to a steeper increase with the frequency in the case of G'. α exhibits a value of 0.32 for cell treated with CytD and a value of 0.35 for the Blebbistatin treated cells. Like before, G' is influenced more by the chemical treatment, now leading to a general increase of η at all frequencies. The transition from a more solid-like behavior to a more fluid-like behavior occurs at lower frequencies indicating a fluidization of the cell when the actin cytoskeleton is ablated or the tension in the actin cytoskeleton is released by administration of Blebbistatin. The measured frequency-dependent rheological data can be explained by means of active soft glassy rheology (SGR), which predicts power-law structural damping (PLSD) behavior (see also

chapter 3.9). (Fabry *et al.*, 2001) The fitting parameters of the power-law structural damping model are listed in Table 4.2.1. In the active soft glassy rheology model (SGR), the cellular cytoskeleton, i.e. the actin cytoskeleton, is assumed as a network of structural elements, which are trapped in energy wells by weak interactions with their neighbors. By active motion induced by motor proteins or external force, the elements are allowed to jump out of their well and fall into another under energy dissipation. The power-law coefficient α describes, how much the structural elements are allowed to jump between energy wells. In terms of SGR, α is a measure for the effective temperature of the material.

Table 4.2.1: Elastic modulus obtained by Hertz model-fit (eq. 3.10) and Parameters of the power-law structural damping fit of the rheological data of MDCK-II cells treated with stabilizing as well as destabilizing agents. G_0 is the scaling parameter describing the overall stiffness of the sample, α is the power-law coefficient and μ is the cellular viscosity.

	E / kPa	$G_0 \pm SE$/ Pa	$\alpha \pm SE$	$\mu \pm SE$/ Pa×s
untreated	1.1	325 ± 62	0.23 ± 0.03	2.1 ± 0.21
CytD	0.1	57 ± 14	0.32 ± 0.04	1.15 ± 0.11
Bleb	0.5	85 ± 12	0.35 ± 0.02	1.77 ± 0.11
PFA	6.5	8723 ± 496	0.02 ± 0.01	8.96 ± 0.5
GDA	16.8	80514 ± 2841	0.02 ± 0.01	14.08 ± 2.17

Fixation of the cell leads to crosslinking of proteins. Thus, the structural elements are kept at their position, which in turn is reducing the level of agitation in the network. Therefore, α approaches zero, which is indicative for a passive, completely elastic material. On the other side, ablation of the actin cytoskeleton and release of the tension in the network by interference with the motor proteins induces a fluidization of the elements. The elements are able to jump more between energy wells due to the lack of crosslinkers also leading to a relative increase in energy dissipation. As a result, the power-law coefficient α as well as the loss tangent η increase. Fabry et al. could observe the same trend, when cells were treated with drugs interfering with the actomyosin network, by using magnetic bead twisting microrheology.(Fabry *et al.*, 2001) They were able to show that an increased contractile tone of the network lead to a weaker power law dependency, while a disruption of the actin cytoskeleton lead to an increased power law coefficient α. G_0 is a scaling factor and exhibits the same trend as

$G'(5\text{Hz})$. Furthermore, the cellular viscosity μ follows a similar trend, whereas the relative changes are larger in G_0 also showing that fixation leads to a more solid like behavior while ablation of actin leads to a more fluid-like behavior.

These examples show, how chemical treatment interferes with cellular microrheology. The measured curves for G' and G'' are well described by the PLSD model fit and the SGR model delivers reasonable explanations for the observed data. Additionally, the measured data are comparable to previous results obtained by magnetic bead twisting rheology. In a next step, I will make use of the AFM-based microrheology to focus on the influence of TGF-β1-induced epithelial-to-mesenchymal transition on cellular morphology and mechanics.

4.2.2.2   TGF-β1-induced   epithelial-to-mesenchymal   transition   of   murine   mammary gland cells

Treatment of normal murine mammary gland (NMuMG) cells with TGF-β1 has been shown to induce epithelial-to-mesenchymal transition (EMT).(Miettinen *et al.*, 1994) EMT is a crucial process during embryogenesis and wound healing, but also seems to be related to tumor progression.(Thiery, 2002) A short introduction to EMT can be found in chapter 2.1.4.
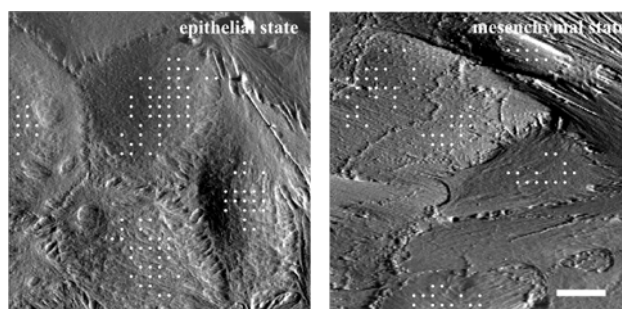
Figure 4.2.4: Exemplary AFM deflection images of living NMuMG cells in epithelial and in mesenchymal state 48h after TGF-β1 administration. White dots mark the positions, where the microrheological experiments were performed. Scale bar: 10 μm.

Transition of cells from an epithelial phenotype to a mesenchymal, fibroblast-like phenotype is accompanied by alterations in protein expression and tremendous morphological changes, which involve rearrangement of actin cytoskeleton. Here, the changes in morphology induced by TGF-β1-treatment of NMuMG cells have been followed by AFM imaging. Exemplary images can be seen in Figure 4.2.4.

Untreated NMuMG cells exhibit a normal epithelial morphology showing a nearly hexagonal shape, although their cell-cell-contacts are not as pronounced as in MDCK-

II cells (see Figure 4.2.1). The structure of the cortical network of actin filaments is also visible in AFM deflection image. Upon treatment with TGF-β1 the cell starts to elongate, finally leading to a fibroblast like morphology with pronounced stress fiber formation. The network structure on the cell surface has vanished completely. Moreover, transformation is followed by a reduction of cell-cell-contacts and cells tend to grow on each other. The loss of cell-cell-junctions has also been observed using impedimetric measurements.(Schneider *et al.*, 2011) Additionally, changes in cytoskeletal structure have been captured by fluorescence microscopy (experiments have been performed by David Schneider, Institute of Physical Chemistry, University of Göttingen). The fluorescence images in Figure 4.2.5 show NMuMG cells before transformation in epithelial state and 48 h after TGF-β1 administration in mesenchymal state.
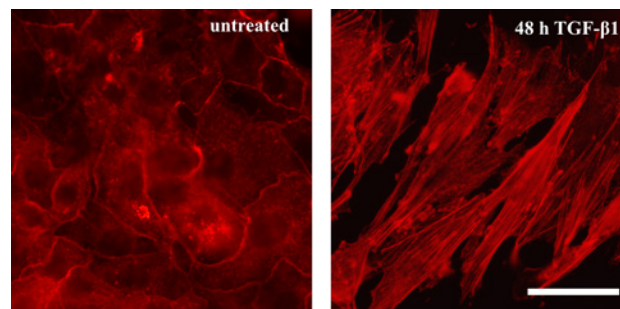
Figure 4.2.5: Epi-fluorescence images showing the arrangement of actin-cytoskeleton in untreated NMuMG cells and NMuMG cells, which have been treated with TGF-β1. (AlexaFluor546-labelled phalloidin, red) Images have been recorded by David Schneider, Institute of Physical Chemistry, Georg-August-University, Göttingen, Germany. Scale Bar: 50 μm

In the epithelial state, the actin cytoskeleton can be found mainly in the cell cortex. Upon 48h of incubation with TGF-β1 the distribution of actin in NMuMG cells has changed. The cortical actin cytoskeleton is rearranged to thick fibers spanning the entire cell. The transformed cells show an elongated, fibroblast-like shape. Similar observations have been made by Brown *et al.*.(Brown *et al.*, 2004)
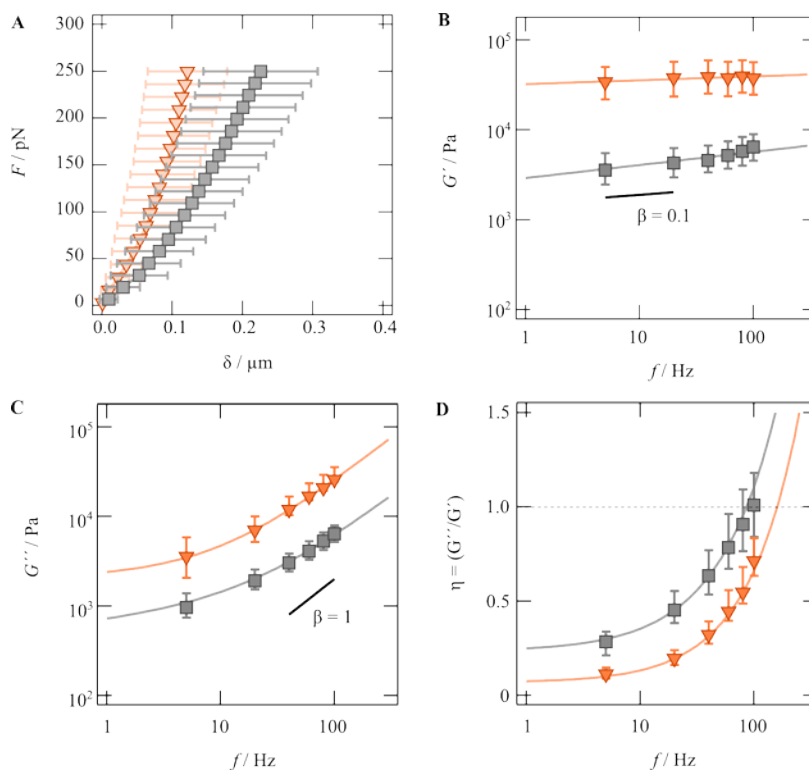
Figure 4.2.6: Cellular mechanics of NMuMG cells (■ untreated cells, ▼ 48 h after treatment with TGF-β1). **A** Averaged force-indentation curves for the different treatments (number of averaged curves: untreated cells (*n*=106), and TGF-β1 (*n*=73)) and Hertz-Model fit of the data (solid lines). **B** Real part of complex shear modulus G' as a function of the oscillation frequency. Black line indicates a power-law exponent of 0.1 **C** Imaginary part of the complex shear modulus G″ as a function of the oscillation frequency. Black line indicates a power-law exponent of 1 **D** Loss tangent η as a function of the oscillation frequency. Solid lines: power-law structural damping model fit (number of analyzed samples: untreated cells (*n*=177), and TGF-β1 (*n*=134)) (see chapter 3.9).

To observe changes in viscoelasticity of cells, AFM-based microrheological measurements were performed. The results are depicted in Figure 4.2.6. Figure 4.2.6 A shows averaged force-distance curves of epithelial and transformed NMuMG cells, which suggest that cells have become stiffer upon transformation. This observation is confirmed by the microrheological data. G' of untreated NMuMG cells at an oscillation frequency of 5 Hz exhibits a value of 3.5 kPa, which is approximately 6 times the value of untreated MDCK-II cells. When treated with TGF-β1 for 48 hours, G'(5 Hz) increases to a value of 25.7 kPa (Figure 4.2.6 B). G'' also increases over the complete measured frequency spectrum, but is not as much affected as G′. Accordingly, the loss tangent η decreases. Even at 100 Hz η stays below one, indicating that solid-like behavior dominates the mechanical response of transformed NMuMG cells. These findings are also reflected in parameters of the power law structural damping model shown in Table 4.2.2. G_0 and the cellular viscosity μ increase upon transformation. The power law coefficient decreases from 0.11 to 0.05. Similar observations have been observed

when treating MDCK-II cells were treated with fixating agents (see chapter 4.2.2.1). Fixed cells also became stiffer, showing properties of a passive, purely elastic material with a power-law coefficient near zero.

Table 4.2.2: Parameters obtained by the power-law structural damping fit of the rheological data of NMuMG cells treated with transforming growth factor-β1 (TGF-β1). G_0 is the scaling parameter describing the overall stiffness of the sample, α is the power-law coefficient and μ is the cellular viscosity.

	$G_0 \pm$ SE/ kPa	$\alpha \pm$ SE	$\mu \pm$ SE/ Pa×s
Epithelial state	2.2 ± 0.3	0.15 ± 0.02	7.9 ± 0.5
Mesenchymal state	25.7 ± 0.8	0.05 ± 0.01	35.78 ± 0.97

However, in the case of TGF-β1-induced EMT the more elastic behavior cannot be explained by crosslinking of proteins by a fixative. Instead, the effect is the result of the structural rearrangements of the actin cytoskeleton accompanied by an increased contractile tone in the new-formed stress fibers near the apical membrane. Bundling proteins, i.e. α-actinin, and myosin II, which is responsible for the force generation in the network, act similar to the fixating agents in the measurements shown previously. Bundling and crosslinking proteins as well as motorproteins also hold the structural elements at their position in the energy landscape preventing them from jumping between wells and dissipating energy. Hence, the cell appears stiffer and more like a passive, elastic material. Similar effects have also been observed by enhancement of actomyosin contractility by stimulation with drugs like histamine or serotonin.(Fabry *et al.*, 2001; Laudadio *et al.*, 2005) Additionally, by fitting of force-indentation curves with an expanded liquid droplet model, we were able to measure an increased pre-tension of transformed NMuMG cells.(Schneider *et al.*, 2013)

For the cell, an increased cytoskeletal tension could promote migration. Simulations by DiMilla et al. show a relationship between contractile force, cellular rheology and migration velocity.(Dimilla *et al.*, 1991) The authors demonstrated that an increased cytoskeletal tension is required to promote cell deformation and adhesion bond rupture, which are prerequisites for cell migration.
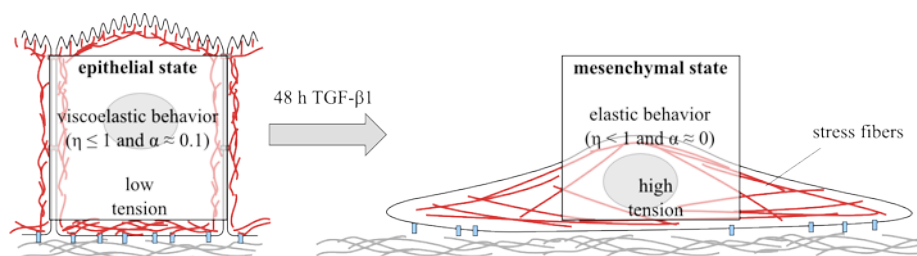
Figure 4.2.7: Scheme of structural and mechanical alteration after TGF-β1- induced epithelial-to-mesenchymal transition. NMuMG cells lose their cell-cell contacts and elongate after incubation with TGF-β1. These morphological alterations are accompanied by a massive formation of stress fibers, which set the cell under high tension. Actin is depicted in red.

Additionally, a moderate increase in the cell's elastic modulus has been found to have positive effects on migration velocity. At the same time, an increased viscosity leads to a decrease in migration speed. Similarly, McGrail and coworkers observed a shift to more elastic behavior of mesenchymal stem cells and fibroblast upon incubation with 4T1 breast tumor cell conditioned media.(McGrail *et al.*, 2012) The more elastic cells also showed increased motility. Enhanced migratory behavior of cells in response to EMT could have either beneficial effects in wound healing promoting a fast regeneration of harmed tissue but also lead to tumor progression if benign tumor cells adopt a motile phenotype. Figure 4.2.7 depicts the structural and mechanical alterations that are followed by TGF-β1-induced EMT in NMuMG cells.

4.2.3   Conclusion

Mechanical properties of cells are inextricably linked to cellular processes involving the cytoskeleton or membrane organization like migration, endocytosis or adhesion. Here, I demonstrated that AFM-based microrheology is a valuable tool to measure frequency-dependent viscoelastic properties of cells. The results depicted in this chapter are comparable to measurements by Fabry et al. and Laudadio et al., who researched the impact of different drugs on cellular rheology by magnetic bead twisting microrheology.(Fabry *et al.*, 2001; Laudadio *et al.*, 2005) I showed that Blebbistatin and CytochalasinD, which perturb the actomyosin network, led to a decrease of both, the real and the imaginary part of the complex shear modulus. At the same time, the power law coefficient α increased. According to SGR theory, an increased power law coefficient can be related to an increase in the agitation level of structural elements. In contrast, when cells were fixed using PFA or GDA or transformed by TGF-β1 administration, which is concomitant with an increase of cytoskeletal tension and actin bundling, the storage and loss modulus increased in comparison to the untreated

sample. In this case α decreased to value near zero. Thus G' becomes largely independent of the frequency and cells behave more like a purely elastic material. In all cases, the storage modulus was more affected than the loss modulus leading to changes in the loss tangent.

4.3 Microrheological characterization of cell lines: relation between cancer and cell mechanics.

4.3.1 Introduction

Results presented in chapter 4.2 showed that AFM based microrheology is able to capture frequency-dependent mechanical changes after administration of different drugs. Furthermore changes in the mechanical behavior of cells after epithelial-to-mesenchymal transition of NMuMG cells were observed, which has also been proposed as a model linked to the progression of tumors transforming cells into a more malignant and motile phenotype.(Thiery, 2002) In this chapter, we address mechanical alterations that go along with malignant transformation of cells. During the progression from a benign tumor to a malign neoplasm the cells undergo many changes on the molecular level. In cancer, not only the cell cycle machinery is out of control, also other regulatory processes like cellular adhesion and migration are affected (see also chapter 2.1.2.1).(Hanahan and Weinberg, 2011) This becomes obvious, when looking at key steps in the formation of metastasis, which include invasion into surrounding tissue and intra- and extravasation into lymphatic or blood vessels. These processes involve dramatic changes in the organization of the cellular cytoskeleton. In particular, changes in the expression of proteins, which are associated with regulation and dynamics of the actin cytoskeleton, play an important role in many types of cancer.(Olson and Sahai, 2009) Therefore, it is conceivable that apart from structural changes also alterations of mechanical and dynamical properties take place during tumor progression providing a signature of malignancy. To date there are several studies available that report on measurements of rigidity of cancer cells in comparison to benign cells. Many studies find that cancer cell are significantly softer than normal cells.(Suresh, 2007) This is understandable since softer cells would more easily penetrate tissues and the extracellular matrix and hence, increase the invasiveness of tumor cells (see chapter 2.1.2.1). Furthermore, cancer cells have been shown to lose requirement to adhere to a surface for survival and to be less sensitive to changes in substrate elasticity.(Agus *et al.*, 2013; Wang *et al.*, 2000; Wittelsberger *et al.*, 1981)

Perturbed adhesion interferes with mechanotransduction and cytoskeletal tension, which in turn influences cellular mechanics. However, there also exist studies, which report on a stiffening of cancer cells compared to benign cells suggesting that tumor progression can have diverging effects on cellular elasticity.(Rosenbluth *et al.*, 2006; Zhang *et al.*, 2002a) Measurements of these mechanical changes are frequently lumped into a single universal parameter, i.e. the Young's modulus. The suitability of the Young's modulus to describe the malignancy of cells is, however, a matter of debate. It is therefore of great interest to identify reliable mechanical descriptors that predict faithfully the malignancy of cells. Here rheological approaches might provide the keydata since they are intimately linked to the activity of motor proteins in cells.(Mizuno *et al.*, 2007) Numerous techniques have been used to quantify the mechanical properties of cells including magnetic bead twisting, micropipette aspiration, particle tracking, optical tweezers, microplate rheology and atomic force microscopy (AFM).(Pullarkat *et al.*, 2007) Among these methods, the atomic force microscope is the technique with the highest spatial resolution and the largest force range covering pN to µN by using a small tip attached to a flexible cantilever.(Binnig *et al.*, 1986) The AFM has widely been used to determine elastic properties of different samples predominantly applying contact models such as Hertz or JKR model.(Kuznetsova *et al.*, 2007) However, the occurrence of a hysteresis between indentation and retraction curve in force-distance measurements indicates that cells do not exhibit a purely elastic behavior making it necessary to describe the mechanical properties of cells in the context of time dependent rheology. To obtain information about the frequency dependent viscoelastic properties of samples using the atomic force microscope, Shroff and co-workers developed a method, which uses small amplitude oscillations of the AFM cantilever as described in the previous chapter.(Shroff *et al.*, 1995). Quantitative models to compute the complex shear modulus G^*, which account for the contact area as a function of the indentation depth, were developed by several groups considering either a spherical or pyramidal indenter geometry to probe the sample (see also chapter 3.9.4).(Alcaraz *et al.*, 2003; Mahaffy *et al.*, 2000; Smith *et al.*, 2005) Microrheological studies of adherent cells carried out by a large variety of techniques suggest that the cytoskeleton resembles the viscoelastic nature of soft glassy materials over a wide frequency range due to its general scaling behavior (see chapter 4.3).(Fabry *et al.*, 2003)

With the focus on malignancy, I investigated eight cell lines (NIH 3T3 fibroblasts, MDCK-II, NMuMG, A549, SW13, MCF-7 MDA-MB-231 and CaKi-1 cells) from four organs that possess different metastatic potentials. We find that cells from the same organ but with higher malignancy are generally softer than benign cells, which is

expressed in a lower real part of the complex shear modulus. However, when comparing cells of different metastatic potential from different organs, there is no clear trend in rigidity. Interestingly, all cancer cell lines displayed a higher loss tangent ($\eta = G''/G'$) at high oscillation frequencies compared to the benign cell lines. The loss tangent is inherently model independent and conveys information whether a cell is rather solid or fluid at a given excitation frequency. My measurements suggest that cancer cells are more fluid-like than epithelial cells or fibroblast, accounting for the migratory behaviour of the malign cells.

4.3.2 Results and Discussion

Spatially resolved microrheological data acquired for eight different cell lines were compared with respect to their malignant potential. Except for fibroblasts, all cell lines were investigated once confluence was reached. Prior to force mapping, the area of interest of each sample was imaged with the AFM to control morphology and confluency of cells. An example of subconfluent NMuMG cells that demonstrates the typical spatial resolution of the microrheological experiment using the AFM is shown in Figure 4.3.1. The height image shows two NMuMG cells in close contact to each other with maximal height of 5.5 µm (see figure 4.3.1).
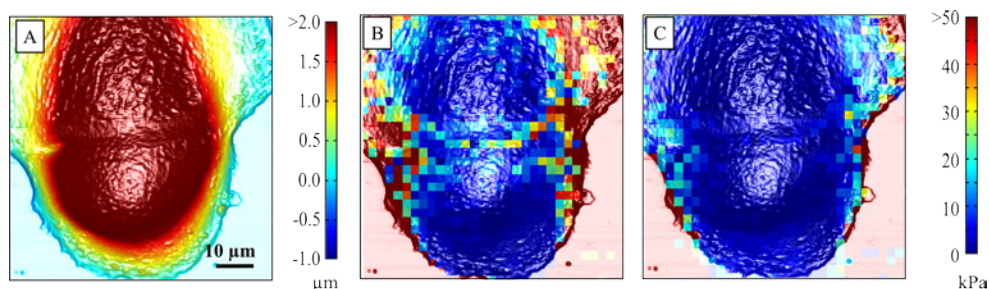
Figure 4.3.1: A AFM-Height image of epithelial NMuMG cells (contact mode). **B/C** Height image overlaid with the force map data of G' (B) and G'' (C) at an oscillation frequency of 20 Hz.

It is assumed that the cells in this image reside in a phase shortly after cytokinesis due to the lack of cell-cell contacts and the presence of a small furrow between the cells.(Clark and Paluch, 2011) Figure 4.3.1 B and C show an overlay of the height image and the corresponding storage and loss modules, respectively. The oscillation frequency of the microrheological measurement was set to 20 Hz in this representative image. Notably, at this frequency the values of G' exceed those of G''. The apical membrane in the peripheral areas of cells exhibits only a distance of a few hundred

nanometers from the substrate. In general, the cells exhibit higher moduli in this region reaching values of more than 50 kPa for G' compared to only 1 to 5 kPa in the center of the cells. The moduli in the center of each cell are lower compared to those in the periphery but also to values at the interface between the two cells. The high values of G' at the cell-cell interface can be explained by the presence of a stiff, contractile acto-myosin ring that is necessary for the separation of the daughter cells during cytokinesis.(Schroede.Te, 1972) The dense network of actin-filaments in direct contact to the cell membrane facilitates a higher resistivity against externally applied forces and therefore leads to higher modules.

Although Figure 5.3.1 demonstrates the feasibility of the method to measure frequency-dependent mechanical parameters with high lateral resolution, the stiff underlying substrate affects the measurement. This effect is known as "bottom effect" and makes the cells appear stiffer especially in thin regions.(Gavara and Chadwick, 2012) This could be a reason for the elevated values of G' and G'' in the periphery of the cells in Figure 4.3.1 B and 4.3.1 C. Besides using mainly confluent monolayers of the different cells lines I analyzed only force-distance curves with an indentation depth between 300 and 800 nm for further analysis to avoid pseudo stiffening of the cells by the bottom effect.

To research the frequency-dependent mechanical response of cancer cells compared to normal cells, I chose seven cell lines from four different organs. MDCKII cells and CaKi-1 cells originate from the kidney, SW13 are derived from the adrenal gland, NMuMG, MCF-7 and MDA-MB-231 are cells from the mammary gland and A549 cells are derived from the lung epithelial layer. MDCK-II and NMuMG cells show epithelial morphology, growing as a monolayer with strong intercellular junctions and a pronounced apical-basal polarity.(Dukes *et al.*, 2011) MCF-7 cells grow in a dense monolayer and but showed also the ability to form metastasis in lung, liver and spleen in athymic nude mice.(Shafie and Liotta, 1980) Although forming a confluent, polarized monolayer being a characteristic of normal epithelial cells, the CaKi-1 line is a representative metastatic renal cancer cell line.(Fujimoto *et al.*, 2005) Similarly, MDA-MB-231 cells are considered to be malignant cancer cells derived from the mammary gland, forming metastases in various organs including lung and bones.(Hiraga *et al.*, 2001) The A549 cell line originates from non-small cell lung cancer adenocarcinoma cells and shows an epithelial-like morphology. However, in contrast to the two epithelial cell lines used in this study, the A549 cells bear the potential to form metastasis in *in vivo* models.(Sussan *et al.*, 2005) SW13 cells belong to the small cell carcinoma and are derived from the adrenal gland.(Ziegler *et al.*, 2009) Apart from the aforementioned

cell lines I also investigated 3T3 fibroblasts as a paradigm for a benign mesenchymal cell.
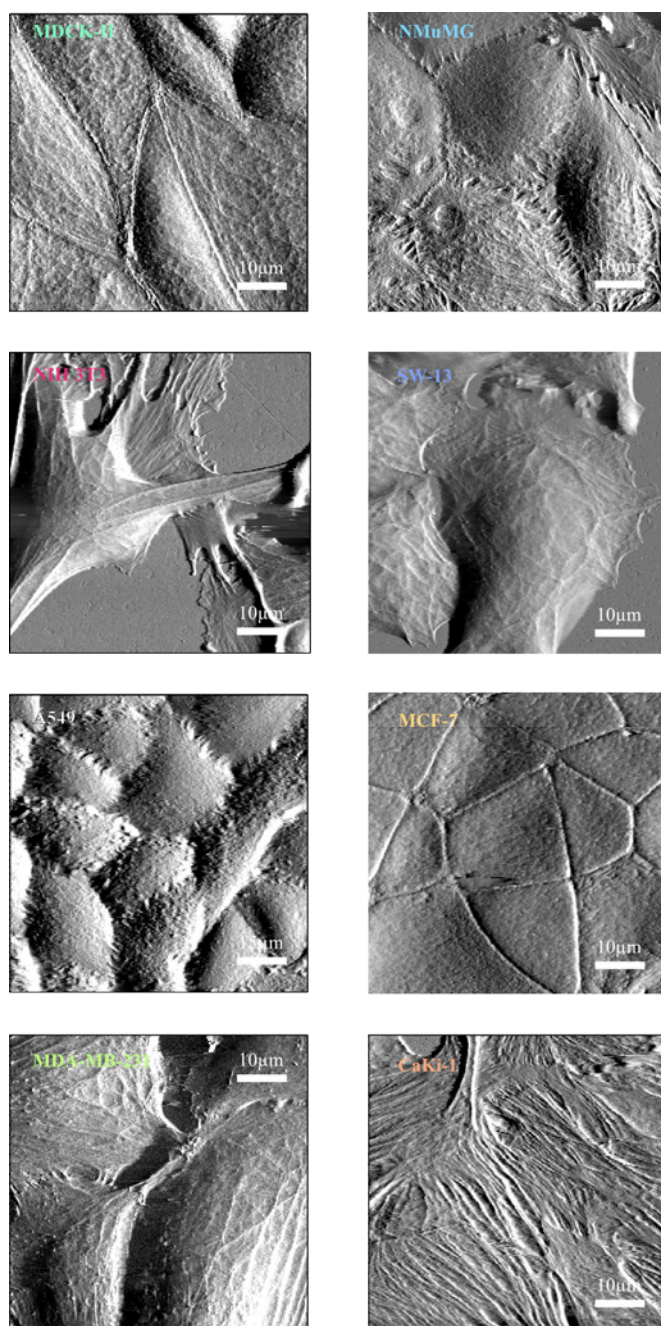
Figure 4.3.2: AFM-deflection images of all eight cell lines used in this study. Living cells were imaged in constant force mode using a pyramidal cantilever-tip geometry.

Representative AFM-deflection images of all cell lines can be found in Figure 4.3.2.
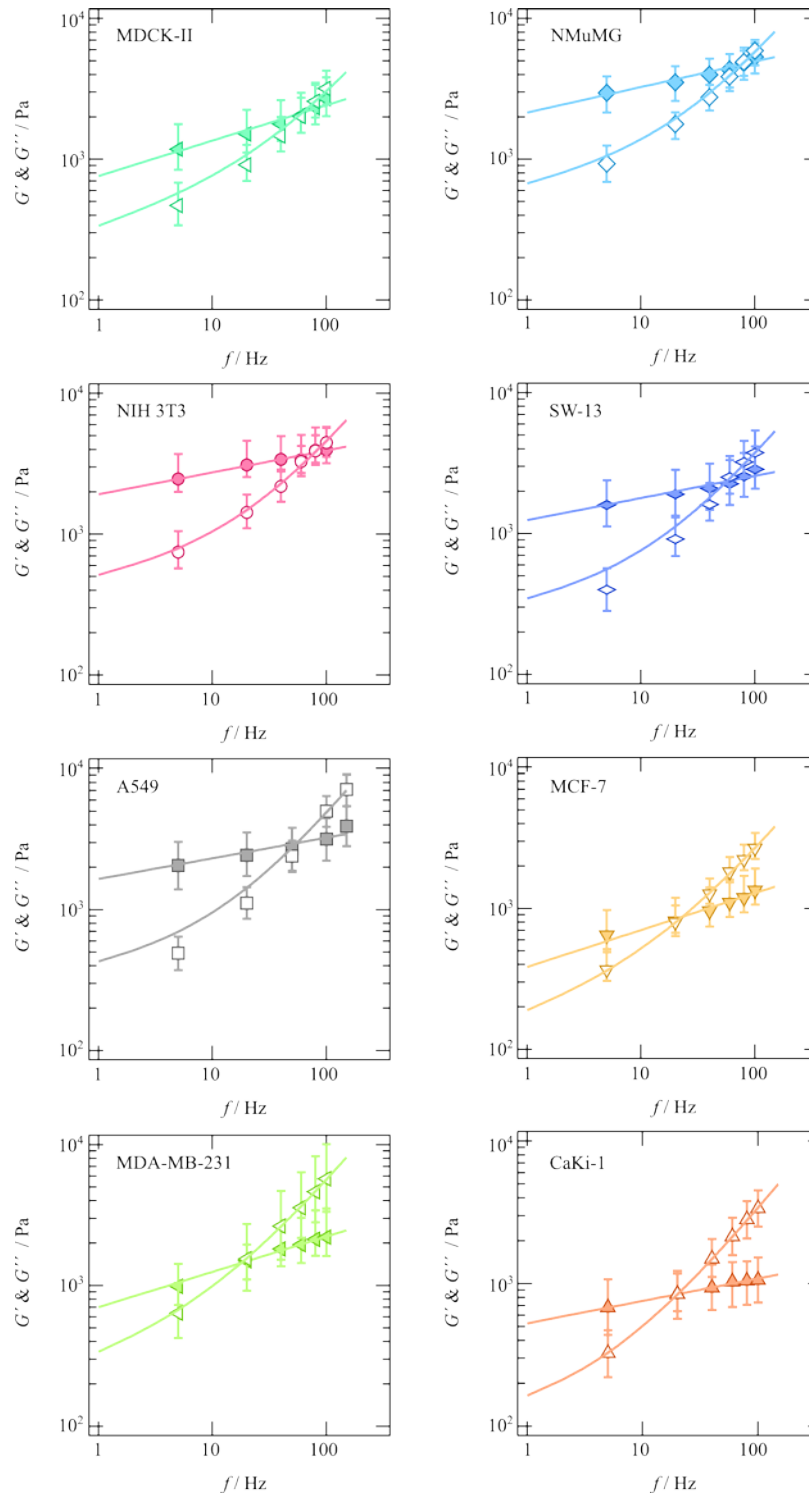
Figure 4.3.3: Median values (± quartiles) of the storage modulus *G´* (filled symbols) and loss modulus *G´´* (unfilled symbols) of cell lines with different metastatic potential as a function of the oscillation frequency. MDCKII and NMuMG cells are non-metastatic immortalized epithelial cells, while NIH 3T3 are benign mesenchymal cells. A549, MCF-7, MDA-MB231, SW13 and the CaKi-1 cells are metastatic cancer cells. The data of the complex shear modulus were fitted using the power-law structural damping model (solid lines, see also chapter 3.9).

Figure 4.3.3 compiles the results of the microrheological investigation of all cell lines measured in this study. Rheological data of the eight different cell lines were computed

from at least 2 force maps per cell line. In general, the complex shear modulus of all cell lines followed the typical frequency dependence found for many other cell types including neutrophils, airway smooth muscle cells, bronchial epithelial cells or pulmonary macrophages with different microrheological methods.(Fabry *et al.*, 2001; Smith *et al.*, 2005) G' increases with frequency following to a weak power-law with exponents α ranging from 0.10 to 0.25 (see Table 1), while G'' exhibits lower values compared to G' in the low frequency regime (<50Hz). In this regime, cells show a more solid-like behavior as the loss tangent $\eta = G''/G'$) does not exceed values larger than 1 (see also Figure 5.3.6). However, the high frequency domain is dominated by G'' indicating that the cells at high frequencies behave more like a viscous liquid ($G''/G'>1$). An attempt to explain this power law behavior in the microrheological spectra of living cells has been suggested by Fabry and Kollmannsberger as aforementioned.(Kollmannsberger and Fabry, 2009) By describing the cell as an active soft glassy material some rheological features can be assigned to cytoskeletal organization and remodelling. The model is based on the soft glassy rheology model first described by Sollich and assumes that the cytoskeleton of the cell consists of many disordered elements, which are held together by weak attractive forces between neighboring elements trapping the elements in energy wells.(Sollich, 1998) These weak interactions allow the elements to occasionally jump between the potential wells. A large distribution of energy well depth leads to a scale-free (power-law) behavior of the lifetime distribution and thus results in a power-law rheological behavior.
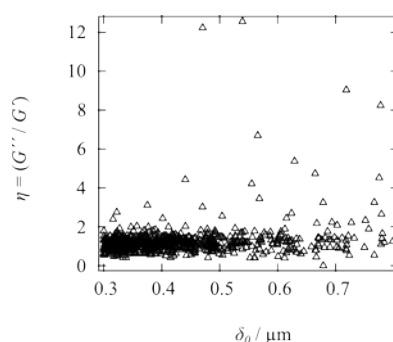
Figure 4.3.4: Loss tangent of NMuMG cells at 100 Hz oscillation frequency as a function of the indentation depth.

The power-law coefficient corresponds to the effective temperature of the material.(Fabry *et al.*, 2001) The material is at the thermal equilibrium if the power law coefficient becomes zero. The model of active soft glassy rheology also predicts power-law structural damping behavior at least at intermediate timescales. The rheological data of all cell lines could be approximated confidently by this model (solid lines in Figure 4.3.3. and 4.3.6). The obtained fitting parameters using to eq. 3.17 are

summarized in Table 4.3.1. However, the measured values of G', G_0, α or μ for all cell lines do not provide a clear correlation to the malignancy of the cell line. MCF-7, CaKi-1 and MDA-MB231 cells, three malignant cancer cell lines, show the lowest G'-values at all frequencies followed by epithelial MDCK-II cells with values slightly higher than those of MDA-MB231 cells.

Table 4.3.1: Fitting parameters G_0, α and μ of the power-law structural damping model (see chapter 3.9)) applied to the used cell lines. G_0 denotes the shear modulus at zero frequency, μ the viscosity and α is the power law coefficient.

	$G_0 \pm$ SE/ kPa	$\alpha \pm$ SE	$\mu \pm$ SE/ Pa×s
NIH 3T3	1.51 ± 0.12	0.15 ± 0.01	5.87 ± 0.25
MDCK-II	0.56 ± 0.10	0.22 ± 0.03	3.24 ± 0.36
NMuMG	1.69 ± 0.17	0.16 ± 0.02	7.19 ± 0.41
A549	1.61 ± 0.29	0.10 ± 0.03	6.85 ± 0.44
MDA-MB231	0.69 ± 0.06	0.22 ± 0.01	8.69 ± 0.21
CaKi-1	0.40 ± 0.02	0.16 ± 0.01	5.00 ± 0.04
MCF-7	0.25 ± 0.02	0.25 ± 0.02	3.44 ± 0.10
SW13	1.15 ± 0.17	0.12 ± 0.03	5.25 ± 0.35

Furthermore, malignant A549, NIH 3T3 and NMuMG cells display the highest storage modules. The effect of malignant transformation of cells on cellular mechanics has been investigated extensively by several groups with different findings. Lekka and coworkers, for instance, investigated the elastic response of normal and cancerous human bladder cell lines using the AFM.(Lekka *et al.*, 1999) They found that cancerous cells exhibit elastic moduli, which are one order of magnitude lower compared to normal cells. A similar trend has been observed by Guck and coworkers measuring the deformability of non-cancerous and cancerous human mammary epithelial cells with a microfluidic optical stretcher.(Guck *et al.*, 2005) Also, the cancerous cells were found to be more deformable than the corresponding benign cells. Treatment of the cancer cells with 12-*O*-tetradecanoylphorbol-13-acetate, a tumor promoting drug, additionally enhanced the deformability of the cancer cells. On the other hand, Zhang and coworkers report on a stiffening of hepatocellular carcinoma cells compared to benign hepatocytes.(Zhang *et al.*, 2002a) These contradictory results mirror the difficulty to categorize the malignancy of cancer cells according to their softness, i.e. Young's

modulus. Apart from G', neither the power law exponent α interpreted as 'noise temperature' in the framework of soft glassy rheology nor G_0, the scaling factor of the power-law structural damping model, display any trend. Nevertheless, the malignant transformation of benign cells into metastatic cancer cells results from a change in the protein expression pattern of the cell, which is accompanied by a reorganization of the cytoskeleton and a change in the adhesive properties of the cells.(Cross *et al.*, 2007; Suresh *et al.*, 2005; Wittelsberger *et al.*, 1981) Taking the histological origin of the cells into account, I observe the trend towards softer cancer cells compared to stiffer benign cells in my measurements. The benign epithelial cell lines NMuMG and MDCKII as well as the very stiff fibroblasts show higher values for G' compared to the corresponding malignant cancer cell lines from the same organ. However, A549 cells do not follow a potentially universal trend of low elastic moduli observed for malignant cells. Problems of using the elastic modulus for the cancer cell detection have been discussed recently by Lekka and Laidler.(Lekka and Laidler, 2009)
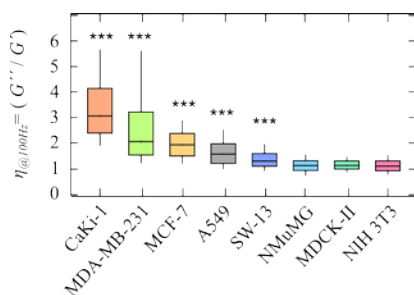
Figure 4.3.5: Loss tangent $\eta = G''/ G'$ of the various cell lines at an oscillation frequency of 100 Hz. (***, p<0.001, Wilcoxon Rank Test)

They pointed out that the Hertz model usually used to determine the elastic modulus is valid only for purely elastic, homogenous and infinitely thick samples. Additionally the indentation is considered to be frictionless and the model neglects adhesion.(Hertz, 1882) All these assumptions are not fulfilled indenting a cell with an AFM cantilever tip of sometimes barely defined geometry, which makes it difficult to compute absolute values of the elastic modulus. The model developed by Alcaraz used throughout this study also relies on Hertzian contact mechanics, facing similar problems.(Alcaraz *et al.*, 2003)
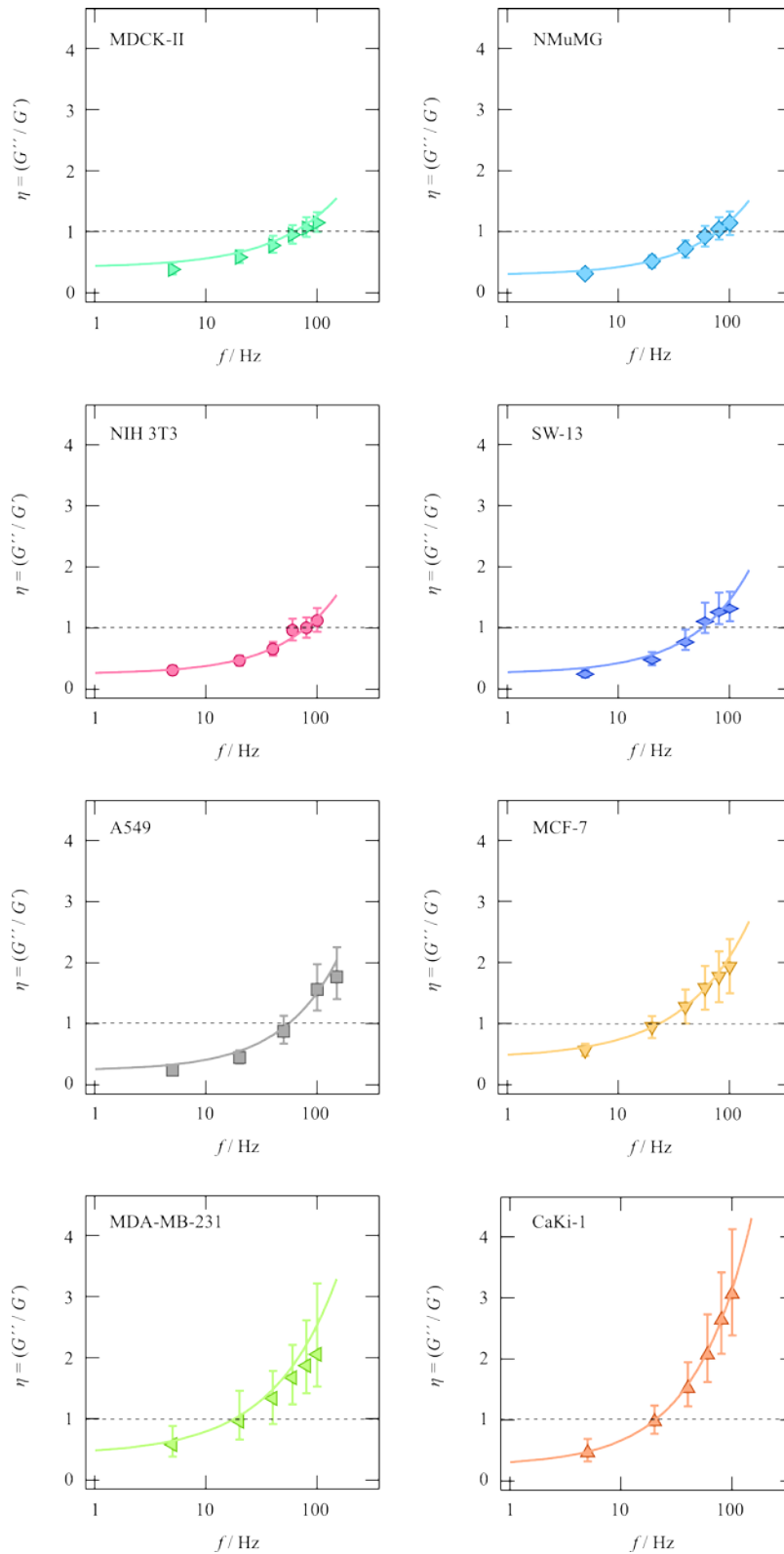
Figure 4.3.6: Loss tangent η of cell lines with different metastatic potential. Solid line shows course of loss tangent determined from the power law structural damping model.

Therefore, the absolute values of G^* need to be treated with care. In contrast, the loss tangent η as a model independent parameter (as it is solely described by the phase

shift between excitation of the cantilever and its response) does not assume a particular geometry of indenter or cell. Thus, it is independent of the indentation depth and details of contact mechanics providing a quantitative measure of the overall rheological behavior of the sample (see Figure 4.3.4). Figure 4.3.5 shows the loss tangent η determined at an oscillation frequency of 100 Hz for all cell lines. The complete frequency-dependence of the loss tangent is depicted in Figure 4.3.6. At 100 Hz, both epithelial cell lines (MDCKII and NMuMG cells) and the fibroblasts (NIH 3T3 cells) exhibit a loss tangent of approximatly 1.1 with a narrow distribution. All cancer cell lines have significantly higher median values of η ranging from 1.3 in the case of A549 cell up to 2 and 3 in the case of MDA-MB-231 cells and CaKi-1 cells, respectively. The effect is also accompanied by a broadening of the distribution. With decreasing frequency the difference between the loss tangent of cancer cells and that of normal cells becomes smaller and finally disappears. On the other side, for higher frequencies, the PLSD model fit of the data measured here predicts larger differences in η. The elevated values of η can be interpreted as a more fluid-like behavior of the malign cancer cells compared to the benign cell lines. To form metastases, cancer cells have to detach from their primary tumor and invade the parenchyma and the vasculature.(Kumar and Weaver, 2009) During this process the cancer cells have to undergo large deformations, i.e. during intra- and extravasation, while they are "squeezing" themselves through endothelial cell layers. Hence, a more fluid like behavior of the cells facilitates this process that is critical for the formation of metastasis in tissues far away from the primary tumor. While a large loss tangent identifies a more fluid-like behavior it does not automatically mean that the stiffness of the cell is low. It just means that viscosity dominates over elasticity. I observed similar effects when interfering with the contractility of MDCK-II cells (see chapter 4.2), although in the case of cancer cells, the background of the observed effects might be more complicated. An increased loss tangent could be the result of their perturbed adhesion and changes in motility. Reduced adhesion could lead to a reduced cytoskeletal tension, which in turn, results in a shift to a more fluid-like or viscous behavior.

4.3.3   Conclusion

The mechanical properties of cells are governed by a multitude of passive and active elements and are far from being understood in its full complexity. Simple contact mechanical models that explain rheology over a wide range of time and length scales

cannot capture all features of the complex cellular structure. Moreover, the response of the cells to external deformation on longer time scales is influenced by biochemical and genetic adaption to the mechanical stimulus rendering the overall response even more intricate. However, it is indisputable that cancer cells and benign cells display different viscoelastic properties, which might serve as a diagnostic tool to readily identify malignant phenotypes by their mechanical signature and response to mechanical stimulation.

Here, a model-free approach based on monitoring the loss tangent is proposed that essentially represents the ratio of loss modulus to storage modulus of the probed cell and therefore quantifies energy dissipation upon deformation at different frequencies. I found that cancer cells show a substantially larger loss tangent in contrast to the benign phenotype which means that the cells behave more like fluid at smaller time scales (larger frequencies).

4.4 Cell-substrate interaction: Effect of macro-porous substrates on cellular morphology and mechanics and measurement of cell-substrate distance.

Data presented in the previous chapters demonstate that there is a strong connection between cellular morphology, cytoskeletal tension and cellular mechanics, which all depend on cellular adhesion. Most cells require adhesion for proper cell function.(Jaalouk and Lammerding, 2009) Cancer cells have lost this dependency; a property of cancer cells, which enables them to metastasize. (Wang *et al.*, 2000) In the first part of this chapter, I will examine the influence of topographical cues, which interfere with cellular adhesion and spreading, on cellular morphology, cytoskeletal arrangement and cellular mechanics of epithelial cells. In the second part, I present a new technique, which enables to measure axial distances with nanometer precision using a confocal laser scanning microscope. The technique is used to measure cell-substrate distances of different adherent cell lines and followed the spreading process of freshly seeded cells with unprecedented precision.

4.4.1 Cytoskeleton remodeling of confluent epithelial cells cultured on porous substrates

4.4.1.1 Introduction

The structure and function of eukaryotic cells heavily depend on their direct environment leading to a close coupling between cells and their surroundings. Sensing of the environment is usually accomplished through a defined molecular contact between a protein layer – the extracellular matrix (ECM) – and specified transmembrane proteins such as integrins that connect the ECM network to the cytoskeleton allowing the transmission of force.(Geiger *et al.*, 2009) Adhesion of cells is the initial step that precedes cell spreading, proliferation, differentiation and cell-cell contact formation. Cellular adhesion determines the function and fate of eukaryotic

cells to a much larger extent than initially expected. Especially environmental cues such as those emanating from the substrate itself like topography, elasticity or surface functionalization govern a large number of cellular responses encompassing cell growth, differentiation, gene expression, apoptosis all accompanied by substantial cytoskeletal remodeling. Strikingly, the differentiation of stem cells is guided by mechanical and adhesive properties of the culture dish.(Levental *et al.*, 2007) Cells are capable of sensing the underlying substrate and respond to variations in elasticity or topography as first shown by Pelham and Wang.(Pelham and Wang, 1998) The authors demonstrated that focal adhesion dynamics and the overall morphology of normal rat kidney cells and fibroblasts change dramatically, when the cells are cultured on soft polyacrylamide gels. Since then, many studies have shown an influence of substrate rigidity on cellular migration, proliferation, cell stiffness and even differentiation.(Engler *et al.*, 2006; Tee *et al.*, 2011; Trichet *et al.*, 2012; Wang *et al.*, 2000). The information about mechanical properties of the surrounding is gathered by cells via a process called mechanotransduction.(Geiger and Bershadsky, 2002;Geiger *et al.*, 2009). Cells possess many mechanisms, which enable them to react to external mechanical stimuli, which have been reviewed by Ingber.(Ingber, 2006) The mediators that are used to sense a mechanical signal depend on the cell type and the mechanical stimulus itself. For example hair cells of the inner ear sense sound waves propagating through the endolymph via specialized structures on their apical surface. Displacement of these structures opens ion channels in the cell membrane, which leads to a Ca^{2+}-influx and depolarization of the cell. However, epithelial cells also sense their mechanical environment - mostly via cell-cell or cell-substrate connections. These mechanosensory elements as well as the stereocilia in the inner ear depend on actin. The actin cytoskeleton is tightly linked to the membrane and is able to generate forces via motor proteins of the myosin-family. It is therefore conceivable that the amount of tension that can be generated due to the substrate's deformability is responsible for the integration of the mechanical signal. While the impact of soft substrates on cell morphology and more particular on cell adhesion is well investigated, less attention has been paid to substrate topography of rigid surfaces. Especially in the context of cell attachment and growth on implant materials, surface roughness and topography are decisive parameters that might increase or reduce the degree of differentiation and polarization of epithelial cells. Numerous hard materials ranging from metals to silicon are used as artificial implant materials.(Thorne *et al.*, 2007) Surface treatment to change the roughness has been proven to modulate adhesion of cells, cytokine release and gene expression of osteoblastic cells.(Ross *et al.*, 2012) Topographical effects on the nanoscale have been first addressed by Spatz and coworkers using

colloidal lithography to provide specific attachment sites for integrins in a defined geometry.(Arnold *et al.*, 2004) The study helped to shine light on the universal length scale that defines the optimal spacing of RGD sequences found in ECM proteins such as collagen to match the intrinsic spacing of integrins in the basal cell membrane. Recently, it has also been found that topographical cues can determine the fate of stem cell differentiation via focal adhesion signaling.(McBeath *et al.*, 2004; McNamara *et al.*, 2012; Teo *et al.*, 2013) The response of cells to their environment heavily depends on the cell type. So far, most studies focused on the influence of topographical cues on single cells.(Curtis and Wilkinson, 1997) Formation of an epithelial cell monolayer on structured substrates and the consequences of substrate topography on cell morphology, polarity and mechanics has only sparsely been addressed or has been neglected. In early studies, Clark and coworkers stated that the influence of substrate topography is mostly governed by the effect of cell-cell-contact mechanosensing in epithelial cells.(Clark *et al.*, 1991) However, finding the right scaffolds for epithelial tissue engineering requires a fundamental understanding how cell adhesion and mechanics are coupled to environmental cues and how cells respond collectively to changes in topography.

Here, I investigated systematically the morphological and viscoelastic properties of confluent MDCK-II cells grown to confluence on porous substrates with varying pore sizes. I found that cells appear softer and more liquid-like with increasing pore size up to 1.2 µm in diameter and start to remodel their actin cytoskeleton to span larger pores, which renders the cells smaller, higher and more ordered. At pore sizes larger than 5 µm in diameter MDCK II cells reproduce the cubic organization of the underlying substrate and also display a higher degree of polarization showing a larger number of microvilli. The study shows how subtle changes in substrate topography substantially influence the morphology and mechanics of epithelial cell layers by forcing the cell to remodel the actin cytoskeleton.

4.4.1.2   Results and Discussion

MDCK-II cells were grown to confluence on substrates displaying regular pores ranging from 0.45 µm to 5.5 µm in diameter. Morphology, cytoskeleton organization and viscoelasticity of MDCK-II cells were investigated to quantify how substrate topography translates into cellular structure and mechanics. Notably, MDCK-II cells grew on all substrates to confluence and span the pores.

Morphology of MDCK-II cells grown on flat and porous substrates:

MDCK-II cells belong to normal epithelia. They polarize when cultured on a petri-dish and exhibit a high density of cell-cell contacts (tight junctions), which is also expressed in a high barrier resistance (R_b) of 30 Ω × cm^2 measured by electric cell-substrate impedance sensing.(Wegener *et al.*, 2000) Figure 4.4.1 shows the influence of substrate topography on the morphology of confluent MDCK-II cells. MDCK-II cells grown on the gold coated, non-porous glass substrates possess an ordinary cobblestone-like morphology with well-developed cell-cell contacts and have a size of approximately 20 × 20 µm^2. The height profile shows rather flat cells with a height difference of 1.5 µm from cell-cell contacts to their highest point at the center of the cell. With increasing pore size from 0.45 µm to 5.5 µm an increase in the average height and a decrease in the spreading area of the MDCK-II cells can be observed.
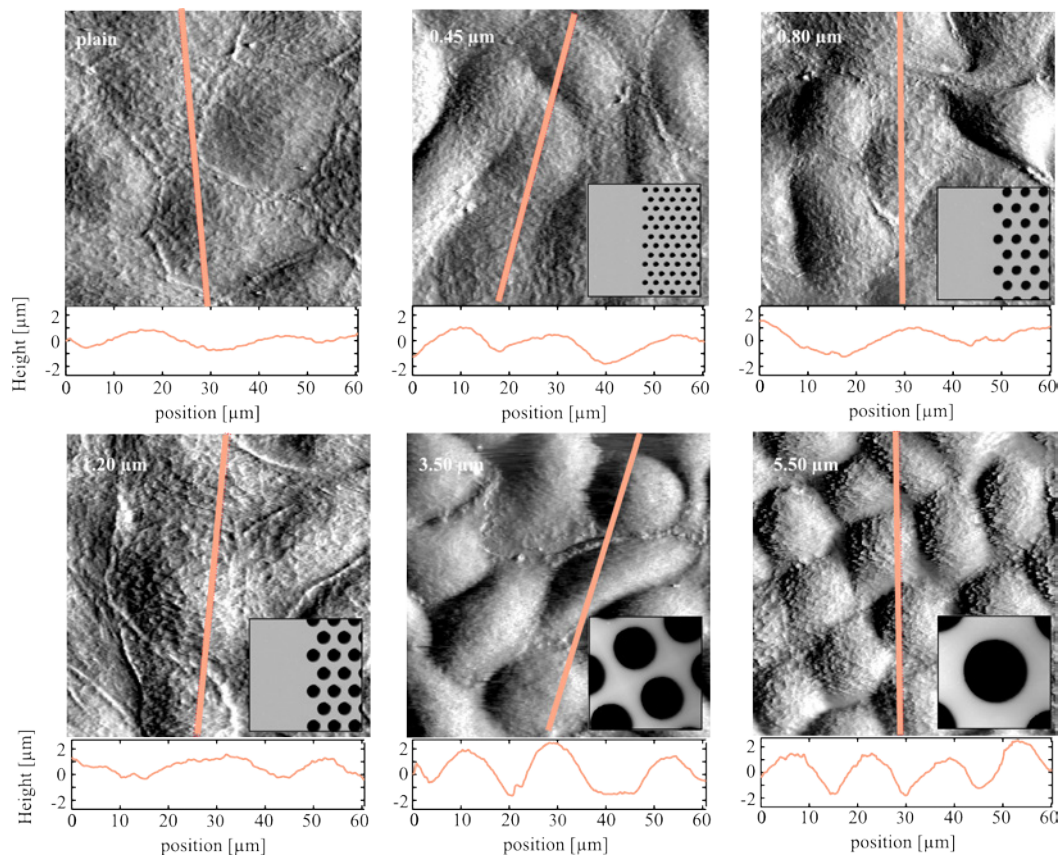
Figure 4.4.1: Morphology of MDCK-II cells grown on substrates with different pore sizes. Images show AFM-deflection images of the cell surface of living MDCK-II cells. The diagrams show height profiles of the cells shown in the picture (red line, average over 5 lines). Inlets show 10 × 10 µm^2 AFM-height images of the pores (approx. 2-fold magnification compared to the corresponding deflection images of the cell surface). Images of the pores have been measured by Matthias Büchsenschütz-Göbeler (I. Institute of Physics, Georg-August-University, Göttingen, Germany)

When cells are grown on a substrate with a pores size of 5.5 µm in diameter, they exhibit a height difference from their lowest point in the cell periphery to their highest point of more than 3 µm. Additionally, the cell size decreases to an area of 13 × 13 µm^2, which might be an effect of a decrease in spreading rate due to the limited surface area and/or an increase in proliferation rate like it was previously shown for hepatocytes cultured on mesoporous anodized aluminum oxide (AAO).(Hoess *et al.*, 2012) Hoess *et al.* used substrates with pore sizes ranging from 57 to 213 nm in diameter and found that the cells grown on larger pore diameters show a faster proliferation rate, which might also be the case in our experiments although the pores used in this study are in the macroporous range. An explanation for an increased proliferation could be a more *in-vivo* like situation concerning the nutrient supply from the basal membrane when cells are cultured on porous material. A decrease in spreading rate and the overall shape of the cell might also be explained by surface energy considerations. On a flat hydrophilic surface the reduction in surface free energy of a cell will be large. Thus, the contact angle will be small, which facilitates spreading of the cell. By removing 30 % of the hydrophilic surface the reduction in surface free energy will be smaller and the contact angle will become larger, which in turn leads to a higher cell occupying a smaller area (see Figure 4.4.1 and Table 4.4.1).

Table 4.4.1 Height *h* of MDCK-II cells cultured on porous substrates determined from confocal laser scanning images of the actin cytoskeleton. Mean values were calculated from 20 positions per category.

	$h \pm$ **STD**/ **µm**
Flat	5.3 ± 0.7
0.45 µm	5.1 ± 0.8
0.80 µm	4.3 ± 0.7
1.20 µm	6.3 ± 0.8
3.50 µm	5.6 ± 1.0
5.50 µm	5.7 ± 0.8

Furthermore, I found a cubic pattern in the cell layer organization, when cells are grown on 5.5 µm pores with cubic pore pattern. The cubic pattern of the cells can also be found by 2D-FFT analysis of the corresponding height image of the image in Figure 4.4.1 (see Figure 4.4.2).
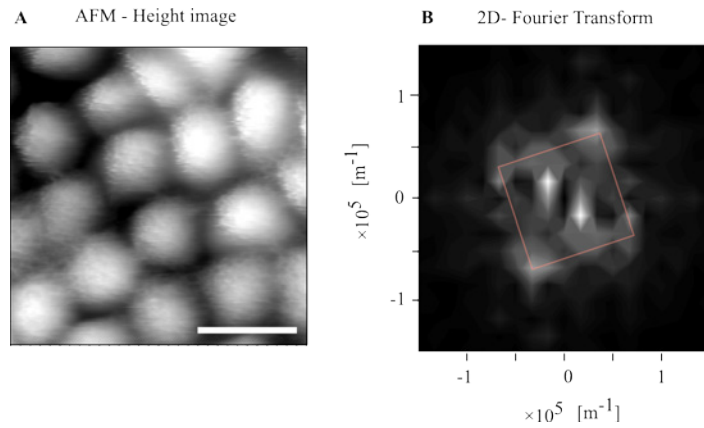
Figure 4.4.2: A AFM-height image of MDCK-II cells grown on 5.5 µm pores. Scale bar: 20 µm **B** 2D-FFT of the AFM-height image of MDCK-II cell grown on 5.5 µm pores with cubic pore pattern shown in A. The image shows a cubic orientation of cells. The maxima at the corners correspond to a distance of 13.3 µm. The red square is only a guide to the eye.

Another effect of culturing cells on macroporous substrates is, that the cell-cell contacts become less pronounced in AFM-images. In general, the bulge at the cell-cell interface in AFM-images is an effect of the relative incompressibility of the cortical actin. Thus, a lack of this structure in AFM-images might be a hint to an impaired actin cytoskeleton arrangement in the lateral regions. A similar trend has been observed for vascular endothelial cells.(Thakur *et al.*, 2012) It should be noted that it is not possible to determine the overall cell height with AFM-contact imaging but only the height of the apical cap of the cell. The overall height was determined from confocal microscopy images of the actin cytoskeleton.

Structure of the actin cytoskeleton:

Actin filaments are stained using AlexaFluor546-labelled phalloidin and are imaged by confocal laser scanning microscopy. Figure 4.4.3 shows the structure of the actin cytoskeleton at the basal level of MDCK-II cells cultured on substrates with different pore sizes. On the flat surface, the actin cytoskeleton is well developed (Figure 4.4.3 A). A large amount of stress fibers, which traverse the entire length of the cells, is observable. In contrast, cells grown on pores show reduced fluorescence intensity on the porous regions (Figure 4.4.3 B - F). The number of stress fibers traversing the cell decreases with increasing pore size as well.
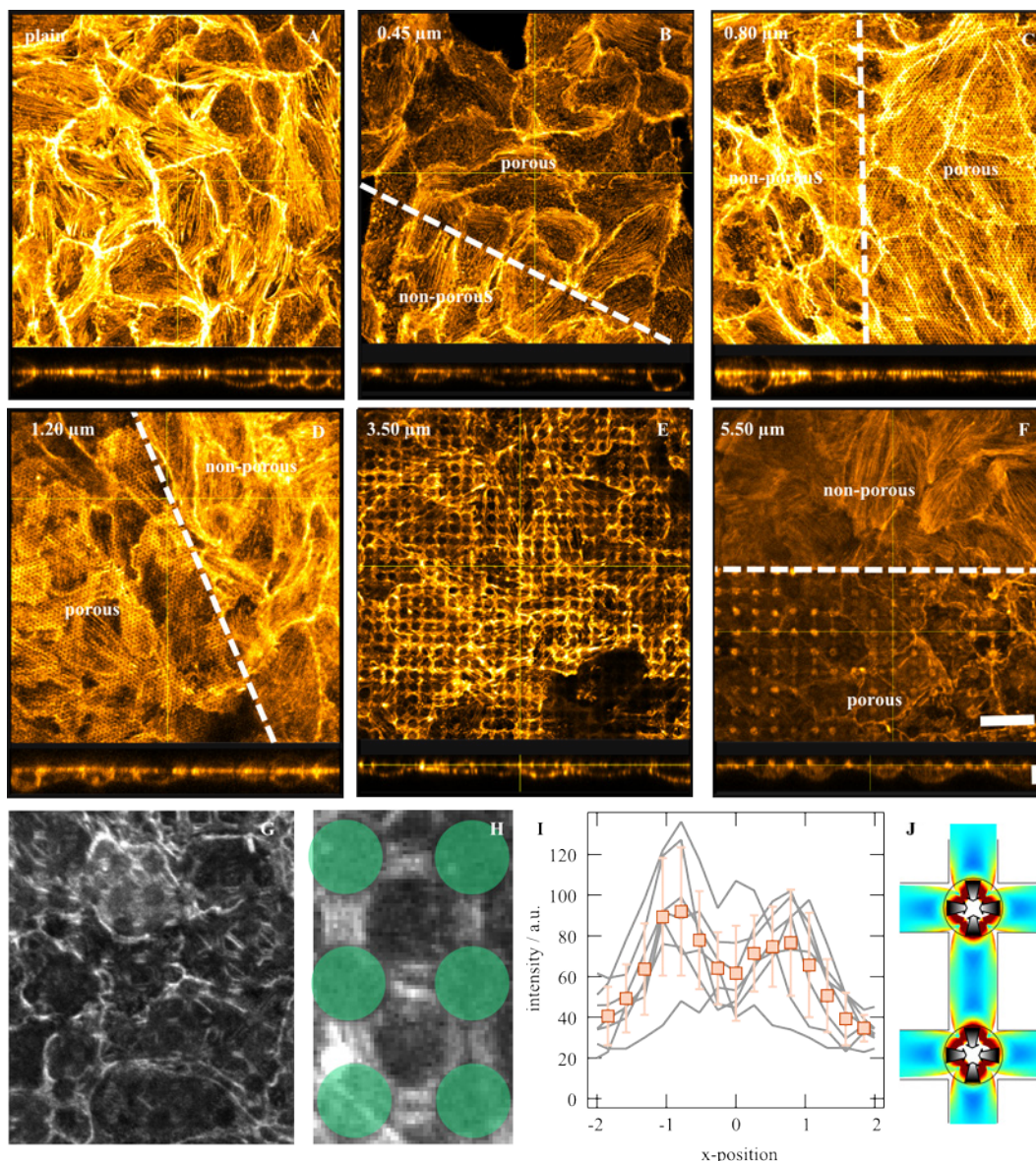
Figure 4.4.3: A-F Confocal micrographs of MDCK-II cells grown on substrates with different pore sizes. Images show the actin cytoskeleton (Alexa-Fluor546-labelled phalloidin, Invitrogen) of the cells on the level of the pores (pseudocolored) and orthogonal views (scale bar: 20 μm). **G** Confocal micrographs of the actin cytoskeleton of MDCK-II cells grown on 5.5 μm substrates above pore level (grey scaled) showing the stress fibers, which connect actin aggregates of actin inside the pores **H** Magnification showing area of 6 pores. Green circles mark the position of the pores **I** Line profiles of the interconnections between pores shown in H (grey) and mean intensity value (red, mean ± std). **J** Finite element simulation of a thin elastic sheet simulating the actin cytoskeleton between two pores. Pores are simulated by holes in the sheet at the crossing. Black lines indicate shape of the sheet before deformation. An inward directed pressure (arrows) is applied to the pore boundaries causing deformation and occurrence of stress. Blue color indicates low stress values, green and yellow intermediate stress values and red high stress values).

Strikingly, we observe an accumulation of actin inside the largest pores (5.5 μm and occasionally also in 3.5 μm pores), which is expressed in periodically occurring bright spots (Figure 4.4.3 F). Pores covered by one cell are interconnected by thick actin fibers producing a square pattern, where the pores are located in the corners (see

4.4.3 G). Another interesting fact is, that numerous actin aggregates are interconnected by *two*, thick stress fibers (Figure 4.4.3 G-I). To explain this phenomenon, I conducted finite element simulations (Figure 4.4.3 J). The actin cytoskeleton is simulated by a cross shaped elastic material. The porous region is represented by the absence of the material. When applying an inwards-directed homogenous pressure to the pore boundaries, the edges of the interconnections are the regions, which exhibit the highest stress values. This means that in a cell these areas need to be strengthened. As one observes this phenomenon, it is also very likely, that there is strong inwards-directed force due to the numerous filaments spanning the pores applying a large tension to the actin-network. This high tension also requires a strong adhesion of the cells to the substrate in proximity to the pores. In epithelial cells adhesion to the substrate is mainly realized by focal adhesions. Wu *at el.* observed an accumulation of the focal adhesion associated protein vinculin along the pore edges, when they cultured preosteoblastic cells on 6 µm pores made of poly(ε-caprolactone), although they did not observe actin aggregates inside the pores. (Wu and Wang, 2012)

To confirm and quantify the previous findings of a reduced or remodeled actin cytoskeleton in cells cultured on porous substrates, scanning electron microscopy was used (Experiments performed by Matthias Büchsenschütz-Göbeler, I. Institute of Physics, Georg-August-University, Göttingen, Germany). By rinsing the samples in a detergent solution before fixation and dehydration, I was able to uncover the cytoskeleton of MDCKII-cells. Analysis of the filament thickness confirms that predominantly actin filaments are visible in the electron micrographs.
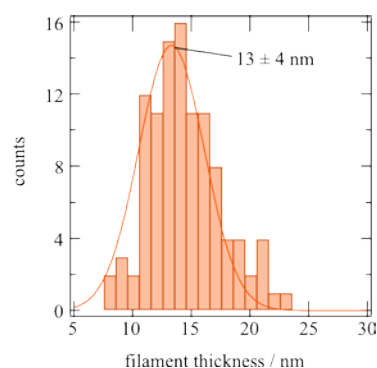
Figure 4.4.4: Analysis of thickness of cytoskeletal elements observed in scanning electron micrographs. (Analysis has been perfomed by Matthias Büchsenschütz-Göbeler, I. Institute of Physics, Georg-August-University, Göttingen, Germany)

The filaments have a thickness of 13 ± 4 nm, which corresponds well to the expected thickness of actin fibers covered by a thin gold layer of approx. 5 nm on the filaments (see Figure 4.4.4).
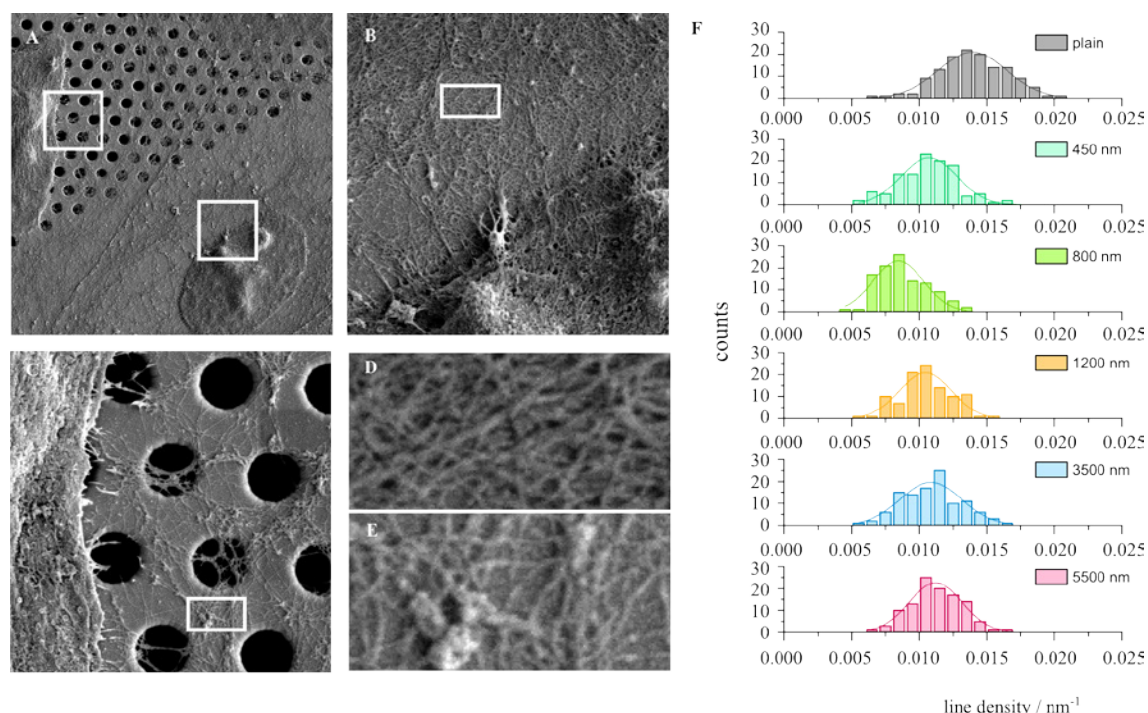
Figure 4.4.5: Scanning electron micrographs of the cytoskeleton of MDCK-II cells grown on a porous substrate (0.8 µm pores). **A** overview of the area. White rectangles mark the areas shown in **B** and **C**. **D** shows the area marked with the rectangle in B. **E** shows the area marked by the rectangle in C. **F** line densities of actin cytoskeleton for MDCK-II cells grown on substrates with different pore sizes obtained from scanning electron micrographs. (Imaging and data analysis of samples has been performed by Matthias Büchsenschütz-Göbeler, I. Institute of Physics, Georg-August-University, Göttingen, Germany)

Figure 4.4.5 A shows a representative scanning electron micrograph of MDCK-II cells grown on a substrate with 0.8 µm pores. In Figure 4.4.5 B and C the perinuclear region of a cell grown on the flat part of the substrate and of a cell grown on the porous part can be seen. A dense network traverses the whole cell. Magnifications are depicted in Figure 4.4.5 D and E. In the case of the cell grown on the porous part the network appears quite loose (Figure 4.4.5 C and E). Additionally, the line density of the actin network was determined. The distribution of line densities as a function of substrate topography is shown in Figure 4.4.5 F. The mean values of the line densities of MDCK-II cells cultured on porous substrates can also be found in Table 4.4.3. The line density allows a rough estimate of the network density. A minimum in the line density of actin filaments is observed for cells grown on the 0.8 µm pores. Cells cultured on a flat support and on larger pores exhibit a significantly denser network as the line density is higher compared to the cells on 0.8 µm pores. The value of 0.014 nm^{-1} for cells

cultured on a flat surface corresponds to an average filament to filament distance of 71 nm, which is in good agreement with mesh sizes in the cortical actin network found for other cells (Salbreux *et al.*, 2012). Micrographs of cells grown on all different substrates can be found in Figure 4.4.6. The images show that in all cases the pores were covered by the actin network.
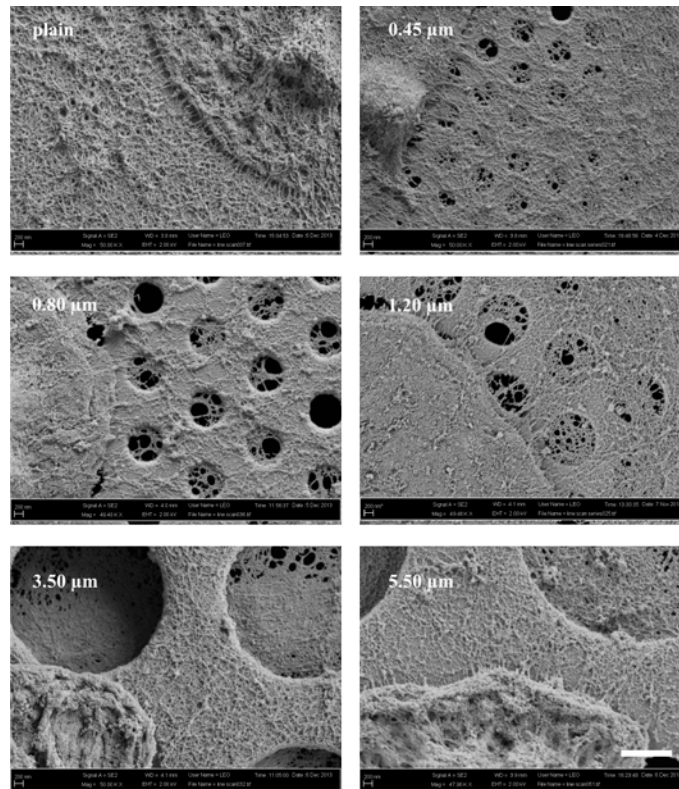
Figure 4.4.6: Representative scanning electron micrographs of the cytoskeleton of MDCK-II cells grown on porous substrates with different pore radii. The plasma membrane was removed by rinsing the sample in a Triton-X100 solution. (Samples were imaged by Matthias Büchsenschütz-Göbeler, I. Institute of Physics, Georg-August-University, Göttingen, Germany)

In the case of the larger pores, the actin network is located a bit under the plane of the pore rims. The reason for this might be that the cells can extend into the pore interior (wetting the pore walls) if the pores are large enough (see also Scheme in Figure 4.4.13).(Sandmann *et al.*, 2014)

Cellular mechanics:

To determine the influence of different pore sizes on cellular mechanics AFM force indentation and AFM-based microrheological experiments were conducted (experiments on non-porous as well as on pores up to 3.5 µm in diameter were

conducted by Helen Nöding, Institute of Physical Chemistry, Georg-August-University, Göttingen, Germany). Force-distance experiments are described quantitatively using a modified liquid droplet model first introduced by Sen *et al.* and expanded by Pietuch *et al.* as this model has been shown to deliver more universal mechanical parameters compared to the Hertz, Sneddon or comparable contact mechanical models, especially, when it comes to different indenter geometries.(Pietuch *et al.*, 2013; Pietuch and Janshoff, 2013; Sen *et al.*, 2005) The liquid droplet model assumes that the cell behaves as an isotropic elastic body with a constant surface tension. The restoring force originates from a tension T, which is the sum of the cortical and the membrane tension T_0 and a contribution from stretching of the plasma membrane. The contribution of stretching to the tension is dependent on the projected cell surface area A_0 and the area compressibility modulus K_A, which needs to be replaced by the apparent area compressibility modulus $\tilde{K}_A$, if the projected cell surface area is smaller than the actual cell surface area due to folds and wrinkles in the membrane in the nanometer scale (see also chapter 3.9.3)

$$T = T_0 + \tilde{K}_A \frac{\Delta A}{A_0}$$
(4.3)

and

$$\tilde{K}_A = K_A \frac{A_0}{A_0 + A_{ex}} \ .$$
(4.4)

A_0 is the projected cell surface area before indentation, ΔA is the change of surface area due to stretching and A_{ex} is the area of the excess membrane. If the excess cell membrane stored in folds like caveolae or microvilli is very small $\tilde{K}_A$ approaches K_A. T_0 dominates the tension at low indentation depth, while at large strains, stretching of the membrane becomes the main contributor to the overall tension – a consequence of the inextensibility of lipid bilayers. As a result, the restoring force F increases nonlinearly with the indentation depth. An overview of the model is given in chapter 3.9.3.
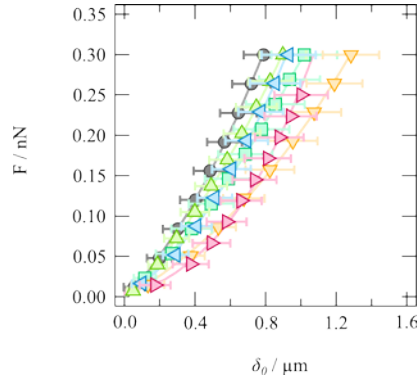
Figure 4.4.7: **A** Averaged force-distance curves of MDCK-II cells grown on substrates with different pore diameters measured with an indentation velocity of 3.0 µm/s (markers (mean ± standard deviation), ● flat (n=92), ■ 0.45 µm pores (n=83), ▲ 0.80 µm pores (n=69), ▼ 1.20 µm pores (n=48), ◄ 3.50 µm pores (n=68), ► 5.50 µm pores (n=66)). Force distance curves were fitted using the liquid droplet model (solid lines).

To fit the force-distance curves using the liquid droplet model the projected cell surface area needs to be calculated using the parameterization described by Sen *et al.*.(Sen BJ 2006) The radius of the cap (apical surface of cells) R_1 and the contact angle φ are obtained from AFM-images (see Figure 4.4.1).

Table 4.4.2: Input parameter R_1 (cell radius at the basis of the apical cap) and φ (contact angle) of the liquid droplet model fit estimated from AFM height images (see chapter 4.4.1.2).

Substrates	Liquid droplet model input parameters	
	R_1 / µm	φ / °
Flat	35	20
0.45 µm	17	30
0.80 µm	25	20
1.20 µm	16	25
3.50 µm	17	35
5.50 µm	10	40

The values of R_1 and φ used to describe the apical cap of MDCK-II cells grown on porous substrates can be found in Table 4.4.2.

Assuming that both, the curvature and the volume, stay constant during indentation, one can calculate the restoring force F for different indentation depths. The mechanical parameters T_0 and $\tilde{K}_A$ can be obtained by fitting the result to the measured force-indentation curves. Figure 4.4.7 shows averaged force-indentation curves for MDCK-II cells cultured on substrates with pore-sizes ranging from 0.45 µm to 5.5 µm and on a

flat support as a reference. I observed that cells grown on a flat surface show a steeper increase of the force with increasing indentation depth compared to cells on porous substrates. The weakest increase can be found for cells grown on the substrate with a pore size of 1.2 µm in diameter.

At small indentation depth cells grown on larger pores show a weaker initial increase of force. This observation directly corresponds to changes in the tension T_0, which comprises the membrane and the cortical tension as the dominating contribution and thus the response to externally applied forces (eq. 4.3) at low indentation depth. T_0 generally decreases when cells are cultured on substrates with increasing pore diameter of the culture substrate. In contrast, the apparent area compressibility modulus $\tilde{K}_A$ shows a minimum at a pore diameter of 1.2 µm (see Figure 4.4.6 and Table 4.4.3). This behavior can be directly guessed from the averaged force-indentation curves as the slope of the force-indentation curves at high indentation depths for cells on larger pores is lower than that of cells cultured on the plane surface (Figure 4.4.6). The tension T_0 of 0.35 mN × m^{-1} observed for cells grown on a flat surface is in excellent agreement with the tension of 0.37 ± 0.04 mN × m^{-1} found by Pietuch *et al.* for MDCK-II cells cultured on a petri dish.(Pietuch *et al.*, 2013) The reduction of tension in cells cultured on pores could eventually be the result of a reduced spreading area and an impaired actin cytoskeleton in cortical regions (lack of bulge at the cell-cell interface), which is responsible for tension generation via motor proteins, in particular myosin II. While a well-spread cell exhibits a high tension, cells showing a disturbed spreading behavior won't be able to generate a high contractile force. Pietuch *et al.* could show that the cortical tension of freshly seeded cells is low. With time, the cells started to spread and along with the proceeding in spreading the tension of the cell increased up to a constant value.(Pietuch and Janshoff, 2013) This also fits to the observation that stress fibers, which are also important for the overall contractile tone of the cell, seem to be shorter or less pronounced on porous substrates. On the other side, also passive material properties explain the observed trends. Adhesion of cells exerts tension in the cortex displayed in a more spread morphology with small curvature. The adhesion to the substrate stretches the cells because volume is conserved and as a consequence the cell tension increases. Looking at the apparent area compressibility modulus $\tilde{K}_A$, I found a minimum value at a pore size of 1.2 µm. Cells grown on a flat surface exhibit the highest value. As discussed by Pietuch *et al.* $\tilde{K}_A$ could be a measure for additional membrane area stored in folds, protrusions and wrinkles like caveolae (basal) or microvilli (apical). The cell itself uses these membrane reservoirs to increase its reactive surface on the one

side but also to regulate its tension T as a response to changed environmental conditions and to prevent bilayer rupture. A decrease in $\tilde{K}_A$ could be elicited by an increased number of microvilli, when MDCK-II cells are grown on porous substrates. This effect has previously been observed by Hoess and coworkers.(Hoess *et al.*, 2012) The increased nutrient supply via the pores might enhance the functionality and polarity of epithelial cells, which in turn might lead to a larger number of microvilli on the apical membrane.
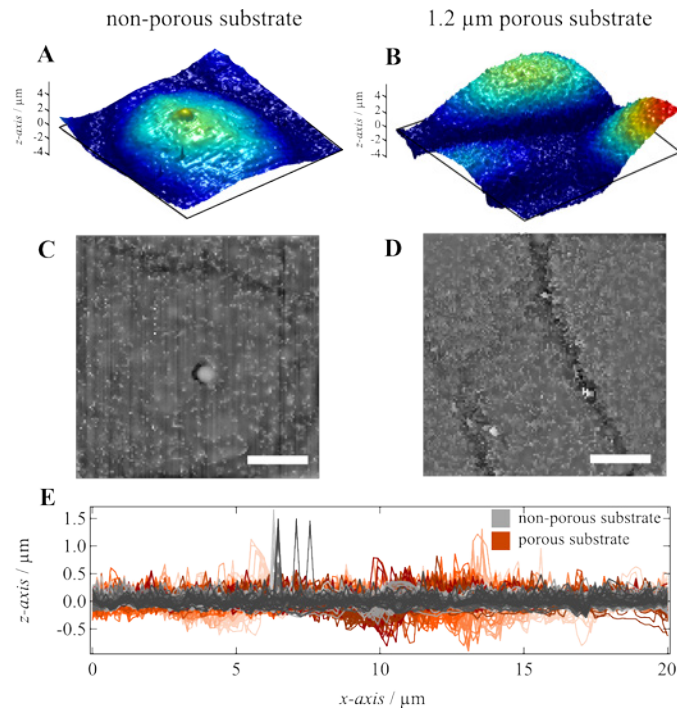
Figure 4.4.8: A and **B** scanning ion conductance micrographs showing the topography of the surface of MDCK-II cells either grown on a petri-dish (A) or on a substrate with 1.2 µm pores (B). Each image has a scan size of 20×20 µm^2 at 128×128 pixels. **C** and **D** are corresponding images of the surface microstructure, which have been calculated from the topography images by subtraction of a 2D-moving average with a box size of 11×11 pixels. **E** shows images C and D along the y-axis. Scale bar: 5 µm.

Comparison of scanning ion conductance micrographs that demonstrate real non-contact measurements of PFA-fixed MDCK-II cells grown either on a petri dish or on a substrate with 1.2 µm pores also reveals an increased surface roughness of the cells grown on the solid support (Figure 4.4.8) supporting the theory of an increased number of microvilli.(Korchev *et al.*, 2000)

Time-dependent or frequency-dependent mechanical data are obtained from AFM-based microrheological experiments explained before (see chapters 3.9.4, 4.2 and 4.3). In Figure 4.4.9 A and C both, the storage modulus G' and the loss modulus G'', are shown as a function of the oscillation frequency f the loss modulus for MDCK-II

cells cultured on porous substrates. In general, G' increases according to a weak power-law with the frequency (linear increase in a double logarithmic diagram), whereas G'' shows a stronger dependency on the oscillation frequency, which leads to a crossing point of G' and G'' at a certain frequency.
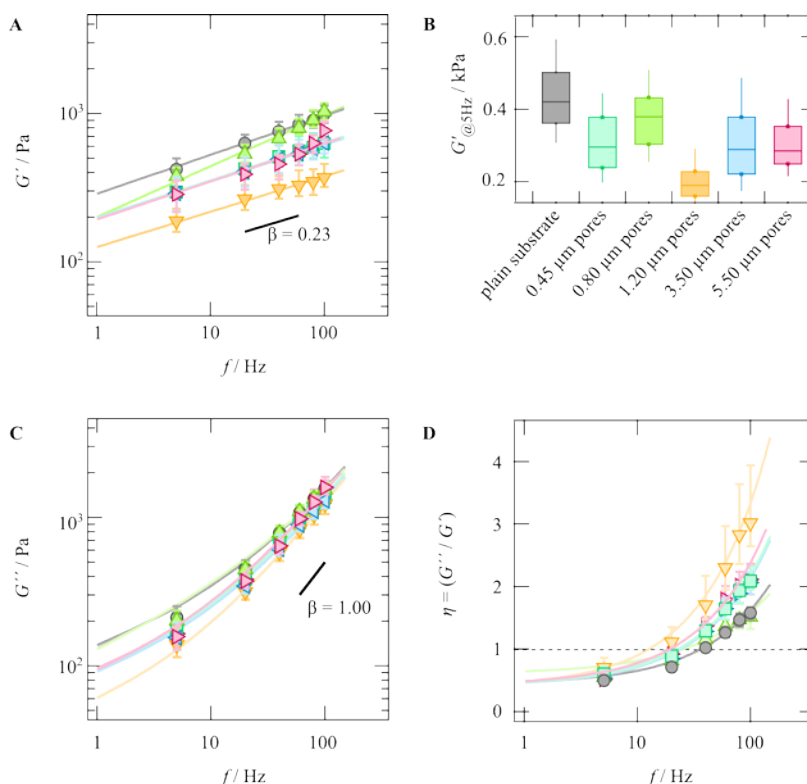
Figure 4.4.9: A Frequency dependency of the real part G'' of the complex shear modulus. Black line indicates a power law dependency with a power law coefficient β of 0.23 **B** Box plot of the real part of the complex shear modulus (G') of MDCK-II cells at an oscillation frequency of 5 Hz in dependency of the pore size. (Median values with quartiles and 10% and 90% whiskers) **C** Frequency dependency of the imaginary part G'' of the complex shear modulus. Black line indicates a power law increase with a power law coefficient β of 1.00 **D** Loss tangent η as a function of oscillation frequency. Markers (median ± quartiles: ● flat (n=175), ■ 0.45 μm pores (n= 160), ▲ 0.80 μm pores (n=126), ▼ 1.20 μm pores (n=110), ◄ 3.50 μm pores (n=135), ► 5.50 μm pores (n=137)) show the values measured by AFM-based microrheological experiments. Lines show the power-law structural damping fits of the frequency dependent complex shear modulus.

At this crossing point, the oscillation of $F(\omega)$ and $\delta(\omega)$ are 45° (or $\pi/2$) out of phase and both quantities, G' and G'', exhibit the same value. Therefore, the loss tangent ($\eta = G''/G'$) equals 1 at this frequency. A loss tangent smaller than 1 means that $G' > G''$ and the elastic properties of the sample dominate the rheological behavior (and the phase shift $\Delta\varphi$ between F and δ is smaller than 45°). Inversely, if $G' < G''$, the loss tangent exceeds 1 and the viscous properties dominate the rheology of the cells displaying a more fluid-like behavior. For MDCK-II cells grown on a flat surface the

crossing point of G' and G'' is found at a frequency of around 40 Hz. For cells cultured on porous substrates the frequency, at which G' and G'' are equal, is decreasing to lower frequencies. G'' is largely unaffected by the substrate. Thus, cells cultured on porous substrates show a more fluid-like behavior at smaller frequencies compared to cells on a non-porous support. An explanation might be, that G' is mainly affected by the elastic properties of the membrane as well as the underlying actin cortex, which is expressed by the apparent area compressibility modulus. Thus, it is not surprising that $\tilde{K}_A$ and $G'(5\,\text{Hz})$ share a common trend, especially considering that the microrheolgical experiments are conducted at an indentation depth, where the force response is mainly governed by $\tilde{K}_A$. Interestingly, the observed line densities of actin filaments (Figure 4.4.5 F) show a similar trend as $\tilde{K}_A$ and G' leading to the conclusion, that the actin cytoskeleton is the main contributor to the two mechanical parameters (Figure 4.4.11). By fitting the power-law structural damping model, first used by Fabry *et al.* to describe the spectra of G^* in cellular microrheology, to the measured rheological data, power-law coefficients between 0.23 and 0.25 were found for all samples (see Table 4.4.3). (Fabry *et al.*, 2001) Only cells cultured on 0.8 µm pore size substrate show a higher power-law coefficient of 0.31.

Table 4.4.3: Mechanical parameters of MDCK-II cells grown on porous substrates. T_0 and $\tilde{K}_A$ are obtained from liquid droplet model fit of force indentation curves. G_0, α and μ are determined by fitting the power-law structural damping model to G' and G''. Line densities of cytoskeletal filaments have been calculated from SEM images.

	Liquid droplet model		AFM-based microrheology			Image analysis
	T_0 / mN × m^{-1}	$\tilde{K}_A$ / mN × m^{-1}	$G_0 \pm$ SE/ Pa	$\alpha \pm$ SE/	$\mu \pm$ SE/ Pa×s	line dens. $\pm$ STD / nm^{-1}
Flat	0.35	0.10	188 ± 21	0.25 ± 0.02	1.86 ± 0.09	0.014 ± 0.005
0.45 µm	0.27	0.02	129 ± 9	0.25 ± 0.01	1.81 ± 0.04	0.011 ± 0.004
0.80 µm	0.31	0.03	127 ± 26	0.31 ± 0.04	1.67 ± 0.17	0.008 ± 0.003
1.20 µm	0.17	0.01	85 ± 8	0.23 ± 0.02	1.79 ± 0.04	0.010 ± 0.004
3.50 µm	0.23	0.08	135 ± 16	0.23 ± 0.02	1.72 ± 0.06	0.011 ± 0.005
5.50 µm	0.10	0.05	120 ± 37	0.26 ± 0.05	1.96 ± 0.17	0.011 ± 0.004

Table 4.4.3 summarizes all fitting parameters of the power-law structural damping model. The scaling factor G_0 shows a similar trend as the storage modulus. Cells on a flat substrate exhibit the highest value (188 ± 21 Pa), cells grown the substrate with the 1.2 µm pores exhibit the lowest value (85 ± 8 Pa). The determined Newtonian viscosity is largely independent of the substrate. Values ranging from 1.7 ± 0.2 Pa × s to 2.00 ± 0.2 Pa × s are observed. Although G' of MDCK-II decreases, when cultured on porous

substrates, the power-law exponent is nearly the same for all samples. One would expect that a decrease in cell stiffness leads to a higher power-law exponent and vice versa, while the loss tangent, especially in the low frequency regime, stays constant. This behavior has been observed for several cell-types treated with various drugs, which either increased the cell's tension leading to a smaller power-law exponent or decreased its contractility by disruption of the actin cytoskeleton leading to a higher power-law coefficient (see also chapter 4.2). In fact, the only parameter of the power-law structural damping model that is influenced by treatment of cells with drugs perturbing the contractility of the actin cytoskeleton is the power-law coefficient.(Fabry *et al.*, 2001; Yamada *et al.*, 2000) Fabry and coworkers interpreted this in means of soft glassy rheology. Soft glassy rheology predicts power-law structural damping behavior in the case of small deformation and for intermediate time scales. Thus, the power-law coefficient becomes a quantity describing the effective temperature of the material. In cells, this effective temperature is thought to be a result of active, energy-consuming processes involved in contractility and cytoskeletal rearrangements keeping the elements out of their equilibrium position. In my experiments, I find that the power-law exponent remains nearly constant for all samples, while the scaling factor G_0 is changing with the topography of the substrate. My interpretation is that passive mechanics, i.e. elastic properties of the cortex like $\tilde{K}_A$ are changing, while active processes or the relative degree of crosslinking in the network, which contribute to cellular rheology, remain unchanged. As observed before for $\tilde{K}_A$, a minimum of G' can be found for cells cultured on substrates with a pore size of 1.2 µm (see Figure 4.4.11)
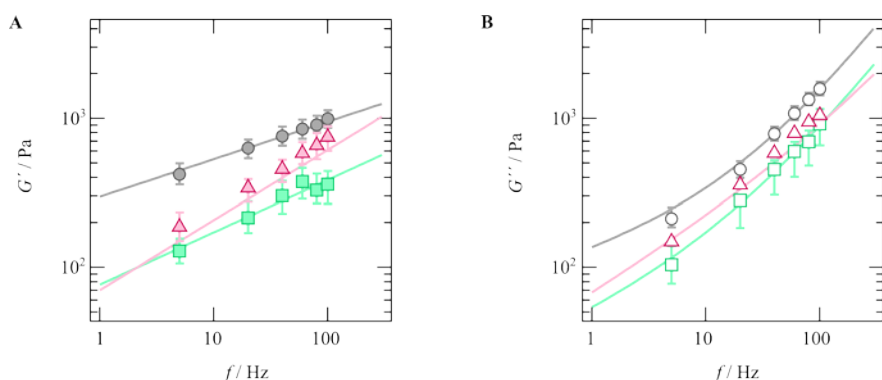
Figure 4.4.10: Influence of Cytochalasin D on the real part (**A**) and the imaginary part (**B**) of the complex shear modulus of MDCK-II cells grown on a flat surface and 1.2 µm porous substrate (● flat, ■ flat Cytochalasin D treated, ▲ 1.2 µm pores Cytochalasin D treated).

To prove if the passive elastic contributions of the actin cytoskeleton are responsible

for the observed effects, I treated cells on pores and on a flat substrate with Cytochalasin D (see Figure 4.4.10). By administration of Cytochalasin D the actin cytoskeleton is disrupted (see chapter 4.2). As expected for this case, G' decreases and shows a stronger dependency with the frequency. G'' is also reduced at all frequencies. Comparison of cells grown on the flat surface and on the porous support shows that G' is reduced in both cases. Especially at low frequencies both samples show comparable values in G'. At higher frequencies, cells on flat supports show a reduced storage modulus compared to cells on a porous substrate. Another hint, that the pure amount actin and not the contractile tone of the cytoskeleton itself is responsible for the decrease in G' or G_0, respectively, is given by the observed line densities of cells cultured on the different substrates. Like in G_0, a minimum of line density is found for intermediate pore diameters (Table 4.4.3 and Figure 4.4.5 F). Figure 4.4.11 shows that a correlation between the apparent area compressibility modulus $\tilde{K}_A$, line density of actin filaments and storage modulus G_0 exists. For every parameter a minimum is found for intermediate pore diameters.
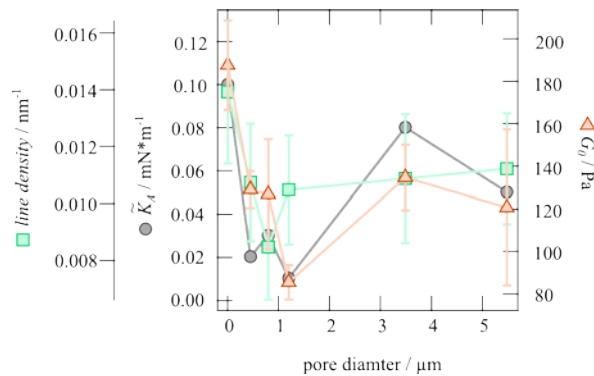
Figure 4.4.11: $\tilde{K}_A$ (●) shows a correlation with the scaling factor of the power-law structural damping model G_0 (▲, ± standard error) and the measured line density of the cytoskeleton (■, ± standard deviation).

I conclude that the main effect on cell mechanics that I observe, when cells are cultured on solid supports, results from remodeling of the actin cytoskeleton. Other contributions might come, as discussed before, from membrane folds like caveolae or microvilli serving as a membrane reservoir to buffer tension exerted on the cells. Since tension is lowest in cells on largest pores, $\tilde{K}_A$ rises, e.g. the membrane excess area decreases, to compensate tension loss.

4.4.1.3   Conclusion

The extracellular environment is an essential mediator of cellular structure and function by providing biochemical and mechanical stimuli to influence single and collective cell behavior. Through adhesion, cells sense the mechanical properties of the environment and translate this information into a signaling cascade, which regulates cellular responses such as spreading, migration and growth. While abnormal mechanotransduction is known to be associated with a number of diseases such as asthma or cancer the robustness of how cells respond collectively to such stimuli is largely unexplored. Here, I provide structural and mechanical information about the impact of pore size on the mechanical response of confluent epithelial cells to substrates with defined topography. Interestingly, I found that the cells can distinguish even subtle changes in pore size and develop strategies to remodel their cytoskeleton in order to explore substrates with large pores that would prevent sufficient adhesion area otherwise by spanning and reinforcing the cytoskeleton of the free standing part. The observation that cells behave more liquid-like with a maximum of excess membrane area on porous substrates up to pores sizes of 1.2 µm in diameter in comparison to cells on flat surfaces can be explained by the reduced overall surface area provided by the substrates. The cells invade into the pores, form a contractile actin clot and thereby manage to maintain an intact cell monolayer covering the entire area.
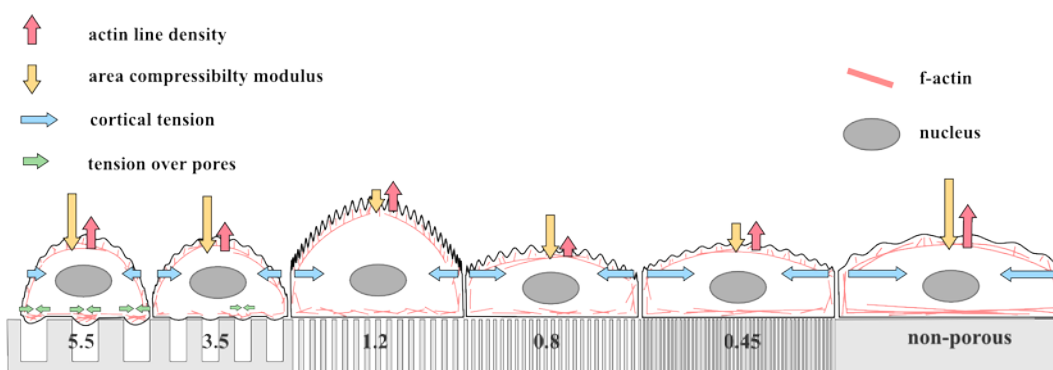
Figure 4.4.12: Scheme compiling the effects of culturing MDCK-II cells on macroporous substrates. Cells decrease their spreading area with increasing pore diameter. This goes along with a reduction in cortical tension, which might be a consequence of a reduced contractile tone of the cell due to fewer and shorter stress fibers. The area compressibility modulus shows a minimum at 1.2 µm pores, which is thought to be the result of an increased membrane area due to an increased number of microvilli. Furthermore, on large pores the cells produce thick actin aggregates over the pores, which generate high tension.

The tension of the apical cap decreases only slightly with pore size, which is in good agreement with tension homeostasis regulated by the cell's surface area. The cells cultured on larger pores compensate the loss in membrane tension by reducing their excess area to maintain a constant value for T_0. Interestingly, the cell size and arrangement reproduced to the underlying porous structure, which I attribute to a self-organization driven by minimizing the area of free-standing membrane over pores. The effect of culturing MDCK-II cells on substrates with different pore sizes is summarized in Figure 4.4.12.

4.4.2   Metal-induced energy transfer for live cell nanoscopy

4.4.2.1   Introduction

Previous chapters highlighted the importance of cell-substrate interactions for many cellular processes. Today, there are only few techniques, which allow optical imaging of cell-substrate interaction with high precision like total internal reflectance (TIRF) microscopy or fluorescence interference contrast (FLIC) microscopy.(Braun and Fromherz, 1997; Mattheyses *et al.*, 2010) However, all of the mentioned methods have drawbacks: TIRF microscopy requires an equal distribution of fluorophores to deliver quantitative results and FLIC is dependent on special substrates. Additionally, the lateral resolution of FLIC is rather small. Here, we present a method, which allows quantitative imaging of the cell-substrate interface with axial nanometer precision. The method is based on resonant energy transfer from an donor molecule to an acceptor, i.e. a metal layer, and is similar to the well-known Förster resonance energy transfer (FRET) describing the energy transfer from a fluorescent donor molecule to an acceptor molecule.(Forster, 1948) In FRET, the transfer efficiency is dependent on the sixth power of the distance between donor and acceptor molecule. This strong dependency between transfer efficiency and distance made FRET one of the most powerful fluorescence-based methods in biophysical and physicochemical research for measuring distances on a molecular scale. Although recent years have seen a burst of new super-resolution methods in fluorescence microscopy, their resolving power is typically still one order of magnitude less than that achievable with FRET.(Betzig *et al.*, 2006; Hell, 2004; Hess *et al.*, 2006; Rust *et al.*, 2006) However, a limitation of FRET is that it typically occurs up to a donor/acceptor-distance of ~10 nm. Another complication is the nontrivial dependence of the FRET efficiency on the mutual orientations of donor and acceptor molecules, which makes a quantitative conversion of FRET efficiency into accurate distance challenging as soon as the donor and acceptor molecules do not rotate freely and rapidly (compared to fluorescence lifetime).(Loura, 2012)

It has been long known that placing a fluorescent molecule into the vicinity of a metal quenches its fluorescence emission and decreases its fluorescence lifetime. From a physics point of view, the mechanism behind this phenomenon is similar to that of

FRET: energy from the excited molecule is transferred, via electromagnetic coupling, into plasmons of the metal, where energy is either dissipated or re-radiated as light. This fluorophore-metal interaction was extensively studied in the seventies and eighties of the last century, and a quantitative theory developed on the basis of semi-classical quantum optics.(Chance *et al.*, 1978; Drexhage, 1974; Lukosz and Kunz, 1977) The achieved quantitative agreement between experimental measurement and theoretical prediction was excellent.

Here, we show that metal-induced energy transfer (MIET) can be used for localizing fluorescent molecules along one dimension with nanometer accuracy. A first proof-of-principle study was given by Berndt and coworkers, but the general idea has found little attention so far.(Berndt *et al.*, 2010) The core idea is that the MIET accelerates the return of excited fluorescent molecules to their ground state, which manifests itself by a shortening of their fluorescence lifetime.(Chizhik *et al.*, 2011; Enderlein, 1999) Due to the fact that the energy transfer rate is dependent on the distance of a molecule form the metal layer, the fluorescence lifetime can be directly converted into a distance value (see figure 4.4.13).

4.4.2.2   Results and Discussion
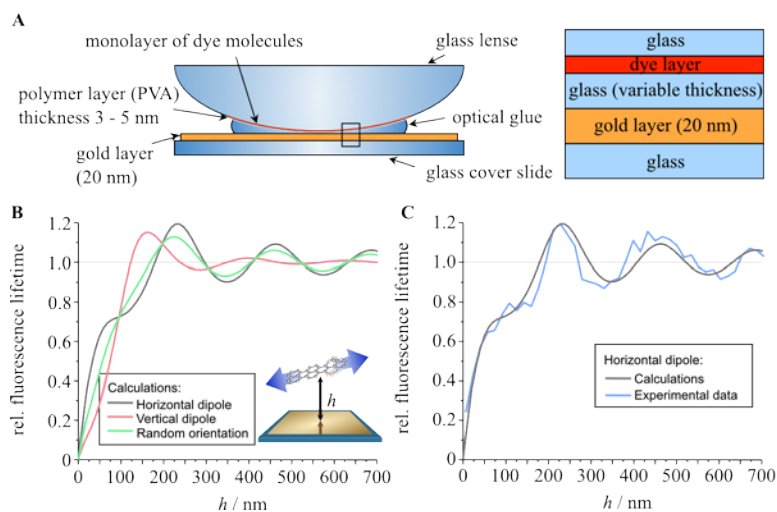
Figure 4.4.13: A Illustration of the test sample used to verify the theoretical model. The surface of a glass lens is coated with a monolayer of dye molecule covered with a thin (3 – 5 nm) polymer layer for preventing the molecules from desorption. The lens is put on the gold-coated glass cover slide. To match the refractive index optical glue is put between the glass lens and the cover slide. **B** Calculated dependence of fluorescence lifetime on the axial distance h from the gold surface. The curves are calculated for 650 nm emission wavelength and for a metal film with 20 nm thickness. **C** Measured dependence of the fluorescence lifetime on axial distance from the metal film shows agreement with the theoretical calculations. (Experiment and theoretical calculations have been performed by Dr. Alexey Chizhik, III. Institute of Physics, Georg-August-university, Göttingen. See also Chizhik A, Rother J et al., Nat. Photon., 2014 dio: 10.1038/NPHOTON.2013.345)

The theoretical basis of the success of this conversion is the perfect quantitative understanding of MIET.(Enderlein, 1999) It is important to emphasize that the energy transfer from the molecule to the metal is dominated by the interaction of the molecule's near field with the metal and is thus a thoroughly near-field effect, similar to FRET. However, due to the planar geometry of the metal film which acts as the acceptor, the distance dependency of the energy transfer efficiency is much weaker than the sixth power of the distance, which leads to a monotonous relation between lifetime and distance over a size range between zero and 100-200 nm above the surface.

To demonstrate the power of MIET the basal membrane of living cells imaged with nanometer accuracy. A large advantage of the method is, that it does not require any hardware modification to a conventional fluorescence-lifetime imaging microscope (FLIM) preserving its full lateral resolution.(Berndt *et al.*, 2010) Three adherent cell lines were chosen as model system: MDA-MB-231 human mammary gland adenocarcinoma cells and A549 human lung carcinoma cells, which are able to form metastasis in-vivo models, and MDCK-II from canine kidney tissue as a benign

epithelial cell line. MIET imaging also allows to monitor cell motility by time elapsed imaging the cell substrate distance. Thereby, we were able to follow the motion of MDA-MB-231 cells over the surface with an axial resolution of 3 nm. Additionally, we also monitored the spreading of single MDCK-II cells visualizing the various stages of adhesion from initial contact to formation of lamellipodia. Knowledge of the precise cell-substrate distance as a function of time and location with unprecedented resolution provides a new means to quantify cellular adhesion and locomotion as it is required for a deeper understanding of fundamental biological processes such as cell differentiation, tumor metastasis, and cell migration.

We used a conventional confocal laser scanning microscope equipped with an objective lens of 1.49 numerical aperture, a pulsed excitation light source (20 MHz repetition rate, 50 ps pulse width, wavelength range 450-800 nm, 1 mW average power per nm, Fianium), and a time correlated single photon counting module (HydraHarp, PicoQuant). The only additional requirement for MIET, when compared to conventional fluorescence-lifetime imaging microscopy (FLIM), is the presence of a thin semitransparent 20 nm gold film deposited on the glass cover slide supporting the sample. A schematic drawing of the setup can also be found in the publication by Chizhik *et al.*.(Chizhik *et al.*, 2014a)

MIET was applied for mapping the cell/substrate-distance of living cells. The cells were stained with a membrane staining fluorophore (Cell Mask Deep Red plasma membrane stain, Life Technologies, Carsbad, CA, USA), which emits photons in the deep red region of the visible spectrum. Using Fluorescence Interference Contrast (FLIC) microscopy, it has previously been shown that the averaged distance of the basal membrane from the substrate typically varies between 20 and 100 nanometers depending on cell type, which is far below the diffraction-limited axial resolution of a confocal microscope.(Braun and Fromherz, 1998) To keep the cells in physiological conditions, the microscope was equipped with an incubator which kept the temperature constant at 37°C. The cells were grown directly on a gold-coated glass substrate (20 nm gold evaporated on glass cover slide with 150 µm thickness (gold coated glass slides were prepared by Dr. Alexey Chizhik, III. Institute of Physics, Georg-August-University, Göttingen, Germany)). Further details of the sample preparation, cell culture and staining can be found in chapter 3.11.2. FLIM images where acquired every 5 minutes with a field of view of 70 by 70 µm^2 (175 by 175 scan positions). As the apical cell membrane is at least 500 nm away from the substrate, only dye molecules within the basal membrane were efficiently excited and detected.

Figure 4.4.14 A and B show an example of the collected fluorescence intensity and lifetime images of the basal membrane of MDA-MB-231 cells, respectively.
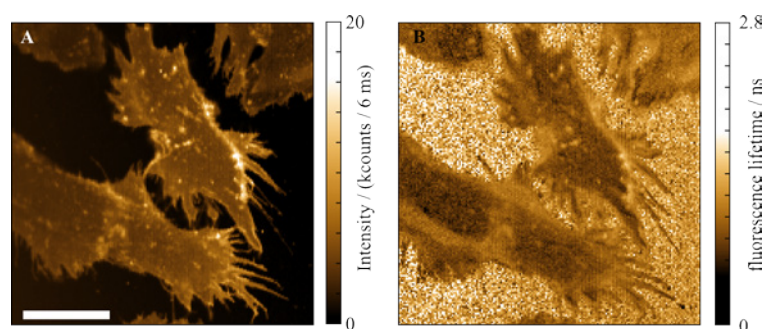
Figure 4.4.14: Fluorescence lifetime imaging near metal surfaces. **A** Fluorescence intensity of the basal membrane of MDA-MB-231 cells (stained using CellMask DeepRed, Invitrogen, Germany) grown on gold-coated cover slide. **B** Fluorescence lifetime of the same area. Scale bar: 20 µm (see also Chizhik A, Rother J *et al.*, Nat. Photon., 2014 dio: 10.1038/NPHOTON.2013.345)

Since the variation of the fluorescence intensity is not only dependent on the metal-induced quenching, but also on the homogeneity of labeling, we used exclusively the lifetime information for reconstructing a 3D map of the basal membrane.

Computation of the local height of the basal membrane above the gold film was accomplished by using the theoretically calculated dependence of the fluorescence lifetime on the distance of a fluorophore from the metal film (Figure 4.4.13 B).

The model takes into account all the details of the optical properties of the glass/gold substrate (thickness and wavelength-dependent complex-valued refractive index of metal film, refractive index of cover slide) as well as the photophysics of the used dye (emission spectrum, dye orientation with respect to the substrate). Orientation of the dye molecules within the cell membrane was checked by defocused imaging.(Patra *et al.*, 2004) A description of the experiments and the results of defocussed imaging can be found in supporting information of the publication by Chizhik *et al.*.(Chizhik *et al.*, 2014b) The dye used throughout this study was found to be randomly oriented within the membrane. Thus, the theoretical distance-lifetime dependence for random dye orientation depicted in Figure 4.4.13 B calculated for the present experimental conditions was used to transfer the lifetime data into a distance of the membrane from the metal layer. We checked the accuracy of our model calculations on applying MIET for mapping the surface profile of a dye-coated glass lens with well-known height profile (4.4.13 A and C). (Experiments and calculations were performed by Dr. Alexey Chizhik, III. Institute of Physics, Georg-August-University, Göttingen, Germany)

Whereas the 3D reconstruction of the membrane profile is recalculated solely from the lifetime image of the sample, the intensity distribution is used for discriminating, in the lifetime images, the membrane fluorescence against the background. Regions with no cells are difficult to identify alone from the lifetime images, which become exceedingly scattered in lifetime at low signal-to-noise ratios. We eliminated such patches by

removing areas where the fluorescence intensity did not exceed the background level. Finally, to make sure that the membrane stain does not internalize during experiment, we did FLIM imaging of the intracellular compartments, which did not yield any sensible fluorescence signal.

Figure 4.4.15 A shows the 3D reconstruction of the basal membrane of MDA-MB-231 cells calculated from the lifetime images shown in Figure 4.4.15.
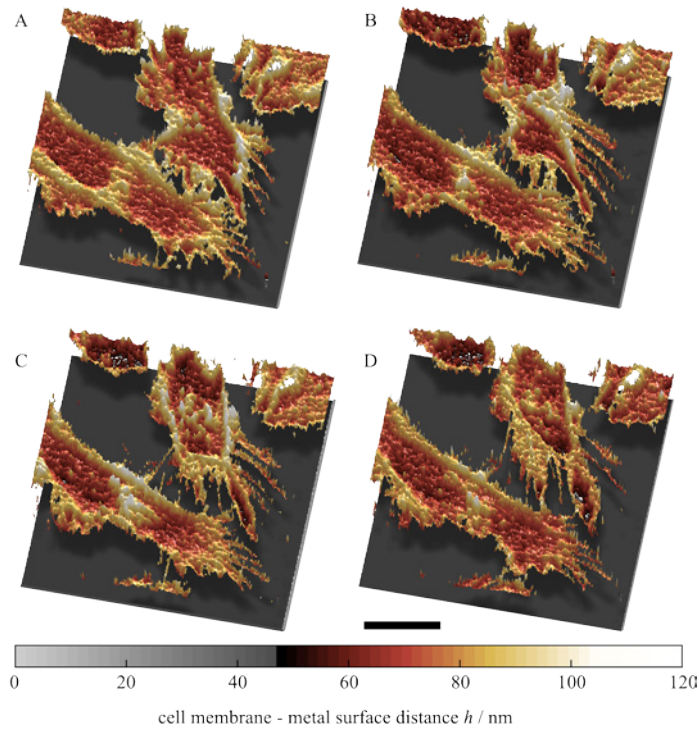
Figure 4.4.15: 3D- reconstruction of the basal cell membrane calculated from recorded fluorescence lifetime images. The four images (A - D) show the same cells over a period of 40 minutes (see also Chizhik A, Rother J *et al.*, Nat. Photon., 2014 dio: 10.1038/NPHOTON.2013.345)

The local cell/substrate-distance varies between 50 and 100 nm, whereby cell boundaries naturally exhibit a larger distance from the surface. The average cell/substrate-distance is in very good agreement with recently reported results of Wegener and colleagues, who determined distances between 27 and 87 nm for MDCK-II cells and NIH 3T3 fibroblasts, respectively.(Heitmann *et al.*, 2007) Differences in cell/substrate-distance between different cell-types can occur due to variations in adhesion strength and in the secretion of extracellular matrix proteins by the cells itself. To follow the temporal dynamics of the cell/substrate distance, we recorded a time-lapse series of the fluorescence lifetime and intensity images in 5-minute time intervals. Figures 4.4.15 A-D show images of MDA-MB-231 cells over a period of 40 minutes. The 3D maps allow for following the cell motion over time with 200 nm lateral (as

defined by the confocal microscope) and 3 nm axial resolution (see below). Although the cell/substrate distance at each lateral position changes over time, the average distance remains the same over the full measurement time. We found that the tumor cells display a larger cell-substrate distance in the periphery compared to the center where they firmly adhere to the gold surface.

A comparison between the three cell lines MDA-MB-231, A549, and MDCK-II with respect to the average distance of the basal membrane from the gold surface as well as exemplary MIET images is shown in figure 4.4.16.
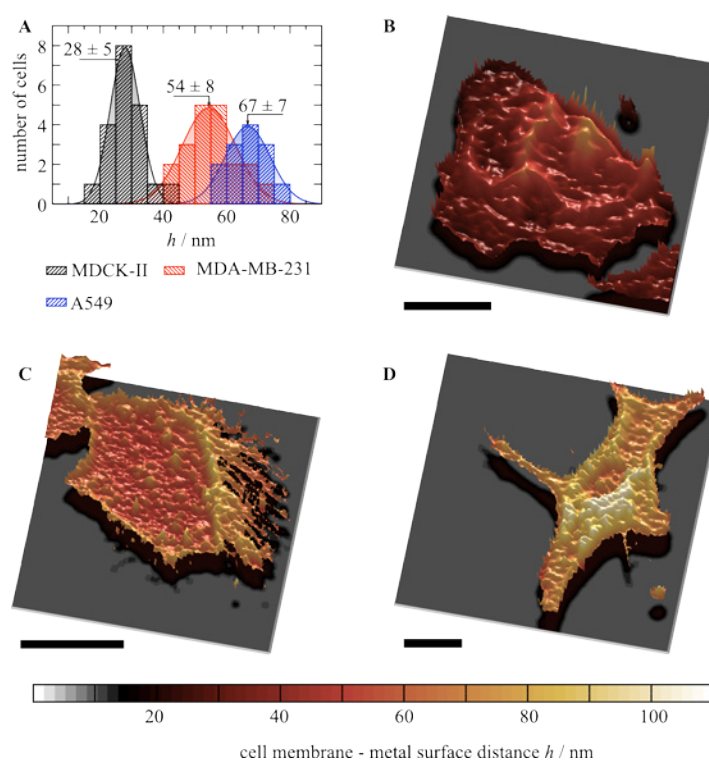
Figure 4.4.16: Comparison between the distances of the basal membrane from the metal film of three cell lines. **A** Histogram showing the distance of the basal membrane from the metal surface of MDCK-II, A549 and MDA-MB-231 cells. Histograms were fitted using a Gaussian function. Numbers depict the average distance of the different cell types from the surface in nanometers. **B-D** Exemplary three dimensional reconstructions of the basal membrane of MDCK-II (B), MDA-MB231 (C) and A549 cells (D). All images are shown in the same color code. Scale bar: 20 μm (see also Chizhik A, Rother J *et al.*, Nat. Photon., 2014 dio: 10.1038/NPHOTON.2013.345)

We found excellent agreement with previously obtained data using FLIC microscopy showing that MDCK-II cells are extremely close to the surface (28 ± 5 nm).(Heitmann *et al.*, 2007) Note that MDCK-II cells are benign epithelial cells, whereas the other cell lines are cancerous showing a higher invasiveness/motility. This might be inferred from a higher cell/substrate-distance of 54 ± 8 nm (MDA-MB-231) and 67 ± 7 nm (A549). Notably, it has been demonstrated, that cancer cells have lost their dependence on adhesion to a solid support and additionally, do not react to changes of the substrate

elasticity.(Wang *et al.*, 2000; Wittelsberger *et al.*, 1981) These changes in mechanosensing could also be reflected in an increased cell-substrate distance, which is observed here.

We also investigated the spreading behavior of MDCK-II cells. Generally, the spreading process of adherent cells can be divided into three distinct temporal phases. The first phase is characterized by the formation of initial bonds between adhesion molecules and molecules of the extracellular matrix (ECM). This process of tethering is followed by the second phase comprising the initial cell spreading, which is driven by actin polymerization that forces the cell surface area to increase by drawing membrane from a reservoir of folded regions and blebs. The third phase encompasses recruitment of additional plasma membrane from the internally stored membrane buffer and extension of lamellipodia occupying a larger area. By means of MIET imaging we could monitor the individual phases by visualizing the cell substrate distance as a function of time (Figure 4.4.17).
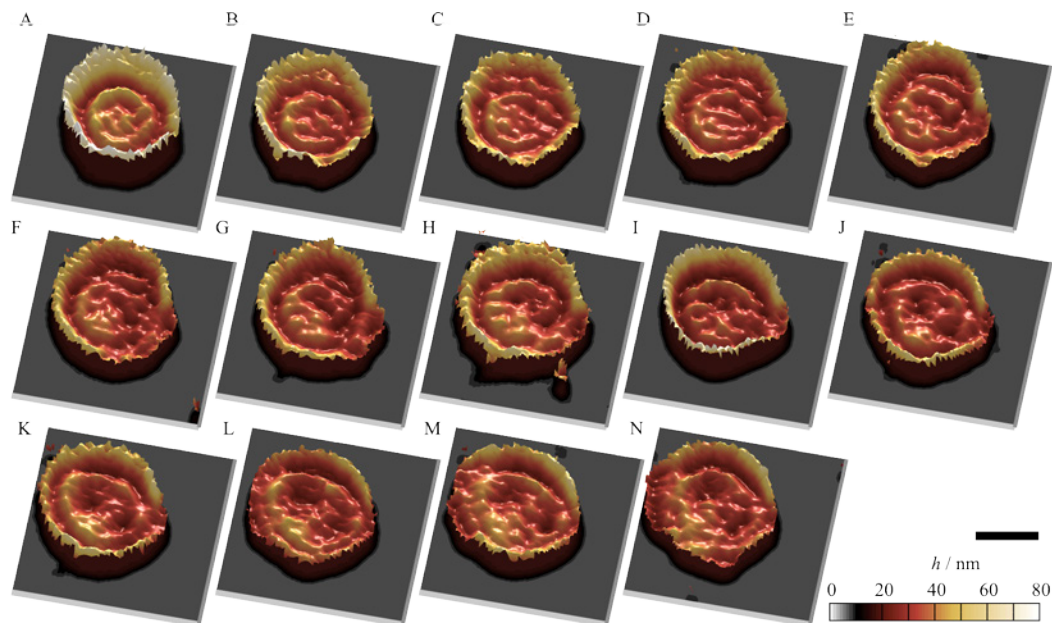
Figure 4.4.17: Time elapsed MIET images recorded in 3 minutes time intervals showing the early stages of cell (MDCK II) spreading on gold. Initially, concentric rings of strong and weaker adhesion (judged by cell-substrate distance) are visible. A darker color refers to lower cell-substrate distance. At later stages K-N first lamellipodia are formed that exhibit a low cell-substrate distance. Scale bar: 10 µm . (see also Chizhik A, Rother J *et al.*, Nat. Photon., 2014 dio: 10.1038/NPHOTON.2013.345)

By means of MIET imaging we observe that the initial contact of the cell is characterized by concentric adhesion areas with alternating low and high distance from the surface. The occupied area rises with time and eventually lamellipodia occur at the border of the cells with a close contact to the gold surface.

To estimate the resolution of the recorded images, we calculated a standard deviation of the cell/substrate-distance values. For the acquired series of images, the resolution of the axial distance as determined with MIET varies between 3 nm (at near 10-15 kcounts/pixel) and 4 nm (at near 5-10 kcounts/pixel), depending on the local signal-to-noise ratio. This substantially exceeds the precision of most of the existing techniques used for axial imaging. In order to prevent fast photo-bleaching of the sample, we used a moderate excitation power and acquisition time. However, as the resolution is determined by the signal-to-noise ratio of the recorded fluorescence decay curves, a further increase in precision can be achieved by collecting more fluorescence signal.

The influence of photon statistics on axial resolution of MIET was checked using test samples (Experiments were performed by Dr. Alexey). The results are shown in supplementary information of the publication by Chizhik *et al*. (Chizhik *et al*., 2014b)

In our current instrument, the MIET image acquisition speed is limited by the scan speed of our confocal scanning microscope, which was sufficient to follow the relatively slow motion of the cell membrane. Using a FLIM imaging system based on time-gated cameras or phase fluorometry, the acquisition speed can be increased by several orders of magnitude.

4.4.2.3 Conclusion

Although we focused in this chapter on the application of MIET to the mapping of the membrane of a living cell, which shows its versatility, relative technical simplicity, and its potential for life-science applications, the potential scope of applications of MIET goes much further. The size range over which MIET works nicely bridges (and complements) the realm of conventional FRET and all the recently developed superresolution imaging techniques. Although MIET has to rely on the perfect theoretical understanding of the fluorophore-metal interaction, which is certainly more involved than that of FRET, this is no serious obstacle in the current age of powerful desktop computers. In contrast to FRET, the infamous orientation-factor problem is much relaxed because one has to know only the relative orientation of one species of fluorescent molecules with respect to the planar metal film. Moreover, in contrast to FRET, one needs to label only one site of a sample with one species of fluorophore instead of double-labeling with a donor and acceptor. MIET is exceedingly simple to set up and does neither require any modification of the FLIM system, nor preparation of complex sample substrates. Coating glass cover slides with a thin metal film is the only prerequisite of the technique. Thus, the technical simplicity of MIET will allow its

application to a wide range of studies where nanometer resolution is required. We envision that its combination with ideas from super-resolution microscopy techniques which are based on photo-switching and high-precision localization of single molecules will enable to resolve inter- and intramolecular distances with nanometer precision and may thus develop into a similarly powerful experimental tool as FRET.

5. Summary

The general aim of this work was the examination of mechanics and dynamics of cells in response to environmental cues encompassing the interaction of cells with nanoparticles, chemical drugs or hormones. Thereby, a central question was, how cells or more precisely the cell membranes are affected by incubation with a new subset of nanoparticles, so-called Janus particles, which exhibit amphiphilic properties. Membrane mechanics play an important role in the membrane interaction of these particles. To measure mechanics of cells, a new method introduced by Alcaraz and coworkers, which enables the measurement of viscoelastic properties of sample using the AFM was established in the laboratory and the influence of chemical drugs or hormones, malignant transformation of cells and culture substrate properties was examined.(Alcaraz *et al.*, 2003) Cell-substrate interaction of different cell lines was additionally quantified by metal induced-energy transfer fluorescence lifetime imaging (MIET-FLIM) allowing measurement of distances between a fluorophore and a metal layer in the nanometer regime. MIET-FLIM was used for this purpose for the first time.

To examine the effect on amphiphilic Janus particles on cells and artificial membranes, we used Au@MnO- heterodimers with a total size of 20 to 25 nm in diameter, in which the MnO-domain was rendered hydrophilic using either a PEG-coating, which was attached to the MnO-surface via dopamine-anchors or by a silica shell, which was afterwards PEGylated. The ends of the PEG-chains were carrying a methoxy- or an amino-group. In all cases the Au-domain was hydrophobic carrying a self-assembled monolayer of 1-octadecanethiol. In fluorescence microscopic experiments using giant unilamellar vesicles as artificial membrane systems, we found that the used Janus particles generally were able to induce membrane deformations in form of membrane tubes in vesicles, with low membrane tension. Spherical control particles did not show an effect on the shape of GUVs. These effects were interpreted by comparison with coarse grain simulation of the interaction between amphiphilic particles with lipid membranes performed by Reynwar *et al.*.(Reynwar *et al.*, 2007) In these simulations Janus particles were able to induce tubulation and vesiculation due to long-range attractive forces induced originating from local membrane bending. Calculation of binding energy of silica-coated Janus particles to lipid monolayers from SPR-spectroscopy experiments showed that the energy released due to binding of the particles to lipids could be sufficient to induce membrane deformation and tube formation, but not high enough to lead to vesiculation, which could explain the

experimentally observed effects. Janus particles carrying a dopamine-PEG-based functionalization also induced the formation of vesicles that hints at a stronger interaction between particles and membrane. However, the mechanism of membrane tube or vesicle formation by Janus particles remains unclear as particles used in this study were not fluorescently labeled and thus could not be followed in the microscope. Increase of membrane tension of the GUVs to a level comparable to the membrane tension in living cells inhibited tube formation. Accordingly, no difference was found in uptake levels of Janus particles into living cells. Also cytotoxicity experiments comparing Janus nanoparticles with their spherical counterparts did not reveal a universal trend of a higher toxicity of either of the particle species. In conclusion, this study hints at the interaction mechanism between membranes and Janus particles proposed by Reynwar *et al.*, but, on the other side, this interaction seems not to play a major role in the uptake of Janus particles into living cells.

To measure the changes in the viscoelasticity of cells under different physical, biological or chemical conditions, AFM-based microrheology was established unraveling the complex rheological properties of cells. In this method, the cantilever tip is excited to sinusoidal oscillations while it is in contact to the sample leading to sinusoidal changes of the indentation depth. At the same time, the force response of the cantilever is measured. Relating the force response to the changes in indentation depth facilitates the calculation of the complex shear modulus G^*.

First, frequency dependent rheological properties of MDCK-II cells treated with fixating agents or drugs interfering with the actomyosin network were examined. Untreated cells showed an increase of the real part of G^* (indicating the elastic properties of the sample) with the oscillation frequency according to a weak power-law. The imaginary part of G^* (indicating the energy dissipation) exhibited smaller values than the real part at low oscillation frequencies but exceeded the real part at high frequencies. The frequency-dependent rheological data could be explained by the active soft glassy rheology model introduced by Fabry *et al.*.(Fabry *et al.*, 2001) When cells were treated with fixating agents, a shift towards a more elastic, solid-like behavior of the cells was observed, while treatment with drugs interfering with the actomyosin network lead to a more fluid-like behavior and provoke a general cell softening. A shift towards more solid-like behavior was also observed upon epithelial-to-mesenchymal transition of NMuMG cells, which could have beneficial effects for the migratory behavior of the transformed cells.

Furthermore, measuring the viscoelastic properties of eight different cell lines, we found a correlation between the malignant state of cells and their viscoelastic behavior

at high frequencies. Malignant cells showed a more fluid like behavior compared to benign cells.

Finally, the method was used to evaluate the influence of substrate properties, i.e. pore size, on the viscoelastic behavior of confluent MDCK-II cells. It was found, that the viscous properties were not affected by cell culture on porous substrates, while the elastic properties of cells cultured on porous substrates were decreased. This effect could be correlated with a reduction of the actin network density measured by scanning electron microscopy. Moreover, cells cultured on porous substrates showed also a reduced formation of stress fibers in fluorescence microscopic images. These results highlight the importance of culture substrate on the general behavior of cells.

Therefore, cell-substrate interactions were further characterized using MIET-FLIM. The method bases on the modification of fluorescence lifetime of a fluorophore, which is in close proximity to a metal layer. Application of a quantitative model enables to determine the axial position of the fluorophore and metal layer with nanometer precision up to a distance of approximately 200 nm. The method was used to measure cell-substrate distances of three cell lines, which exhibited cell substrate-distances between 28 and 67 nm and to follow the initial spreading of cells with a yet unprecedented axial resolution. The presented method is not limited to measurement of cell substrate distances and can potentially be used as a universal tool in fluorescence microscopic studies closing the gap between Förster resonance energy transfer measurements and new super-resolution techniques.

6. References

Agus, D.B., Alexander, J.F., Arap, W., Ashili, S., Aslan, J.E., Austin, R.H., Backman, V., Bethel, K.J., Bonneau, R., Chen, W.C., *et al.* (2013). A physical sciences network characterization of non-tumorigenic and metastatic cells. Sci Rep-Uk *3*.

Alberts, B. (2002). Molecular Biology of the Cell (Garland).

Alcaraz, J., Buscemi, L., Grabulosa, M., Trepat, X., Fabry, B., Farre, R., and Navajas, D. (2003). Microrheology of human lung epithelial cells measured by atomic force microscopy. Biophys J *84*, 2071-2079.

Alcaraz, J., Buscemi, L., Puig-de-Morales, M., Colchero, J., Baro, A., and Navajas, D. (2002). Correction of microrheological measurements of soft samples with atomic force microscopy for the hydrodynamic drag on the cantilever. Langmuir *18*, 716-721.

Alexeev, A., Uspal, W.E., and Balazs, A.C. (2008). Harnessing Janus nanoparticles to create controllable pores in membranes. Acs Nano *2*, 1117-1122.

Angelova, M.I., and Dimitrov, D.S. (1986). Liposome Electroformation. Faraday Discuss *81*, 303-+.

Arnold, M., Cavalcanti-Adam, E.A., Glass, R., Blummel, J., Eck, W., Kantlehner, M., Kessler, H., and Spatz, J.P. (2004). Activation of integrin function by nanopatterned adhesive interfaces. Chemphyschem *5*, 383-388.

Arpin, M., Chirivino, D., Naba, A., and Zwaenepoel, I. (2011). Emerging role for ERM proteins in cell adhesion and migration. Cell Adhes Migr *5*, 199-206.

Berndt, M., Lorenz, M., Enderlein, J., and Diez, S. (2010). Axial Nanometer Distances Measured by Fluorescence Lifetime Imaging Microscopy. Nano Lett *10*, 1497-1500.

Betzig, E., Patterson, G.H., Sougrat, R., Lindwasser, O.W., Olenych, S., Bonifacino, J.S., Davidson, M.W., Lippincott-Schwartz, J., and Hess, H.F. (2006). Imaging intracellular fluorescent proteins at nanometer resolution. Science *313*, 1642-1645.

Bilodeau, G.G. (1992). Regular Pyramid Punch Problem. J Appl Mech-T Asme *59*, 519-523.

Binnig, G., Quate, C.F., and Gerber, C. (1986). Atomic Force Microscope. Phys Rev Lett *56*, 930-933.

Boal, D. (2012). Mechanics of the Cell (Cambridge University Press).

Braun, D., and Fromherz, P. (1997). Fluorescence interference-contrast microscopy of cell adhesion on oxidized silicon. Appl Phys a-Mater *65*, 341-348.

Braun, D., and Fromherz, P. (1998). Fluorescence interferometry of neuronal cell adhesion on microstructured silicon. Phys Rev Lett *81*, 5241-5244.

Bretscher, A. (1999). Regulation of cortical structure by the ezrin-radixin-moesin protein family. Curr Opin Cell Biol *11*, 109-116.

Briscoe, B.J., Sebastian, K.S., and Adams, M.J. (1994). The Effect of Indenter Geometry on the Elastic Response to Indentation. J Phys D Appl Phys *27*, 1156-1162.

Brown, K.A., Aakre, M.E., Gorska, A.E., Price, J.O., Eltom, S.E., Pietenpol, J.A., and Moses, H.L. (2004). Induction by transforming growth factor-beta 1 of epithelial to mesenchymal transition is a rare event in vitro. Breast Cancer Res *6*, R215-R231.

Butt, H.J., Cappella, B., and Kappl, M. (2005). Force measurements with the atomic force microscope: Technique, interpretation and applications. Surf Sci Rep *59*, 1-152.

Carl, P., and Schillers, H. (2008). Elasticity measurement of living cells with an atomic force microscope: data acquisition and processing. Pflug Arch Eur J Phy *457*, 551-559.

Chance, R.R., Prock, A., and Silbey, R. (1978). Molecular Fluorescence and Energy Transfer Near Interfaces. In Advances in Chemical Physics (John Wiley & Sons, Inc.), pp. 1-65.

Chen, Q., Bae, S.C., and Granick, S. (2011). Directed self-assembly of a colloidal kagome lattice. Nature *469*, 381-384.

Chizhik, A.I., Chizhik, A.M., Khoptyar, D., Bar, S., Meixner, A.J., and Enderlein, J. (2011). Probing the Radiative Transition of Single Molecules with a Tunable Microresonator. Nano Lett *11*, 1700-1703.

Chizhik, A.I., Rother, J., Gregor, I., Janshoff, A., and Enderlein, J. (2014a). Metal-induced energy transfer for live cell nanoscopy. Nat Photon *8*, 124-127.

Chizhik, A.I., Rother, J., Gregor, I., Janshoff, A., and Enderlein, J. (2014b). Metal-induced energy transfer for live cell nanoscopy. Nat Photonics *8*, 124-127.

Choi, J.Y., Lee, S.H., Bin Na, H., An, K., Hyeon, T., and Seo, T.S. (2010). In vitro cytotoxicity screening of water-dispersible metal oxide nanoparticles in human cell lines. Bioproc Biosyst Eng *33*, 21-30.

Clark, A.G., and Paluch, E. (2011). Mechanics and Regulation of Cell Shape During the Cell Cycle. Results Probl Cell D *53*, 31-73.

Clark, P., Connolly, P., Curtis, A.S.G., Dow, J.A.T., and Wilkinson, C.D.W. (1991). Cell Guidance by Ultrafine Topography Invitro. J Cell Sci *99*, 73-77.

Conner, S.D., and Schmid, S.L. (2003). Regulated portals of entry into the cell. Nature *422*, 37-44.

Cooper, J.A. (1987). Effects of Cytochalasin and Phalloidin on Actin. J Cell Biol *105*, 1473-1478.

Costi, R., Saunders, A.E., Elmalem, E., Salant, A., and Banin, U. (2008). Visible light-induced charge retention and photocatalysis with hybrid CdSe-Au nanodumbbells. Nano Lett *8*, 637-641.

Cross, S.E., Jin, Y.S., Rao, J., and Gimzewski, J.K. (2007). Nanomechanical analysis of cells from cancer patients. Nat Nanotechnol *2*, 780-783.

References

Curtis, A., and Wilkinson, C. (1997). Topographical control of cells. Biomaterials *18*, 1573-1583.

De Gennes, P.G. (1992). Soft Matter (Nobel Lecture). Angew Chem Int Edit *31*, 842-845.

del Rio, A., Perez-Jimenez, R., Liu, R.C., Roca-Cusachs, P., Fernandez, J.M., and Sheetz, M.P. (2009). Stretching Single Talin Rod Molecules Activates Vinculin Binding. Science *323*, 638-641.

Dendukuri, D., and Doyle, P.S. (2009). The Synthesis and Assembly of Polymeric Microparticles Using Microfluidics. Adv Mater *21*, 4071-4086.

Dimilla, P.A., Barbee, K., and Lauffenburger, D.A. (1991). Mathematical-Model for the Effects of Adhesion and Mechanics on Cell-Migration Speed. Biophys J *60*, 15-37.

Ding, H.M., and Ma, Y.Q. (2012). Interactions between Janus particles and membranes. Nanoscale *4*, 1116-1122.

Doherty, G.J., and McMahon, H.T. (2009). Mechanisms of Endocytosis. Annu Rev Biochem *78*, 857-902.

Drexhage, K.H. (1974). IV Interaction of Light with Monomolecular Dye Layers. In Progress in Optics, E. Wolf, ed. (Elsevier), pp. 163-232.

Dukes, J.D., Whitley, P., and Chalmers, A.D. (2011). The MDCK variety pack: choosing the right strain. Bmc Cell Biol *12*.

Ehrlicher, A.J., Nakamura, F., Hartwig, J.H., Weitz, D.A., and Stossel, T.P. (2011). Mechanical strain in actin networks regulates FilGAP and integrin binding to filamin A. Nature *478*, 260-U154.

Enderlein, J. (1999). Single-molecule fluorescence near a metal layer. Chem Phys *247*, 1-9.

Engler, A.J., Sen, S., Sweeney, H.L., and Discher, D.E. (2006). Matrix elasticity directs stem cell lineage specification. Cell *126*, 677-689.

Fabry, B., Maksym, G.N., Butler, J.P., Glogauer, M., Navajas, D., and Fredberg, J.J. (2001). Scaling the microrheology of living cells. Phys Rev Lett *87*.

Fabry, B., Maksym, G.N., Butler, J.P., Glogauer, M., Navajas, D., Taback, N.A., Millet, E.J., and Fredberg, J.J. (2003). Time scale and other invariants of integrative mechanical behavior in living cells. Phys Rev E *68*.

Forster, T. (1948). *Zwischenmolekulare Energiewanderung Und Fluoreszenz. Ann Phys-Berlin *2*, 55-75.

Frese, D., Steltenkamp, S., Schmitz, S., and Steinem, C. (2013). In situ generation of electrochemical gradients across pore-spanning membranes. Rsc Adv *3*, 15752-15761.

Fujimoto, E., Sato, H., Shirai, S., Nagashima, Y., Fukumoto, K., Hagiwara, H., Negishi, E., Ueno, K., Omori, Y., Yamasaki, H.*, et al.* (2005). Connexin32 as a tumor suppressor gene in a metastatic renal cell carcinoma cell line. Oncogene *24*, 3684-3690.

Gavara, N., and Chadwick, R.S. (2012). Determination of the elastic moduli of thin samples and adherent cells using conical atomic force microscope tips. Nat Nanotechnol *7*, 733-736.

Geiger, B., and Bershadsky, A. (2002). Exploring the neighborhood: Adhesion-coupled cell mechanosensors. Cell *110*, 139-142.

Geiger, B., Spatz, J.P., and Bershadsky, A.D. (2009). Environmental sensing through focal adhesions. Nat Rev Mol Cell Bio *10*, 21-33.

Giaever, I., and Keese, C.R. (1984). Monitoring Fibroblast Behavior in Tissue-Culture with an Applied Electric-Field. P Natl Acad Sci-Biol *81*, 3761-3764.

Giaever, I., and Keese, C.R. (1991). Micromotion of Mammalian-Cells Measured Electrically. P Natl Acad Sci USA *88*, 7896-7900.

Giaever, I., and Keese, C.R. (1993). A Morphological Biosensor for Mammalian-Cells. Nature *366*, 591-592.

Gu, H.W., Yang, Z.M., Gao, J.H., Chang, C.K., and Xu, B. (2005). Heterodimers of nanoparticles: Formation at a liquid-liquid interface and particle-specific surface modification by functional molecules. Journal of the American Chemical Society *127*, 34-35.

Guck, J., Schinkinger, S., Lincoln, B., Wottawah, F., Ebert, S., Romeyke, M., Lenz, D., Erickson, H.M., Ananthakrishnan, R., Mitchell, D.*, et al.* (2005). Optical deformability as an inherent cell marker for testing malignant transformation and metastatic competence. Biophys J *88*, 3689-3698.

Gupta, A.K., and Gupta, M. (2005). Synthesis and surface engineering of iron oxide nanoparticles for biomedical applications. Biomaterials *26*, 3995-4021.

Hanahan, D., and Weinberg, R.A. (2000). The hallmarks of cancer. Cell *100*, 57-70.

Hanahan, D., and Weinberg, R.A. (2011). Hallmarks of Cancer: The Next Generation. Cell *144*, 646-674.

Heitmann, V., Reiß, B., and Wegener, J. (2007). The Quartz Crystal Microbalance in Cell Biology: Basics and Applications. In Piezoelectric Sensors, C. Steinem, and A. Janshoff, eds. (Springer Berlin Heidelberg), pp. 303-338.

Hell, S.W. (2004). Strategy for far-field optical imaging and writing without diffraction limit. Phys Lett A *326*, 140-145.

Henderson, E., Haydon, P.G., and Sakaguchi, D.S. (1992). Actin Filament Dynamics in Living Glial-Cells Imaged by Atomic Force Microscopy. Science *257*, 1944-1946.

Herrmann, H., Strelkov, S.V., Burkhard, P., and Aebi, U. (2009). Intermediate filaments: primary determinants of cell architecture and plasticity. J Clin Invest *119*, 1772-1783.

Hertz, H. (1882). Ueber die Berührung fester elastischer Körper. Journal für die reine und angewandte Mathematik *92*, 156 - 171.

References

Hess, S.T., Girirajan, T.P.K., and Mason, M.D. (2006). Ultra-high resolution imaging by fluorescence photoactivation localization microscopy. Biophys J *91*, 4258-4272.

Hiraga, T., Williams, P.J., Mundy, G.R., and Yoneda, T. (2001). The bisphosphonate ibandronate promotes apoptosis in MDA-MB-231 human breast cancer cells in bone metastases. Cancer Res *61*, 4418-4424.

Hoess, A., Thormann, A., Friedmann, A., and Heilmann, A. (2012). Self-supporting nanoporous alumina membranes as substrates for hepatic cell cultures. J Biomed Mater Res A *100A*, 2230-2238.

Holle, A.W., Tang, X.Y., Vijayraghavan, D., Vincent, L.G., Fuhrmann, A., Choi, Y.S., del Alamo, J.C., and Engler, A.J. (2013). In Situ Mechanotransduction Via Vinculin Regulates Stem Cell Differentiation. Stem Cells *31*, 2467-2477.

Homola, J., Yee, S.S., and Gauglitz, G. (1999). Surface plasmon resonance sensors: review. Sensor Actuat B-Chem *54*, 3-15.

Ingber, D.E. (2006). Cellular mechanotransduction: putting all the pieces together again. Faseb J *20*, 811-827.

Jaalouk, D.E., and Lammerding, J. (2009). Mechanotransduction gone awry. Nat Rev Mol Cell Bio *10*, 63-73.

Janmey, P.A., Euteneuer, U., Traub, P., and Schliwa, M. (1991). Viscoelastic Properties of Vimentin Compared with Other Filamentous Biopolymer Networks. J Cell Biol *113*, 155-160.

Janshoff, A., Lorenz, B., Pietuch, A., Fine, T., Tarantola, M., Steinem, C., and Wegener, J. (2010). Cell Adhesion to Ordered Pores: Consequences for Cellular Elasticity. J Adhes Sci Technol *24*, 2287-2300.

Jiang, X.E., Musyanovych, A., Rocker, C., Landfester, K., Mailander, V., and Nienhaus, G.U. (2011). Specific effects of surface carboxyl groups on anionic polystyrene particles in their interactions with mesenchymal stem cells. Nanoscale *3*, 2028-2035.

Kalluri, R. (2009). EMT: When epithelial cells decide to become mesenchymal-like cells. J Clin Invest *119*, 1417-1419.

Kalluri, R., and Weinberg, R.A. (2009). The basics of epithelial-mesenchymal transition. J Clin Invest *119*, 1420-1428.

Kollmannsberger, P., and Fabry, B. (2009). Active soft glassy rheology of adherent cells. Soft Matter *5*, 1771-1774.

Korchev, Y.E., Gorelik, J., Lab, M.J., Sviderskaya, E.V., Johnston, C.L., Coombes, C.R., Vodyanoy, I., and Edwards, C.R.W. (2000). Cell volume measurement using scanning ion conductance microscopy. Biophys J *78*, 451-457.

Kovacs, M., Toth, J., Hetenyi, C., Malnasi-Csizmadia, A., and Sellers, J.R. (2004). Mechanism of blebbistatin inhibition of myosin II. J Biol Chem *279*, 35557-35563.

Kumar, S., and Weaver, V. (2009). Mechanics, malignancy, and metastasis: The force journey of a tumor cell. Cancer Metast Rev *28*, 113-127.

Kuznetsova, T.G., Starodubtseva, M.N., Yegorenkov, N.I., Chizhik, S.A., and Zhdanov, R.I. (2007). Atomic force microscopy probing of cell elasticity. Micron *38*, 824-833.

Kwon, K.W., and Shim, M. (2005). gamma-Fe2O3/II-VI sulfide nanocrystal heterojunctions. Journal of the American Chemical Society *127*, 10269-10275.

Laerme, F., Schilp, A., Funk, K., and Offenberg, M. (1999). Bosch deep silicon etching: improving uniformity and etch rate for advanced MEMS applications. Paper presented at: Micro Electro Mechanical Systems, 1999 MEMS '99 Twelfth IEEE International Conference on.

Laudadio, R.E., Millet, E.J., Fabry, B., An, S.S., Butler, J.P., and Fredberg, J.J. (2005). Rat airway smooth muscle cell during actin modulation: rheology and glassy dynamics. Am J Physiol-Cell Ph *289*, C1388-C1395.

Le Clainche, C., and Carlier, M.F. (2008). Regulation of actin assembly associated with protrusion and adhesion in cell migration. Physiol Rev *88*, 489-513.

Lekka, M., and Laidler, P. (2009). Applicability of AFM in cancer detection. Nat Nanotechnol *4*, 72-72.

Lekka, M., Laidler, P., Gil, D., Lekki, J., Stachura, Z., and Hrynkiewicz, A.Z. (1999). Elasticity of normal and cancerous human bladder cells studied by scanning force microscopy. Eur Biophys J Biophy *28*, 312-316.

Levental, I., Georges, P.C., and Janmey, P.A. (2007). Soft biological materials and their impact on cell function. Soft Matter *3*, 299-306.

Levental, K.R., Yu, H.M., Kass, L., Lakins, J.N., Egeblad, M., Erler, J.T., Fong, S.F.T., Csiszar, K., Giaccia, A., Weninger, W.*, et al.* (2009). Matrix Crosslinking Forces Tumor Progression by Enhancing Integrin Signaling. Cell *139*, 891-906.

Lewinski, N., Colvin, V., and Drezek, R. (2008). Cytotoxicity of nanoparticles. Small *4*, 26-49.

Lipowsky, R. (2013). Spontaneous tubulation of membranes and vesicles reveals membrane tension generated by spontaneous curvature. Faraday Discuss *161*, 305-331.

Lo, C.M., Glogauer, M., Rossi, M., and Ferrier, J. (1998). Cell-substrate separation: effect of applied force and temperature. Eur Biophys J Biophy *27*, 9-17.

Lo, C.M., Wang, H.B., Dembo, M., and Wang, Y.L. (2000). Cell movement is guided by the rigidity of the substrate. Biophys J *79*, 144-152.

Loura, L.M.S. (2012). Simple Estimation of Forster Resonance Energy Transfer (FRET) Orientation Factor Distribution in Membranes. Int J Mol Sci *13*, 15252-15270.

Lukosz, W., and Kunz, R.E. (1977). Light-Emission by Magnetic and Electric Dipoles Close to a Plane Interface .1. Total Radiated Power. J Opt Soc Am *67*, 1607-1615.

Lulevich, V., Zink, T., Chen, H.Y., Liu, F.T., and Liu, G.Y. (2006). Cell mechanics using atomic force microscopy-based single-cell compression. Langmuir *22*, 8151-8155.

References

Mahaffy, R.E., Shih, C.K., MacKintosh, F.C., and Kas, J. (2000). Scanning probe-based frequency-dependent microrheology of polymer gels and biological cells. Phys Rev Lett *85*, 880-883.

Mattheyses, A.L., Simon, S.M., and Rappoport, J.Z. (2010). Imaging with total internal reflection fluorescence microscopy for the cell biologist. J Cell Sci *123*, 3621-3628.

McBeath, R., Pirone, D.M., Nelson, C.M., Bhadriraju, K., and Chen, C.S. (2004). Cell shape, cytoskeletal tension, and RhoA regulate stem cell lineage commitment. Dev Cell *6*, 483-495.

McGrail, D.J., Ghosh, D., Quach, N.D., and Dawson, M.R. (2012). Differential Mechanical Response of Mesenchymal Stem Cells and Fibroblasts to Tumor-Secreted Soluble Factors. Plos One *7*.

McNamara, L.E., Burchmore, R., Riehle, M.O., Herzyk, P., Biggs, M.J.P., Wilkinson, C.D.W., Curtis, A.S.G., and Dalby, M.J. (2012). The role of microtopography in cellular mechanotransduction. Biomaterials *33*, 2835-2847.

Miettinen, P.J., Ebner, R., Lopez, A.R., and Derynck, R. (1994). Tgf-Beta Induced Transdifferentiation of Mammary Epithelial-Cells to Mesenchymal Cells - Involvement of Type-I Receptors. J Cell Biol *127*, 2021-2036.

Milliron, D.J., Hughes, S.M., Cui, Y., Manna, L., Li, J.B., Wang, L.W., and Alivisatos, A.P. (2004). Colloidal nanocrystal heterostructures with linear and branched topology. Nature *430*, 190-195.

Mitra, S.K., Hanson, D.A., and Schlaepfer, D.D. (2005). Focal adhesion kinase: In command and control of cell motility. Nat Rev Mol Cell Bio *6*, 56-68.

Mizuno, D., Tardin, C., Schmidt, C.F., and MacKintosh, F.C. (2007). Nonequilibrium mechanics of active cytoskeletal networks. Science *315*, 370-373.

Mofrad, M.R.K., and Kamm, R.D. (2006). Cytoskeletal Mechanics: Models and Measurements in Cell Mechanics (Cambridge University Press).

Nel, A., Xia, T., Madler, L., and Li, N. (2006). Toxic potential of materials at the nanolevel. Science *311*, 622-627.

Nie, L., Liu, S.Y., Shen, W.M., Chen, D.Y., and Jiang, M. (2007). One-pot synthesis of amphiphilic polymeric Janus particles and their self-assembly into supermicelles with a narrow size distribution. Angewandte Chemie-International Edition *46*, 6321-6324.

Olson, M.F., and Sahai, E. (2009). The actin cytoskeleton in cancer cell motility. Clin Exp Metastas *26*, 273-287.

Papagrigoriou, E., Gingras, A.R., Barsukov, I.L., Bate, N., Fillingham, I.J., Patel, B., Frank, R., Ziegler, W.H., Roberts, G.C.K., Critchley, D.R.*, et al.* (2004). Activation of a vinculin-binding site in the talin rod involves rearrangement of a five-helix bundle. Embo J *23*, 2942-2951.

Paszek, M.J., Zahir, N., Johnson, K.R., Lakins, J.N., Rozenberg, G.I., Gefen, A., Reinhart-King, C.A., Margulies, S.S., Dembo, M., Boettiger, D.*, et al.* (2005). Tensional homeostasis and the malignant phenotype. Cancer Cell *8*, 241-254.

Patra, D., Gregor, I., and Enderlein, J. (2004). Image analysis of defocused single-molecule images for three-dimensional molecule orientation studies. J Phys Chem A *108*, 6836-6841.

Pelham, R.J., and Wang, Y.L. (1998). Cell locomotion and focal adhesions are regulated by substrate flexibility (vol 94, pg 13661, 1997). P Natl Acad Sci USA *95*, 12070-12070.

Pellegrino, T., Fiore, A., Carlino, E., Giannini, C., Cozzoli, P.D., Ciccarella, G., Respaud, M., Palmirotta, L., Cingolani, R., and Manna, L. (2006). Heterodimers based on CoPt3-Au nanocrystals with tunable domain size. Journal of the American Chemical Society *128*, 6690-6698.

Peng, S., Lee, Y.M., Wang, C., Yin, H.F., Dai, S., and Sun, S.H. (2008). A Facile Synthesis of Monodisperse Au Nanoparticles and Their Catalysis of CO Oxidation. Nano Res *1*, 229-234.

Peng, Y.K., Lai, C.W., Liu, C.L., Chen, H.C., Hsiao, Y.H., Liu, W.L., Tang, K.C., Chi, Y., Hsiao, J.K., Lim, K.E.*, et al.* (2011). A New and Facile Method To Prepare Uniform Hollow MnO/Functionalized mSiO(2) Core/Shell Nanocomposites. Acs Nano *5*, 4177-4187.

Pietuch, A., Bruckner, B.R., Fine, T., Mey, I., and Janshoff, A. (2013). Elastic properties of cells in the context of confluent cell monolayers: impact of tension and surface area regulation. Soft Matter *9*, 11490-11502.

Pietuch, A., and Janshoff, A. (2013). Mechanics of spreading cells probed by atomic force microscopy. Open Biol *3*.

Pollard, T.D., Earnshaw, W.C., and Lippincott-Schwartz, J. (2008). Cell biology (Saunders/Elsevier).

Pullarkat, P.A., Fernandez, P.A., and Ott, A. (2007). Rheological properties of the Eukaryotic cell cytoskeleton. Physics Reports-Review Section of Physics Letters *449*, 29-53.

Radisky, D.C. (2005). Epithelial-mesenchymal transition. J Cell Sci *118*, 4325-4326.

Radmacher, M. (1997). Measuring the elastic properties of biological samples with the AFM. Ieee Eng Med Biol *16*, 47-57.

Reiss, P., Protiere, M., and Li, L. (2009). Core/Shell Semiconductor Nanocrystals. Small *5*, 154-168.

Reynwar, B.J., and Deserno, M. (2011). Membrane-mediated interactions between circular particles in the strongly curved regime. Soft Matter *7*, 8567-8575.

Reynwar, B.J., Illya, G., Harmandaris, V.A., Muller, M.M., Kremer, K., and Deserno, M. (2007). Aggregation and vesiculation of membrane proteins by curvature-mediated interactions. Nature *447*, 461-464.

Robb, M.J., Connal, L.A., Lee, B.F., Lynd, N.A., and Hawker, C.J. (2012). Functional block copolymer nanoparticles: toward the next generation of delivery vehicles. Polym Chem-Uk *3*, 1618-1628.

References

Romer, W., Berland, L., Chambon, V., Gaus, K., Windschiegl, B., Tenza, D., Aly, M.R.E., Fraisier, V., Florent, J.C., Perrais, D*., et al.* (2007). Shiga toxin induces tubular membrane invaginations for its uptake into cells. Nature *450*, 670-U673.

Rosenbluth, M.J., Lam, W.A., and Fletcher, D.A. (2006). Force microscopy of nonadherent cells: A comparison of leukemia cell deformability. Biophys J *90*, 2994-3003.

Ross, A.M., Jiang, Z.X., Bastmeyer, M., and Lahann, J. (2012). Physical Aspects of Cell Culture Substrates: Topography, Roughness, and Elasticity. Small *8*, 336-355.

Rother, J., Pietuch, A., Koll, K., Schladt, T.D., Kohler, O., Schick, I., Tremel, W., and Janshoff, A. (2013). Enhanced motility of alveolar cancer cells induced by CpG-ODN-functionalized nanoparticles. J Nanopart Res *15*.

Rotsch, C., and Radmacher, M. (2000). Drug-induced changes of cytoskeletal structure and mechanics in fibroblasts: An atomic force microscopy study. Biophys J *78*, 520-535.

Rust, M.J., Bates, M., and Zhuang, X.W. (2006). Sub-diffraction-limit imaging by stochastic optical reconstruction microscopy (STORM). Nat Methods *3*, 793-795.

Salbreux, G., Charras, G., and Paluch, E. (2012). Actin cortex mechanics and cellular morphogenesis. Trends Cell Biol *22*, 536-545.

Sandmann, R., Henriques, S.S.G., Rehfeldt, F., and Koster, S. (2014). Micro-topography influences blood platelet spreading. Soft Matter.

Schafer, E., Kliesch, T.T., and Janshoff, A. (2013). Mechanical Properties of Giant Liposomes Compressed between Two Parallel Plates: Impact of Artificial Actin Shells. Langmuir *29*, 10463-10474.

Schick, I., Lorenz, S., Gehrig, D., Schilmann, A.-M., Bauer, H., Panthöfer, M., Fischer, K., Strand, D., Laquai, F., and Tremel, W. (2014). Multifunctional Two-Photon Active Silica-Coated Au@MnO Janus Particles for Selective Dual Functionalization and Imaging. Journal of the American Chemical Society *136*, 2473-2483.

Schladt, T.D., Graf, T., and Tremel, W. (2009). Synthesis and Characterization of Monodisperse Manganese Oxide Nanoparticles-Evaluation of the Nucleation and Growth Mechanism. Chem Mater *21*, 3183-3190.

Schladt, T.D., Koll, K., Prufer, S., Bauer, H., Natalio, F., Dumele, O., Raidoo, R., Weber, S., Wolfrum, U., Schreiber, L.M*., et al.* (2012). Multifunctional superparamagnetic MnO@SiO2 core/shell nanoparticles and their application for optical and magnetic resonance imaging. J Mater Chem *22*, 9253-9262.

Schladt, T.D., Shukoor, M.I., Schneider, K., Tahir, M.N., Natalio, F., Ament, I., Becker, J., Jochum, F.D., Weber, S., Kohler, O*., et al.* (2010). Au@MnO Nanoflowers: Hybrid Nanocomposites for Selective Dual Functionalization and Imaging. Angewandte Chemie-International Edition *49*, 3976-3980.

Schneider, D., Baronsky, T., Pietuch, A., Rother, J., Oelkers, M., Fichtner, D., Wedlich, D., and Janshoff, A. (2013). Tension Monitoring during Epithelial-to-Mesenchymal Transition Links the Switch of Phenotype to Expression of Moesin and Cadherins in NMuMG Cells. Plos One *8*.

Schneider, D., Tarantola, M., and Janshoff, A. (2011). Dynamics of TGF-beta induced epithelial-to-mesenchymal transition monitored by Electric Cell-Substrate Impedance Sensing. Bba-Mol Cell Res *1813*, 2099-2107.

Schroede.Te (1972). Contractile Ring .2. Determining Its Brief Existence, Volumetric Changes, and Vital Role in Cleaving Arbacia Eggs. J Cell Biol *53*, 419-&.

Sen, S., Subramanian, S., and Discher, D.E. (2005). Indentation and adhesive probing of a cell membrane with AFM: Theoretical model and experiments. Biophys J *89*, 3203-3213.

Shafie, S.M., and Liotta, L.A. (1980). Formation of Metastasis by Human-Breast Carcinoma-Cells (Mcf-7) in Nude-Mice. Cancer Lett *11*, 81-87.

Shi, W.L., Sahoo, Y., Zeng, H., Ding, Y., Swihart, M.T., and Prasad, P.N. (2006). Anisotropic growth of PbSe nanocrystals on Au-Fe3O4 hybrid nanoparticles. Adv Mater *18*, 1889-+.

Shroff, S.G., Saner, D.R., and Lal, R. (1995). Dynamic Micromechanical Properties of Cultured Rat Atrial Myocytes Measured by Atomic-Force Microscopy. Am J Physiol-Cell Ph *269*, C286-C292.

Shukoor, M.I., Natalio, F., Tahir, M.N., Wiens, M., Tarantola, M., Therese, H.A., Barz, M., Weber, S., Terekhov, M., Schroder, H.C*., et al.* (2009). Pathogen-Mimicking MnO Nanoparticles for Selective Activation of the TLR9 Pathway and Imaging of Cancer Cells. Adv Funct Mater *19*, 3717-3725.

Smith, B.A., Tolloczko, B., Martin, J.G., and Grutter, P. (2005). Probing the viscoelastic behavior of cultured airway smooth muscle cells with atomic force microscopy: Stiffening induced by contractile agonist. Biophys J *88*, 2994-3007.

Sohaebuddin, S.K., Thevenot, P.T., Baker, D., Eaton, J.W., and Tang, L.P. (2010). Nanomaterial cytotoxicity is composition, size, and cell type dependent. Part Fibre Toxicol *7*.

Sollich, P. (1998). Rheological constitutive equation for a model of soft glassy materials. Phys Rev E *58*, 738-759.

Subramanian, V., Wolf, E.E., and Kamat, P.V. (2004). Catalysis with TiO2/gold nanocomposites. Effect of metal particle size on the Fermi level equilibration. Journal of the American Chemical Society *126*, 4943-4950.

Suresh, S. (2007). Biomechanics and biophysics of cancer cells. Acta Mater *55*, 3989-4014.

Suresh, S., Spatz, J., Mills, J.P., Micoulet, A., Dao, M., Lim, C.T., Beil, M., and Seufferlein, T. (2005). Connections between single-cell biomechanics and human disease states: gastrointestinal cancer and malaria. Acta Biomater *1*, 15-30.

Sussan, T.E., Pletcher, M.T., Murakami, Y., and Reeves, R.H. (2005). Tumor suppressor in lung cancer I (TSLCI) alters tumorigenic growth properties and gene expression. Mol Cancer *4*.

Takei, K., and Haucke, V. (2001). Clathrin-mediated endocytosis: membrane factors pull the trigger. Trends Cell Biol *11*, 385-391.

References

Tarantola, M., Pietuch, A., Schneider, D., Rother, J., Sunnick, E., Rosman, C., Pierrat, S., Sonnichsen, C., Wegener, J., and Janshoff, A. (2011). Toxicity of gold-nanoparticles: Synergistic effects of shape and surface functionalization on micromotility of epithelial cells. Nanotoxicology *5*, 254-268.

Tarantola, M., Schneider, D., Sunnick, E., Adam, H., Pierrat, S., Rosman, C., Breus, V., Sonnichsen, C., Basche, T., Wegener, J.*, et al.* (2009). Cytotoxicity of Metal and Semiconductor Nanoparticles Indicated by Cellular Micromotility. Acs Nano *3*, 213-222.

Tee, S.Y., Fu, J.P., Chen, C.S., and Janmey, P.A. (2011). Cell Shape and Substrate Rigidity Both Regulate Cell Stiffness. Biophys J *100*, L25-L27.

Tenzer, S., Docter, D., Kuharev, J., Musyanovych, A., Fetz, V., Hecht, R., Schlenk, F., Fischer, D., Kiouptsi, K., Reinhardt, C.*, et al.* (2013). Rapid formation of plasma protein corona critically affects nanoparticle pathophysiology. Nat Nanotechnol *8*, 772-U1000.

Teo, B.K.K., Wong, S.T., Lim, C.K., Kung, T.Y.S., Yap, C.H., Ramagopal, Y., Romer, L.H., and Yim, E.K.F. (2013). Nanotopography Modulates Mechanotransduction of Stem Cells and Induces Differentiation through Focal Adhesion Kinase. Acs Nano *7*, 4785-4798.

Thakur, S., Massou, S., Benoliel, A.M., Bongrand, P., Hanbucken, M., and Sengupta, K. (2012). Depth matters: cells grown on nano-porous anodic alumina respond to pore depth. Nanotechnology *23*.

Thiery, J.P. (2002). Epithelial-mesenchymal transitions in tumour progression. Nat Rev Cancer *2*, 442-454.

Thorne, C., Grabb, W.C., Smith, J.W., and Beasley, R.W. (2007). Grabb and Smith's Plastic Surgery (Wolters Kluwer Health/Lippincott Williams & Wilkins).

Treuel, L., Jiang, X.E., and Nienhaus, G.U. (2013). New views on cellular uptake and trafficking of manufactured nanoparticles. J R Soc Interface *10*.

Trichet, L., Le Digabel, J., Hawkins, R.J., Vedula, R.K., Gupta, M., Ribrault, C., Hersen, P., Voituriez, R., and Ladoux, B. (2012). Evidence of a large-scale mechanosensing mechanism for cellular adaptation to substrate stiffness. P Natl Acad Sci USA *109*, 6933-6938.

Vasir, J.K., and Labhasetwar, V. (2008). Quantification of the force of nanoparticle-cell membrane interactions and its influence on intracellular trafficking of nanoparticles. Biomaterials *29*, 4244-4252.

Walde, P., Cosentino, K., Engel, H., and Stano, P. (2010). Giant Vesicles: Preparations and Applications. Chembiochem *11*, 848-865.

Wang, H.B., Dembo, M., and Wang, Y.L. (2000). Substrate flexibility regulates growth and apoptosis of normal but not transformed cells. Am J Physiol-Cell Ph *279*, C1345-C1350.

Wegener, J., Keese, C.R., and Giaever, I. (2000). Electric cell-substrate impedance sensing (ECIS) as a noninvasive means to monitor the kinetics of cell spreading to artificial surfaces. Exp Cell Res *259*, 158-166.

Winter, R., and Noll, F. (1998). Methoden der Biophysikalischen Chemie (Teubner B.G. GmbH).

Wittelsberger, S.C., Kleene, K., and Penman, S. (1981). Progressive Loss of Shape-Responsive Metabolic Controls in Cells with Increasingly Transformed Phenotype. Cell *24*, 859-866.

Wolfenson, H., Bershadsky, A., Henis, Y.I., and Geiger, B. (2011). Actomyosin-generated tension controls the molecular kinetics of focal adhesions. J Cell Sci *124*, 1425-1432.

Wu, X.H., and Wang, S.F. (2012). Regulating MC3T3-E1 Cells on Deformable Poly(epsilon-caprolactone) Honeycomb Films Prepared Using a Surfactant-Free Breath Figure Method in a Water-Miscible Solvent. Acs Appl Mater Inter *4*, 4966-4975.

Wurm, F., and Kilbinger, A.F.M. (2009). Polymeric Janus Particles. Angewandte Chemie-International Edition *48*, 8412-8421.

Xu, C.J., Xu, K.M., Gu, H.W., Zheng, R.K., Liu, H., Zhang, X.X., Guo, Z.H., and Xu, B. (2004). Dopamine as a robust anchor to immobilize functional molecules on the iron oxide shell of magnetic nanoparticles. Journal of the American Chemical Society *126*, 9938-9939.

Xu, W.W., Mezencev, R., Kim, B., Wang, L.J., McDonald, J., and Sulchek, T. (2012). Cell Stiffness Is a Biomarker of the Metastatic Potential of Ovarian Cancer Cells. Plos One *7*.

Yamada, S., Wirtz, D., and Kuo, S.C. (2000). Mechanics of living cells measured by laser tracking microrheology. Biophys J *78*, 1736-1747.

Yamamoto, S., Tanaka, M., Sunami, H., Ito, E., Yamashita, S., Morita, Y., and Shimomura, M. (2007). Effect of honeycomb-patterned surface topography on the adhesion and signal transduction of porcine aortic endothelial cells. Langmuir *23*, 8114-8120.

Yue, T., Zhang, X., and Huang, F. (2014). Membrane monolayer protrusion mediates a new nanoparticle wrapping pathway. Soft Matter *10*, 2024-2034.

Yue, T.T., Wang, X.J., Huang, F., and Zhang, X.R. (2013). An unusual pathway for the membrane wrapping of rodlike nanoparticles and the orientation- and membrane wrapping-dependent nanoparticle interaction. Nanoscale *5*, 9888-9896.

Zellner, R., Blechinger, J., Bräuchle, C., Hilger, I., Janshoff, A., Lademann, J., Mailänder, V., Meinke, M.C., Nienhaus, G.U., Patzelt, A.*, et al.* (2013). Biological Responses to Nanoparticles. In Safety Aspects of Engineered Nanomaterials (Pan Stanford Publishing), pp. 157-218.

Zhang, G., Long, M., Wu, Z.Z., and Yu, W.Q. (2002a). Mechanical properties of hepatocellular carcinoma cells. World J Gastroentero *8*, 243-246.

Zhang, Y., Kohler, N., and Zhang, M.Q. (2002b). Surface modification of superparamagnetic magnetite nanoparticles and their intracellular uptake. Biomaterials *23*, 1553-1561.

Zhou, E.H., Trepat, X., Park, C.Y., Lenormand, G., Oliver, M.N., Mijailovich, S.M., Hardin, C., Weitz, D.A., Butler, J.P., and Fredberg, J.J. (2009). Universal behavior of the osmotically compressed cell and its analogy to the colloidal glass transition. P Natl Acad Sci USA *106*, 10632-10637.

References

Ziegler, C.G., Brown, J.W., Schally, A.V., Erler, A., Gebauer, L., Treszl, A., Young, L., Fishman, L.M., Engel, J.B., Willenberg, H.S.*, et al.* (2009). Expression of neuropeptide hormone receptors in human adrenal tumors and cell lines: Antiproliferative effects of peptide analogues. P Natl Acad Sci USA *106*, 15879-15884.

Zimmer, C. (2009). Origins on the Origin of Eukaryotes. Science *325*, 666-668.

Zimmerberg, J., and McLaughlin, S. (2004). Membrane curvature: How BAR domains bend bilayers. Curr Biol *14*, R250-R252.

7. List of figures

8. List of tables

9. List of abbreviations

AAO	anodized aluminum oxide
AAS	atomic absorption spectrometry
AC	alternating current
AFM	atomic force microscope
ADP	adenosine diphosphate
ATP	adenosine triphosphate
Bleb	blebbistatin
BSA	bovine serum albumine
CM	cardiomyocyte
CME	clathrin mediated endocytosis
CPE	constant phase element
CTAB	cetyl trimethylammonium bromide
CytD	cytochalasinD
DLS	dynamic light scattering
DMEM	Dulbecco's modified eagle medium
DNA	deoxyribonucleic acid
DOPA	dopamine-anchor
DOPC	1,2-dioleoyl-s,n-glycerol-3-phosphatidylcholine
ECIS	electric cell-substrate impedance sensing
ECM	extracellular matrix
EMT	epithelial-to-mesenchymal transition
ERK	extracellular signal regulated kinase
FA	focal adhesion
FAK	focal adhesion kinase
Fb	fibroblast
FCS	fetal calf serum
FFT	fast Fourier transformation
FITC	fluorescein isothiocynate
FLIC	fluorescence interference contrast
FLIM	fluorescence lifetime imaging
FRET	Förster resonance energy transfer
GDA	glutardialdehyde
GDP	guanosine diphosphate

GTP	guanosine triphosphate
GUV	giant unilamellar vesicle
HEPES	4-(2-hydroxyethyl)-1-piperazineethanesulfonic acid
ITO	iridium tin oxide
κ_B	bending modulus
k_B	Boltzmann constant
L_p	persitence length
MAPK1	mitogen-activated proteins kinase 1
MEM	minimum essential medium
MIET	metal induced energy transfer
µRIU	reflectivity units
MTS	3-(4,5-dimethylthiazol-2-yl)-5-(3-carboxymethoxyphenyl)-2-(4-sulfophenyl)-2H-tetrazolium
NAD	nicotinamide adenine dinucleotide
NP	nanoparticle
ODT	1-octadecanethiol
PAA	polyacrylamide
p.a.	pro analysi
PBS	phosphate buffered saline
PDMS	polydimethylsiloxane
PEG	polyethylene glycol
PFA	paraformaldehyde
PKC	protein kinase C
PLSD	power-law structural damping
RNA	ribonucleic acid
ROCK	Rho-associated protein kinase
ROS	reactive oxygen species
SEM	scanning electron microscope/microscopy
SICM	scanning ion conductance microscope/microscopy
SMAD	small mother against decapentaplegic
SPR	surface plasmon resonance
SUV	small unilamellar vesicle
TEM	transmission electron microscope/microscopy
TGF-β1	transforming growth factor β1
TIRF	total internal reflectance microscopy
TR-DHPE	TexasRed® 1,2-dihexadecanoyl-sn-glycero-3- phosphoethanolamine

ULF   unit-length filament

Danksagung

An dieser Stelle möchte ich mich bei den Menschen bedanken, die mich während meiner Doktorarbeit unterstützt haben.

Ich danke:

- Anna für die vielen Unterhaltungen und lustigen Momente während der Pausen, im Büro oder auch bei langen Autofahrten.

- Marco für die tolle Zusammenarbeit sowie seine musikalische Kompetenz, eine fantastische Zeit und Obdach in den USA sowie viele Stunden Bundesliga.

- Edith Schäfer für viele aufheiternde Momente, ihre direkte Art und eine fantastische Zeit und Obdach in den USA. Nur das *whale watching* mit dem Kanu hätte nicht sein müssen :-).

- Milena dafür, dass ich mich trotz der weiten Entfernung zum Saarland doch irgendwie wie zuhause gefühlt habe.

- Gesa für ihre unkomplizierte Art, ihre Hilfsbereitschaft und ihre Toleranz gegenüber Menschen, die regelmäßig ihre Couch bevölkern um Fußball zu schauen.

- Bärbel und Eva für das tolle Arbeitsklima in den ersten Jahren.

- Allen gegenwärtigen sowie ehemaligen Mitgliedern der Arbeitskreise Janshoff und Steinem, die ich noch nicht genannt habe für eine tolle Zeit.

- Benni, Jonas und den Jungs für legendäre Abende und unvergessliche OpenFlair Besuche.

- Sven, Anne. Frank und Ela für ihre Freundschaft und viele, schöne Wochenenden in Mainz oder Göttingen

- Helen für alles, was sie für mich getan hat.

- meiner Schwester und meinem Schwager für ein immer offenes Ohr sowie meinem Neffen und meiner Nichte für die wunderbaren, aufheiternden Momente.

- meinen Großeltern.

- meinen Eltern für alles, was sie für mich getan haben sowie für die seelische und moralische Unterstützung.

Curriculum Vitae

Name	Jan Henrik Rother
Born	01/21/1985 in Birkenfeld (Nahe)
Address	
Marital status	
Nationality	German

Education

1995 – 2004	Arnold-Janssen Gymnasium, Sankt Wendel

Acadamic studies

10/2004 – 05/2010	Studies of „biomedical chemistry" at the Johannes Gutenberg-University, Mainz
05/2010	Diploma degree in biomedical chemistry (graduate chemist, grade: 1.0 out of 1.0)
	Diploma thesis at the Institute of Inorganic and Analytical Chemistry (Johannes Gutenberg-University, Mainz) in the group of Prof. Dr. W. Tremel; Title of diploma thesis: *„Wirkung immunstimulatorischer Nanopartikel auf humane Krebszellen in vitro"*
Since 10/2010 –	PhD student at the Institute of Physical Chemistry at Georg-August-University, Göttingen, in the group of Prof. Dr. A. Janshoff.

Stipends

05/2011 – 04/2013	PhD fellowship of Boehrringer Ingelheim Fonds

Publications

1. Tarantola, M., A. Pietuch, D. Schneider, **J. Rother**, E. Sunnick, C. Rosman, S. Pierrat, C. Sonnichsen, J. Wegener and A. Janshoff (2011). "Toxicity of gold-nanoparticles: Synergistic effects of shape and surface functionalization on micromotility of epithelial cells." Nanotoxicology **5**(2): 254-268.

2. Schneider, D., T. Baronsky, A. Pietuch, **J. Rother**, M. Oelkers, D. Fichtner, D. Wedlich and A. Janshoff (2013). "Tension Monitoring during Epithelial-to-

Mesenchymal Transition Links the Switch of Phenotype to Expression of Moesin and Cadherins in NMuMG Cells." <u>Plos One</u> **8**(12).

3. **Rother, J.**, A. Pietuch, K. Koll, T. D. Schladt, O. Kohler, I. Schick, W. Tremel and A. Janshoff (2013). "Enhanced motility of alveolar cancer cells induced by CpG-ODN-functionalized nanoparticles." <u>Journal of Nanoparticle Research</u> **15**(12).

4. Chizhik, A. I., **J. Rother**, I. Gregor, A. Janshoff and J. Enderlein (2014). "Metal-induced energy transfer for live cell nanoscopy." <u>Nat Photon</u> **8**(2): 124-127.